Acoustical Physics, Vol. 46, No. 5, 2000, pp. 505–510. Translated from Akusticheskiĭ Zhurnal, Vol. 46, No. 5, 2000, pp. 581–587.

Vertical Structure of the Acoustic Characteristics of Deep Scattering Layers in the Ocean

I. B. Andreeva, N. N. Galybin, and L. L. Tarasov

Andreev Acoustics Institute, Russian Academy of Sciences, ul. Shvernika 4, Moscow, 117036 Russia

e-mail: bvp@akin.ru

Received December 27, 1999

Abstract—Quantitative data on the vertical structure of the acoustic characteristics of deep scattering layers in the ocean are obtained for the first time from multiple full-scale measurements. The measurement procedure used to obtain the acoustic data for thousands of geographic points of the World Ocean in the frequency range from 3 to 20 kHz is briefly described. A simplified model of the vertical structure under study is suggested in the form of several scattering sheets that are split in depth. The parameters of the model are the depths of the sheets, the contribution of every sheet to the total column strength, and the mean backscattering coefficient corresponding to every sheet. The model is illustrated by the description of the daytime structure along five sections in the Atlantic Ocean; the lengths of these sections measure up to several thousand kilometers. The parameters of the model are shown to depend on the oceanic conditions and the sounding frequencies. The latter is evidence that, depending on frequency, the scattering is governed by different populations of the scattering layer inhabitants differently responding to variations in hydrology. In particular, for sections crossing powerful currents, the changes in the vertical structure and the variations the model parameters essentially depend on the frequency of sound. © *2000 MAIK "Nauka/Interperiodica".*

The properties of acoustic inhomogeneities of biological nature in the bulk of ocean waters continue to attract the interest of researchers (see, e.g., [1]). The horizontally extended accumulations of small living creatures called deep scattering layers (DSL) represent one of the most widespread type of inhomogeneities. They were investigated in many papers; however, this phenomenon is far from being exhaustively understood today. In particular, the vertical structure of the acoustic characteristics of DSL and its dependence on various factors are poorly known.

In a deep ocean, the scattering layers are characterized by a fairly complicated structure in the vertical direction. This structure depends on the ocean area and the hydrological and biological features characteristic of this area. The acoustical structure of DSL is poorly understood; at least, as far as we know, there is no exhaustive consideration of this problem in the literature. The features of this structure are known only qualitatively; namely, by daytime, the scattering layers descend to depths of hundreds of meters, and, by nighttime, they rise closer to the surface. This phenomenon is called diurnal vertical migrations of DSL. It is known to be less pronounced in polar regions where other temporal scales govern the daytime duration. The vast majority of researchers who carried out acoustic measurements published only the results concerning the total column strength at a given point in the ocean and give no information on the interval of depths where the scattering occurs.

This paper describes our data (obtained during the expeditions organized by the Andreev Acoustics Institute, Russian Academy of Sciences) on the vertical structure of the acoustic characteristics of DSL for a number of areas of the Atlantic ocean. The data include the depth-dependent coefficient of volume backscattering m and the column strength M, which is the integral of m over the depth z. The information was obtained in daytime for sounding frequencies from 3 to 20 kHz. The experimental records are stored in the Andreev Acoustics Institute's database on the acoustic properties of DSL [2].

During these expeditions of the Andreev Acoustics Institute, we used several procedures for studying the vertical structure of DSL. On the one hand, these procedures differ in their errors and the reliability of the results, and, on the other hand, they are of different complexity and require different time for carrying out the full-scale measurements. The most reliable data were obtained either by sounding the scattering accumulations with directional multifrequency cw/pulsed lowered systems of transmission and reception or by alternative acoustic sounding of these accumulations with explosive sound sources from above and from below. The first procedure requires the vessel to be equipped with complicated stationary equipment. Both these procedures are time-consuming; the measurements at a single point can take several hours. Some results obtained with the second procedure are published in [3] and demonstrate the unique potentiality of

1063-7710/00/4605-0505$20.00

the procedure for describing the acoustic structure of DSL during both daytime and night.

The well known procedure using explosions of small charges in the upper water layer as the sound source (see, e.g., [4]) offers a "prompt" method for determining the acoustic characteristics of DSL. This is not a precision procedure; however, it appears simple and convenient for sounding the DSL in a wide range of frequencies and allows one to estimate the fundamental characteristics of DSL, including their vertical structure. We obtained the data given below according to this very procedure.

We used a small trinitrotoluene charge (0.2 kg), which was detonated in water near the surface, and a broadband omnidirectional receiver located near the charge to record the pressure p of the scattered signal as a function of time t. Within the first 0.2–0.3 s after the explosion, the signal scattered by the surface could prevail; however, later, the sound scattering in the water bulk predominated. The surface scattering determined the skip depth of about 150–200 m and provided no reliable information on the vertical structure of DSL during hours of darkness. The signal processing started from six 1/3-octave filters in the range from 3 to 20 kHz. In every frequency band, the dependence $p(t)$ was squared and detected. At this point, we introduced corrections for the sound divergence and absorption during the propagation, as well as the factors describing the energy characteristics of the source and the receiver, to calculate the column strength M as a function of time t. Then, we recalculated the function $M(t)$ for every frequency into $M(z)$ assuming that the accumulation of scatterers is a plane-layered one. The total column strength is determined as $M_0 = M(z_{max})$, where z_{max} is the maximum depth of DSL recorded in the experiment.

At this point, the standard processing of experimental records is usually terminated (see, e.g., [5]); however, we were able to advance the processing. In principle, one can find the volume backscattering coefficient as a function of depth $m(z)$ by differentiating the measured function $M(z)$ with respect to z. In our processing, we used a simplified procedure for calculating the derivative. Namely, we approximated the curve $M(z)$ by several intersecting straight-line segments whose slopes were considered, to a certain scale, as the mean values of m over the approximation intervals (between the points of intersection). The number of segments and their slopes were chosen so as to (i) reflect the behavior of $M(z)$ as accurately as possible and (ii) to ensure that the average values of m in adjacent intervals differ by no less than 5 dB and exceed the threshold values. The choice of the number of segments (usually three segments or less) was the task of the operator, and this fact introduced an arbitrary element in the processing.

We considered the intervals of depths selected according to the above procedure as separate sheets of the deep scattering layer, and the whole set of these sheets as the model of the DSL vertical structure. The sheets were numbered. For every ith sheet, we calculated the depths of its upper and lower boundaries, the backscattering coefficient m determined as the mean value of the backscattering coefficient between the upper and lower boundaries, and the percentage ΔM_i corresponding to the contribution of the sheet to the total column strength M_0 of the layer. These characteristics were considered as the parameters of the DSL model. The sheets of the DSL model could either contact the adjacent sheets or be separated from them by layers of clean water. We considered the clean water layer as significant when its width exceeded 20 m. For a narrower clean water layer, the sheets were combined in the course of processing. The data given below for M and m are measured in decibels relative to unity and to 1 m^{-1}, respectively.

Each experiment consisted of 5–12 explosions following one after another every 3–5 min with subsequent averaging of the measured results. In a single experiment, the scatter in the measured column strength and scattering coefficient did not exceed 1.0–1.5 dB, from one explosion to another; the corresponding scatter in the depths of the sheet boundaries was below 10–15 m. Such a scatter can be considered as characteristic of random errors inherent in the measurement procedure. For different experiments separated in time by several hours or days, the scattering in the experimental data was more significant; however, this scatter characterizes the instability of the phenomenon rather than the measurement error. All experiments were carried out with the drifting vessel, which did not allow one to reliably distinguish between the spatial and temporal variability of the results.

Figure 1 shows the map with sections *1–5* along which the acoustic characteristics described in this paper were measured. The measurements were carried out from 1960 to 1974 aboard the research vessels *Petr Lebedev* and *Mikhail Lomonosov.*

Figure 2 shows the model of the vertical acoustic structure of DSL typical of a deep ocean and obtained from the data measured along section *1*. The depths of the boundaries of the model sheets are slightly smoothed along the section. The curves correspond to frequencies 5 and 20 kHz characteristic of DSL. For these frequencies, scatterers of different types predominate in DSL. At a frequency of 5 kHz (and near this frequency), the resonance or nearly resonance scattering on swim bladders of fishes predominates. At a relatively high frequency of 20 kHz, the tissues of various creatures with size of several centimeters and greater play the predominant role in the scattering [3]. For frequencies below 5 kHz, the level of scattering in DSL sharply decreases, and, for frequencies above 20 kHz, the results loose reliability because of the strong absorption of the signal in the course of its propagation.

In the eastern part of the section, the model of the DSL structure shows three scattering sheets for both frequencies. The middle sheet (*1*) produces the major

portion of the scattered field; the inequality $\Delta M_1 \geq \Delta M_2 + \Delta M_3$ (the substripts correspond to the sheet numbers) holds along the entire section, and the magnitude of m_1 exceeds both m_2 and m_3. We will call such a sheet the principal sheet of the model, and sheets *2* and *3* the upper and lower sheets, respectively.

At a frequency of 5 kHz, only two sheets occurred in the western part of the section. The principal sheet (*1*) is extended from 700 to 1100 m, its percentage in the column strength ΔM_1 is about 90%, and the coefficient m_1 is about –75 dB. The thickness of the sheet gradually decreases in the eastern direction, and the sheet itself raises toward the surface. In the eastern part of the section, especially in the region of mixture of the Atlantic and Mediterranean waters, the depth of this sheet was very unstable and disorderly varied by hundreds of meters within several hours. The scattering coefficient m_1 of the principal sheet showed a stable tendency toward increasing in the Eastern direction; however, its magnitude randomly varied along the section by several decibels.

Above the principal sheet, a thinner and weaker upper sheet *2* was observed at many points of the section, and it was adjacent to the principal sheet. Sheet *2* is characterized by ΔM_2 below 5–10% and the coefficient m_2 by 5–8 dB less than the corresponding coefficient of the principal sheet. At lower frequencies, the lower sheet *3* of the DSL model occurred only in the eastern half of the section. Its bottom boundary was as deep as 1000–1200 m and over. Despite the fact that the scattering coefficient m_3 was appreciably less than the corresponding coefficient of the principal sheet, the sheet *3* substantially contributed to the total column strength. This contribution was as high as nearly 50% for longitudes between 30° W and 40° W and exceeded 25% for other longitudes.

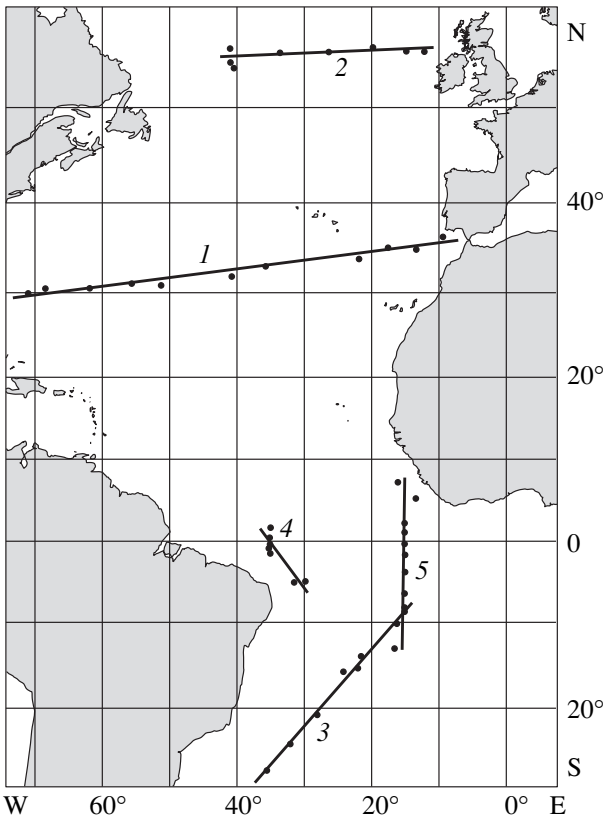

Fig. 1. Location and numbers of the sections along which the vertical structure of the acoustic characteristics of DSL is described. The dots on the map correspond to the measurement sites.

At a frequency of 20 kHz, the pattern of the scatterer stratification was different. In this case, the model is composed of three sheets occupying the depth interval from 300 to 1000 m, and this pattern holds within the

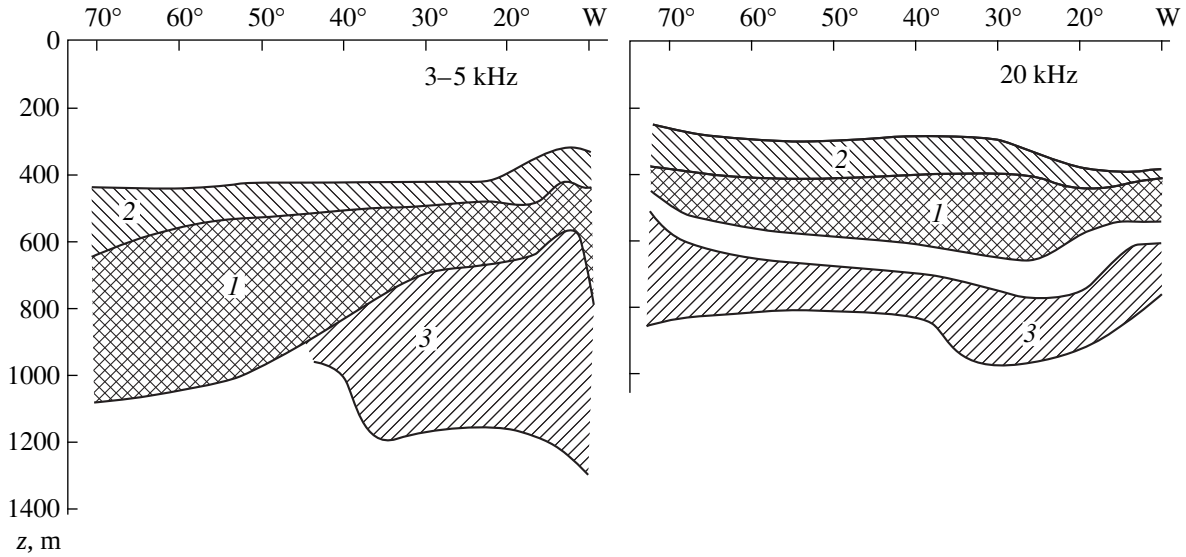

Fig. 2. Model of the vertical structure of DSL along section *1* across the Atlantic Ocean: (*1*) the principal sheet, (*2*) the upper sheet, and (*3*) the lower sheet.

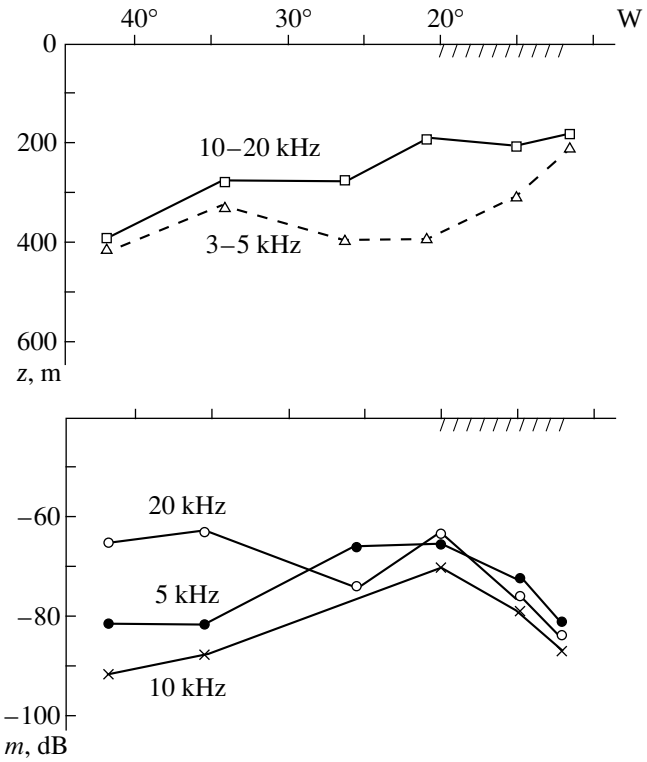

Fig. 3. Depth of the upper boundary and the mean scattering coefficient *m* of the principal scattering sheet along section *2*. The hatched region shows the position of the channel of the North Atlantic Current.

whole section. The principal and upper sheets are adjacent to one another, and the lower sheet is separated from the principal sheet by a 100-m-thick layer of "clean" water. The principal sheet contribution to the column strength ΔM_1 is about 80% at the ends of the section and decreases to 55–60% in the middle. This effect occurs mainly due to an increase in the scattering intensity of the lower sheet *3* where ΔM_3 in the middle of the section was as high as 40% and even greater. The contribution of the upper sheet ΔM_2 was everywhere below several percent. The scattering coefficients m_i of all the sheets decreased from the west to east; in the principal sheet, this coefficient decreased from –73 to –80 dB, and in the upper and lower sheets, it decreased from approximately –83 to –88 dB.

A simpler structure of DSL was recorded in the Northern Atlantic, on section *2* passing along the latitude 55° N and crossing the North Atlantic Current. Here, the DSL structure can be described by a single-sheet model with the sheet thickness of about 200 m. The pattern holds for all frequencies and along the whole section. Due to this fact, we omit the sheet thickness and show only the depth of the upper boundary of the sheet (see Fig. 3). This depth and the scattering coefficient *m* appreciably depend on both the frequency and the position of the measurement point on the section. For all frequencies, the depth of the sheet decreases from west to east, and the low-frequency scatterers occur deeper than the high-frequency ones. In the stream and near the stream, the difference between these depths was about 200 m. At the eastern end of the section, the coefficient *m* averaged over the thickness of the sheet was very low and measured from –85 to –90 dB; in the current zone, it increased to about –70 dB, and at the western end of the section, it again decreased for lower frequencies and increased at a frequency of 20 kHz. This is evidence that there are differences in the behavior of the inhabitants of DSL of different acoustic types.

The next section for which we describe the vertical acoustic structure of DSL is section *3* passing in the Southern Hemisphere, from the equatorial zone to the southwest (see map in Fig. 1). The beginning of this section corresponds to tropical waters, which are relatively rich in the biological sense, and its end falls on the biologically poor region of anticyclone circulation. This fact correlates with the general variation of the DSL intensity along the section, which was most pronounced for lower frequencies. Two series of measurements were carried out along this section (February 1961 and September 1963). Only slight systematic differences were found between these series, although the scatter of data measured in each of the series was quite appreciable (especially for higher frequencies).

For a frequency of 5 kHz, the three-sheet model can be used to describe the vertical DSL structure along the entire section. The principal (middle) sheet *1* was usually characterized by $\Delta M_1 \cong 80$–90%, the thickness about 200 m, and the coefficient m_1 showing a general decrease in the southern direction despite its chaotic variations from –75 to –85 dB. From north to south, the principal sheet gradually descended, and the depth of its upper boundary increased from 450 to 600 m. A thin upper sheet *2* about 50 m thick occurred much higher, at depths of about 300 m. The parameters characteristic of this sheet at the frequency 5 kHz are as follows: ΔM_2 about 10% and *m* from –85 to –90 dB. In the low-frequency range, the lower sheet *3* was could be detected only for a relatively small number of points lying on the southern half of the section. This sheet was almost everywhere adjacent to the principal sheet, and its lower boundary was as deep as 1200–1300 m; at a frequency of 5 kHz, its contribution to the total column strength was about 25% despite the small scattering coefficient m_3. This model failed only for the southern end point of the section. At a frequency of 5 kHz, this point is characterized by the existence of two principal sheets with approximately equal values of ΔM about 40–50% and the scattering coefficients about –77 dB, but essentially different depths: 500–700 m and 1100–1300 m. The interval between these sheets is filled with a weakly scattering medium characterized by $m \le 90$ dB and ΔM of several percent. Generally, this interval of depths should be identified as an additional sheet of the model. The occurrence of the second, strongly scattering sheet at greater depths resulted in an increase in the

total column strength at this point by more then 10 dB. It is quite probable that more accurate measurement procedures (such as the above-mentioned procedure of deep-water sounding) can provide an opportunity for detecting the deeper, strongly scattering sheet for other points of the section.

For the frequencies 10 and 20 kHz, the pattern of the vertical structure of DSL along section *3* showed a still lesser stability, but allowed a description in terms of the three-sheet model. Independently of the season, the upper boundary of the principal sheet was located at a depth of about 400 m in the northern part of the section and gradually descended in the southern direction to a depth of 500 m in February, and to a depth of 650 m in September. In line with this process, the thickness of the principal sheet decreased from 200 to ~100 m. The percentage of the column strength ΔM_1 disorderly varied along the section from 95 to 70% showing a tendency of decreasing toward the south. The scattering coefficient m_1 also showed random variations from one measuring point to another in every expedition; the interval of variations was from –65 to –80 dB. For higher frequencies, the weaker upper and lower sheets were recorded irregularly. The upper sheet was adjacent to the principal sheet, its contribution to the column strength was only several percent, and its thickness measured tens of meters. The lower sheet extended to a depth of 1000 m and over, but was recorded for not all points of the section (more often, in September); it is characterized by a relatively high value of ΔM—up to 30% for the southern part of the section. It should be admitted that, for higher frequencies, the quantitative information on the weakly scattering sheets along this section is fairly contradictory and hardly can provide reliable data.

Consider now the sections crossing the channel of the Southern Equatorial Current. We have the results for two sections of this kind (sections *4* and *5* in Fig. 1). These results show that the vertical structure of DSL drastically changes in the zone of the current.

The western equatorial section *4* passed near the South America. To avoid coastal effects, the section was made not strictly along the meridian. The section starts at 2° N, i.e., in the northern part of the Equatorial Current channel. The scattering region was not clearly defined here and extended from 300–400 to 800 m for higher frequencies, and even to 1200 m for lower frequencies. The sheet structure was formed closer to the equator and was especially prominent for frequencies 5 and 20 kHz.

At the frequency 5 kHz, the two-sheet model is characteristic of section *4*. Near the equator, the principal sheet occupies the depths between 630 and 750 m and is characterized by $\Delta M_1 \cong 90\%$ and the scattering coefficient $m_1 \cong -50$ dB. In the southern part of the section, the sheet descended to depths 800–900 m, its ΔM_1 decreased to 60–70%, and its scattering coefficient m_1 decreased to –60 dB. The upper sheet *2* was not adjacent to the principal sheet and occupied the depths between 200 and 400 m along the whole section. Near the equator, its contribution to the column strength was small, and its scattering coefficient m_2 was about –65 dB. In the southern part of the section, its scattering level increased, and the value of ΔM_2 was as high as 30 to 40%.

At a frequency of 20 kHz, only one sheet was clearly defined over most of the section. It occupied depths between 300 and 800 m in the northern part of the section, and depths between 250 and 450 m to the South from the equator. The mean scattering coefficient m of this sheet was –65 dB. For intermediate frequencies, the scatterer stratification pattern was less pronounced and randomly varied from point to point.

The eastern equatorial section *5* passed along the meridian 15° W. The acoustic structure of DSL along this section is given in Fig. 4.

For the frequencies 3–10 kHz, the principal sheet *1* (its percentage ranges from 70 to 90% of the total column strength M_0 along the whole section) abruptly changed its depth in the region of the stream. To the north of the equator, it occupied relatively small depths between 250 and 400 m, and, to the South, it descended to depths between 500 and 700 m. For these low frequencies, we were able to distinguish the weaker scattering sheets *2* and *3* separated from the principal sheet by intervals of clean water. The upper sheet *2* occurred only to the south of the stream channel, and the lower sheet *3* was observed only to the north of it. Their percentages ΔM were about several percent. In the northern part of the section, another scattering sheet was sometimes discernible between the depths 1200 and 1300 m in addition to sheet *3* (this sheet is not shown in Fig. 4). The sheets *2* and *3* occupy the depths as though they were respective continuation of the principal sheet *1* in the southern and northern parts of the section. This behavior is evidence in favor of the fact that only a portion of sea inhabitants changed their depth as they passed across the Equatorial Current. Additionally, Fig. 4 shows the scattering coefficient m_1 measured in the principal sheet along section *5*. At a frequency of 5 kHz, it was maximal (about –50 dB) near the equator and gradually decreased to –70 dB in the northern direction and to –80 dB to the south.

For frequencies between 15 and 20 kHz, the principal scatterers are the tissues of the DSL inhabitants. Correspondingly, the vertical structure of DSL and its variations along section *5* drastically changed. The most common pattern consisted of a single scattering sheet with a thickness of about 200 m. Its upper boundary was near the depth 200 m in the middle of the section and descended to about 350 m toward the section ends. The scattering coefficient m of this sheet decreased, on average, from –60 dB in the northern part of the section to –90 dB in the southern part. However, this regularity was violated near the equator by a narrow local peak of about 20 dB in magnitude. Besides, weakly scattering lower sheets were recorded between the depths 900 and 1000 m at two or three points of the

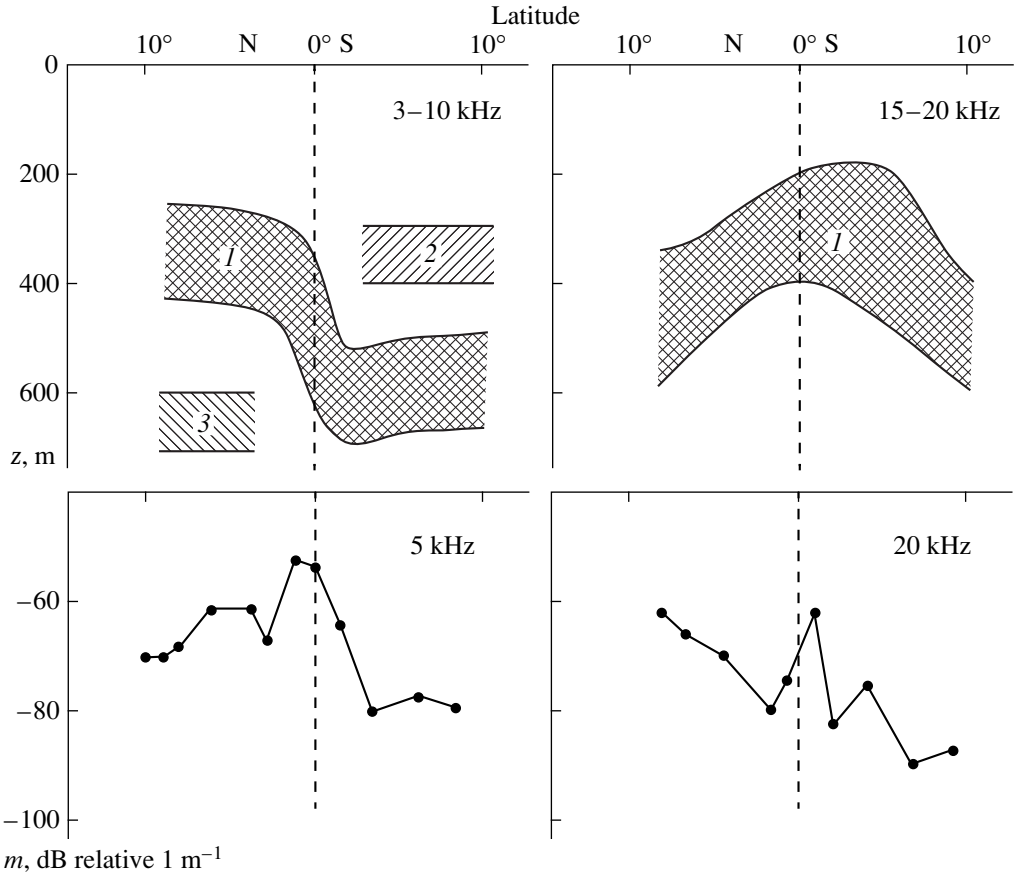

Fig. 4. Model of the vertical structure and the scattering coefficient m_1 of DSL along section *5* crossing the Equatorial Current at 15° W (for the frequencies 3–10 and 15–20 kHz).

southern part of section *5* for the frequencies 15–20 kHz. Their percentages ΔM were low; however, they showed some increase in the southern part of the section, which seems characteristic of the Southern Atlantic.

To conclude, we summarize the results described above.

Multiple data of full-scale measurements of the vertical structure of the acoustic characteristics of DSL in the frequency range from 3 to 20 kHz are described for the first time. A simplified model of this vertical structure is suggested. As a rule, the model consists of several scattering sheets lying at different depths and described by different numerical values of the scattering characteristics. The parameters of the model are shown to depend on oceanic conditions and sounding frequencies.

The model is illustrated by the description of the vertical structure along five sections in various areas of the Atlantic Ocean; the lengths of these sections reach several hundreds and even thousands of kilometers. It is noted that the construction of more accurate models of the vertical structure of DSL requires the use of more sophisticated procedures of full-scale measurements. These procedures are mentioned in the paper; however, they are not widely used for a variety of reasons.

ACKNOWLEDGMENTS

We are grateful to our colleagues who took part in the studies and the crews of the research vessels who made the multiple full-scale experiments possible.

This work was supported by the Russian Foundation for Basic Research, project no. 98-05-64849.

REFERENCES

1. Dezhang Chu and Zhen Ye, J. Acoust. Soc. Am. **106**, 1732 (1999).
2. I. B. Andreeva, N. N. Galybin, L. L. Tarasov, and V. Ya. Tolkachev, Akust. Zh. **46**, 21 (2000) [Acoust. Phys. **46**, 15 (2000)].
3. I. B. Andreeva, Akust. Zh. **45**, 437 (1999) [Acoust. Phys. **45**, 385 (1999)].
4. I. B. Andreeva, in *Acoustics of the Ocean*, Ed. by L. M. Brekhovskikh (Nauka, Moscow, 1975), pp. 491–558.
5. R. P. Chapman, O. Z. Bluy, R. H. Adlington, and A. E. Robinson, J. Acoust. Soc. Am. **56**, 1722 (1974).

Translated by A. Vinogradov

Acoustical Physics, Vol. 46, No. 5, 2000, pp. 511–517. Translated from Akusticheskiĭ Zhurnal, Vol. 46, No. 5, 2000, pp. 588–595.

Pitch Extraction Using a Generated Decision Function

I. O. Arkhipov and V. B. Gitlin

Izhevsk State Technical University, Studencheskaya ul. 7, Izhevsk, 426069 Russia

e-mail: vbg@zuko.istu.udm.ru

Received May 18, 1999

Abstract—A pitch extraction method is considered that employs a decision function whose maximum is greater than the possible spurious maxima of the analyzed signal on the pitch period. Smoothing by a wavelet window is proposed as a preprocessing procedure for the telephone signal. Experiments have shown that the proposed pitch extraction method is advantageous in almost all situations except for the case of the undistorted signal, where the LLK method proved to be the best one. © *2000 MAIK "Nauka/Interperiodica".*

Extracting the pitch, which is one of the basic speech parameters, presents severe difficulties, because (i) the speech signal is nonstationary, (ii) it contains intervals with increasing and decreasing energy, and (iii) the signal waveform within the pitch period may change, including the possibility of appearance of spurious maxima, whose magnitude is greater than that of the main lobe corresponding to the moment of the speech excitation [1]. In addition, when the speech signal is recorded, transmitted through a communication link, and reproduced, it can experience various distortions. Among these are the nonlinear clipping and frequency distortions such as, for example, the suppression of the frequency spectrum near the pitch in the telephone channel. The pitch extraction algorithms are a substantial part of the speech identification and compression systems; they require a considerable amount of computations and time for signal processing.

The top–down identification model [2] suggests a hierarchical search beginning with the upper hierarchy levels toward the lower ones. For example, the order may be as follows: sentence, syntagma, word, and syllable. In the framework of this approach, first, the features of the speech signal that indicate the end of one information event and the beginning of the next information event are found. Only after that are the characteristic features of the signal within the selected interval analyzed. In other words, the top–down identification requires signal analysis methods that find the unit events belonging to one hierarchy level. The selected unit events can be regarded as marks of the information boundaries. The introduction of the boundaries divides a continuous information-carrying signal into discrete information units. This approach reconciles the contradiction between the continuous nature of the information-carrying signal and the discrete nature of the transmitted information [3].

Two important features of the top–down identification follow from these circumstances:

(1) The boundaries between the information units should be marked somehow in the information-carrying signal. In the speech message, its natural properties, for example, pauses in breath between sentences, may be used as these marks, as well as artificial changes in the signal parameters introduced at the boundaries between the information units, for example, at junctures between sentences and sintagmas.

(2) The boundaries of information messages can be found without analyzing the signal within these boundaries only if the identification system generates a certain hypothetical template determined by the expected information unit. This hypothetical template was called the GS signal [3]. It limits the search for the boundary to the search for the place or feature of its expected location without considering the signal behavior within the boundaries.

In our earlier paper [4], the hyperbolic secant function was chosen as the GS signal for the pitch extraction. A flowchart of the GS pitch extraction algorithm is shown in Fig. 1; a time diagram illustrating its operation is given in Fig. 2.

The GS method constructs the pitch trajectory by placing marks at the maxima of the main lobes that correspond to possible moments of excitation of the speech tract (referred to as the main lobes henceforth). The time of the generation onset of the new main lobe is assumed to correspond to the time when the signal exceeds the decision function $G(n)$ generated by the algorithm. A significant particularity of the proposed algorithm is the presence of the counter generation process in the search for a solution under the condition that the decision function must be greater than the possible maxima on the pitch period. As $G(n)$, one can use an approximation of the $\mathrm{sech}(x)$ function by the exponent $K_1\exp(-|K_2x|)$. Here, K_1 and K_2 are the factors,

1063-7710/00/4605-0511$20.00

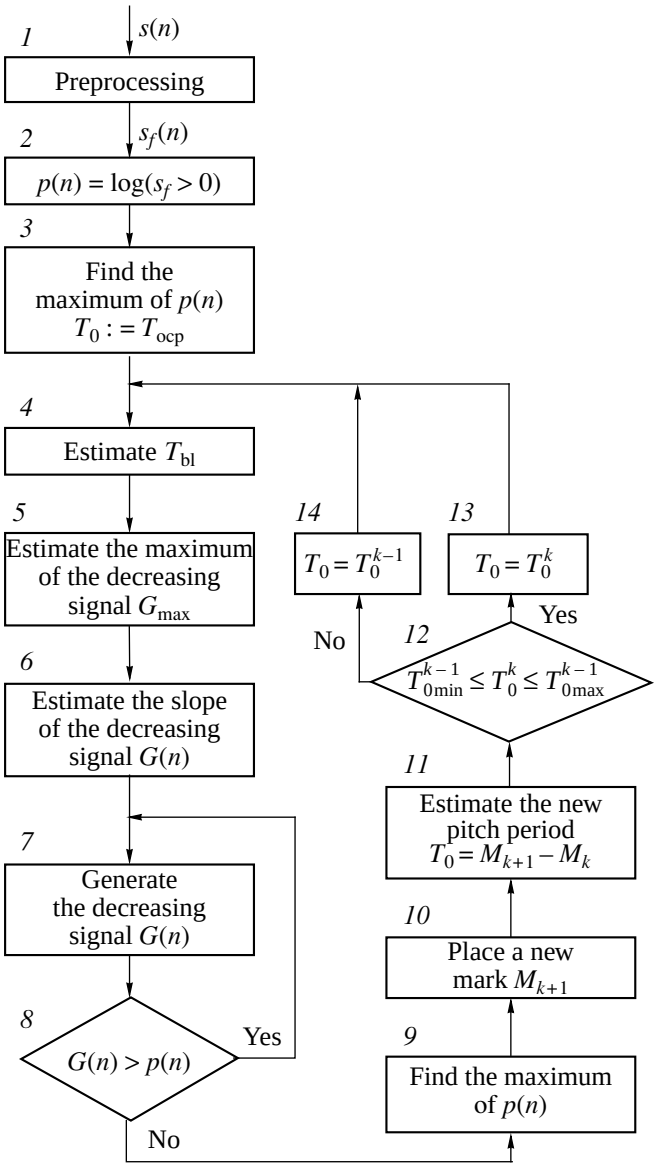

Fig. 1. Flowchart of the GS pitch extraction algorithm.

which are modified in the course of running the algorithm. The modification of K_1 and K_2 adapts the decision function $G(n)$ to the duration of the current pitch period.

The preprocessing subjects the signal to a nonlinear transformation and filtering in order to make the pitch extraction more reliable. The type of preprocessing depends on the quality of the input signal and on the applied pitch extraction method; it will be addressed below, after the description of the pitch extraction algorithm.

For the preprocessed signal, the logarithm of its positive values is calculated. This operation allows one to represent $G(n)$ as a linear function of time, which significantly simplifies the following adaptation process. It also favors the amplitude signal normalization.

In Fig. 2, T_{bl} is the duration of the time interval where the decision function increases and, therefore, where taking a decision on whether a new excitation is present is blocked:

$$T_{\text{bl}} = QT_0. \tag{1}$$

Here, $Q < 1$ is the factor, which determines the fraction of the current period corresponding to the blocking. Initially, T_0 is taken as the expected mean duration of the speaker's pitch. At the subsequent stages, T_0 is modified.

The blocking is terminated at the time B_k; at this point, the decision function attains its maximum $G^k_{\max}$ calculated as

$$G^k_{\max} = A_k + D, \tag{2}$$

where A_k is the maximal logarithm of the signal corresponding to the mark M_k, and D is the magnitude of the increment of $G^k_{\max}$ above A_k, which is determined from the statistics of the speech signal so as to make $G^k_{\max}$ higher than the amplitude of the possible spurious maxima on the pitch period in order to reliably extract the beginning of the subsequent pitch period.

The slope of the increasing part of the decision function $G(n)$ is

$$R_k = D/T^k_{\text{bl}}. \tag{3}$$

The slope of the decreasing part of $G(n)$ can be found from R_k:

$$L_k = R_kA_s, \tag{4}$$

where A_s is the asymmetry factor determined from the speech statistics. The decreasing part of $G(n)$ is generated according to the formula

$$G_k(n) = G^k_{\max} - L_k(n - B_k). \tag{5}$$

When $G(n)$ becomes less than the signal logarithm, the main lobe of the next pitch period is assumed to be found, after which the search for the maximum of this lobe is started. The location of the maximum is marked by M_{k+1}, and the duration of the current pitch period is calculated as

$$T^k_0 = M_{k+1} - M_k. \tag{6}$$

If T^k_0 remains within admissible boundaries, i.e., if

$$\begin{cases} (1-\delta_t)T^{k-1}_0 \le T^k_0 \le (1+\delta_t)T^{k-1}_0 \\ T_{0\,\min} \le T^k_0 \le T_{0\,\max}, \end{cases} \tag{7}$$

where δ_t is the admissible difference in the durations of two sequential pitch periods, $T_{0\,\min} = 2.0$ ms, and $T_{0\,\max} =$

20 ms, then, T_0 in formula (1) is replaced by T_0^k. Otherwise, T_0 remains the same as at the preceding stage of the algorithm.

As follows from the description of the GS pitch extraction algorithm, the signal behavior within the pitch period does not significantly affect the results of the pitch extraction. However, the method places certain requirements on the shape of the main lobe on the pitch period: (i) the main lobe amplitude must exceed the function $G(n)$ at the moment of the expected excitation of the speech tract and (ii) the shape of the main lobe near its maximum must be smooth and free from spurious maxima on its leading edge and at its top. These requirements imposed on the shape of the main lobe determine the type of preprocessing performed at the initial stage of the GS algorithm.

For extracting the pitch of the undistorted signal whose spectrum contains the fundamental harmonic, it is sufficient to apply an eighth-order Butterworth filter with the cutoff frequency f_c = 1500 Hz [5]. This cutoff frequency provides a time resolution of about 0.7-ms [6] and a constant group delay in the frequency band near the pitch. On the other hand, at f_c = 1500 Hz, the effect of the third formant (and the higher formants), which produces spurious local maxima in the main lobe, is suppressed. When processing noisy signals with the signal-to-noise ratio (SNR) from 0 to 10 dB, we decreased the cutoff frequency of the low-pass filter (LPF) to 800 Hz.

Figure 3a shows an oscillogram of the sentence *Ne vidali my takogo nevoda* pronounced by a male speaker (VBG). A standard pitch contour manually plotted by the oscillogram is shown in Fig. 3b; its marks are placed at the moments when the main excitation lobe crosses the zero level. Figure 3c shows the pitch contour obtained by the GS method. Note that the GS method correctly processed the regions with rapid variations in the pitch trajectory at the voice/unvoice and unvoice/voice junctures and at the short vowel *a* positioned between two occlusive consonants *t* and *k* in the word *takogo*.

Figure 3d shows the original signal (Fig. 3a) contaminated with white noise with SNR = 0 dB. The pitch contour obtained by the GS method for the noisy signal is shown in Fig. 3e. The comparison with the template contour (Fig. 3b) shows that, at this SNR, the pitch-extraction quality is satisfactory. Figure 3f shows the signal illustrated in Fig. 3a clipped at ±1 quantization step, and Fig. 3g presents the respective pitch contour extracted by the GS method. The comparison of Figs. 3g and 3b shows that the pitch contour extracted by the GS method from the clipped signal is in sufficiently good agreement with the true pitch contour.

In the case of a signal limited to the telephone channel passband (300–3300 Hz), which is referred to as the telephone signal henceforth, the low-pass filtering fails to provide the signal quality required for the reliable pitch extraction. A half-wave rectification does not improve the situation significantly, because the amplitude of the reconstructed harmonic is small [1]. An enhancement of the pitch by narrowing the LPF's passband is impossible because of the low time resolution of such a filter. Furthermore, the LPF implementation as the Butterworth filter does not allow one to adapt it to the pitch period when the algorithm operates in real time.

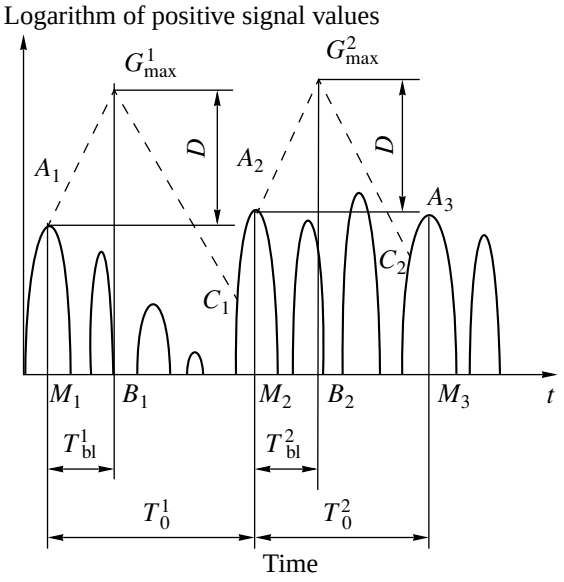

Fig. 2. Time diagram illustrating the pitch extraction by the GS method.

In the case of our concern, the time-resolution of a filter with a low cutoff frequency can be improved with the use of the wavelet window [7] in the form of a bell-shaped pulse [6]

$$w(t) = (1 - c^2 t^2) e^{-\sigma^2 t^2}, \tag{8}$$

where c and σ are the window parameters. The wavelet window determined by formula (8) is illustrated in Fig. 4. Filtering (smoothing) by the wavelet window $w(t)$ is performed as a convolution of the detected telephone signal with the filter impulse response $w(t)$. The impulse response $w(t)$ (8) is symmetric about the origin; therefore, this filter has a linear phase characteristic.

Figure 5a presents an oscillogram of the segment *ogo* of the sentence *Ne vidali my takogo nevoda* (an undistorted signal, a VGB speaker). Figure 5b shows an oscillogram of the same segment obtained from the telephone signal. The comparison of Figs. 5a and 5b shows that, in the telephone channel, information about the pitch is lost to a considerable extent. This is especially noticeable at junctures between high- and low-

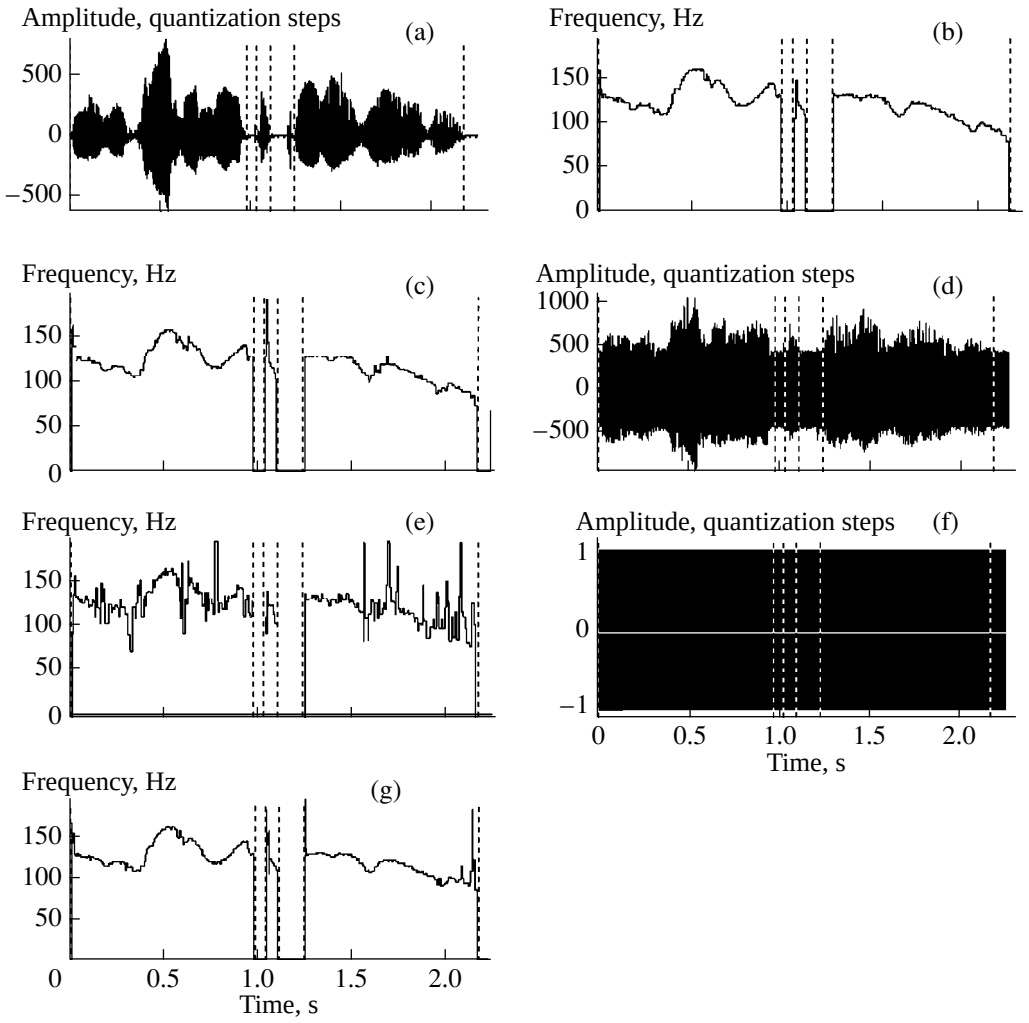

Fig. 3. Examples illustrating the GS method: (a) oscillogram of the sentence *Ne vidali my takogo nevoda* pronounced by a male speaker (VBG); (b) template pitch contour plotted manually; (c) pitch contour of the original signal obtained by the GS method; (d) original signal contaminated with white noise with SNR = 0 dB; (e) pitch contour obtained by the GS method for a noisy signal; (f) original signal clipped at ±1 quantization step; and (g) pitch contour of the clipped signal obtained by the GS method.

energy intervals. This effect can be attributed to overlapping in the telephone channel. Smoothing the telephone signal by the wavelet window with $c = 3.2 \times 2F_0$ (see Appendix) restores the information about the pitch on the stationary intervals (Fig. 5c). However, at junctures of the segments *og* and *go*, one can notice distortions. Though the information about the intensity ratio at the vowel–consonant junctures is useful for the speech perception [8], in our case, it is superfluous and hampers the pitch extraction.

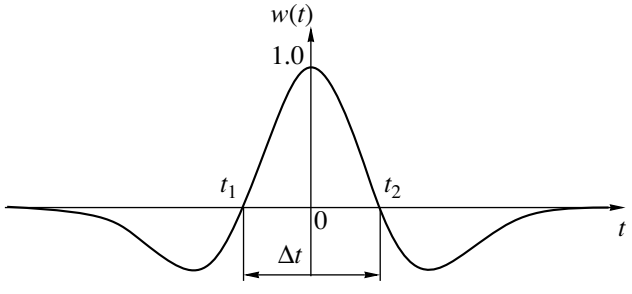

Fig. 4. Wavelet window.

Consider the telephone signal clipped to ±1 quantization step and preprocessed by smoothing with the wavelet window illustrated in Fig. 5d. The figure shows that this preprocessing provides a satisfactory quality of the pitch-information recovery.

We experimentally compared the pitch-extraction accuracy by the GS method with the standard pitch-extraction methods used in the SIS system [9]: the peak method (PIC), the cepstral method (CEP), the autocorrelation method (AC), the Rabiner–Gold method (RG), the filtering method (FIL), and the LLK method. As the original speech signals, we used the sentence *Ne vidali my takogo nevoda* pronounced by three male and three

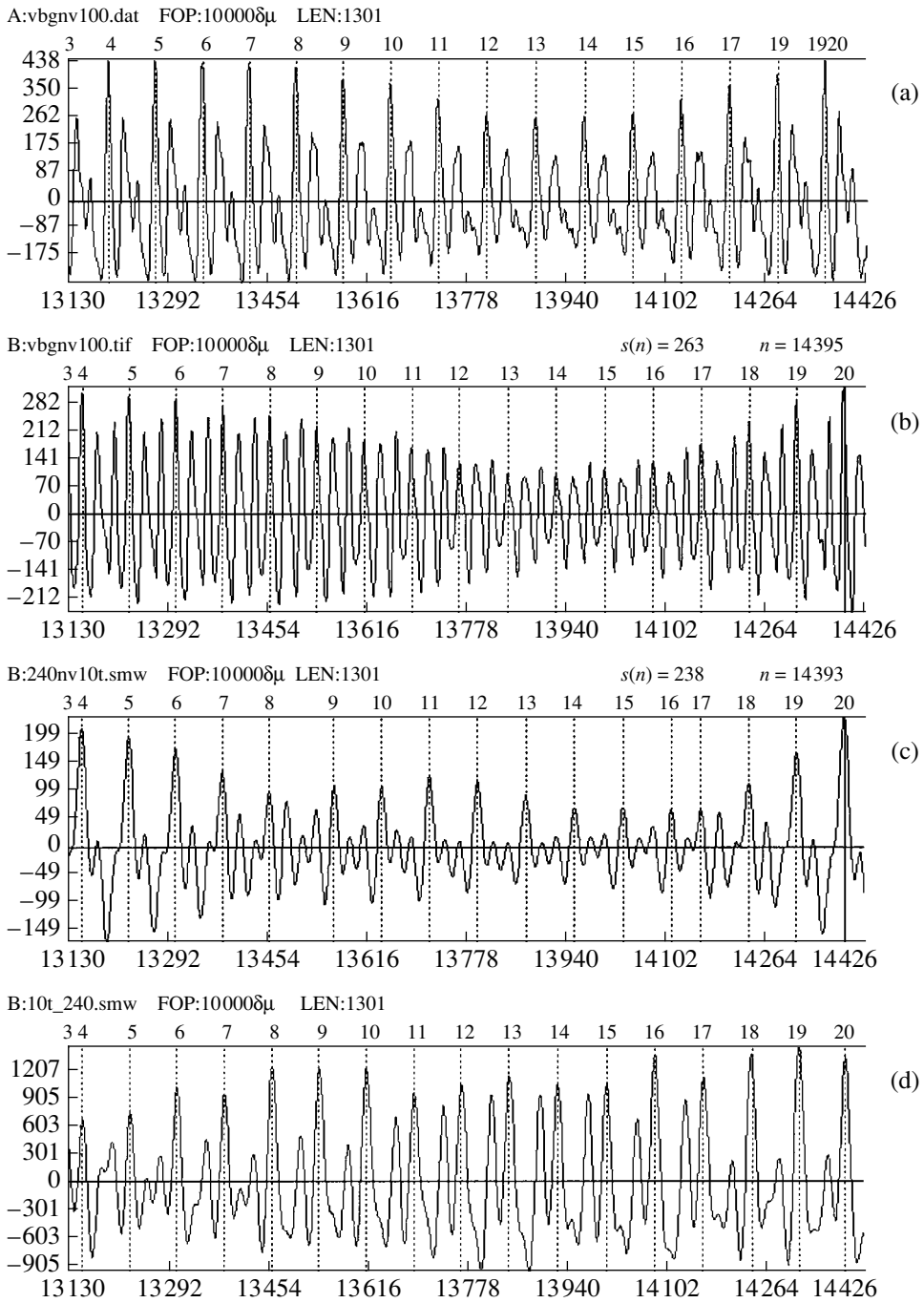

Fig. 5. Examples of smoothing the signal by the wavelet window. The segment *ogo* of the sentence *Ne vidali my takogo nevoda* pronounced by a VGB speaker: (a) original undistorted signal; (b) signal limited to the telephone channel passband; (c) telephone signal smoothed by the wavelet window; (d) clipped telephone signal after smoothing by the wavelet window.

female speakers. The original signals were sampled at a rate of 10 kHz and quantized by a 12-bit analog-to-digital converter. The noisy signals were produced by adding the white noise with SNR = 5 dB. The telephone signals were obtained by applying the original signals to a 16-order bandpass (300–3300 Hz) Butterworth filter. The telephone signals were preprocessed using the wavelet window.

The oscillograms of the original signals were used to manually construct the trajectories of the instantaneous pitch periods. Simultaneously, the original signals were segmented into voiced and unvoiced intervals. In order to estimate the quality of the integral pitch extraction methods, the template trajectory of the instantaneous pitch periods was smoothed by the moving-average method. When the difference between the

Generalized error of pitch extraction methods in percent

Signal type	Method						
	GS	PIC	CEP	AC	RG	FIL	LLK
Original signal	2.32	3.38	5.08	2.80	2.89	3.76	2.28
Noisy signal with SNR = 5 dB	6.25	9.44	9.10	10.06	8.79	9.75	15.00
Telephone signal	2.76	4.77	5.35	6.97	4.11	5.19	5.45

estimated and template trajectories was less than 5%, it was ignored; differences from 5 to 15% and those higher than 15% were classified as the small and the large ones, respectively. Errors in making the decision *unvoiced* when the signal in the template contour is classified as a voiced one are called the *v*/*uv* errors. Errors in making the decision *voiced* when the signal in the template contour is classified as an unvoiced one are called the *uv*/*v* errors. The percentages of the *v*/*uv* and *uv*/*v* errors were calculated relative to the total speech duration; the percentages of the large and small errors were calculated relative to the vocalized part of the speech.

The pitch-extractor performance was integrally estimated by the norm of the multidimensional error vector:

$$s = \frac{1}{4}(w_{v/uv}\delta^2_{v/uv} + w_{uv/v}\delta^2_{uv/v} + w_g\delta^2_g + w_{sm}\delta^2_{sm})^{1/2}, \quad (9)$$

where $\delta_{v/uv}$, $\delta_{uv/v}$, δ_g, and δ_{sm} are the relative *v*/*uv*, *uv*/*v*, large, and small errors in percent, respectively; $w_{v/uv}$, $w_{uv/v}$, w_g, and w_{sm} are the weighting factors, which were assumed to be equal to 1.0. The results of our tests averaged over all speakers and all pairwise comparisons between the methods are summarized in the table. A more detailed description of this experiment and the justification of the chosen pitch-extractor performance criterion is given in [10]. The table shows that the GS method was preferable in all cases except for the original signal, where the LLK method gave slightly better results.

APPENDIX

ESTIMATION OF THE WAVELET WINDOW PARAMETERS

One of the requirements imposed on the wavelet window is that its mean over an infinite interval, i.e., the integral over $-\infty < t < +\infty$, be equal to zero [11]. According to formula (8), we use the wavelet window

$$w(t) = (1 - c^2t^2)e^{-\sigma^2t^2}. \quad (A1)$$

As a result of the preliminary experiments, we found that the wavelet function $w(t)$ satisfies the uncertainty relation [6]

$$\Delta\omega\Delta t = 2.5\pi, \quad (A2)$$

where Δt is the time resolution of the window defined as the width of the main lobe at the zero level (see Fig. 4) and $\Delta\omega$ is the frequency resolution defined as the upper frequency of the window spectrum at –40 dB below the maximum. In order to meet the requirement that the second harmonic must be filtered out, we specify $\Delta\omega$ as

$$\Delta\omega = 4\pi F_0, \quad (A3)$$

where F_0 is the pitch cyclic frequency. Setting $w(t)$ equal to zero, we find from formula (A1) that

$$\Delta t = 2/c. \quad (A4)$$

The requirement that the mean of the window function be zero gives $\int_{-\infty}^{\infty} w(t)dt = 0$, where $w(t)$ is defined by formula (A1). Since $\int_{-\infty}^{\infty} e^{-x^2}dx = \sqrt{\pi}$ and $\int_{-\infty}^{\infty} x^2e^{-x^2}dx = \frac{\sqrt{\pi}}{2}$ [12], we obtain

$$\sigma = c/\sqrt{2}. \quad (A5)$$

By solving equations (A2)–(A5) simultaneously, c and σ can be expressed in terms of F_0:

$$\begin{cases} c = 3.2F_0 \\ \sigma = 2.2627F_0. \end{cases} \quad (A6)$$

Using expressions (A3), one can represent c and σ as a function of $\Delta\omega$.

The spectrum of this window is calculated as the Fourier transform $W(j\omega) = \int_{-\infty}^{\infty} w(t)\,e^{-j\omega t}dt$, where $w(t)$ is given by formula (A1). By virtue of formula (A5) [12], we obtain

$$W(j\omega) = \int_{-\infty}^{\infty}(1 - ct^2)e^{-\sigma^2t^2 - j\omega t}dt = \frac{2\sqrt{\pi}}{\sigma}x^2e^{-x^2}, \quad (A7)$$

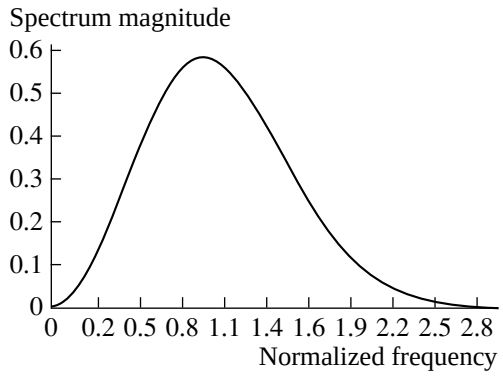

Fig. A1. Spectrum of the wavelet window.

where $x = \omega/(2\sigma)$ is the normalized angular frequency. The spectrum is a purely real one, because $w(t)$ is an even function of time. The spectrum calculated from formula (A7) is plotted in Fig. A1. This figure shows that the smoothing of a signal by the window $w(t)$ can be regarded as the filtering by a bandpass finite impulse-response filter.

REFERENCES

1. V. B. Gitlin, Avaliable from VINITI, No. 1206-V98 (1998).
2. V. B. Kasevich, E. M. Shabel'nikova, and V. V. Rybin, *Stress and Pitch in Language and in Speech Activity* (Leningrad. Gos. Univ., Leningrad, 1990).
3. V. B. Gitlin, in *Pattern Recognition and Image Analysis: Novel Information Technology* (Novosibirsk, 1998), Part I, pp. 64–68.
4. I. O. Arkhipov and V. B. Gitlin, in *Pattern Recognition and Image Analysis: Novel Information Technology* (Novosibirsk, 1998), Part I, pp. 23–27.
5. I. O. Arkhipov and V. B. Gitlin, in *Proceedings of the Young Scientists School "Information-Measuring Systems on the Basis of High Technologies," Izhevsk, 1998*, p. 12.
6. A. A. Kharkevich, in *Selected Works. Linear and Nonlinear Systems* (Nauka, Moscow, 1973), Vol. 2, pp. 87–252.
7. I. O. Arkhipov and V. B. Gitlin, in *Pattern Recognition and Image Analysis: Novel Information Technology* (Novosibirsk, 1998), Part I, pp. 18–22.
8. E. Kennedy, H. Levitt, A. C. Neuman, and M. Weiss, J. Acoust. Soc. Am. **103**, 1098 (1998).
9. *Technical Recommendations on the Practical Use of the SIS Program in Working with Speech Signals* (Tsentr Rechevykh Tekhnologiĭ, St. Petersburg, 1997).
10. I. O. Arkhipov and V. B. Gitlin, in *Proceedings of the IX Session of the Russian Acoustical Society "Modern Speech Technology"* (GEOS, Moscow, 1999), p. 38.
11. Y. Meyer, *Wavelets and Operators* (Cambridge Univ. Press, Cambridge, 1993).
12. A. P. Prudnikov, Yu. A. Bychkov, and O. I. Marichev, *Integrals and Series* (Nauka, Moscow, 1981; Gordon and Breach, New York, 1986).

Translated by A. Khzmalyan

Acoustical Physics, Vol. 46, No. 5, 2000, pp. 518–522. Translated from Akusticheskiĭ Zhurnal, Vol. 46, No. 5, 2000, pp. 596–600.

Experimental Investigation of the Resolution and Sensitivity of an Ultrasonic Imaging Camera with an Immersion Lens

S. V. Baĭkov, V. D. Svet, and V. I. Sizov

Andreev Acoustics Institute, Russian Academy of Sciences, ul. Shvernika 4, Moscow, 117036 Russia

e-mail: bvp@akin.ru

Received February 25, 1999

Abstract—An experimental evaluation of the space resolution of a prototype ultrasonic imaging camera with an immersion acoustic lens is performed. It is shown that the measured parameters agree well with the theoretical calculations. The measurements of the level of internal noise and the absolute sensitivity of the imaging camera are performed; the sensitivity is found to be 0.008 Pa/Hz$^{1/2}$. © *2000 MAIK "Nauka/Interperiodica".*

The physical-mathematical model of an acoustic immersion lens for obtaining acoustic images was described in [1]. On the basis of this model, it is possible for a given numerical aperture to optimize a number of important parameters of the lens design, such as the angle of view, the angle resolution over the field of view, the side field level, the irregularity of the amplitude distribution in the image plane, and some other parameters. Since in the suggested model some assumptions were made (the transverse waves, the scattering by the lens walls, and other factors of the lens defocusing were not taken into account), it is of interest to compare the results of modeling with experimental measurements. For this purpose, a series of experiments were performed in a hydroacoustic tank with a prototype ultrasonic imaging camera [2] (Fig. 1).

First we recall the principle of its operation. Two acoustic radiators "illuminate" a given area. Acoustic waves reflected from an object fall on an acoustic lens that forms the image of the input pressure field distribution on a multielement piezoelectric matrix, which, in its turn, is a target of a Unikon beam-switching tube. This input pressure field distribution is actually the acoustic image of the object. Under the action of this field, a space distribution of the electric potential is formed on the piezoelectric matrix, which is read out line-by-line from the matrix elements (91 rows and 75 columns) by an electron beam sweep system. The beam current creates a voltage across the input resistance of the videoamplifier, which results in conversion of a two-dimensional potential field (the pressure field) into a one-dimensional voltage function of time. Thus, the total time signal consists of 75×91 separate signals, or samplings, and the duration of each sampling equals the time of the beam travel across the matrix element.

Further, this signal, after amplification, is detected, filtered, and fed to a 12-bit A/D converter. Synchronously with the sweep, the computer forms a matrix of intensity values (75×91), which actually is the image on the monitor screen. A single act of the matrix readout makes a single frame. The software permits one to combine (average) as many as 128 frames.

DETERMINATION OF THE DISTANCE FOR THE BEST FOCUSING AND THE MAXIMAL RESOLUTION

The acoustic lens of our ultrasonic imaging camera provides no adjustment for sharpness. Hence, the sharpest image is formed only at a certain distance from the object. It should be noted that, when the lens works within the Fresnel zone, the small wave dimension of the lens and its relatively "long focal length" give rise to a pulse response of the lens that is rather extended in the depth of the field (see [1]); i.e., the observed sharp-

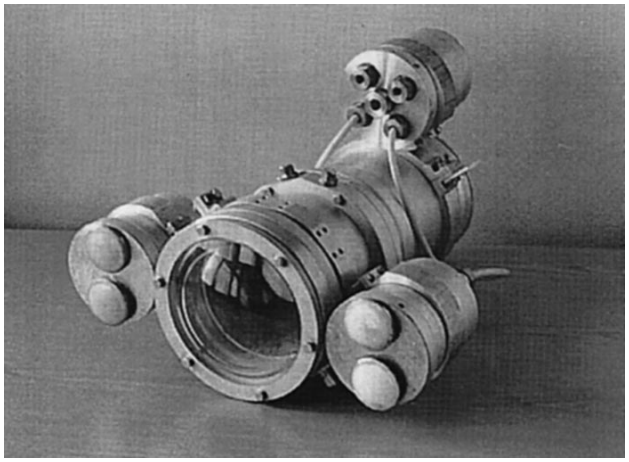

Fig. 1. Photograph of the ultrasonic imaging camera.

1063-7710/00/4605-0518$20.00

ness of the image will seem identical for the object displacements toward the lens and away from it. However, there is an optimal distance that provides the best focusing.

This distance was determined by measuring the angular width of the spatial pulse response to a signal of a point source (a hydrophone) as a function of the distance to the lens along the optical axis. The angular dimension of the hydrophone is much less than the calculated angular resolution of the imaging camera. A typical pulse characteristic obtained by averaging over 128 frames and its cross section are shown in Fig. 2. In this figure, the coordinate axes show not the numbers of rows and columns, but the corresponding values in degrees within the angle of view of the lens.

The angular width of the response was chosen as the criterion for determining the distance of the best focusing. The distance at which this width is minimal will be the best. Calculations [1] show that, for a lens of diameter 180 mm, the distance providing the best focusing is 1.4 m with an angular resolution of 1.5°. The graph in Fig. 3 illustrates the results of the experimental measurements. The vertical segments show the confidence intervals. As is seen from the graph, the agreement between the calculated data for a distance of 1.4 m and the experiment is quite satisfactory.

The angular dimension of the pulse characteristic not completely determines the resolution of the lens, because it works in the Fresnel zone, and the quality of focusing is the same only at paraxial angles. So it was necessary to complement the experiment with direct measurements over the whole angle of view. For this purpose, at a distance of 1.4 m from the lens, two point hydrophones were installed with some shifts relative to the horizontal axis, and the lens responses were measured similarly to the measurements of the pulse response.

For a hydrophone spacing of 5 cm, which corresponds to an angular separation of 5°, the lines of equal level of the measured pulse response are shown in Fig. 4. Then, the camera was rotated in the horizontal plane through the angles ±5° and ±10° relative to the direction to the hydrophones, and the measurements were repeated. The angular resolution, according to the Rayleigh criterion, was about 2° (by the level –3 dB), which is somewhat greater than the calculated angular resolution (Fig. 5). The same measurements were carried out in the vertical plane and with point reflectors represented by metal balls of small diameter. The results practically coincided with those of the previous measurements with hydrophones.

Some disagreement between the calculated and measured values can be explained by the fact that the resolution was calculated only for the lens, whereas the experimental images were the result of the operation of the whole system with certain inevitable instrumntation loss.

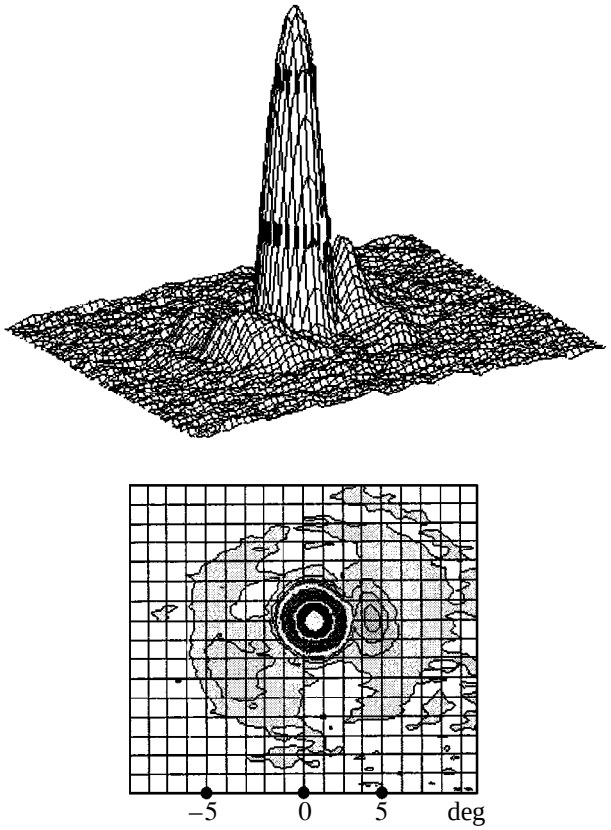

Fig. 2. Averaged two-dimensional pulse characteristic.

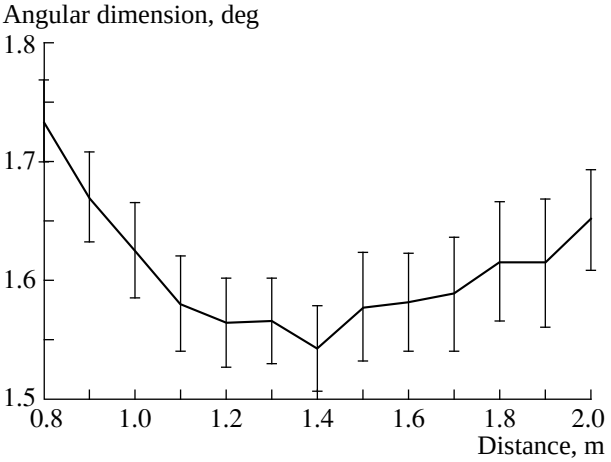

Fig. 3. Angular width of the pulse characteristic as a function of distance to the lens.

MEASUREMENT OF THE ABSOLUTE SENSITIVITY OF THE IMAGING CAMERA WITH AN ACOUSTIC LENS

This series of experiments was aimed at determining the absolute sensitivity of the imaging camera. The noise of the imaging camera is only of instrumentation nature and is caused by the noise of the wideband input

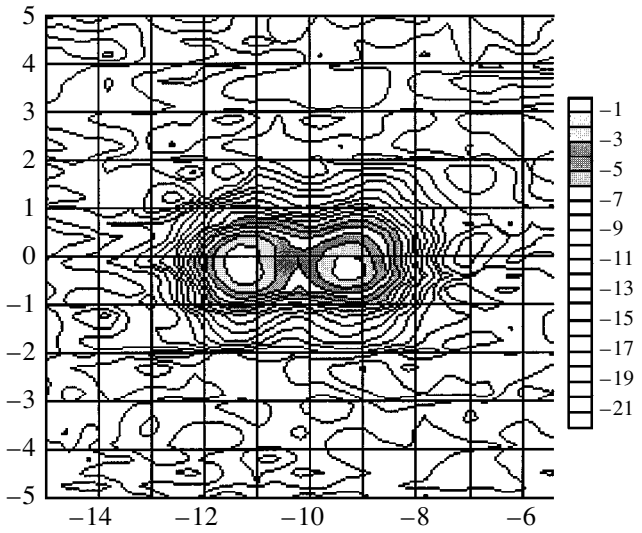

Fig. 4. Lines of equal level of the lens pulse response for two hydrophones spaced 5 cm apart at a distance of 1.4 m to the lens.

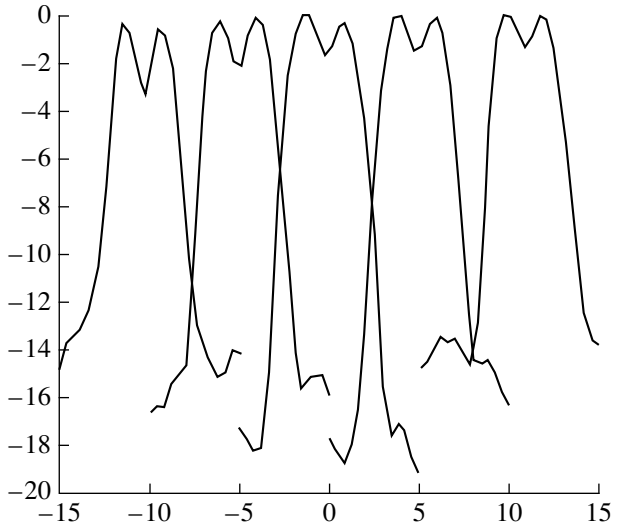

Fig. 5. Cross sections of the imaging camera responses to a pair of sources in the operating field of view.

amplifier and the shot noise of Unikon. The thermal noise of the piezoelectric matrix and the surrounding medium can be neglected in this case. Due to internal noise, even in the absence of the external signal, a "psuedoimage" of noise is formed as a sample of the amplitudes of the detected narrow-band noise of the amplifier (Fig. 6). To determine the absolute sensitivity of the imaging camera, it is necessary to recalculate this noise to the input aperture in pressure units by assuming that the internal noise of the imaging camera is absent, and the noise is coming from the outer space. This means that referencing to the absolute value of the acoustic pressure should be performed in a hydroacoustic tank.

When a reference signal is generated by a hydrophone, it adds linearly with the noise at the input of the amplifier, and, after transformation (amplification, detection, and filtering), the image of the signal appears as a peak on the background of a noise pedestal in a single frame. Due to random imposition of noise on the signal, its maximum value will fluctuate and migrate over the matrix in the area close to the maximum in a single frame. The position of the maximum of the averaged pulse characteristic (Fig. 2) can be considered as the position of the maximum of the signal that would occur in the total absence of noise. After determining the numbers of the row and column for the position of the maximum in this case, one can use them for taking random sample values of amplitudes in a digital matrix for this point from a set of single frames of the signal–noise mixture.

Since the signal is sinusoidal and noise is a narrow-band one, the distribution of the probability density of the sample values of amplitudes from the mixture is described by a generalized Rayleigh distribution, because the detection of the signal–noise mixture is carried out by a linear amplitude detector:

$$\omega(X) = \frac{X}{\sigma^2}\exp\left(-\frac{X^2 + A^2}{2\sigma^2}\right)I_0\left(\frac{AX}{\sigma^2}\right),$$

where X is a random sample value, σ^2 is the variance of the narrow-band noise, A is the amplitude of the sinusoidal signal, and I_0 is the modified Bessel function of zeroth order.

Here, the unknown parameters are A and σ. We seek their estimates by the maximum likelihood method. The one-dimensional likelihood function has the form

$$I(X) = \frac{1}{\sigma^2}\exp\left(-\frac{X^2 + A^2}{2\sigma^2}\right)I_0\left(\frac{AX}{\sigma^2}\right),$$

and its logarithm can be written as

$$\ln[I(X)] = -2\ln\sigma - \frac{X^2 + A^2}{2\sigma^2} + \ln\left[I_0\left(\frac{AX}{\sigma^2}\right)\right].$$

Taking a derivative of the logarithm with respect to A and equating it to zero, we obtain the likelihood equation for A:

$$\frac{\partial \ln}{\partial A} = -A + \frac{I_1\left(\frac{AX}{\sigma^2}\right)}{I_0\left(\frac{AX}{\sigma^2}\right)}X = 0,$$

where I_1 is a modified Bessel function of the first order.

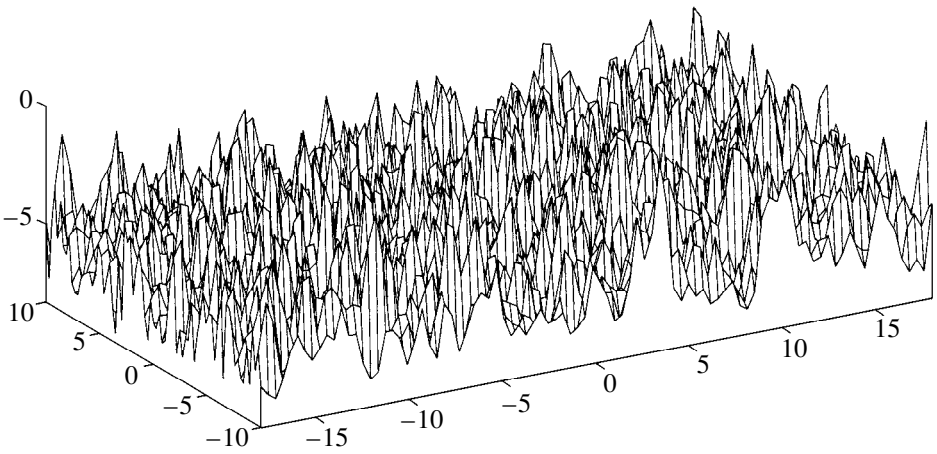

Fig. 6. Two-dimensional distribution of noise over the receiver matrix for a frame duration of 50 ms.

It is easy to see that, for many-dimensional sampling of volume n, the likelihood equation can be written as

$$-nA + \sum_{1}^{n} \frac{I_1\left(\frac{AX_n}{\sigma^2}\right)}{I_0\left(\frac{AX_n}{\sigma^2}\right)} X_n = 0.$$

For $AX_n/\sigma^2 \geq 2$, we have the ratio $I_1/I_0 \approx 1$; then, we obtain

$$\hat{A} = \frac{1}{n}\sum_{1}^{n} X_n.$$

Thus, the estimate $A = \hat{A}$ is simply a sample mean m_1.

Now, we take a derivative of the logarithm with respect to σ and obtain the likelihood equation for the variance for an n-dimensional sampling:

$$\hat{\sigma}^2 = \frac{1}{2n}\sum_{1}^{n} (X_n - A)^2.$$

Substituting A for the estimate $\hat{A}$, we obtain the estimate for the variance $\hat{\sigma}^2 = M_2/2$ equal to half the central sample moment of the second order.

It is also easy to find the Rao-Cramer boundaries for the estimates of the variance and amplitude:

$$D_{\hat{A}} \geq M_2/2 \quad \text{and} \quad D_{\hat{\sigma}} \geq \frac{M_2^2}{10M_2 + 16m_1^2}.$$

The procedure of the experimental measurements was as follows. A point source (a transmitting hydrophone) was installed at a distance of 1.4 m from the imaging camera along the optical axis. Immediately before the lens, near its center, a calibrated hydrophone was placed for measuring the absolute value of the pressure generated by the source at the lens aperture.

In the experiments, we recorded 128 single frames of signal–noise mixture on a PC's hard disc. Then, we determined the coordinates of the maximum of the pulse characteristic on the digital matrix. Those were the 39th row and the 45th column. At this point, out of a total of 1128 frames, we chose 128 "instantaneous" values X_n, which formed the sample statistics. Since we used a 12-bit A/D converter, the sample data in decimal code should lie within 0 to 4095. The sample mean m_1 was equal to 1735, the standard deviation $\sqrt{M_2}$ was equal to 297, $X_{\min} = 891$, and $X_{\max} = 2554$.

Using the above formulas, we found that $\hat{A} = 1735$ and $\hat{\sigma} = 211$. Consequently, the signal-to-noise ratio in the experiment was $N = \hat{A}/\hat{\sigma} = 8.2$. However, since the noise at the input of aperture was actually absent, the value of $\hat{A}$ corresponded to the pressure measured by the reference hydrophone. It was equal to 16.5 Pa. Hence, the effective value of noise reduced to the input aperture was equal to 16.5 / 8.2 = 2 Pa.

The absolute sensitivity of the imaging camera can be considered as the value of the signal for which the signal-to-noise ratio equals unity, i.e., 2 Pa. Since the effective bandwidth of the input and video amplifiers is 70 kHz, the normalization to a bandwidth of 1 Hz gives a value of the absolute sensitivity of 0.008 $\text{Pa}/\text{Hz}^{1/2}$. Note that this measured sensitivity value correlates well with theoretical calculations [1].

CONCLUSIONS

The experimental measurements showed that the procedure suggested in [1] for calculating the parameters of acoustic lenses describes with reasonable accu-

racy the main features of the experimental acoustic images formed by the ultrasonic imaging camera. The experimentally measured value of the angular resolution over the field of view of the imaging camera was 1.8°, while the calculated value was equal to 1.5°. Since the calculated value refers only to the lens and the measured value refers to the whole system, the difference of 17% between the estimates can be considered as a measure of technical losses.

The sensitivity of the ultrasonic imaging camera proved to be fairly high for this kind of hydroacoustic instruments, and it only slightly differs from the sensitivity of experimental imaging cameras with matrix receivers and electronic readout that are made as single LSI circuits [3]. However, the latter cannot compete with the developed prototype imaging camera in speed of operation and cost.

ACKNOWLEDGMENTS

This work was supported by the ONREUR grant no. 68171-96-C-9098.

REFERENCES

1. S. V. Baĭkov and T. A. Tikhonova, Akust. Zh. **43**, 749 (1997) [Acoust. Phys. **43**, 651 (1997)].
2. S. V. Baykov, V. D. Svet, and V. I. Sizov, in *Acoustical Imaging* (Plenum, New York, 1998), pp. 122–131.
3. K. Erikson, A. M. Nikoli, *et al.*, in *Acoustical Imaging* (Plenum, New York, 1998), pp. 87–95.

Translated by A. Svechnikov

Acoustical Physics, Vol. 46, No. 5, 2000, pp. 523–529. Translated from Akusticheskiĭ Zhurnal, Vol. 46, No. 5, 2000, pp. 601–608.

Measuring Scanning Acoustic Microscope with a Harmonic Sounding Signal

A. N. Bogachenkov, R. G. Maev, and S. A. Titov

Emanuel Institute of Biochemical Physics, Russian Academy of Sciences, ul. Kosygina 4, Moscow, 117977 Russia

e-mail: chembio@glas.apc.org

Received April 12, 1999

Abstract—A concept of a scanning acoustic microscope with a harmonic sounding signal for measuring the parameters of local homogeneous regions of flat samples is proposed. The distinctive feature of the device is the utilization of the Doppler effect that occurs in the sounding wave reflected from the sample surface when the sample is uniformly moved relative to the focusing ultrasonic transducer of the microscope. It is theoretically demonstrated that the spectrum of the received signal is determined by the product of the reflection coefficient and the transfer function of the transducer. The errors of the measurement technique are considered, and the sources of signal distortions are analyzed. High sensitivity of the measurement results to the errors of the scanning system is demonstrated. The developed measuring microscope is described, in which an acoustic interferometer is used to provide the necessary precision of the scanning coordinate measurement. The microscope transfer function is measured for the frequency of the sounding signal 65 MHz, and the values of density and bulk wave velocities are determined for a homogeneous sample by the measured phase of the reflection coefficient using the technique of nonlinear estimation of parameters. With fused quartz used as an example, it is shown that the measurement error is 7.2% for density and 2.3 and 0.7% for the velocities of longitudinal and transverse waves, respectively. In addition, the velocity of a leaky surface wave (SAW) is determined by two methods. One method is based on measuring the position of the inflexion point for the experimental phase of the reflection coefficient, and the other is based on calculating the SAW velocity corresponding to the measured values of density and bulk wave velocities. The errors of these methods are found to be equal to 0.42 and 0.17%, respectively. *© 2000 MAIK "Nauka/Interperiodica".*

Scanning acoustic microscopy [1] provides an opportunity not only to visualize with high resolution the spatial distribution of structural inhomogeneities in an object, but also to conduct the measurements of the acoustic parameters of its local regions. One of the measuring techniques is the so-called $V(z)$ method [2, 3], where the output signal of the acoustic focusing transducer V is recorded as a function of the sample displacement z along the axis of the lens, perpendicularly to the sample surface. As a rule, the shape of the curves $V(z)$ strongly depends on the acoustic parameters of the local region under investigation. A technique for measuring the velocity and damping of leaky surface acoustic waves (SAW) on the basis of analyzing the period and amplitude of the characteristic oscillations of the absolute value $|V(z)|$ is widely known [4, 5].

At the same time as it was shown by Hildebrand *et al*. [6] and Liang *et al*. [7], the spectral analysis of the complex function $V(z)$ provides an opportunity to reconstruct the reflection coefficient $R(\theta)$ of a plane sound wave as a function of its angle of incidence θ upon the surface under investigation. This method is potentially more informative, but it requires measuring not only the amplitude but also the phase of the pulsed signal V. The reflection coefficient can also be measured using the technique suggested by Nakaso *et al*. [8]. In this case, the spatial spectrum of the wave reflected from the sample is analyzed by a receiver, which can be oriented at various angles and has a high angular selectivity. However, in the case of such a configuration of the measuring system, it is impossible to conduct an analysis for small angles of incidence.

Usually, it is easy enough to estimate the velocity of a leaky surface wave according to the measured reflection coefficients, because, in the case of the critical angle of its excitation, the phase of the reflection coefficient has a sharp peak. At the same time, the measurement results turn out to be distorted because of many unavoidable factors, such as noise or a limited interval of signal detection. Thus, a correct determination of the velocity of a surface wave, as well as other acoustic parameters, from experimental data is an important problem.

This paper considers a Doppler acoustic microscope with a harmonic sounding signal. The results obtained by determining the parameters of an isotropic sample (the density and the velocities of bulk and surface waves) with the use of this microscope are presented.

The relative motion of the sample along the acoustic axis of the lens in the measuring Doppler acoustic microscope is conducted with a constant velocity [9].

1063-7710/00/4605-0523$20.00 © 2000 MAIK "Nauka/Interperiodica"

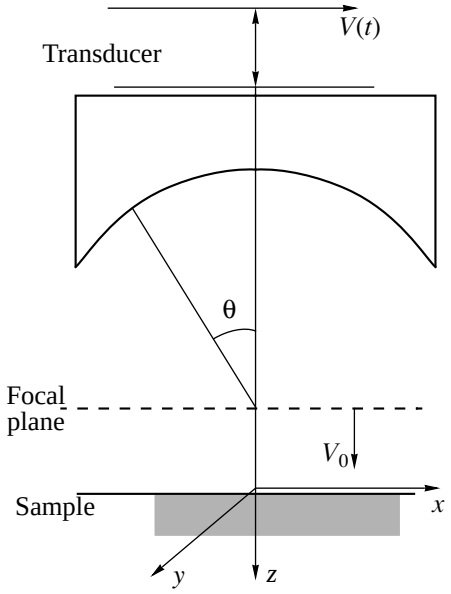

Fig. 1. Schematic representation of the acoustic system of the microscope.

Because of the Doppler effect, a plane ultrasonic wave reflected from the moving surface of the sample experiences a frequency shift ω_d with respect to the sounding signal frequency ω_0. The value of the motion velocity v_0, which can be realized in the device in practice, is much smaller than the velocity of ultrasonic waves in an immersion medium C. Therefore, we consider only the first-order approximation with the parameter v_0/C for the Doppler frequency:

$$\omega_d = 2k_z v_0. \tag{1}$$

Here, $k_z = k_0\cos\theta$ is the component of the wave vector $k_0 = \omega_0/C$ along the z-axis of the lens. The presence of this frequency shift allows one to use a harmonic signal as a sounding one [10] and to receive the reflected signal by processing in the frequency domain rather than in the time domain.

In order to develop a theoretical model for an acoustic microscope using the Doppler effect for signal formation, let us consider the scheme of the measuring system (Fig. 1). The plane $z = 0$ coincides with the sample plane, and the focal plane of the acoustic lens is perpendicular to the z-axis. The position of the lens focus is determined by the coordinates $x = y = 0$. Let us assume that the lens forms the field $h_1(x, y, t)$ in the focal plane. The space-time expansion of this field into the spectrum of plane waves is determined by the Fourier transform:

$$H_1(k_x, k_y, \omega) = F[h_1(x, y, t)]$$
$$= \int_{-\infty}^{\infty}\iiint h_1(x, y, t)\exp\{i(\omega t - k_x x - k_y y)\}dxdydt. \tag{2}$$

This wave propagates to the surface of the sample positioned at a distance z from the focal plane; then, it is reflected from the liquid–solid interface and returns to the focal plane after reflection. The space-time spectrum of the returned wave in the focal plane can be represented in the form

$$U(k_x, k_y, \omega)$$
$$= H_1(k_x, k_y, \omega)R(k_x, k_y, \omega)\exp(-2ik_z z). \tag{3}$$

Here, $R(k_x, k_y, \omega)$ is the reflection coefficient and $\exp(-2ik_z z)$ is the phase shift acquired by space-time spectral components in the course of the propagation to the sample and back [11]. Correspondingly, the field distribution $u(x, y, t)$ in the focal plane can be represented by the inverse Fourier transform.

Let this field be detected by a receiving acoustic system with the space-time pulsed response $h_2(x, y, t)$. In this case, we can represent the input signal of the receiving system as a function of its position (x_p, y_p) in the focal plane of the transmitting lens, the sample displacement z from the focal plane, and time t in the form of the convolution

$$V(x_p, y_p, z, t)$$
$$= \int_{-\infty}^{\infty}\iiint u(x, y, t_1)h_2(x_p - x, y_p - y, t - t_1)dxdydt_1. \tag{4}$$

On the basis of the convolution theorem, the output signal can be written in the form

$$V(x_p, y_p, z, t)$$
$$= F^{-1}[H_1 H_2 R(k_x, k_y, \omega)\exp(-2ik_z z)]. \tag{5}$$

Here, we introduced the notation $H_2(k_x, k_y, \omega)$ for the transfer function of the receiving system analogously to expression (2). The transmitting acoustic system in the measuring system under consideration is at the same time the receiving system. Therefore, their independent motion is impossible, and it is necessary to take $x_p = y_p = 0$.

The reflection coefficient for homogeneous and isotropic samples is axially symmetric and, therefore, can be expressed by the function $R(k_z, \omega)$. In this case, by changing over from the coordinates (k_x, k_y) to the coordinates (k_z, φ), expression (5) can be represented, correct to an insignificant constant factor, in the form

$$V(z, t)$$
$$= \int_{-\infty}^{\infty}\iint H_0(k_z, \omega)R(k_z, \omega)\exp\{-i(2k_z z + \omega t)\}dk_z d\omega. \tag{6}$$

Here, the generalized transfer function of the microscope is determined by the expression

$$H_0(k_z, \omega) = \int_0^{2\pi} H_1(k_z, \varphi, \omega) H_2(k_z, \varphi, \omega) k_z d\varphi. \quad (7)$$

To study anisotropic samples, the common practice is to use a cylindrical acoustic lens [5]. The aperture (transfer) function of such a system can be approximately represented by the expression

$$H_1(k_z, \varphi, \omega) H_2(k_z, \varphi, \omega) = H_A(k_z, \omega)\delta(\varphi - \varphi_0). \quad (8)$$

Here, $\delta()$ is the delta-function, and the angle φ_0 determines the orientation of the cylindrical lens in the focal plane. It is easy to demonstrate that the output signal of the microscope in the case of an anisotropic sample is also described by expression (6), the reflection coefficient being measured in the direction determined by the orientation of the cylindrical lens $R(k_z, \omega) = R(k_z, \varphi_0, \omega)$, and the generalized transfer function being equal to

$$H_0(k_z, \omega) = H_A(k_z, \omega) k_z. \quad (9)$$

Both considered examples of acoustic lens systems can be used in a Doppler microscope with a harmonic sounding signal. In the case of utilization of a harmonic sounding signal with the frequency ω_0, the generalized transfer function is determined by the expression

$$H_0(k_z, \omega) = H_0(k_z, \omega_0)\delta(\omega - \omega_0). \quad (10)$$

Let the lens motion be governed by the law $z = v_0 t$. In this case, with the change of variables according to expression (1), formula (6) is recast in the form

$$V(t) = \frac{1}{2v_0} \times \int_{-\infty}^{\infty} H_0\left(\frac{\omega_d}{2v_0}, \omega_0\right) R\left(\frac{\omega_d}{2v_0}, \omega_0\right) \exp\{-i(\omega_d + \omega_0)t\} d\omega_d \quad (11)$$

and, if we ignore an insignificant constant factor, the spectrum of this output signal can be represented as

$$S(\omega - \omega_0) = H_0\left(\frac{\omega_d}{2v_0}, \omega_0\right) R\left(\frac{\omega_d}{2v_0}, \omega_0\right). \quad (12)$$

Thus, the spectral density of the received Doppler signal is determined by the product of the reflection coefficient and the generalized transfer function of the acoustic system. From the qualitative point of view, this relationship is grounded on the fact that different components of the angular spectrum of the ultrasonic wave acquire different frequency shifts as a result of the reflection from a moving surface. The values of the frequency shifts depend on the angle of propagation of the considered components of the angular spectrum, which determines the possibility of separating their responses in the resulting output signal.

Now let us consider the influence of the characteristic instrumental errors inherent in all modifications of measuring microscopes upon a reconstructed spectrum. For this purpose, we represent the output signal as a function of the sample displacement z:

$$V(z) = F^{-1}[S_0(k)] = \int_{-\infty}^{\infty} H_0(k) R(k) \exp(-ikz) dk. \quad (13)$$

Here, we used the notation $k = 2k_z$ (for short).

The signal detected in the experiment differs from signal (13) obtained from the theoretical model. It is evident that noise of radioelectronic origin is present in the real signal, and the result of measurements is affected by the parameters of the immersion medium, which may vary, e.g., with temperature. The received signal is also distorted because of the inaccuracy of the scanning mechanical system, manifests itself as errors in the measurement of the z coordinate and in the inclination of the acoustic axis of the transducer in the course of motion. Moreover, it is possible to measure the signal only for a finite interval of displacements z, while the theoretical signal is unbounded in its duration because of the finiteness of its spectrum.

Let the displacement of the acoustic system be measured with an error, and the direction of motion slightly deviate from the normal to the surface of the flat sample. It is natural to assume that a linear error is small as compared to the focal length, and the constant and variable components of the angular error are small as compared to the aperture angle. In addition, let the generalized transfer function of the system be a smooth function. This allows us to ignore its variation within the limits of the angular aperture, because of the inclination of the acoustic system in the course of motion.

Thus, the imperfection of the scanning system can be expressed by the error of measurement of the scanning coordinate $z_0 + \varepsilon(z)$, which has a constant and a variable parts. Then, the measured signal $V_R(z)$ can be represented in the form

$$V_R(z) = p(z) \int_{-\infty}^{\infty} S_0(k) \exp\{-ik(z + z_0 + \varepsilon(z))\} dk. \quad (14)$$

In this expression, the gate function is $p(z) = 0$ for $|z| > D/2$, where D is the gate width equal to the length of the interval of signal detection. The spectrum of the measured signal has the form

$$S_R(k) = F[V_R(z)] = \int_{-\infty}^{\infty} S_0(l) \exp(-ilz_0) A(l, k) dl,$$
$$A(l, k) = \int_{-\infty}^{\infty} p(z) \exp(-il\varepsilon(z)) \exp(i(k - l)z) dz. \quad (15)$$

This result shows that the experimental spectrum is determined by the superposition of the ideal spectrum and the instrument function A. If there is no error in the measuring system $\varepsilon(z) = 0$, the instrument function becomes a space-invariant function

$$A(l, k) = F[p(z)] = A_0(l - k). \quad (16)$$

Then, the resulting spectrum is determined by the convolution

$$S_R(k) = \{S_0(k)\exp(-ikz_0)\} * A_0(k). \quad (17)$$

The angular resolution of the technique or, in other words, the width Δk of the instrument function A, is determined mainly by the width D of the gate function $\Delta k \sim 1/D$. The gate functions used in spectral analysis (for example, the Hamming function) insignificantly degrade the resolution in comparison with a rectangular function, but they suppress to a considerable extent the parasitic oscillations in the regions of sharp variations of the spectrum $S_R(k)$. Typical kinds of spectrum distortions because of the finiteness of the interval of signal detection were considered, in particular, by Liang *et al*. [7], Bogachenkov, and Titov [10].

The phase factor $\exp(-ikz_0)$ expresses mainly the error in the determination of the position of the focal plane. Usually, the value of z_0 does not exceed several ultrasonic wavelengths in the immersion liquid λ, and, therefore, the period $1/z_0$ of the function $\exp(-ikz_0)$ far exceeds the width Δk of the instrument function A_0. Thus, a slowly varying phase factor is present in the experimental spectrum. This factor must be taken into account when interpreting the experimental results.

If the errors of the mechanical system are nonnegligible, $\varepsilon(z) \neq 0$, we can assume that the gate function $p(z)$ in expression (15) is modulated by an additional phase factor $\exp\{-il\varepsilon(z)\}$. The effect of this modulation upon the instrument function consists in its broadening and rise of numerous powerful sidelobes. If the value of the error becomes comparable with the wavelength λ, then the level of such distortions becomes unacceptable. This conclusion is confirmed by the results of numerical simulations and by experimental data. Hence, it is necessary to require the following:

$$\varepsilon(z) \ll \lambda. \quad (18)$$

In the previously developed Doppler microscope with a harmonic sounding signal of frequency 300 MHz, in order to provide the necessary precision of measurement of the scanning coordinate, a laser interferometer was used [10]. The microscope described in this paper employs an acoustic interferometer.

The focusing transducer of the microscope and the acoustic interferometer formed by a flat transducer were positioned close to each other and excited by harmonic signals with the frequency $\omega_0/2\pi = 65$ MHz. The output voltages of the transducers, which corresponded to the waves reflected from the sample, were subjected to A/D conversion (after radio-wave processing), and their further processing was conducted in digital form. The maximal value of the signal-to-noise ratio was no less than 30 dB. The acoustic lens had a focusing distance of 2.7 mm and a aperture half-angle of 40°, while the diameter of the transducer interferometer was equal to 2 mm. The motion of the acoustic element with respect to the sample was performed by an electromagnetic scanning system with an elastic suspension utilizing membranes. The motion velocity was maintained approximately equal to $v_0 = 6.2$ mm/s by controlling the scanner with the use of a velocity feedback, and the length of the interval of signal detection was $D = 1.85$ mm.

The interferometer signal is formed on account of the reflection of a quasi-plane ultrasonic wave from the surface of the moving sample. Since the focused and plane waves are transmitted through the same liquid cell and reflected from the same surface, the result of measurement proves to be more resistant to vibrations and changes in sound velocity in the immersion medium as compared to the previous scheme of the device. The inherent error of the interferometer caused by the diffraction effects can be determined according to Lependin [15]. The numerical estimates of distortions of the phase of the interferometer signal, which were made for specific parameters of the measurement system, show that the diffraction component of the error does not exceed $0.01\lambda = 0.23$ μm. The Abbe error due to the deviation of the motion from a rectilinear one in the case of the misalignment of the acoustic axes of the interferometer and the lens turns out to be more significant [16]. This component of the error is equal to $L\sin(\delta\theta)$, where $L = 5$ mm is the distance between the aforementioned axes and $\delta\theta$ is the variation of the angular position of the sample in the course of the signal recording. The value of $\delta\theta = 2 \times 10^{-4}$ rad was measured by the deviation of a laser beam reflected from a mirror moving together with the sample. Thus, the error in the measurement of the scanning coordinate is approximately 1 μm, which meets condition (18).

Processing of the received signals consisted of the following steps. The phase of the interferometric signal, which reflected the real law of the mechanical scanner motion $z = z(t)$, was measured by a complex demodulation [14]. In order to compensate the inconstancy of the velocity, the signal of the focusing transducer V was determined at the instants $t_n = t_{\text{inv}}(\delta z n)$, where t_{inv} is the function inverse to the function $z(t)$, δz is the interval of discretization in the coordinate z, and n is an integer. The digital signal V_n corrected in such a way was subjected to the spectral analysis. On the basis of expressions (12) and (1), the spectral density of this signal was represented as a function of the angle $S(\theta) = H_0(\theta)R(\theta)$ and used for measuring the transfer function of the microscope and the acoustic parameters of the samples.

The transfer function of the system can be measured by studying a material, whose reflection coefficient is

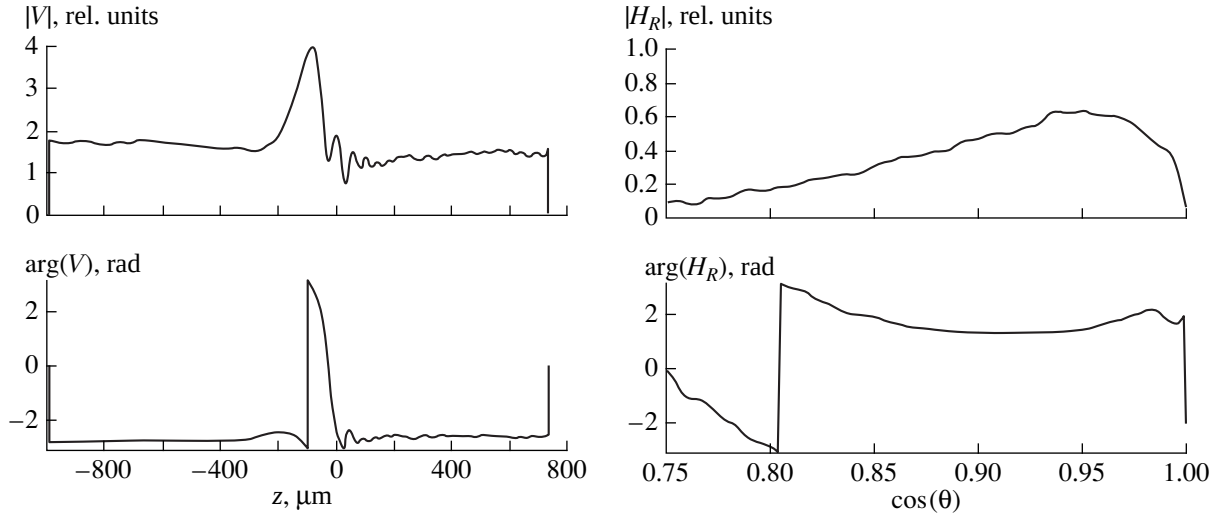

Fig. 2. The magnitude $|V(z)|$ and phase $\arg(V(z))$ of the signal measured for lead and the magnitude $|H_R(\theta)|$ and phase $\arg(H_R(\theta))$ of the transfer function of the microscope.

constant within the aperture angle of the lens system. Lead was used as such a reference material. It has a low velocity of longitudinal waves C_L = 2200 m/s and a high density ρ = 11.2 g/cm^3. Water at a temperature of 21°C was the immersion medium. The sound velocity in it was C = 1485 m/s.

The reflection coefficient of a plane wave incident from a liquid upon a homogeneous isotropic solid half-space can be calculated according to the formula [12]

$$R(\theta) = \frac{Z_L\cos^2 2\theta_T + Z_T\sin^2 2\theta_T - Z}{Z_L\cos^2 2\theta_T + Z_T\sin^2 2\theta_T + Z}, \qquad (19)$$

where $Z_L = \rho C_L/\cos\theta_L$, $Z_T = \rho C_T/\cos\theta_T$, and $Z_L = \rho_0 C/\cos\theta$ are the impedances, ρ_0 is the liquid density, and the propagation angles θ_L and θ_T of longitudinal and transverse waves in the solid satisfy the relationships $\sin\theta_L = C_L\sin\theta/C$ and $\sin\theta_T = C_T\sin\theta/C$.

The critical angle of a longitudinal wave for the lead–water pair is equal to $\theta_1 = \arcsin(C/C_L) = 42.5°$, which exceeds the aperture angle of the acoustic lens. As follows from formula (19), the absolute value of the reflection coefficient for the angles $\theta < \theta_1$ by virtue of strong mismatch of impedances is approximately equal to 0.9, and its phase is exactly equal to zero. Thus, the signal spectrum (Fig. 2) measured for lead can be treated as the experimental transfer function of the measuring system $H_R(k) = H_R(\theta)$.

The signal for quartz (Fig. 3) has characteristic oscillations within the interval of negative values of z, in contrast to the signal for lead. As it was noted above, such oscillations in the functions $V(z)$ occur when the excitation of leaky surface waves takes place. In this case, the phase of the reflection coefficient and, therefore, the phase of the signal spectrum, experience a jump by a value somewhat less than 2π in the region of the critical angle of SAW excitation θ_R.

The velocity of a leaky surface wave C_{R1} was measured by the obtained dependences. Preliminarily, the phase of the reflection coefficient $\arg(R_R(\theta))$ was estimated in the region of the critical angle as the difference between the phases of the measured signal and the transfer function: $\arg(S(\theta)) - \arg(H_R(\theta))$. After that, we determined the position θ_R of the maximum of the derivative of the phase of reflection coefficient, and the velocity was calculated by the formula $C_{R1} = C/\sin(\theta_R)$. The results of the measurements are given in the table.

From the theoretical point of view, the velocity of a leaky surface wave is determined by the positions of the poles and zeros of the reflection coefficient [12], and the technique used above is approximate. The results of numerical simulations show that such an approximation is fairly accurate. For example, for fused quartz, the velocity calculated by the point of inflexion of the phase is higher than the theoretical value by 2 m/s.

The phases of the reflection coefficient measured in the region of the critical Rayleigh angle (Fig. 4) were also used for a nonlinear evaluation of the parameters of the studied object: the density ρ and the velocities of longitudinal and transverse waves C_L and C_T. The solution was sought in the form of the vector (ρ, C_L, C_T) that minimizes the objective function equal to the sum of the squares of deviations of the experimental data and the values of a model function. As the model function, we used the phase of the reflection coefficient $\arg\{R(\theta)\}$ calculated according to formula (19), and the initial approximation was selected in the form of the vector (ρ = 3 g/cm^3, $C_L = 2C_{R1}$, $C_T = C_{R1}$), where C_{R1} is the previously measured value of the velocity of a leaky SAW. The calculations were conducted with the help of the MATLAB software package. In particular, the "cur-

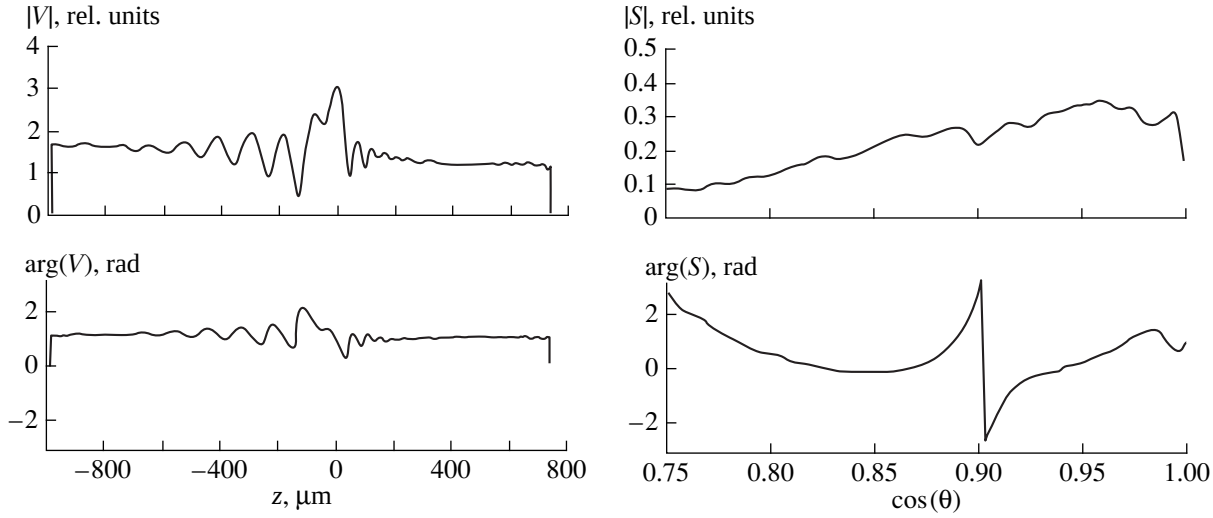

Fig. 3. The magnitude $|V(z)|$ and phase $\arg(V(z))$ of the signal measured for fused quartz and the magnitude $|S(\theta)|$ and phase $\arg(S(\theta))$ of its spectrum.

vefit" function realizing the Lewenberg–Marquardt minimization algorithm was used [13].

The processing results given in the table demonstrate that the best relative error (0.7%) is attained for the velocity of transverse waves. This effect can be easily explained, since there is a strong coupling between the velocity of a transverse wave and the velocity of Rayleigh waves ($0.87 < C_R/C_T < 0.95$), and the velocity of a surface wave can be measured to a relatively high accuracy. The measured density value ($\rho = 2.07$ g/cm^3) is somewhat below the real one, which can be explained as follows. The result of measuring the phase of the reflection coefficient is smoothed out on account of the convolution with the instrument function, and a more smooth behavior of the phase of the reflection coefficient corresponds to a material with a lower density. This means that, in order to increase the precision of measurements, it is desirable to perform the deconvolution of the experimental spectrum or to smooth out the model reflection coefficient in the course of fitting.

The values obtained for the density and the velocities of bulk waves were used, in turn, for the determination of the velocity of a leaky SAW. The reflection coefficient was calculated by the reconstructed parameters (ρ, C_L, C_T), its pole and zero in the region of the Rayleigh angle were determined, and the velocity of a leaky wave C_{R2} was calculated by the real part of these singularities. As one can see from the table, the relative error of measurement for this technique is 0.17%, which is noticeably less than the error of measurement by the point of inflexion of the phase (0.42%). Apparently, the measuring result of C_{R2} is more stable, because, in the process of the determination of the parameters (ρ, C_L, C_T), the selection of the best approximation for the measured phase of the reflection coefficient is performed, and the full information is used rather than the data on a local interval.

The main results of this study are as follows. An acoustic microscope with a harmonic sounding signal was designed. This microscope is intended for measuring the acoustic parameters of the homogeneous isotropic regions of flat samples. The theoretical analysis of the error inherent in the technique demonstrated high sensitivity of measurement results to the errors of the

Results of measurements for fused quartz

Parameter	Measured value, $\langle C \rangle$	Variance, σ	Relative error, $3\sigma/\langle C \rangle$, %	Known value [1]
C_{R1}, m/s	3437	4.8	0.42	3429.1*
ρ, g/cm^3	2.07	0.05	7.2	2.2
C_{L1}, m/s	5898	45	2.3	5970
C_T, m/s	3779.5	9.2	0.7	3765
C_{R2}, m/s	3432.7	2.0	0.17	3429.1*

* Calculated for the known parameters and the temperature of water 21°C.

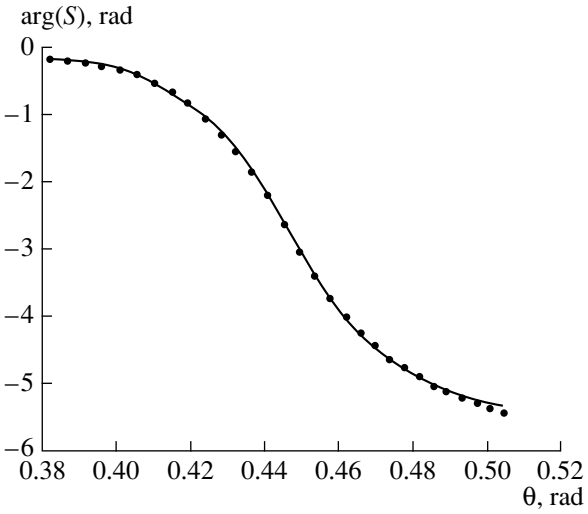

Fig. 4. Phase of the reflection coefficient for fused quartz: the dots show the results of measurements, and the solid line corresponds to the results of calculation for the determined parameters (ρ, C_L, C_T).

scanning system. Therefore, an acoustic interferometer is utilized in this device for detecting the displacement of the sample plane. An algorithm for the determination of the sample parameters, namely, the density and velocities of longitudinal and transverse waves and leaky surface waves, by the measured phase of the reflection coefficient is developed. Using fused quartz as an example, it was demonstrated that the measurement error is 7.2% for the density and 2.3 and 0.7% for the velocities of longitudinal and transverse waves, respectively. The error in the determination of the velocity of a leaky SAW by calculating the singularity of the reflection coefficient corresponding to the measured values of density and bulk wave velocities is equal to 0.17%, which is much better than the error in the direct determination of the SAW velocity by the phase of the measured reflection coefficient (0.42%).

REFERENCES

1. A. Briggs, *Acoustic Microscopy* (Clarendon Press, Oxford, 1992).
2. H. L. Bertoni, IEEE Trans. Sonics Ultrason. **31**, 105 (1984).
3. A. Atalar, J. Appl. Phys. **49**, 5130 (1978).
4. M. A. Kulakov and A. I. Morozov, Akust. Zh. **31**, 817 (1985) [Sov. Phys. Acoust. **31**, 502 (1985)].
5. J. Kushibiki and N. Chubachi, IEEE Trans. Sonics Ultrason. **32**, 189 (1985).
6. J. A. Hildebrand, K. Liang, and S. D. Bennet, J. Appl. Phys. **54**, 7016 (1983).
7. K. K. Liang, G. S. Kino, and B. T. Khuri-Yakub, IEEE Trans. Sonics Ultrason. **32**, 213 (1985).
8. N. Nakaso, K. Ohira, M. Yanaka, and Y. Tsukahara, IEEE Trans. Ultrason. Ferroelectr. Freq. Control **41**, 494 (1994).
9. L. D. Bakhrakh and S. A. Titov, Akust. Zh. **36**, 552 (1990) [Sov. Phys. Acoust. **36**, 308 (1990)].
10. A. N. Bogachenkov and S. A. Titov, in *Problems of the Design and Production of Radioelectronic Means and Electric and Radio Articles* (Moscow Institute of Radio Electronics and Automation, Moscow, 1996), pp. 115–123.
11. D.-L. Liu and R. C. Waag, IEEE Trans. Ultrason. Ferroelectr. Freq. Control **44**, 1 (1997).
12. L. M. Brekhovskikh, *Waves in Layered Media* (Nauka, Moscow, 1973; Academic, New York, 1980).
13. Y. Bard, *Nonlinear Parameter Estimation* (Academic, New York, 1974; Finansy i Statistika, Moscow, 1979).
14. S. A. Titov, R. G. Maev, and A. N. Bogachenkov, Prib. Tekh. Éksp., No. 2, 140 (2000) (in press).
15. L. F. Lependin, *Acoustics* (Vysshaya Shkola, Moscow, 1978).
16. V. P. Koronkevich, V. S. Sobolev, and Yu. N. Dubnishchev, *Laser Interferometry* (Nauka, Novosibirsk, 1983).

Translated by M. Lyamshev

Acoustical Physics, Vol. 46, No. 5, 2000, pp. 530–533. Translated from Akusticheskiĭ Zhurnal, Vol. 46, No. 5, 2000, pp. 609–612.

Acoustical Method for the Determination of the Elastic and Piezoelectric Constants of Crystals of Classes 6*mm* and 4*mm*

S. V. Bogdanov

Institute of Semiconductor Physics, Siberian Division, Russian Academy of Sciences, pr. Akademika Lavrent'eva 13, Novosibirsk, 630090 Russia

e-mail: bogd@isp.nsc.ru

Received August 28, 1999

Abstract—An acoustical method is proposed for the determination of the elastic and piezoelectric constants of crystals of classes 6*mm* and 4*mm*. The method is based on the technique developed for orthorhombic crystals of class *mm*2 and described in the previous paper [9]. Only three samples are required for the determination of all elastic and piezoelectric constants of crystals belonging to the two symmetry classes of interest; for the crystals of class 6*mm*, only two samples are necessary. The proposed method can be used only when the signs of the piezoelectric constants are known beforehand. Knowing the sign of electrostriction for the crystals under study, the relative signs of the piezoelectric constants can be uniquely determined in accordance with the data reported earlier [10]. This approach allows one to extend the method used in the previous paper [9] to crystals of classes 6*mm* and 4*mm*. © *2000 MAIK "Nauka/Interperiodica".*

Permanent interest in the determination of the elastic and piezoelectric constants of crystals is driven by the fact that, along with the density and permittivity, these constants are the fundamental parameters of a material. For much-studied crystals, these constants are refined [1], and for new materials, they are determined for the first time [2]. In most cases, the piezoelectric constants are measured by the resonance method [1–3]. However, this method has some disadvantages and is not always applicable. Therefore, a search for new methods of measuring the piezoelectric constants is currently in progress [4–7]. Recently, an acoustical method for the determination of these constants was proposed by the author of this paper [8, 9]. In the cited papers, the elastic c_{ijkl}^E and piezoelectric e_{mpq} constants were determined for a variety of crystals (of classes 23, $\bar{4}3m$, 422, $\bar{4}2m$, 622, and *mm*2), and requirements to the accuracy of the phase velocity measurements ($\delta V \sim 1$ m/s) and the sample orientation ($\delta\varphi \sim 20'$) were specified for the case $K^2 \sim 0.01$ in order to determine e_{mpq} with an accuracy of ~10%. The requirements imposed on the sample and transducer dimensions and on the sound wavelength are as follows [8]: the selected dimensions should provide such conditions that the phase velocity of a plane wave propagating in the sample is equal to that observed in an unbounded crystal. In this paper, we consider the crystals of symmetry classes 6*mm* and 4*mm*.

As in the previous publications, we assume that the density ρ of the samples and their permittivity components ε_{mn}^{ξ} are known. For simplification, we will drop the superscripts marking the quantities c_{ijkl}^E and ε_{mn}^{ξ} (E indicates that the measurements were taken in a constant electric field, and ξ denotes the measurements taken at constant strains). Thus, we have $c_{ijkl} \equiv c_{ijkl}^E$ and $\varepsilon_{mn} \equiv \varepsilon_{mn}^{\xi}$.

The determination of the elastic and piezoelectric constants of crystals by the acoustical method is based on the measurements of the phase velocities $V_{[n_1n_2n_3]}^{[u_1u_2u_3]}$ of elastic waves and was described in detail in the previous papers [8, 9]. (The bracketed subscripts marking the velocity V are the direction cosines (or their multiples) of the wave normal n, and the bracketed superscripts are those of the displacement u.)

Crystals of classes 6*mm* and 4*mm* have a higher symmetry than orthorhombic crystals of class *mm*2 for which the determination of the elastic and piezoelectric constants is described in [9]. In crystals of the two symmetry classes under study, the crystal axis X_2 is equivalent to the crystal axis X_1, and, hence, these crystals have $c_{11} = c_{22}$, $c_{13} = c_{23}$, $c_{44} = c_{55}$, $e_{31} = e_{32}$, $e_{15} = e_{24}$, and $\varepsilon_{11} = \varepsilon_{22}$. These relations have some consequences for the measurement technique. On the one hand, they allow one (taking into account the equivalence of the X_1- and X_2-axes) either to noticeably reduce the number of measurements or to increase the accuracy in the determination of the constants of interest by performing the necessary measurements along both axes. On the other

1063-7710/00/4605-0530$20.00 © 2000 MAIK "Nauka/Interperiodica"

hand, they make it impossible to determine the constant e_{33} and, hence, the constant c_{13}. In the cited paper [9], it was assumed that the signs of the piezoelectric constants were unknown, which made the procedure of their determination much more complicated and restricted the variety of the crystals under investigation to the *mm*2 class for which $e_{31} \neq e_{32}$ and $e_{15} \neq e_{24}$. These inequalities are necessary for an unambiguous determination of e_{33}. Therefore, the measuring technique described in [9] cannot be applied to the crystals of classes 6*mm* and 4*mm* studied in this paper. However, this difficulty can be overcome, if the signs of the piezoelectric constants are known in advance. Then, in most cases, the ambiguity in the determination of the piezoelectric constants is automatically eliminated. For example, if we know that $e_{15} > 0$, the sign of the square root $e_{15} = \pm\sqrt{e_{15}^2}$ will be uniquely defined.

For the determination of all elastic and piezoelectric constants of crystals belonging to the 6*mm* and 4*mm* classes, three samples are necessary:

sample 1 is oriented strictly along the crystal axes X_1, X_2, and X_3;

sample 2 is rotated about the X_3 axis through the angle $\alpha = 45°$;

sample 3 is rotated about the X_2 (or X_1) axis through the angle $\varphi \simeq 25°$–$30°$.

For crystals of class 6*mm*, only two samples, namely, samples 1 and 3, are required.

The measurements on sample 1 provide the constants $c_{11} = c_{22}$, c_{33}^D, $c_{44} = c_{55}$, $c_{44}^D = c_{55}^D$, c_{66}, and $e_{15}^2 = e_{24}^2$, where

$$c_{33}^D = c_{33} + e_{33}^2/\varepsilon_{33}, \quad c_{55}^D = c_{55} + e_{15}^2/\varepsilon_{11}.$$

The relationships between these constants and the velocities $V_{[n_1n_2n_3]}^{[u_1u_2u_3]}$ are shown in the table. (The sign of the piezoelectric constant $e_{15} = \pm\sqrt{e_{15}^2}$ will be determined below.)

The elastic constant c_{12} is determined from the measurements of the velocities $V_{[110]}^{[110]}$ and $V_{[110]}^{[\bar{1}10]}$ on sample 2, i.e., the measurements of the velocities of elastic waves propagating in the [110] direction and polarized in the X_1X_2 plane. The formula for calculating the constant c_{12} has the form

$$c_{12} = \rho[(V_{[110]}^{[110]})^2 - (V_{[110]}^{[\bar{1}10]})^2] - c_{66}, \qquad (1)$$

which is obtained from the expression for c_{12} from [9].

For crystals of class 6*mm*, the elastic constant c_{66} in not an independent one: $c_{66} = 0.5(c_{11} - c_{12})$. Therefore, the elastic constant c_{12} can be determined without using sample 2:

$$c_{12} = c_{11} - 2c_{66}. \qquad (2)$$

Table

$V_{[100]}^{[100]} = \sqrt{c_{11}/\rho}$	$V_{[100]}^{[010]} = \sqrt{c_{66}/\rho}$	$V_{[100]}^{[001]} = \sqrt{c_{55}^D/\rho}$
$V_{[010]}^{[100]} = \sqrt{c_{66}/\rho}$	$V_{[010]}^{[010]} = \sqrt{c_{11}/\rho}$	$V_{[010]}^{[001]} = \sqrt{c_{55}^D/\rho}$
$V_{[001]}^{[100]} = \sqrt{c_{55}/\rho}$	$V_{[001]}^{[010]} = \sqrt{c_{55}/\rho}$	$V_{[001]}^{[001]} = \sqrt{c_{33}^D/\rho}$

On sample 2, it is advisable also to measure the velocity $V_{[110]}^{[001]}$, i.e., the velocity of a shear wave propagating in the [110] direction and polarized along the X_3 axis. Knowing this velocity, it is possible to refine the value of e_{15}^2:

$$e_{15}^2 = \varepsilon_{11}[\rho(V_{[110]}^{[001]})^2 - c_{55}] \qquad (3)$$

(see [9] with allowance for the symmetry of the crystals under study).

The unknown constants c_{13}, e_{31}, and e_{33} are determined from the measurements on sample 3. For this purpose, it is necessary to measure the velocities of the elastic waves polarized in the X_1X_3 plane (the quasi-longitudinal and quasi-transverse waves) in two orthogonal directions, i.e., the velocities

$$V_{[n_10n_3]}^{[1]}, \quad V_{[n_10n_3]}^{[2]}, \quad V_{[n_30n_1]}^{[1]}, \quad \text{and } V_{[n_30n_1]}^{[2]}.$$

Here, the bracketed superscripts, 1 and 2, correspond to the quasi-longitudinal and quasi-transverse waves, respectively. These data are sufficient for the determination of e_{31}, e_{33}, and c_{13}. The calculation is performed according to the scheme described in [9]. However, in this scheme, it is necessary to introduce some changes related to taking into account the specific signs of the sought-for piezoelectric constants.

In the recent publication [10], it was shown that the relative signs of the piezoelectric constants of crystals belonging to the classes 6*mm*, 4*mm*, and *mm*2 are not arbitrary but are determined by the sign of electrostriction of these crystals. Specifically, the results reported in [10] offer the following conclusions:

1. For all piezoelectric crystals, the signs of all like piezoelectric constants (d_{mij}, e_{mij}, g_{mij}, and h_{mij}) that are used with differently selected sets of independent variables should be identical; i.e., the signs of d_{33} and e_{33} coincide. For crystals of symmetry classes under study, it is generally agreed [11] that $d_{33} > 0$ and, hence, $e_{33} > 0$.

2. When the choice of independent variables is made, the relative signs of the piezoelectric constants of crystals belonging to the classes 6*mm*, 4*mm*, and *mm*2 depend on the type of electrostriction of each specific crystal:

(a) crystals with positive electrostriction have

$$e_{33} > 0, \quad e_{31} < 0, \quad e_{32} < 0, \quad e_{15} > 0, \quad e_{24} > 0;$$

(b) crystals with negative electrostriction have

$$e_{33} > 0, \quad e_{31} < 0, \quad e_{32} < 0, \quad e_{15} < 0, \quad e_{24} < 0.$$

With allowance for the given signs of the piezoelectric constants, their determination is performed as follows.

I. Determination of e_{15}(e_{24}). Since the experiment provides the value of e_{15}^2, we obtain $e_{15} = \pm\sqrt{e_{15}^2}$. The sign of the square root is selected automatically:

1. For crystals with positive electrostriction, we have

$$e_{15} = +\sqrt{\ldots}.$$

2. For crystals with negative electrostriction, we have

$$e_{15} = -\sqrt{\ldots}.$$

II. Determination of e_{31}(e_{32}). For all crystals of symmetry classes under study (with both positive and negative electrostriction), we have $e_{31} < 0$. Therefore, the right-hand side of expression (4) from paper [9],

$$e_{31} = -e_{15} \pm \sqrt{m},$$

must be negative. However, the sign of e_{15} depends on the sign of electrostriction. Then:

1. For crystals with positive electrostriction, we have

$$e_{31} = -e_{15} \pm \sqrt{m};$$

(a) if $m > e_{15}^2$, the sign of the square root is uniquely determined:

$$e_{31} = -e_{15} - \sqrt{m};$$

(b) if $m < e_{15}^2$, the ambiguity remains. However, in the following calculations, it is eliminated, as was shown in [9].

2. For crystals with negative electrostriction, we have

$$e_{31} = |e_{15}| \pm \sqrt{m}.$$

The solution will be physically meaningful when $m > e_{15}^2$ and the minus sign is taken before the square root. Thus, in this case, the constant e_{31} is unambiguously determined:

$$e_{31} = |e_{15}| - \sqrt{m}.$$

III. Determination of e_{33}. The piezoelectric constant e_{33} is determined by expression (4) from [9]:

$$e_{33} = \frac{\varepsilon_{33}}{\varepsilon_{11}} e_{15}\left[1 \pm \sqrt{1 - \frac{\varepsilon_{11}k}{\varepsilon_{33}e_{15}^2}}\right]. \qquad (4)$$

For all crystals under study, $e_{33} > 0$. However, the crystals with positive and negative electrostriction should be treated in different ways.

1. Crystals with positive electrostriction.

We note that the quantity k involved in the radicand in expression (4) can be both positive and negative.

(a) The case $k > 0$.

Solution (4) has a physical meaning only when the condition

$$\frac{\varepsilon_{11}k}{\varepsilon_{33}e_{15}^2} < 1$$

is fulfilled. (If this is not the case, one can conclude that the accuracy of the measurements is low.) With this condition being satisfied, the radicand in expression (4) is less than unity. Then, we have

$$\sqrt{1 - \frac{\varepsilon_{11}k}{\varepsilon_{33}e_{15}^2}} < 1,$$

and the expression enclosed in the square brackets in (4) is positive, no matter what the sign of the square root. Thus, both solutions are physically meaningful, and the ambiguity in the determination of e_{33} persists.

(b) The case $k < 0$.

When $k < 0$, the radicand is greater than unity; i.e.,

$$\sqrt{1 + \frac{\varepsilon_{11}|k|}{\varepsilon_{33}e_{15}^2}} > 1,$$

and, since $e_{33} > 0$, the only possible sign in (4) is the plus sign. Then, for $k < 0$, we obtain

$$e_{33} = \frac{\varepsilon_{33}}{\varepsilon_{11}} e_{15}\left[1 + \sqrt{1 + \frac{\varepsilon_{11}|k|}{\varepsilon_{33}e_{15}^2}}\right].$$

2. Crystals with negative electrostriction.

Crystals with negative electrostriction have $e_{15} < 0$, and expression (4) takes the form

$$e_{33} = -\frac{\varepsilon_{33}}{\varepsilon_{11}}|e_{15}|\left[1 \pm \sqrt{1 - \frac{\varepsilon_{11}k}{\varepsilon_{33}e_{15}^2}}\right].$$

Since $e_{33} > 0$, the expression enclosed in the square brackets must be negative, so that the radicand is positive and greater than unity, and the square root should be taken with the minus sign. Hence, the quantity k should be negative. The positive values of this quantity, $k > 0$, mean that the measurement errors are too large.

Thus, for crystals with negative electrostriction, the constant e_{33} is unambiguously determined:

$$e_{33} = -\frac{\varepsilon_{33}}{\varepsilon_{11}}|e_{15}|\left[1 - \sqrt{1 + \frac{\varepsilon_{11}|k|}{\varepsilon_{33}e_{15}^2}}\right].$$

From the above consideration, it follows that, in most cases, for crystals of classes $6mm$ and $4mm$, the piezoelectric constants $e_{31}(e_{32})$, e_{33}, and $e_{15}(e_{24})$ are unambiguously determined, provided that their signs are known beforehand. The only exclusion is the determination of e_{33} when

$$m < e_{15}^2, \quad k > 0 \quad \text{and} \quad \frac{\varepsilon_{11}k}{\varepsilon_{33}e_{15}^2} < 1.$$

It is only in this case that the constant e_{33} cannot be uniquely determined.

Thus, from the measurements on sample 3, we determine the constants e_{31} and e_{33}. Then, knowing c_{33}^D, we calculate c_{33}. Using expression (7) from [9], we determine c_{13}. Hence, the method proposed in [9] allows one to determine all elastic and piezoelectric constants for crystals of symmetry classes $6mm$ and $4mm$.

ACKNOWLEDGMENTS

This work was supported by the Russian Foundation for Basic Research, project no. 97-02-18555.

REFERENCES

1. M. Zgonik, P. Bernasconi, M. Duelli, *et al.*, Phys. Rev. B **50**, 5941 (1994).
2. Jung Hee-rac, Jin Byung-Moon, Cha Jung-Won, and Kim Jung-Nam, Mater. Lett. **30** (1), 41 (1997).
3. V. Bobnar, Z. Kutnjak, and A. Levstik, Jpn. J. Appl. Phys., Part 1 **37**, 5634 (1998).
4. Sato Yoko, Wu Chen-Xu, Majima Yutake, and Iwamoto Mitsumasa, Jpn. J. Appl. Phys., Part 1 **37**, 215 (1998).
5. S. Muensit and I. L. Guy, Appl. Phys. Lett. **72**, 1896 (1998).
6. J. A. Christman, R. P. Woolcott, A. I. Kingon, and R. J. Nemanich, Appl. Phys. Lett. **73**, 3851 (1998).
7. J. P. Rivera, Ferroelectrics **224**, 533 (1999).
8. S. V. Bogdanov, Akust. Zh. **41**, 751 (1995) [Acoust. Phys. **41**, 661 (1995)].
9. S. V. Bogdanov, Akust. Zh. **43**, 304 (1997) [Acoust. Phys. **43**, 260 (1997)].
10. S. V. Bogdanov, Avtometriya, No. 1, 3 (1999).
11. Yu. I. Sirotin and M. P. Shaskol'skaya, *Foundations of Crystal Physics* (Nauka, Moscow, 1975).

Translated by E. Golyamina

Acoustical Physics, Vol. 46, No. 5, 2000, pp. 534–543. Translated from Akusticheskiĭ Zhurnal, Vol. 46, No. 5, 2000, pp. 613–623.

Effect of Tide on Sound Propagation in the Shelf Zone of the Sea of Japan

L. F. Bondar', L. K. Bugaeva, and A. N. Rutenko

Pacific Institute of Oceanology, Far East Division, Russian Academy of Sciences, Baltiĭskaya ul. 43, Vladivostok, 690041 Russia

e-mail: pacific@online.marine.su

Received November 18, 1999

Abstract—Experimental and numerical studies of the effect of surface and internal tides on 315-Hz sound waves propagating along fixed paths, 260 m to 23 km in lengths, oriented across the shelf of the Sea of Japan, are discussed. The measurements are performed using self-contained radio-hydroacoustic receiving stations, which are equipped with hydrophones and scalar-vector receivers, and two vertical acoustic-hydrophysical measuring systems. For the sound signals propagating along the longer paths, the intensity fluctuations are shown to loose their linear relation to the tide-caused changes in the waveguide parameters because of the refraction by the sound speed inhomogeneities induced by different hydrodynamic processes. However, it is established that the phase variations can serve as quantitative indicators of the integral changes in the waveguide parameters. *© 2000 MAIK "Nauka/Interperiodica".*

INTRODUCTION

Nowadays, to monitor hydrophysical processes over sea areas, "translucence" acoustic methods based on sounding the water medium by continuous or pulsed signals are thought to be the most promising ones [1]. Sound waves are refracted and scattered by the spatial inhomogeneities of the sound speed field, which are produced by both front and vortex structures, as well as by the seasonal pycnocline perturbed by the wave of internal tide and short internal waves (IW) propagating along it. All these phenomena affect the propagation of sound waves. The problem is to obtain information on this effect.

In the late 1960s, American scientists arranged an acoustic path across the Florida Strait, between Miami and Bimini [2]. Long-term observations showed that the variations in the parameters of the sound signal (especially, the signal phase) were governed by changes that occurred in the Gulf Stream due to the effect of tides. The tidal effects are natural harmonic sources of periodic perturbations for hydrophysical fields, these perturbations affect the sound propagation in the water layer. Their periodicity considerably simplifies the selection of these effects from the background variations in the parameters for the sound field that propagates in an irregular acoustic waveguide, e.g., in the shelf zone of a tidal sea.

In this paper, we consider the effect of the surface tide and tide-caused perturbations on the low-frequency sound field for the shelf of the Sea of Japan. The study is based on the analysis of in-sea measurements carried out on fixed paths, 260 m and 23 km in length, oriented across the shelf. We also use data of numerical experiments that allow one to study the effects of the surface and internal tides in a "pure" form in the framework of the mode approach. By comparing the data of acoustic measurements performed on the same paths in different hydrological conditions, we managed to quantitatively estimate the effects of the surface tide and the displacement of the temperature front extending along the shelf and to extract the variations that occur in the parameters of the acoustic field due to the internal tide waves propagating over the seasonal pycnocline.

EXPERIMENTAL SITE AND NUMERICAL MODELING

Figure 1 shows the map of the region where the experiments were carried out. The points of sound transmission and reception and the propagation paths are indicated in the map. The experimental site area is nearly free of ice all over the year: in winter, ice is only formed in the coastal zone and in harbors. In these regions, because of cooling (down to –1.8°C) and convective mixing, relatively "heavy" water is formed that moves along the sloping sea floor to the shelf edge. At the same time, the warm water (0.5°C) of the Sea of Japan advects into the shelf zone. The seasonal thermocline starts to form in April, and, in July, the gradients of temperature (ΔT) and salinity (ΔS) in the thermocline can reach 0.9°C/m and 0.08 ‰/m, respectively. In August, because of south and south-east

1063-7710/00/4605-0534$20.00

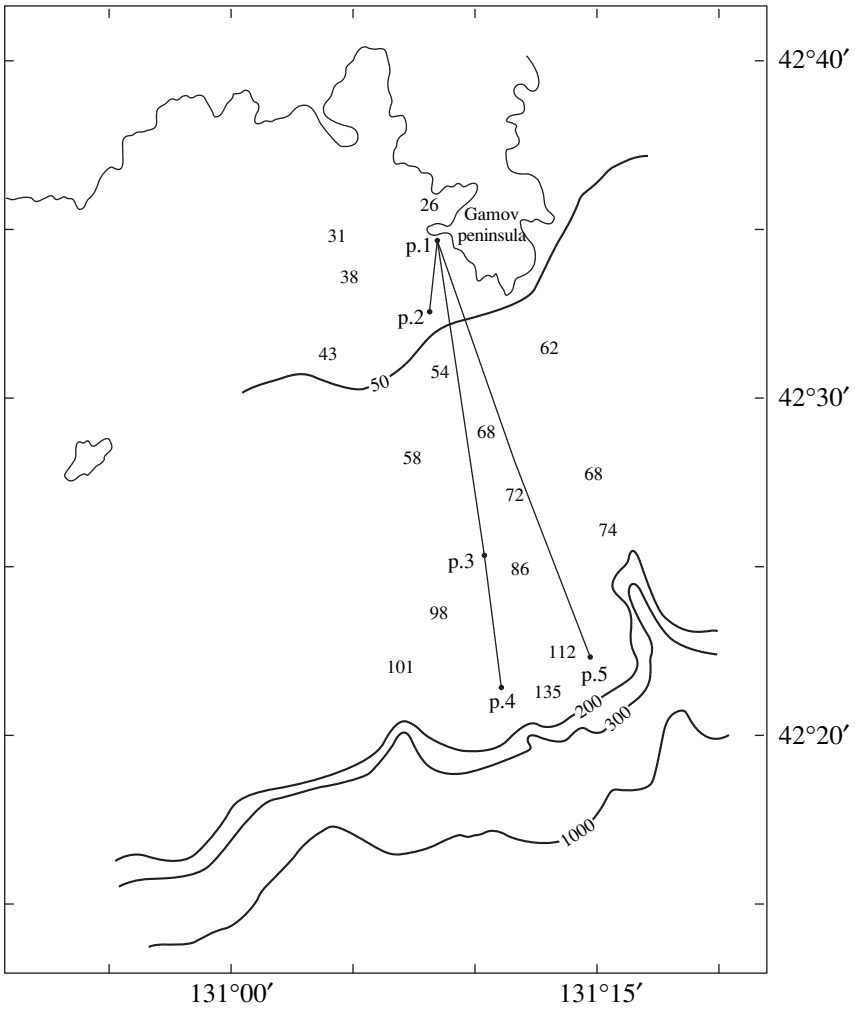

Fig. 1. Map of the experimental site with the indicated locations of measuring instruments and propagation paths.

winds, the seasonal thermocline is expelled from the shallow-water part of the shelf. For instance, on August 24, 1997, 1.5 km ashore, the following values were obtained: $\Delta T = 0.15$°C/m, $\Delta S = 0.01$ ‰/m, and, on August 26, 1998, the thermocline was resting on the sea floor at a depth of 65 m, 9 km ashore. In autumn, north and northwest winds carry warm surface water to the sea, and the thermocline is again formed in the coastal region because of the income of relatively cold (2.5°C) and salty (34.2‰) water into the shallow-water part of the shelf. Within this season, the thermocline with $\Delta T \approx$ 1°C/m can extend from the shelf edge to the coastal zone; in this case, it serves as the upper boundary of the near-bottom sound channel and is perturbed by the internal tide wave and shorter IW [3]. The autumn thermocline differs from the spring-summer one in the thickness of its upper layer, but again becomes closer to the sea surface under the influence of the autumn–winter monsoon and due to the cooling of surface waters.

Before discussing the data of in-sea measurements, let us consider the theoretical estimates characterizing the effect of surface and internal tides on the propagation of sound waves with a frequency of 315 Hz along the path crossing the shelf. The internal tide wave is generated by tidal currents near the shelf edge and propagates over the inclined bottom toward the coast in the form of a free internal wave. This wave is affected by many hydrophysical phenomena that can vary even within several ours, e.g., because of changes in the velocities and directions of wind-induced currents. Therefore, the internal tide waves measured in the shallow-water part of the shelf loose the periodicity of the surface tide. The measurements showed that, when the thermocline extends from the shelf edge to the coastal zone, two internal tide waves can simultaneously propagate over it. Numerical modeling of the sound propagation was performed for two spatial positions of the thermocline. The propagating sound waves were modeled by normal waves in the adiabatic approximation with the use of the MOATL computer code [4]. This code allows one to compute the propagation loss for a waveguide with a range-dependent sound speed profile

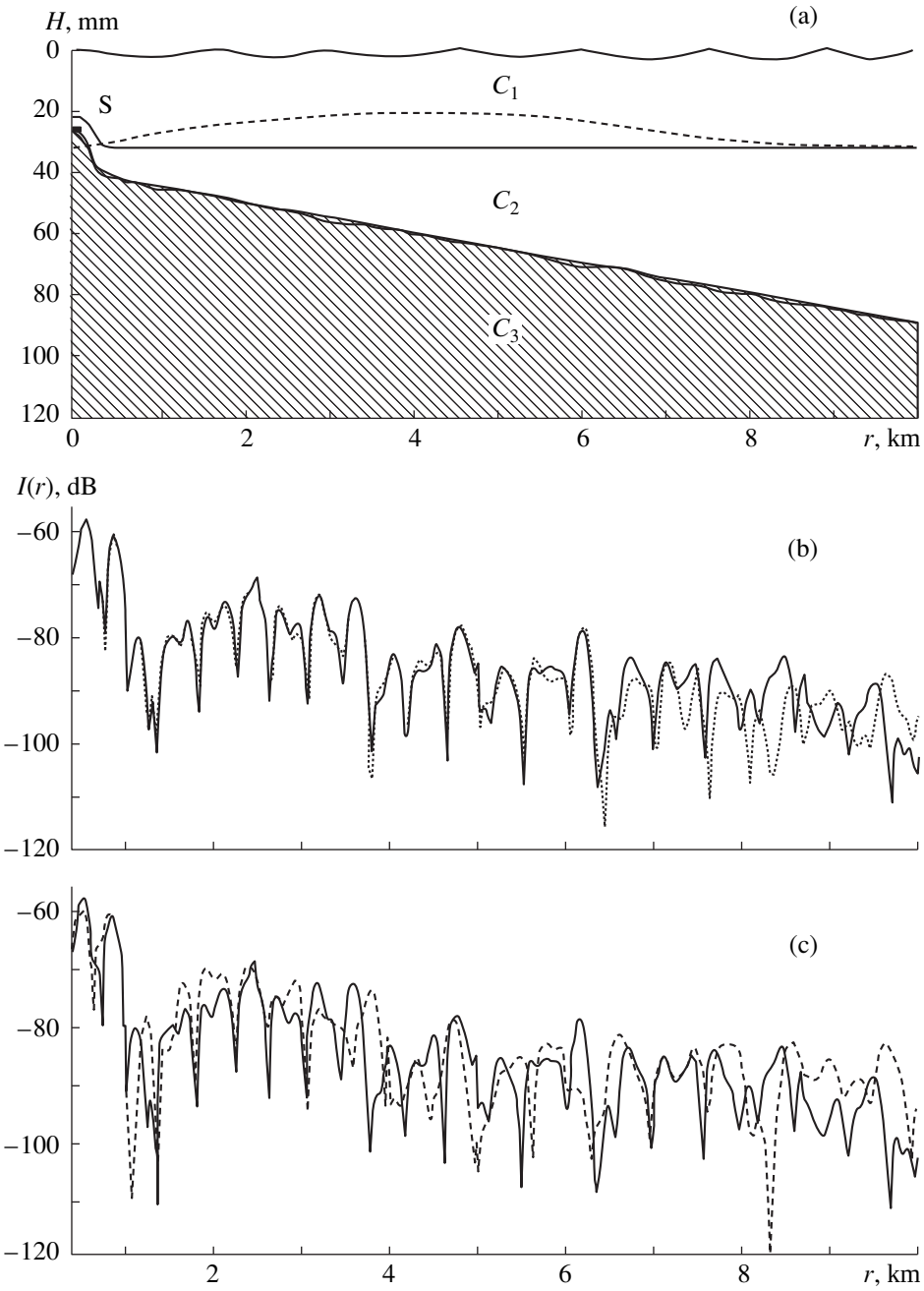

Fig. 2. (a) Profile of the 10-km fraction of the modeled acoustic path. The calculated propagation loss for the 315-Hz sound signals: the solid curve corresponds to the unperturbed waveguide; (b) the dotted curve corresponds to the water surface elevated by 20 cm over the entire path with the thermocline position being unchanged (see the solid curve in Fig. 2a); (c) the dashed curve is for the waveguide perturbed by the internal tide wave (see the dashed curve in Fig. 2a). Notation: S is the sound source, C_1 = 1510 m/s, C_2 = 1470 m/s, C_3 linearly varies with depth from 1600 to 1900 m/s within the fluid bottom layer.

in view of the actual geometry of the sea floor. With each change in the sound speed profile or bottom geometry, the mode parameters were recalculated, and the attenuation coefficient of each mode was integrated over the range. In the case at hand, seven modes propagated. The bottom was modeled as a two-layer fluid. Within the upper layer, the sound speed changed linearly in depth, from 1600 to 1900 m/s. The thickness of this layer changed along the 20-km propagation path, from 80 m at its beginning to 1 m at its end. The lower layer was modeled by a homogeneous halfspace with the sound speed 2500 m/s. For the two layers, absorption coefficients of 0.7 and 0.11 dB/km and densities of 1.029 and 1.758 g/cm^3 were respectively specified. The amplitude of the surface waves was 0.2 m. The bottom profile and the sound speed distribution are shown in

Fig. 2a for the 10-km fragment of the path. The plots $I(r)$ shown in Fig. 2b correspond to the propagation loss for the signal with a frequency of 315 Hz, generated by a point source located at p.1 (see Fig. 1) at a depth of 25 m. The sound receivers were 1 m above the bottom surface. The solid curves in Fig. 2 correspond to the unperturbed two-layer water waveguide with sound speeds of 1510 and 1470 m/s. The changes in the waveguide parameters produced by the internal tide were modeled by the 0.2-m elevation of the water surface along the entire path, with no changes in the thermocline position. The plot $I(r)$ (the dotted curve in Fig. 2b) corresponds to such a model. The perturbation of the waveguide by the internal tide is shown by the dashed curve in Fig. 2a. The plots $I(r)$ in Fig. 2c illustrate the changes in the spatial distribution of the sound field for the near-bottom layer. These changes are induced by an internal tide wave with the parameters observed in the in-sea experiment. Figure 2 shows that, at the specified sound frequency, the surface tide affects the propagation to a much lesser extent than the wave of the internal tide.

RESULTS OF MEASUREMENTS

Figure 3 illustrates the in-sea measured variations in intensity I and phase φ for tonal sound signals of frequency 315 Hz. These data were obtained for different seasons on fixed paths oriented across the shelf. A tonal signal of 315 Hz (TON-315) generated by the G3-122 high-precision oscillator (with a frequency instability below $\pm 3 \times 10^{-8} \times f_0$ for 16 h of continuous operation) was transmitted at a depth of 25 m from p.1 (a sea depth of 26 m). At points p.3–p.5, the signal was received by the self-contained bottom-moored radio-hydroacoustic buoys. At p.2, the combined receiver (CR) of the OTK-LIK-91D digital self-contained radio-hydroacoustic station was used [5]. The CR measures three orthogonal components (V_x, V_y, V_z) of the particle velocity V and the sound pressure P. Here, for both V and P, we refer to the quantities I and φ as the intensity and phase of the sound field, respectively, with indication of the transducer used in the measurement. Now, let us consider the technique used in the numerical evaluation of these quantities in more detail.

The data that continuously arrive from the measuring devices (including the reference emitted signal) are digitized. The obtained digital sequences are fed into the computer as synchronous trains containing 4096 values each. Then, upon Hamming weighting, the fast Fourier transform (FFT) is used to compute the amplitude spectra. The spectral values are stored within the preliminarily chosen narrow frequency bands that contain the frequencies of the transmitted acoustic signals. We study the characteristics of the harmonic signals by using the periodograms calculated by a standard FFT algorithm from the realizations that are finite in time: $T = N/f_d$, where N is the realization length and f_d is the digitizing frequency. This procedure calls for additional explanations.

If the measuring time of the function $x(t) = A\cos(2\pi f_0 t)$ is limited by the interval $-T/2 \le t \le T/2$, the contraction of $x(t)$ into this interval, which is denoted by $x_T(t)$, can be written in the form $x_T(t) = x(t)u(t)$, where $u(t) = 1$ for $-T/2 \le t \le T/2$ and $u(t) = 0$ for other t [6]. With $X_T(f)$ representing the Fourier transform (FT) of the function $x_T(t)$, we obtain $X_T(f) = \frac{A}{2}\left(\frac{\sin[\pi(f - f_0)T]}{\pi(f - f_0)} + \frac{\sin[\pi(f + f_0)T]}{\pi(f + f_0)}\right)$. This expression is associated with the convolution of two delta-functions with the function $(\sin x)/x$, the latter being governed by the finite length of the interval. The maxima of $X_T(f)$ correspond to the frequencies $\pm f_0$, and, because $\lim_{x \to 0} \frac{\sin(xT)}{x} = T$, they are equal to $AT/2$, the power spectral density $Sx_T(f_0) = T^{-1}X_T^2(f_0) = A^2T/4$ depending on T. Actually, we use the FT that is determined for a finite interval of discrete values of time. Therefore, when $f_0 = n/(NT)$ (i.e., when $x(t)$ produces an integer number of cycles), we have $Sx_T(f_0) = A^2T/4$ at $f_0 = \pm n$, and it equals to zero at $f_0 \ne \pm n$. Otherwise, the function $(\sin x)/x$ will again appear, but, in any case, the integration of $Sx_T(f)$ will lead to the rms value of the cosinusoid that is equal to $A^2/2$. Calculating the FT is equivalent to approximating the function by a linear combination of sines and cosines (matching). Because of discontinuities, such a matching procedure is known to lead to oscillations of the form $(\sin x)/x$—the Gibbs effect. If the discontinuities, namely, the beginning and the end of the realization, are "rounded off," the error in matching will decrease. We do so by using the Hamming weighting function. Therefore, we assume that the leak of the signal energy from the spectral window $\Delta f \cong T^{-1}$ is negligibly small.

The main hydrodynamic sources of the fluctuations of I and φ are relatively slow. So we believe that, from the periodogram value $G(k)$ $(0 \le k \le 2047)$ corresponding to the interval $\Delta f = 1/T$ ($T = 4096/f_d \approx 3$–4 s) that contains the emitted frequency f_0, the intensity of the received signal can be determined as follows: $I = A^2 = 2aT^{-1}G(k)$, where a is a factor that compensates for the decrease in the variance, which is caused by weighting the data in the time domain. Below, this value will be called the intensity value of the measured signal (with reference to the type of the used transducer). Because only variations in I are of interest for us, it is advantageous to consider the values of $I(t)$ expressed in dB relative to the level of a digit of the A/D converter. Synchronously with the received sound signals, the reference (emitted) signal was entered into the computer, and, by using the co-spectrum (with averaging in a band), the phase differences $\Delta\varphi$ between the measured and the reference signals were computed. The functions

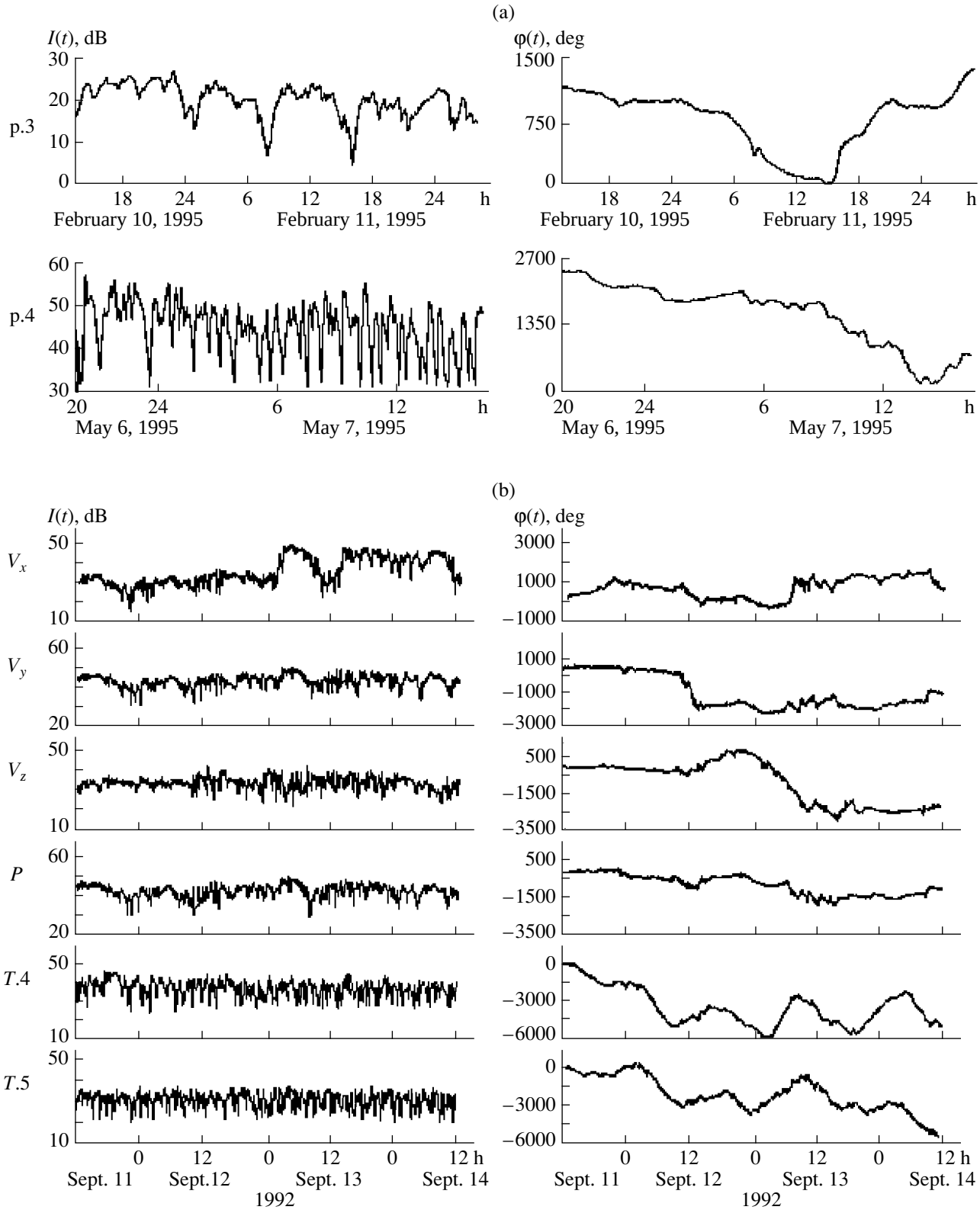

Fig. 3. (a) Intensity and phase variations for 315-Hz sound signals received by bottom-moored hydrophones of anchored radio-hydroacoustic buoys in February and May, 1995. (b) Synchronous measurements (September, 1992) by the scalar-vector receiver (plots V_x, V_y, V_z, and P) at the point p.3 (see Fig. 1) and by the bottom-moored hydrophones of the buoys at the points p.4 and p.5 (plots *T*.4 and *T*.5, respectively).

$\Delta\varphi(t)$ and $\varphi(t)$ differ by a constant value, but their variations (the object of our study) must be the same. Thus, we analyze the variations of $\Delta\varphi$, but attribute them to the phase with the notation $\varphi(t)$. The values of $\varphi(t)$ were calculated with the use of the arctangent function, which is known to be determined within the interval from –90° to 90°. Therefore, to obtain a continuous sequence of $\varphi(t)$, the following algorithm was applied: $\varphi_i = \varphi_i^{\arctan} + \Delta\varphi_i$; $\varphi_{i+1} = \varphi_{i+1}^{\arctan} + \Delta\varphi_{i+1}$, where $\Delta\varphi_{i+1} = \Delta\varphi_i$ when $\left|\varphi_i^{\arctan} - \varphi_{i+1}^{\arctan}\right| \le 90°$, and, when $\varphi_i^{\arctan} - \varphi_{i+1}^{\arctan} > 90°$, we have $\Delta\varphi_{i+1} = \Delta\varphi_i + 180°$, and $\Delta\varphi_{i+1} = \Delta\varphi_i - 180°$ for $\varphi_i^{\arctan} - \varphi_{i+1}^{\arctan} < -90°$.

Thus, as a result of the preprocessing of the experimentally measured sound signals, we obtain synchronous sequences of the values of I (in dB) and φ (in deg) at equal time intervals Δt. If failures in the radio-telemetry channels occur or the devices are temporally switched, the sequences of $I(t)$ and $\varphi(t)$ were additionally corrected. For instance, the time intervals within which no measurements were carried out were filled with the appropriate number of $I(t)$ and $\varphi(t)$ values that were obtained by a linear interpolation. Such a procedure is most critical for the sequences of $\varphi(t)$. Each analyzed value of $\varphi(t)$ is a mean phase of the sound field at the reception point within a single realization 3 to 4 s long. In view of the fact that the hydrodynamic phenomena produce relatively slow variations of $\varphi(t)$, we assume that, for the time interval $\Delta t \cong 8$–12 s, the probability for the difference $\Delta\varphi_i = |\varphi_i - \varphi_{i-1}|$ to exceed a value of 60° is extremely small. However, in the experimental data, such deviations do exist (though they are rare). In such cases, the data on φ were corrected by adding (subtracting) a value of $\Delta\varphi_i$ to (from) all subsequent values of φ_i. Thus, as a result of the correction, false phase jumps were eliminated from the many-hour-long sequences of the $\varphi(t)$ values.

In Fig. 3, the plots of $I(t)$ and $\varphi(t)$ are presented for the data obtained on the propagation paths p.1–p.3 (February 10–12, 1995), p.1–p.4 (May 6–7, 1995), p.1–p.5 and p.1–p.4 (September 11–14, 1992), along with the theoretical estimates. The presented data show a strong influence of the thermocline perturbed by the internal tide wave on the sound propagation in the shallow sea. According to the hydrological data, the water was inhomogeneous in its temperature along the path p.1–p.3. A front can be even noticed that is caused by the motion of relatively cold and "heavy" water from the shallow coastal part of the shelf toward the shelf edge and by the advection of the warmer water of the Sea of Japan into the shelf zone. In the plot of $I(t)$ (Fig. 3a, February), drops in the signal level by 10 to 15 dB occur with a periodicity of 7–9 h. In other seasons, the fadings are observed much more frequently. The irregular semidiurnal tide causes changes by a value of ≤30 cm in the sea level. At the same time, the phenomena of inshore and ashore currents, both wind driven and caused by nonlinear surface waves, noticeably affect the surface displacements. The plots of $\varphi(t)$, which correspond to the winter and spring measurements, exhibit no variations with periods of the semidiurnal tide. On the other hand, they are well pronounced in the plots of $\varphi(t)$ corresponding to the synchronous measurements carried out on the paths p.1–p.4 and p.1–p.5 in September 1992. This fact is presumably associated with the attenuation of the higher acoustic modes that propagate in the shallow-water waveguide. In this case, several lower modes interfere at the reception point, and, because of the close values of their phase velocities, considerable changes in their propagation are required to produce changes in the amplitude of the total received signal. The bottom relief and the acoustic properties of the bottom material remain unchanged, but the thickness of the water layer varies with the period of the semidiurnal tide. However, according to the curves $\varphi(t)$ (February, May), the aforementioned phenomena affect the sound field much weaker than the space-time variations of the temperature fronts. During the May experiment [7], the seasonal thermocline began to form at the depth 5–10 m with $\Delta T \approx 0.3$°C/m at the transmission point, and at the depth 12–18 m with $\Delta T \approx 0.5$°C/m at the reception point. The profiles $T(z)$ measured from the anchored research vessel at a point with the sea depth 48 m exhibited a change of 1–2°C in the water temperature within the near-surface water layer. Hence, similarly to the winter conditions, the temperature field was inhomogeneous along the path, but this time the inhomogeneity was caused by a faster water warming in the shallow-water part of the shelf. The decrease in the mean period of the variations of I can be explained by the sound refraction and scattering by the IW-produced spatial inhomogeneities of the sound speed field. In these processes, the acoustic energy flows from lower modes to higher ones, thereby compensating for the decay of the higher modes in the course of their propagation. The latter phenomenon may have a resonant nature [8].

Figure 3b shows the plots of $\varphi(t)$ and $I(t)$ for the sound signals received in September, 1992 [5], at a distance of 3.7 km from the sound source at the point p.2 with the use of the CR (curves V_x, V_y, V_z, and P). For the signals observed at p.4 and p.5 (plots T.4 and T.5), the fluctuations of $I(t)$ and $\varphi(t)$ are relatively stationary and stable. On the other hand, the plots obtained at p.2 exhibit a high variability of the fluctuations in time. The V_x-sensor of the CP was oriented approximately perpendicularly to the path. Therefore, the sound signal received by it was significantly affected by the sound signals that arrived at the reception point (p.2) after their reflection from bottom areas whose insonification strongly depended on the thermocline depth. This is a possible explanation for the considerable variations of $I(t)$ (up to 30 dB, plot V_x in Fig. 3b, September 13) measured by the V_x-sensor. The observed phase changes in the CR-received signals confirm this hypothesis. Before noon of September 12, the phase $\varphi(t)$ of the sig-

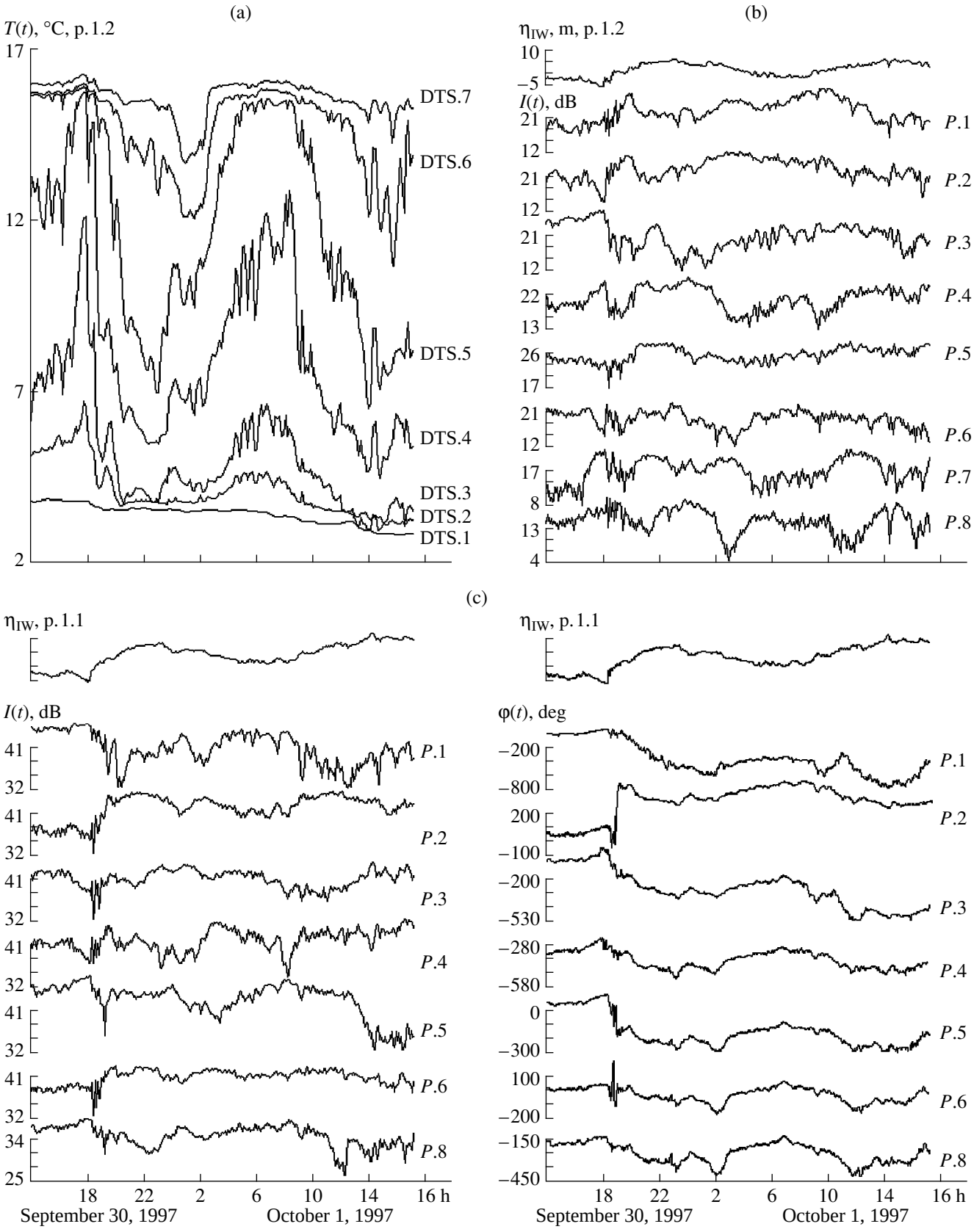

Fig. 4. Variations of the water temperature $T(t)$ and the IW profile η_{IW} along with the intensity and phase fluctuations ($I(t)$ and $\varphi(t)$) for 315-Hz sound signals according to the measurements on a fixed acoustic-hydrophysical path in 1997.

nals received by the CR was relatively stable. After that, because of the change in the mean water temperature and the vertical displacements of the thermocline, the signal phase significantly varies, and the curve $\varphi(t)$ obtained with the V_x-sensor is similar to the IW profile that is typical for this region. Such IW follow the intrusion of cold water into shallow-water areas [9]—the "boras" with subsequent oscillations superimposed on longer IW. The phase variations at the V_z-sensor, which reach a value of 4000°, confirm the significant changes in the vertical structure of the sound speed field along the experimental path. The phase variations of the signal received by the *P*-sensor did not exceed 1500° within three days, and no pronounced tide-induced oscillations are observed in the phase plot.

The following conclusions can be drawn from the performed experiments. The fluctuations of I of the low-frequency sound signals that propagate across the shelf along the longer paths lose their linear relation to the regular changes in the waveguide properties, which are induced by the tide-forming forces. This loss is caused by the sound refraction by the sound speed inhomogeneities that are generated by various hydrodynamic processes. In contrast to the intensity, the phase variations do not saturate [5, 7] and can serve as a quantitative indicator of integral changes in the water layer of the acoustic waveguide. According to Fig. 3a, in winter and spring seasons, the effect of the surface tide is insignificant for the site at hand in comparison with the variations produced by the moving front formations. In autumn, the phase $\varphi(t)$ is governed by the wave of the internal tide, whose period does not always correspond to that of the surface tide because of the details of its propagation over the inclined bottom [10]. Figure 3 shows that the variations in φ observed in the winter, spring, and autumn experiments reached 1500°, 2600°, and 5000°, respectively. The relative stability ("saturation") of the intensity fluctuations observed with the V_z-sensor of the CR, 3.7 km away from the source, is explained by the selectivity of this sensor to the sound energy carried by steep rays or higher modes of the sound field, the parameters of these rays strongly depending on the acoustic inhomogeneities of the water layer and the sea floor.

In 1997, a fixed acoustic-hydrophysical path was arranged on the site [11] with a sound source installed 50 m from the steep coast, at a point with the 26-m sea depth. Two vertical acoustic-hydrophysical measuring systems, MOLLYUSK-96 (M-96) and MOLLYUSK-97 (M-97) [12], were used. These systems synchronously measured the following parameters: the sound pressure within the frequency band 20–600 Hz, at eight horizons (hydrophones *P*.1, …, *P*.8, which were vertically separated by $\Delta z = 4.5$ m); the water temperature (T) at eight (M-97, $\Delta z = 4.5$ m) and five (M-96, $\Delta z = 4$ m) horizons; and the mean temperature variations of water layers covered by seven (M-97) distributed temperature sensors (DTS), each 4.5 m long, and by two (M-96) DTS,

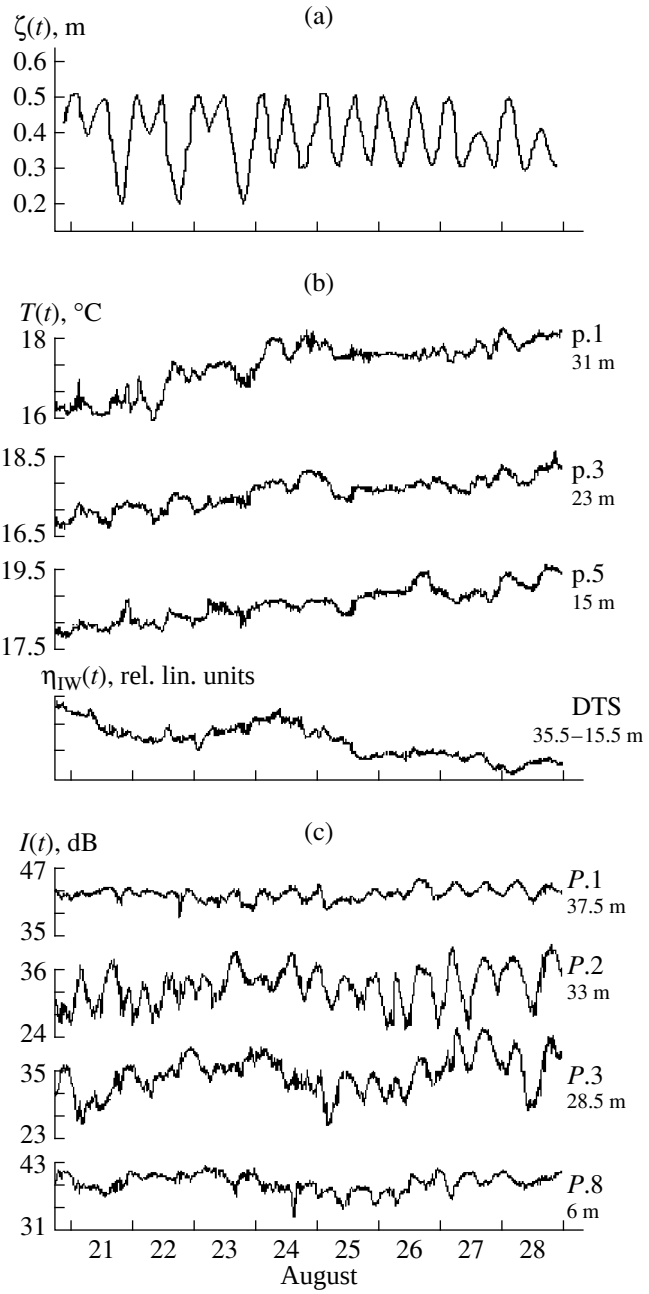

Fig. 5. Variations of the water temperature and the intensity of 315-Hz sound signals according to the measurements by the MOLLYUSK-96 vertical acoustic-hydrophysical measuring system; the dependence $\zeta(t)$ corresponds to the surface tide plotted with the use of the data from the Tide Guide.

20 m in length. The M-96 system was moored at 260 m from the source, at the point p.1.1 (with a sea depth of 38 m); the M-97 system was 420 m away from the source, at the point p.1.2 (a sea depth of 40 m). In Fig. 4, the variations of the water temperature are plotted for p.1.2, as measured by the sensors DTS.1, …, DTS.7 of the M-97 system. The figure also shows the IW profiles η_{IW} for p.1.2 and p.1.1 and the plots of $I(t)$ and $\varphi(t)$ for

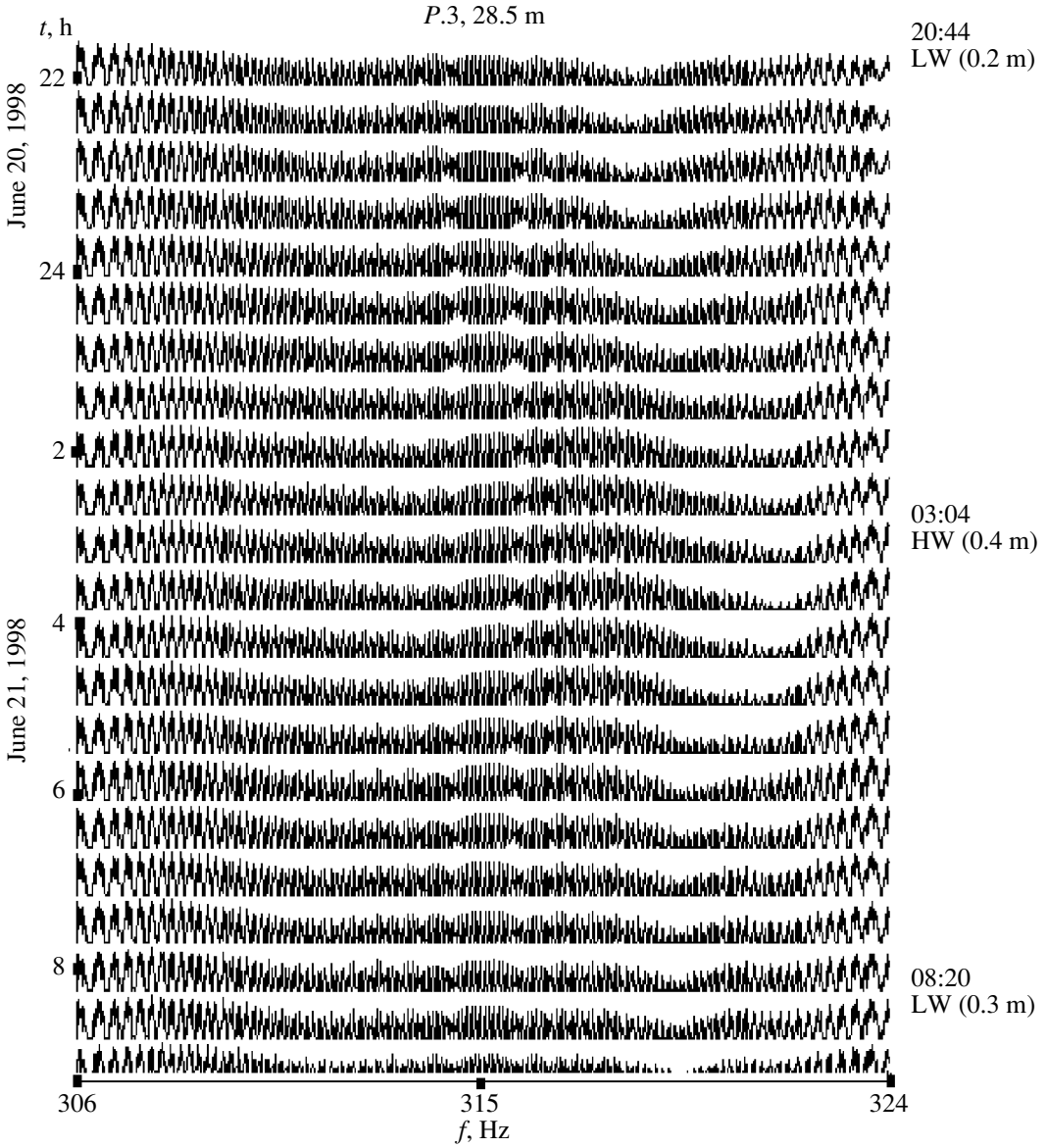

Fig. 6. Sonogram $\hat{G}(\omega)$ of the frequency-modulated sound signal received by the hydrophone *P*.3 of the MOLLYUSK-96 system at a depth of 28.5 m.

the TON-315 sound signal measured by the hydrophones of the M-96 and M-97 systems.

The plots $T(t)$ illustrate changes in the vertical temperature structure that are caused by the internal tide wave and the short-period IW. According to the plot of η_{IW} obtained from the temperature measurements at p.1.2 with the point and distributed temperature sensors of the M-97 system (see Fig. 4b), the height of the internal tide wave reaches 14 m in autumn. In combination with the IW, this wave generates in-phase vertical displacements of water particles within a 27-m thick layer. The plots $I(t)$ exhibit variations that correlate with the IW passing over the path. The effect of internal tide can be noticed from the plots of $\varphi(t)$. The tide-periodicity phase variations of the sound signals propagating along the 250-m path did not exceed 30° for the winter measurements [7].

By the end of August, 1998, in the shallow-water part of the hydrophysical site, the 40-m thick layer was nearly homogeneous in temperature (see Fig. 5b). Therefore, the variations of $I(t)$ of the TON-315 signal, which were measured by the M-96 system on the 260-m-long path and presented in Fig. 5c, are mainly caused by the tidal oscillations of the sea level—the plot $\zeta(t)$ in Fig. 5a. Figure 5b shows the variations of the water temperature $T(t)$ measured at three horizons with the point transducers of the M-96 system. The figure also shows the IW profile $\eta_{IW}(t)$ corresponding to the variations of the mean temperature in the water layer covered by the 20-m DTS. Figure 5 shows that, for the

environment at hand, the variations in I correlate with the surface tide better than with the changes in the water temperature.

EFFECT OF TIDE ON THE FREQUENCY INTERFERENCE STRUCTURE OF THE SOUND FIELD

Experiments [13] showed a possibility of diagnostics the surface tide by measuring the frequency shifts in the interference structure of a broadband sound field propagating in a shallow sea. For a waveguide of the depth H_0, an algorithm is proposed to estimate the frequency shift δf of the extrema in the frequency interference structure of the sound field under the influence of tidal variations of the surface level ΔH:

$$\delta f \approx -\frac{2f\Delta H}{H_0}.$$

On our experimental site, the height of the irregular semidiurnal surface tide was $\Delta H \approx 0.21$ m. Hence, according to this formula, for the sound frequency f = 315 Hz and the mean waveguide depth H_0 = 38 m, we have δf = –3.5 Hz.

Figure 6 shows the sonogram of the power spectrum, $\hat{G}(\omega, t)$, for the frequency-modulated signal propagating along the 260-m path. The sound field was received by a hydrophone of the M-96 system at a depth of 28.5 m. The sound power spectrum $\hat{G}(\omega)$ is estimated with a frequency resolution of 0.02 Hz. In this experiment, because of the specific environmental conditions in the coastal shelf zone, the internal tide wave and the IW were weak. Therefore, the shifts of the minima in the frequency interference structure of the sound field (with a nearly semidiurnal period) are caused by the surface tide. In Fig. 6, the times and heights are indicated for low and high waters (LW and HW) on the site; the values were taken from the Tide Guide. The shift $\delta f \approx 3$ Hz of the minimum agrees well with that estimated by the aforementioned algorithm.

REFERENCES

1. V. V. Goncharov, V. Yu. Zaĭtsev, V. M. Kurtepov, A. G. Nechaev, and A. I. Khil'ko, *Acoustic Tomography of the Ocean* (Inst. Prikl. Fiz. Ross. Akad. Nauk, Nizhni Novgorod, 1997).
2. J. C. Steinberg, J. G. Clark, H. A. DeFerrari, *et al.*, J. Acoust. Soc. Am. **52**, 1521 (1972).
3. A. N. Rutenko, in *Proceedings of the School–Workshop of Academician L. M. Brekhovskikh "Acoustics of the Ocean"* (GEOS, Moscow, 1998), pp. 160–163.
4. J. F. Miller and S. N. Wolf, *Modal Acoustic Transmission Loss (MOATL): A Transmission-Loss Computer Program Using a Normal-Mode Model of the Acoustic Field in the Ocean* (Naval Research Laboratory, Washington, 1980).
5. L. F. Bondar', S. V. Borisov, A. V. Gritsenko, *et al*., Akust. Zh. **40**, 561 (1994) [Acoust. Phys. **40**, 497 (1994)].
6. R. Otnes and L. Enochson, *Applied Time Series Analysis*, Vol. 1: *Basic Techniques* (Wiley, New York, 1978; Mir, Moscow, 1982).
7. A. N. Rutenko, Akust. Zh. **43**, 98 (1997) [Acoust. Phys. **43**, 84 (1997)].
8. B. G. Katsnel'son and S. A. Pereselkov, Akust. Zh. **44**, 786 (1998) [Acoust. Phys. **44**, 684 (1998)].
9. A. N. Rutenko, Morsk. Gidrofiz. Zh., No. 3, 58 (1989).
10. P. E. Holloway, E. Pelinovsky, T. Talipova, and B. Barnes, J. Phys. Oceanogr. **27**, 871 (1997).
11. L. F. Bondar', A. V. Gritsenko, A. N. Rutenko, and M. Yu. Trofimov, in *Proceedings of the School–Workshop of Academician L. M. Brekhovskikh "Acoustics of the Ocean"* (GEOS, Moscow, 1998), pp. 178–182.
12. A. N. Rutenko, Prib. Tekh. Éksp., No. 5, 141 (1998).
13. V. M. Kuz'kin, A. V. Ogurtsov, and V. G. Petnikov, Akust. Zh. **44**, 94 (1998) [Acoust. Phys. **44**, 77 (1998)].

Translated by E. Kopyl

Acoustical Physics, Vol. 46, No. 5, 2000, pp. 544–550. Translated from Akusticheskiĭ Zhurnal, Vol. 46, No. 5, 2000, pp. 624–631.

Low-Frequency Sound Absorption and Attenuation in Marine Medium

R. A. Vadov

Andreev Acoustics Institute, Russian Academy of Sciences, ul. Shvernika 4, Moscow, 117036 Russia

e-mail: bvp@akin.ru

Received November 25, 1999

Abstract—Original experimental data are analyzed on the low-frequency sound attenuation in the Mediterranean, Black, and Baltic Seas, Sea of Japan, and the north-western region of the Pacific Ocean. In these regions, waters significantly differ in their temperatures and salinities. The analysis is aimed at obtaining an expression for calculating the low-frequency absorption coefficient in sea water. The analysis uses the previously published data on the measured (by the temperature discontinuity method) low-frequency relaxation times associated with boron present in sea water. The dependence of the absorption on the pH value (which was revealed in the 1970s) and the experimental data on sound absorption at frequencies higher than 5–10 kHz are also taken into account. As a result of the analysis based on the assumption that low-frequency relaxation takes place, an expression is proposed that relates the low-frequency absorption to the temperature, salinity, and pH value and equally well describes the experimental frequency dependences of attenuation for the four regions at hand (except for the Baltic Sea). Increased attenuation coefficients are noticed for shallow seas and deep-water regions where waters are influenced by intense currents, strait zones, and zones of mixing waters of different origin, i.e., for the ocean areas where, in addition to the attenuation, sound scattering by inhomogeneities of the marine medium and sound energy leakage into the sea floor are significant. *© 2000 MAIK "Nauka/Interperiodica".*

One of the main medium parameters that govern the sound field intensity is the sound absorption coefficient. This parameter quantitatively estimates the portion of acoustic energy that changes to heat in the course of sound propagation. The sea water is a complex electrolyte in which periodic pressure variation leads to periodic (somewhat shifted in phase) variations in its ionic composition. To describe sound absorption in such a medium, in addition to the shear viscosity, one should take into account the volume viscosity that has a relaxation nature and leads to a specific frequency dependence of the absorption coefficient.

At high frequencies (higher than 10 kHz), the range dependence of the sound-field level is almost completely governed by the geometric spread (in view of the refraction phenomena) and by the sound absorption in the medium. At low frequencies, in addition to absorption, the sound scattering by the medium inhomogeneities may sometimes be important. To characterize the total losses, the sound attenuation was determined as the exponential component of the sound field level decay, which must be added to the geometric spread to obtain the experimentally observed range dependence of the sound field. The concept of attenuation was used by experimentalists, even when the nature of decay was not clear. The problem of separate components of attenuation had been solved as their physical mechanisms had been determined.

In the experimental studies of low-frequency (below 5 kHz) sound attenuation in the ocean, the sound field decay was commonly measured in the underwater sound channel (USC), with the sound source and receiver located near the channel axis. The attenuation coefficient was determined by the offset of the experimental decay from the cylindrical law. At frequencies of 1–5 kHz, at which a propagation path of 100–150 km in length is sufficient, such an approach is quite reasonable. In this case, except for the regions of mixing waters of different origin, one can treat the sea medium as horizontally layered and the sound field level as cylindrically decaying with distance.

At frequencies of 0.5–1.0 kHz, path lengths of 500–1000 km or more are required to estimate the attenuation coefficient, and the problem becomes more complicated. For such path lengths, the sea medium can hardly be considered a horizontally layered one. The profiles $c(z)$ considerably vary along the path, which leads to a geometric spread of the sound field that differs from the cylindrical one. Sometimes, the difference reaches 7–12 dB at a 1000-km range [1]. This difference is caused by the redistribution of the acoustic energy in depth and is unrelated to the sound absorption. In this case, the aforementioned difference can be considered as a systematic error in the attenuation estimates. However, it is not easy to eliminate this error. It seems that the correction can be achieved by computing

1063-7710/00/4605-0544$20.00

the sound field in view of the medium changes along the path with subsequent calculation of the attenuation coefficient from the deviation of the experimental decay curve from the calculated law rather than the cylindrical one. Unfortunately, an experimentalist often possesses insufficient information on the spatial variability of the sound speed field, especially for the time of the experiment. On a 1000-km path, five to seven sound speed profiles are typically measured prior to and after the acoustic experiment. From such data, one gets nothing but the extent of the variability of $c(z)$ along the path and the character of possible deviations of the actual geometric spread of the sound field from the cylindrical law.

To correct the aforementioned systematic error in estimating the attenuation coefficient (β), some experimentalists use the "differential" method. This method implies that wide-band acoustic signals are emitted, e.g., explosion-generated ones. With the differential technique, the offset from the cylindrical law is eliminated by considering the decays of the sound field levels at different frequencies, these decays being normalized to that at some "reference" frequency f_0. Then, the "excess" is calculated for the attenuation coefficients at different frequencies over that at the reference one. Obtaining the absolute values of the attenuation coefficient is possible if its frequency dependence is assumed to be monotonic, with β tending to zero at $f = 0$. This method has been used by Sheehy and Halley [2], Vadov [3], and other researchers.

With the progress in the experimental studies of sound attenuation in a marine medium, the sound frequencies had become lower, laboratory measurements have been replaced by in-sea ones, and physical explanations have been repeatedly sought for the "excess" values of the attenuation (absorption) coefficient, as compared with those extrapolated from higher frequencies. Thus, in the 1930s and 1940s, the main problem was to explain the attenuation coefficients measured in fresh water, which were three times higher than those yielded by the Kirchhoff–Stokes calculations. This problem was solved by considering the structural relaxation of water molecules (with the relaxation frequencies 10^{10}–10^{11} Hz) and introducing the concept of volume viscosity [4]. At frequencies lower than 1 MHz, the fresh-water sound absorption is proportional to the squared frequency, and the factor of proportionality can be expressed as

$$K = 1.42 \times 10^{-8} \times 10^{1240/T} \text{ dB/km kHz}^2, \qquad (1)$$

where T is the absolute temperature (in K).

In the late 1940s to early 1950s, the problem was to explain the 10-times excess in the sea-water sound attenuation over the fresh-water one at frequencies about 100 kHz. The reason for this excess was found, and a theory was developed for the relaxation of the dissociation degree of the magnesium sulfate [5, 6]. As a result of laboratory studies carried out at the Acoustics Institute, Academy of Sciences of the USSR, in the late 1950s to early 1960s, with the use of the experimental data published by that time, an expression was proposed for describing the sound absorption in the sea water at frequencies from 5 to 10 kHz:

$$\beta = \frac{A_{\mathrm{MgSO_4}} f}{f/f_{r\mathrm{MgSO_4}} + f_{r\mathrm{MgSO_4}}/f} + K f^2, \qquad (2)$$

where the parameters of the relaxation absorption caused by the magnesium sulfate are defined as

$$f_{r\mathrm{MgSO_4}} = 1.125 \times 10^{(9 - 2038/T)} \text{ kHz},$$

$$A_{\mathrm{MgSO_4}} = 62.5ST \times 10^{-6} \text{ dB/km kHz}.$$

The second term on the right-hand side of expression (2) describes the fresh-water absorption, the factor K is defined by expression (1), and S is the sea-water salinity (‰).

In the 1960s and 1970s, the excess sound attenuation in the marine medium at low frequencies (below 3–5 kHz) initiated theoretical consideration and thorough analysis of a number of physical processes that could be potentially responsible for the observed phenomenon. In this connection, the following hypotheses were discussed in the literature: sound scattering by thermal inhomogeneities or marine organisms, "imperfections" of the underwater sound channel, additional attenuation due to nonlinear effects (in the case of explosion-generated sound signals), and low-frequency relaxation processes associated with the eddy viscosity or with structural rearrangement of water molecules, with beryllium sulfate, etc.

The most correct explanation for the observed sound attenuation proved to be the low-frequency relaxation associated with the boron present in the sea water. This hypothesis was proposed in 1972–1974. The main argument in its favor was, and still remains, the data of the measurements of the relaxation time, which were carried out with the method of temperature discontinuity for sea waters with and without boron [7]. Unfortunately, no other data have been obtained to confirm the hypothesis, although some investigators tried to apply the laboratory-measured sea-water absorption coefficients at frequencies higher than 6–10 kHz to the problem [8]. As the reliable experimental data on the attenuation coefficients at 0.2–5 kHz, only those obtained by in-sea measurements in the underwater sound channel should be considered.

In the late 1970s to early 1980s, for calculating the low-frequency sound absorption in the ocean, expressions were recommended (see, e.g., [9, 10]) that allowed for the relaxation processes. These expressions often yielded good agreement with the experimental data for some ocean regions but failed to do so for others.

Table 1

Region	North-western Pacific	Mediterranean	Black Sea	Sea of Japan	Baltic Sea
USC axis depth	50–100 m	150–250 m	40–60 m	120–180 m	40–50 m
$t°$ near USC axis	1–2°C	12.5–13°C	8.5–9°C	0.5–1°C	4–5°C
S‰ near USC axis	33–33.5‰	38–39‰	18–20‰	34–34.5‰	6–10‰
pH near USC axis	8.1–8.25	8.0–8.17	8.15–8.25	8.1–8.25	7.8–8.0
pH_{eff}	8.2	8.1	8.17	8.22	7.85

In this paper, in view of the hypothesis of boron-associated relaxation absorption, we analyze the experimental data obtained in five ocean regions that widely differ in water temperature and salinity. As such "reference" regions, we chose the north-western (deep-water) region of the Pacific Ocean, the Mediterranean, Black, and Baltic Seas, and the Sea of Japan. Some characteristics of these regions are summarized in Table 1.

For all these regions, a shallow USC is typical (50–250 m) with high variations in the salinity (6–39‰) and temperature (0.5–13°C) of waters. The Baltic Sea is the only shallow-water region. The regions are well investigated: representative data on sound attenuation at frequencies of 0.2–5 kHz had been obtained for all of them.

As an example, the experimental data for three of these regions are presented in Figs. 1a–1c. For each chosen region, the frequency dependence of the attenuation coefficient in the frequency band 0.2–5 kHz can be described well by both the power law $\beta = pf^n$ and expression (2) complemented with the function

$$\Delta\beta = \frac{A_B f}{f/f_{rB} + f_{rB}/f} \tag{3}$$

that corresponds to a low-frequency relaxation process with the appropriate parameters A_B and f_{rB}. In analyzing the experimental data for these regions, one can neglect the dependence of the absorption on the hydrostatic pressure because of the shallow position of the USC. The values of the factor p and the exponent n, along with the parameters A_B and f_{rB}, specified by us for each chosen region are presented in Table 2. Many researchers attribute different values of the parameters A_B and f_{rB} to different ocean regions without any rigorous justification of their choice. We used the method of least squares to choose the parameters of the relaxation curves for individual sets of experimental data.

As a preliminary step, we analyzed the "sharpness" of the minimum for the sum of squared deviations of

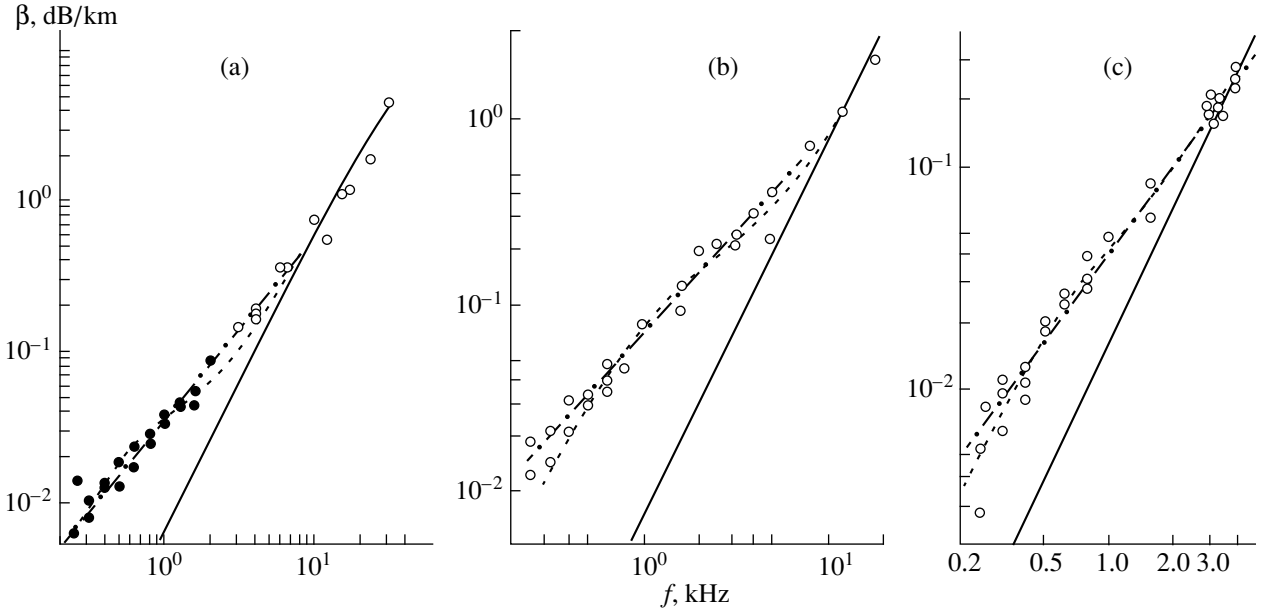

Fig. 1. Experimental data on the low-frequency sound attenuation in (a) the Black Sea, (b) the Mediterranean Sea, and (c) the Sea of Japan, which significantly differ in water temperature and salinity: (– – – – –) frequency dependence approximated by the relaxation curve; (— · — · — · —) attenuation approximated by the power law; (— — —) frequency dependence of the absorption associated with the relaxation of the degree of dissociation of magnesium sulfate.

Table 2. Characteristics of the low-frequency attenuation (from experimental data)

Region	North-western Pacific	Mediterranean	Black Sea	Sea of Japan	Baltic Sea
p, dB/km kHz^n	0.0275	0.071	0.035	0.04	0.04
n	1.35	1.1	1.25	1.28	0.65
f_{rB}, kHz	0.844	1.230	0.640–0.683	0.848	0.290
A_B, dB/km kHz	0.044	0.147	0.06	0.058	0.120
A_B/S	0.00132	0.00382	0.00316	0.00169	0.015
$A_B/S10^{(0.78\text{pH}-5)}$	0.000053	0.000184	0.000133	0.000065	0.00123

the experimental values of β from the calculated ones and estimated the variability of the parameter A_B for the approximating relaxation curve as a function of the compulsorily chosen value of f_{rB}. For the Mediterranean Sea, for instance, variations of ±30% in the values of f_{rB} led to as small as ±3–6% changes in the optimized parameter A_B. If the experimental values of β are used to determine the parameters of the relaxation curve, the reliability of the estimate obtained for A_B becomes significantly higher than that for the relaxation frequency f_{rB}. In view of the fact that the dependences of the relaxation frequency on temperature and boron concentration had been specially studied [7], we decided to use the data obtained by the temperature discontinuity method to choose the parameters of the relaxation curve describing the frequency dependence of the attenuation and to estimate the frequency f_{rB}. At the same time, the data of the experiments on long-range sound propagation in the USC were used to estimate the parameter A_B.

In accordance with the relaxation times measured with the use of the method of temperature discontinuity [7], the relaxation frequency of the process that is probably responsible for the low-frequency sound absorption depends on the sea-water temperature and the boron concentration and does not depend on the pH value.

Boron is one of the main salt components of sea water; the ratio of its concentration to the chlorine content or salinity of the water varies within ±10% in the entire ocean. For the chosen regions, at depths close to the USC axis, the ratio of the concentration of boron to that of chlorine is 0.23–0.24 (B mg/kg to Cl‰). The Black Sea water is the exception: here, this ratio reaches a value of 0.25–0.27. With the relaxation times measured by the temperature discontinuity method at two temperatures (9.7°C and 25.5°C) and three salinities of the standard sea water (35, 17.5, and 7‰, respectively), one can obtain the expression relating the relaxation frequency to temperature and salinity of the sea water:

$$f_{rB} = 37.9S^{0.8}e^{-1800/T}\ \text{kHz}. \quad (4)$$

Figure 2 shows the results of these measurements and their approximations as functions of temperature and salinity. The curves shown in this figure were used to obtain expression (4). We preferred to use the experimental data for estimating the salinity dependence of the relaxation frequency, although some theoretical considerations [11] lead to the dependence $f_{rB} \sim S^{0.5}$.

According to the expressions obtained for the north-western region of the Pacific Ocean (t = 1–2°C, S = 33–33.5‰), the Mediterranean Sea (t = 13°C, S = 38–39‰), the Black Sea (t = 8.5–9°C, S = 18–20‰), the Sea of Japan (t = 0.5–1°C, S = 34–34.5‰), and the Baltic Sea (t = 4–5°C, S = 6–12‰), we specified the values of the relaxation frequency that are summarized in Table 2. For the same regions, the values of the parameter A_B of the approximating dependence (3) are also presented, these values being obtained from the experimental values of β by the method of least squares, in view of the specified values of f_{rB}.

The dotted curves in Figs. 1a–1c shows the relaxation frequency dependences of the attenuation, which are obtained with these parameters for the Sea of Japan and the Black and Mediterranean Seas. One can see that these parameters provide an adequate description of the experimental data on attenuation.

The figures also show the empirical power-law dependence proposed for estimating the attenuation in these regions (the dash-and-dot curve). It reasonably agrees with both the relaxation frequency dependence and the experimental attenuation data. Thus, from the viewpoint of reliability in describing the frequency dependence of sound attenuation for the aforementioned regions, both expressions, namely, the relaxation and power-law ones, are equivalent. However, the relaxation expression pretends to be associated with specific physical processes responsible for the attenuation.

A similar agreement between the experimental data and the curve calculated with allowance for the parameters f_{rB} and A_B is obtained both for the Baltic Sea and for the north-western region of the Pacific Ocean (these data are not presented in the figures).

To find the expressions that equally well describe the attenuation in all chosen regions, let us try to find the most probable functional relations of the attenuation coefficients to the parameters of the sea water.

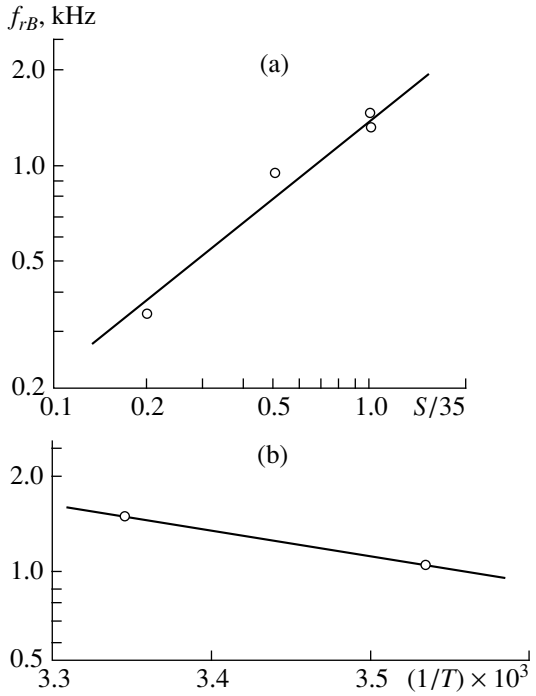

Fig. 2. Boron-associated relaxation frequency measured by the temperature discontinuity method [7]: (a) versus the sea-water salinity and (b) versus the reciprocal sea-water temperature.

In theoretical and experimental studies of the relaxation absorption in water solutions of electrolytes, it was established that the parameter A is proportional to the concentration. One can expect the same relation to be valid for the low-frequency relaxation caused by the boron–borate complexes present in the sea water.

The values of the parameter A_B normalized to salinity are presented in Table 2. These normalized values show that the Baltic Sea drops out of the set of other regions at hand. Actually, the value of A_B/S determined for the Baltic Sea is by a factor of 5–10 higher than those for other regions. A probable explanation for this phenomenon is the small sea depth leading to a significant leakage of the propagating acoustic energy into the sea floor, in spite of the fully developed sound channel.

Some researchers mentioned the twofold difference in the attenuation data for the Atlantic [12] and Pacific [13] Oceans. With reference to data from the US National Oceanographic Center [11], noticeably different median values of 8.09 and 7.67 for the pH value were reported for these two oceans. On this basis, a hypothesis was advanced that the parameter A_B could depend on the pH value. To explain the observed difference for the Atlantic and Pacific Oceans, the following relation [14] was proposed:

$$A_B \approx 10^{(0.78\mathrm{pH}-5)}.$$

This relation was commonly used with the pH value taken at the USC axis. However, the pH value is usually characterized by a strong depth dependence; for instance, in the Black Sea, its variations with depth are as high as 0.8. Such variations lead to threefold to fourfold changes in the parameter A_B (and hence, in the absorption coefficient $\Delta\beta$). When using the archive data, one should also remember that different publications report pH values normalized to the atmospheric pressure and a temperatures of 0°C ($\mathrm{pH_B}$) or 18°C ($\mathrm{pH_B}$). The values of these two types may differ by 0.2–0.3. Below, we will drop the subscript B implying that pH means $\mathrm{pH_B}$. In addition, to take into account the pH value, one should use its efficient value averaged over the ray (over the entire ray cycle) that passes through different ocean layers. In the first approximation, such a value, $\mathrm{pH_{eff}}$, can be determined from the relation

$$10^{(0.78\mathrm{pH_{eff}}-5)} = \frac{1}{L}\int_{(L)} 10^{(0.78\mathrm{pH}(z)-5)}\,dl,$$

where the integration is performed along the ray and L is the length of the full ray cycle.

For the northwestern Pacific Ocean, Mediterranean and Black Seas, and the Sea of Japan where the experiments were carried out, we used the archive data on the depth dependence of pH. With these data, the values of $\mathrm{pH_{eff}}$ were calculated for different "water" rays, in view of the $c(z)$ profiles measured in the experiments.

The values of $\mathrm{pH_{eff}}$ ranged from 0.06 (in the Mediterranean Sea) to 0.4 (in the Black Sea). When only the initial one third of the total angular range of water rays is taken into consideration (this part of the range covering the main energy-significant rays), $\mathrm{pH_{eff}}$ varies within 0.04–0.07 for all four regions at hand, and the pH-associated changes in the attenuation coefficient are within 10–15%.

The values of $\mathrm{pH_{eff}}$ refined in this way are shown in Table 1. In view of the variations in the pH values reported in different publications for the same region, one can note an acceptable agreement of the values of $\mathrm{pH_{eff}}$ with those of pH at the channel axis.

As the next stage, with the improved pH values, the dependence of low-frequency attenuation on the pH value was considered. In Table 2, the values of $A_B/S \times 10^{(0.78\mathrm{pH}-5)}$ are presented for all five regions. A trend can be noticed in the changes of these values from one region to another: being nearly close for the Sea of Japan and the Pacific Ocean (where the water temperatures are almost equal at the channel axes), the values increase as the water temperature increases. A similar temperature dependence of the parameter A (although a less strong one) was observed in the experiments at frequencies of several tens to several hundreds kilohertz.

Figure 3 shows the values of $A_B/S \times 10^{(0.78\mathrm{pH}-5)}$ for four deep-water regions versus the reciprocal absolute

temperature ($1/T$). From the slope of the regression line for the experimental points, one can easily determine the best form for the temperature dependence of A_B:

$$A_B/S \times 10^{(0.78\text{pH} - 5)} = 1.65 \times 10^{(9 - 3696/T)}.$$

Thus, by adopting the proposed form of temperature dependence of A_B, we can match the experimental data on the sound attenuation for the four deep-water regions that widely differ in their water temperature and salinity.

Finally, the expression for the low-frequency absorption, which results from the performed analysis of the experimental data, can be written as

$$\beta = \frac{A_B f}{f/f_{rB} + f_{rB}/f} + \frac{A_{\text{MgSO}_4} f}{f/f_{r\text{MgSO}_4} + f_{r\text{MgSO}_4}/f} + K f^2, \quad (5)$$

where f is the frequency (kHz), $K = 1.42 \times 10^{-8} \times 10^{1240/T}$ (dB/km kHz^2),

$$f_{r\text{MgSO}_4} = 1.125 \times 10^{(9 - 2038/T)} \text{ kHz},$$

$$A_{\text{MgSO}_4} = 62.5ST \times 10^{-6} \text{ dB/km kHz},$$

$$f_{rB} = 37.9S^{0.8} \times 10^{-780/T} \text{ kHz},$$

$$A_B = 1.65S \times 10^{(4 + 0.78\text{pH} - 3696)} \text{ dB/km kHz},$$

S is the salinity (‰), T is the temperature (K), and pH is the effective pH value.

The first term on the right-hand side of expression (5) characterizes the relaxation absorption associated with boron, the second one stands for the relaxation absorption associated with magnesium sulfate, and the third one determines the fresh-water absorption.

The low-frequency expression obtained above was tested by the experimental data [9] for the Atlantic and Pacific Oceans, the Gulf of Aden, and the Mediterranean Sea. Table 3 summarizes the values of temperature, salinity, and parameter A_B estimated by Mellen and Browning, as well as the values of A_B calculated by the above formulas. The pH values were determined according to our consideration. They somewhat differ from those proposed by Shulkin and Marsh [10]. Thus, for the Mediterranean Sea, the value presented in Table 1 was specified. For the Pacific Ocean, we used the value 8.1 corresponding to depths of 50–80 m at which the USC axis was located in one of the Lovett's experiments [13]. For the Gulf of Aden, the calculations were carried out with two pH values: 7.82 taken from Shulkin and Marsh [10] and 7.7 which significantly reduces the difference in the calculated and experimental values of A_B.

The calculated values of A_B agree well with experimental data for the four regions, except for the Atlantic Ocean, where the experiment was carried out on the Eleuthera—Bermuda path that crossed a large area of the Antilles Stream. The latter fact seems to be the cause of the increased values of the attenuation coefficient.

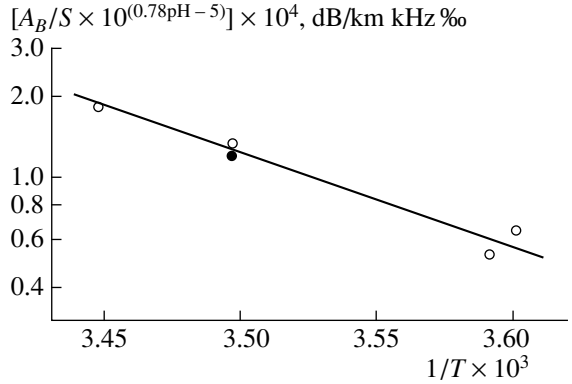

Fig. 3. Temperature dependence of the parameter $A_B/S \times 10^{(0.78\text{pH} - 5)}$ describing the low-frequency relaxation absorption according to the experimental data obtained for the Black and Mediterranean Seas, the Sea of Japan, and the north-western region of the Pacific Ocean. Two parameter values are shown for the Black Sea: (○) for the actual water salinity and (●) for the salinity corrected to the boron concentration corresponding to the ratio B (mg/kg): Cl (‰) = 0.24.

It would be naive to think that the experimental data for all ocean regions could be explained in terms of the low-frequency attenuation associated with boron present in the sea water. Indeed, regions where the low-frequency attenuation is noticeably higher than that predicted by the aforementioned relations do exist in the ocean. Such regions include the deep-water areas that are close to intense sea currents, front zones, and zones of active mixing of waters that differ in temperature and salinity. The deep-water part of the Sea of Okhotsk (near the Kuril Straits) [15] and the Greenland Sea (the region of mixing of Polar and Atlantic waters) [3] are examples. In such regions, the sound attenuation is governed by both absorption and scattering by thermal inhomogeneities of the marine medium in the form of thin-layered structures. As we have already seen, shallow-water seas should also be attributed to such regions: in these seas, sound energy leaks into the sea

Table 3

Region	Temperature, °C	Salinity, ‰	pH	A_B, dB/km kHz (experiment)	A_B, km kHz (calculation)
Atlantic	4	35	8.09	0.110	0.055
Pacific	4	34	8.1	0.055	0.054
Gulf of Aden	15	36	7.8 (7.7)	0.078	0.110 (0.09)
Mediterranean	13	38	8.1	0.150	0.158

floor even in the presence of a fully developed USC (as in the Baltic Sea).

ACKNOWLEDGMENTS

This work was supported by the Russian Foundation for Basic Research, project no. 99-02-18359.

REFERENCES

1. R. A. Vadov, in *Problems of Ocean Acoustics* (Nauka, Moscow, 1984) pp. 31–42.
2. M. J. Sheehy and R. Halley, J. Acoust. Soc. Am. **29**, 464 (1957).
3. R. A. Vadov, Akust. Zh. **46**, 47 (2000) [Acoust. Phys. **46**, 37 (2000)].
4. L. Hall, Phys. Rev. **73**, 775 (1948).
5. G. Kurtze and K. Tamm, Acustica **3** (1), 33 (1953).
6. V. P. Glotov, Akust. Zh. **3**, 220 (1957) [Sov. Phys. Acoust. **3**, 236 (1957)].
7. E. Yeager, F. H. Fisher, J. Miceli, and R. Bressel, J. Acoust. Soc. Am. **53**, 1705 (1973).
8. R. H. Mellen, D. G. Browning, and V. P. Simmons, J. Acoust. Soc. Am. **68**, 248 (1980); **69**, 1660 (1981); **70**, 143 (1981).
9. F. H. Fisher and V. P. Simmons, J. Acoust. Soc. Am. **62**, 558 (1977).
10. M. Shulkin and H. W. Marsh, J. Acoust. Soc. Am. **63**, 43 (1978).
11. V. P. Glotov, Akust. Zh. **22**, 125 (1976) [Sov. Phys. Acoust. **22**, 67 (1976)].
12. W. H. Thorp, J. Acoust. Soc. Am. **38**, 648 (1965).
13. J. R. Lovett, J. Acoust. Soc. Am. **58**, 620 (1975).
14. R. E. Francois and G. R. Garrison, J. Acoust. Soc. Am. **72**, 1879 (1982).
15. R. A. Vadov, Akust. Zh. **45**, 174 (1999) [Acoust. Phys. **45**, 143 (1999)].

Translated by E. Kopyl

Acoustical Physics, Vol. 46, No. 5, 2000, pp. 551–558. Translated from Akusticheskiĭ Zhurnal, Vol. 46, No. 5, 2000, pp. 632–639.

Two-Dimensional Phased Arrays for Application in Surgery: Scanning by Several Focuses

L. R. Gavrilov*, J. W. Hand, and I. G. Yushina*****

** Andreev Acoustics Institute, ul. Shvernika 4, Moscow, 117036 Russia*

e-mail: bvp@akin.ru

*** Hammersmith Hospital, Imperial College, London, W12 0HS, UK*

**** Shirshov Oceanology Institute, Russian Academy of Sciences, Nakhimovskiĭ pr. 36, Moscow, 117851 Russia*

Received October 11, 1999

Abstract—Numerical simulation and comparative analysis of acoustic fields formed by two-dimensional phased arrays designed for ultrasonic surgery are conducted for the case of scanning by several focuses (in particular, by nine focuses arranged in a line and also by an array of nine focuses forming a 3×3 square grid). Calculations are performed for arrays with elements positioned at the surface both regularly (in square, ring, or hexagonal patterns) and randomly. Criteria for evaluating the "quality" of the intensity distributions in the field formed by the array in the case of scanning by several focuses are proposed. The quality of the intensity distributions for arrays containing 255 and 256 elements 5 mm in diameter arranged in regular patterns on the array's surface (in square, ring, or hexagonal patterns) is inferior to that for arrays containing 256 randomly positioned elements. Among the regular arrays, the highest quality of intensity distributions is obtained for ring arrays, and the lowest quality is obtained for arrays with elements arranged in square or hexagonal patterns. The irregularity in the element positioning the array's surface improves the quality of intensity distributions by reducing the secondary intensity peaks in the field formed by the array and, primarily, in the focal plane. © *2000 MAIK "Nauka/Interperiodica".*

The ability of ultrasonic phased arrays to synthesize several focuses in preset areas [1–9] determines the considerable interest in their possible application in surgery and, especially, when the object to be destroyed is some deep-seated tissue of relatively large volume. The application of arrays provides an opportunity to considerably reduce the duration of such a procedure as compared to the utilization of simpler focusing systems forming a single focus at a fixed focal distance [5]. Wan *et al.* [6] theoretically studied several possible techniques for obtaining a large area of ultrasonic energy concentration in tissues with the help of phased arrays: (1) successive scanning of the whole volume of a tissue to be destroyed by a single focus; (2) scanning by a "grid" of several focuses; and (3) simultaneous formation of numerous focuses in a tissue (without scanning) within the coordinates of the area of the tissue to be destroyed. Considering all distinctive features of these approaches, one can see that they are united by a single "side effect," namely, by the possibility of overheating the tissues outside the preset area of operation because of the appearance of secondary intensity peaks. This problem and ways to minimize the overheating of tissues in the path of ultrasound propagation to the area intended for the treatment were discussed by many researchers [3–8].

In our previous paper [10], we conducted a numerical simulation and comparative analysis of the acoustic fields formed by two-dimensional phased arrays for the case of scanning by a single focus with the help of an array shaped as a part of a spherical shell. Calculations were conducted for arrays with elements positioned on the surface both regularly (in square, ring, or hexagonal patterns) and randomly. Criteria for the evaluation of the "quality" of intensity distributions in the field formed by an array in the case of the motion of a single focus were proposed. Considering the arrays studied by us [10], the best distribution quality evaluated according to the criterion of existence of secondary intensity peaks in the generated field was obtained for the array of 256 elements 5 mm in diameter, which were randomly positioned the array's surface. The quality of the intensity distributions for the arrays of 255, 256, and 1024 elements positioned regularly the array's surface (in square, ring, or hexagonal patterns) was inferior to that obtained for the arrays with randomly positioned elements. It was demonstrated that the irregularity in element positioning considerably improved the quality of the intensity distributions as a result of the reduction of the level of secondary intensity peaks in the field formed by the array.

1063-7710/00/4605-0551$20.00

It was interesting to determine to which extent the utilization of phased arrays with irregular positioning of elements on the surface can be advantageous when the array is used for the formation of and scanning by several focuses. In this paper, we conduct numerical simulation and comparative analysis of the "quality" of the acoustic fields formed by arrays with random and regular distributions of elements over their surfaces shaped as parts of spheres for the case of scanning by several focuses.

The technique described in our previous paper [10] was used for calculating the acoustic fields formed by two-dimensional phased arrays in the case of successive displacements of a single focus over a preset volume. In the case of the formation and motion of several focuses, this method was modified as follows. The complex particle velocity u_n at the nth element of the total set of N elements was determined using the technique developed by Ebbini and Cain [2]. The values of u_n are connected with the complex sound pressure p_m in each of M test points by a matrix equation

$$\boldsymbol{u} = H^{*t}(HH^{*t})^{-1}p,$$

where $\boldsymbol{u} = [u_1, u_2, \ldots, u_n, \ldots u_N]^t$, $p = [p_1, p_2, \ldots, p_m, \ldots p_M]^t$, and H is the matrix of $M \times N$ elements. The elements of the matrix $h_{mn} = \exp(-jkr_{mn})/r_{mn}$ were used, where r_{mn} is the distance from the mth test point to the center of the nth element of the array; H^{*t} is the matrix conjugate to H, the index t denoting transposition of the matrix. In this study, M test points (corresponding to localizations of focuses) were positioned in the same focal plane at equal distances from each other in a pattern that had the form of a grid of $\sqrt{M} \times \sqrt{M}$ elements. In order to determine u_n ($n = 1, 2, \ldots, N$), it is necessary to select the phases and amplitudes of the sound pressure at the test points p_m ($m = 1, 2, \ldots, M$). The amplitudes were assumed equal for simplicity of calculation. The method of selection of the phases at the test points is considered below.

As in our previous paper [10], we assume that ultrasound propagates through a biological tissue with the density 1000 kg m^{-3}, the sound velocity 1500 m s^{-1}, and the attenuation coefficient 10 Np m^{-1} MHz^{-1}. The frequency of ultrasound is 1.5 MHz in all cases. Calculations are conducted for arrays with surfaces shaped as parts of spherical shells with a curvature radii equal to 120 mm. The diameters of all arrays are identical and equal to 110 mm. All arrays consist of disk-shaped elements with a diameters of 5 mm. The intensity distributions in the field formed by four types of arrays are compared:

(1) An array of 256 elements positioned the surface in a quasi-random way (a true random distribution was modified in such a way that the minimum distance between the centers of elements was 5.5 mm). The distance between the centers of the most distant elements is 100 mm:

(2) An array of 256 elements positioned or the surface regularly, in square patterns. The minimum distance between the centers of elements is 5.5 mm.

(3) An array of 255 elements positioned on the surface regularly, in hexagonal patterns. The minimum distance between the centers of elements is 5.5 mm.

(4) A regular array of 255 elements consisting of a central element and nine concentric rings with the radii from 5.5 to 49.5 mm (with a step of 5.5 mm). The rings consist of 5, 11, 17, 23, 28, 33, 40, 46, and 51 elements, respectively. The distance between the centers of elements is 6 mm.

Sketches of these arrays were given in our previous paper [10]. The computing facilities were also described therein.

Since the volume irradiated by ultrasound in practice can be significantly greater than the volume of a single focus, the necessity to form and move several focuses arises. Naturally, in this case, the time-average value of intensity in the region along the path of ultrasound to the desired region of action (we will call it a "prefocal" region) can far exceed that in the case of a single movement of a single focus. Correspondingly, the possible criteria for evaluating the quality of intensity distributions in the case of formation and movement of several focuses will be inevitably less strict as compared to the criteria used by us for the case of a single movement of a single focus [10].

We used the following considerations in the process of selecting these criteria. First, we assumed that the values of ultrasonic intensity in the prefocal region are much less than the values of the cavitation threshold in tissues. (It is known that at frequencies 1–1.5 MHz, the cavitation threshold in tissues under the action of focused ultrasound corresponds to an intensity of approximately 1000–1500 W cm^2 [11, 12].) In other words, we assumed that the mechanism of possible destruction in the prefocal region (if such destruction occurs) is of purely thermal origin. It is known that the threshold thermal dose necessary for the thermal necrosis of tissues is equivalent to a rise in temperature of up to 53.5°C in 10 s or up to 56.8°C in 1 s [5]. The maximum temperature T_{max} attainable in ultrasonic surgery is 80–90°C [5, 8]. Thus, in terms of the temperature increase ΔT with respect to 37°C, thermal necrosis of tissues can be attained in the interval from approximately $0.4\Delta T_{max}$ to $1.0\Delta T_{max}$, where ΔT_{max} is the maximal temperature increase (≈43–53°C). If the ultrasonic action does not last too long (about several seconds), then, we can ignore the heat conductivity of tissues and the withdrawal of heat through blood flow and assume that ΔT and the intensity I are linearly related. In this case, it is possible to propose to a first approximation

the following criteria for evaluating the quality of intensity distributions in the field created by an array in the case of the formation and scanning by several focuses. Quality I: the intensity in the secondary peaks is less than 30% of that at the center of the focus I_{max}; quality II: the intensity in the secondary peaks lies within the range $0.3I_{max} < I \le 0.4I_{max}$; quality III: the intensity in the secondary peaks is $I > 0.4I_{max}$. It is evident that the risk of thermal necrosis in the prefocal region must be small for quality I and considerable for quality III. These criteria can be considered as excessively strict, because the effect of tissue cooling in the case of utilization of several exposures to ultrasound is not taken into account.

Numerical simulation was conducted for two methods of formation of several focuses: (1) a single focus moved in one plane in short time periods (afterwards, the obtained "line" consisting of several focuses can be moved in the scanning mode); (2) formation of a grid consisting of several focuses, which can also be moved over a preset volume. Two-dimensional contour distributions in the prefocal region and focal plane were used for the qualitative analysis of the intensity distributions. The plots given below present nine contours, which correspond to intensity values from 10 to 90% for I_{max} at a step of 10% I_{max}.

The ultrasonic intensity distribution that corresponds to the first method is given in Fig. 1 for the case of nine focuses positioned along a straight line with a distance of 3 mm between their centers. The coordinates of the focuses were z = 110 mm, x = 0 mm, y = –12, –9, –6, –3, 0, 3, 6, 9, and 12 mm, where z is the coordinate in the direction of the acoustic axis of the array, and x and y are the coordinates in the directions perpendicular to the array axis. The results for an array of 256 elements randomly positioned on the surface are given in the left part of the figure (Figs. 1a, 1b), and the right part of this figure (Figs. 1c, 1d) presents the results for an array of 256 elements positioned on the surface regularly, in square patterns. In the lower part of the figure, the distributions in the prefocal region (in the y–z plane) are given, and the distributions in the focal x–y plane (z = 110 mm) are presented in the upper part. The amplitudes of signals on the array's elements were selected in such a way that maximal intensities at all focuses were the same, which could be realized only in the case of utilization of a randomized array. One can see that, in the case of utilization of the latter, nine focuses of equal intensity are observed on the preset points. In the case of a regular array, it is possible to distinguish at least 13 focuses with different intensities, which is the result of summation of intensities in the main and secondary peaks. One can also see that the quality of intensity distributions for the randomized array is noticeably better than that for the regular array, both in the focal plane and in the prefocal region. Only five points with intensity above $0.2I_{max}$ were present in the whole prefocal region of the randomized array (they are shown by thicker lines). In the case of the regular array, the number of such points or areas was about 100. Both presented distributions can be attributed to the criterion of quality I, since the intensity in the secondary peaks does not exceed $0.3I_{max}$.

Localization and relative values of phases for nine focuses positioned in one plane

$x + 4, y - 4, z$	$x + 4, y, z$	$x + 4, y + 4, z$
•	•	•
0	$\pi/4$	$\pi/2$
$0, y - 4, z$	$0, y, z$	$0, y + 4, z$
•	•	•
$7\pi/4$	$\pi/2$	$3\pi/4$
$x - 4, y - 4, z$	$x - 4, y, z$	$x - 4, y + 4, z$
•	•	•
$3\pi/2$	$5\pi/4$	π

Let us consider the second method of tissue destruction, which is grounded on the formation of several focuses, for the case of scanning by a 3×3 square grid of nine focuses with a distance of 4 mm between the centers. The characteristics of these focuses are given in the table. The coordinates of the focuses (the upper numbers) are given with respect to the position of the central focus ($x = 0, y, z$), and displacement is expressed in millimeters. The relative values of the phase of the complex pressure on the focuses are given by the lower numbers. As one can see, these phases rotate uniformly and clockwise about the axis of the given set of focuses in a way similar to that described by Fan and Hynynen [8].

Figure 2 presents examples of intensity distributions in the prefocal region (the y–z plane) in the case of scanning by the indicated grid of focuses with the help of a randomized array of 256 elements. In each case, the central focus of nine ones was located on the array's axis at distances of 100 mm (Fig. 2a), 110 mm (Fig. 2b), and 120 mm (Fig. 2c). The intensity distributions corresponded to the criteria I, II, and III.

Figure 3 summarizes the results of investigations of the intensity distributions for one randomized and three regular arrays in the case of the movement of a grid of nine focuses, when the coordinates of the central focus moved in the y–z plane. The following data are presented: for an array of 256 elements randomly positioned on the surface (Fig. 3a); for an array of 256 elements positioned regularly in square patterns (Fig. 3b); for an array of 255 elements positioned regularly in hexagonal patterns (Fig. 3c); and a regular array of

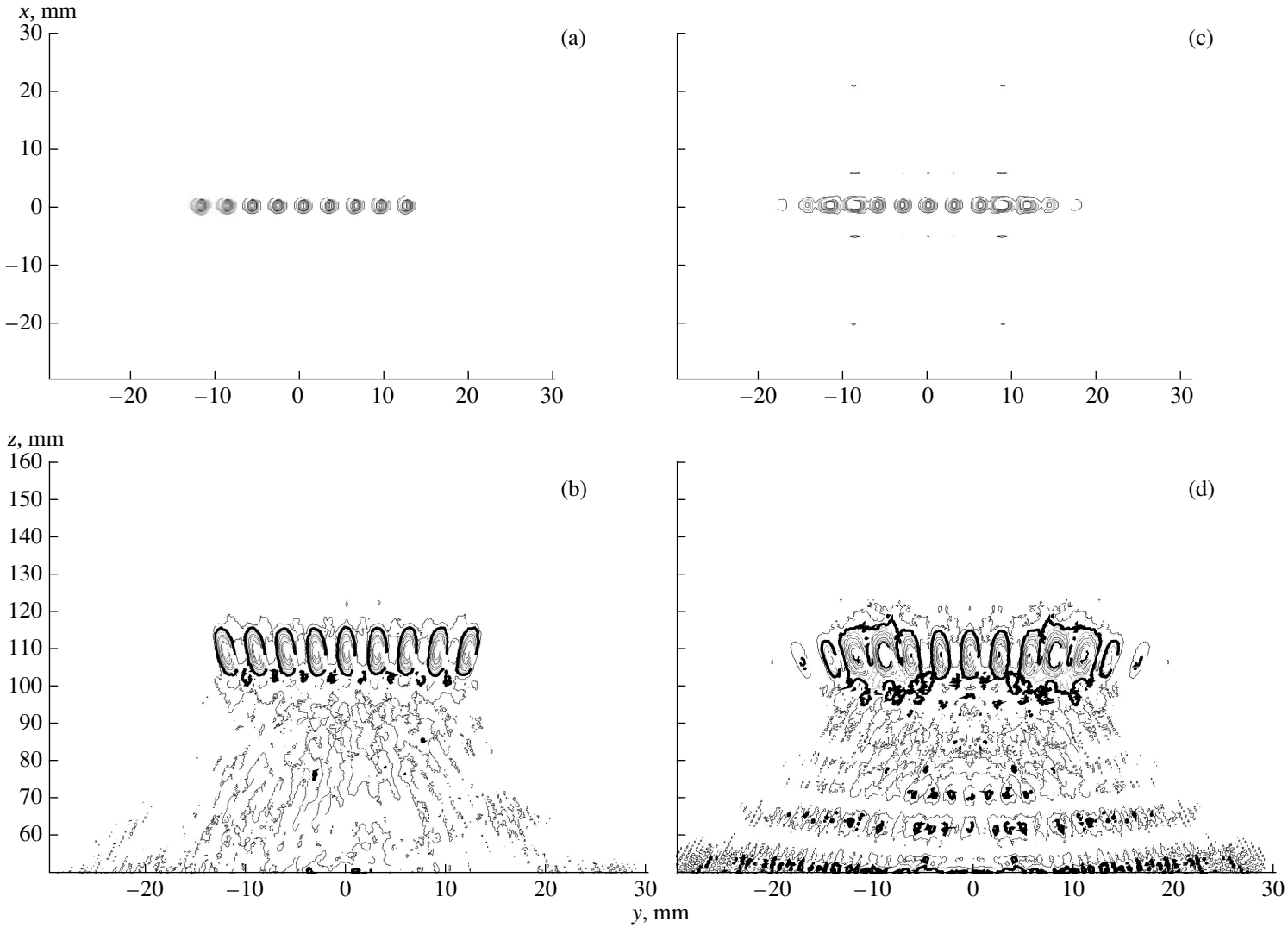

Fig. 1. Distributions of ultrasonic intensity for the case of motion of nine focuses arranged in a single line. On the left, the results for an array of 256 elements randomly positioned on its surface are given, and, on the right, the results for an array of 255 elements positioned regularly in square patterns are shown. In the lower part of the figure, the distributions in the prefocal region are given, and those in the focal plane (z = 110 mm) are shown in the upper part.

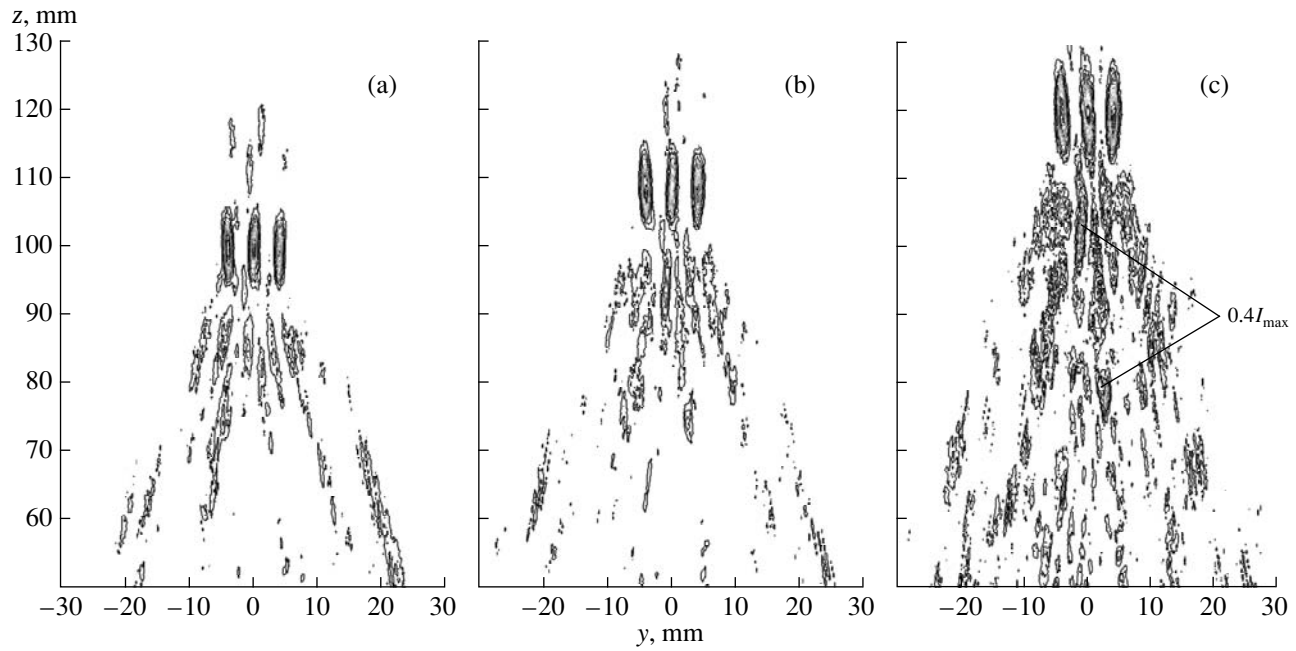

Fig. 2. Changes in the quality of intensity distributions in the case of the movement of a grid of nine focuses (a 3×3 square with the distance between the centers of focuses 4 mm) with the help of a randomized array of 256 elements. The central focus is on the axis of the array at distances of (a) 100, (b) 110, and (c) 120 mm. The distributions correspond to the selected criteria of quality: (a) criterion I; (b) criterion II; and (c) criterion III.

255 elements consisting of the central element and nine concentric rings (Fig. 3d). The comparison of the distribution quality confirms the trend observed in the case of a single scan by a single focus [10]. In the case of the randomized array (Fig. 3a), the grid of nine focuses can be moved along the central axis from 76 to 104 mm and to a distance of 10 mm away from the axis with a quality corresponding to criterion I. The quality of the distributions was considerably reduced when the array elements were positioned in square of hexagonal patterns (Figs. 3b, 3c). In these cases, the distributions of quality I were absent, and the distributions of quality II were present only in the case of a movement along the array axis to distances from 86 to 105 mm. Almost any displacement of the grid of focuses away from the axis led to distributions of quality III, primarily, because of the rise of a secondary intensity peak in the focal plane. The intensity in this maximum could exceed the intensity in the focus itself. The array of 255 elements constructed in the form of concentric rings (Fig. 3d) occupies an intermediate position between the randomized array and the regular arrays formed in square and hexagonal patterns. Its utilization provided an opportunity to shift the indicated grid of focuses from 81 to 99 mm along the array's axis and 5 mm away from the axis.

Figure 4 shows the intensity distributions in the focal plane (x–y) at a distance $z = 100$ mm in the case of scanning by the same grid of 3×3 focuses. The intensity distributions belong to the array with a random distribution of elements (Fig. 4a), the regular array with elements positioned in square patterns (Fig. 4b), the regular array with elements positioned in hexagonal patterns (Fig. 4c), and the regular array with elements positioned in rings (Fig. 4d). The upper plots correspond to the case with the central focus being located on the array axis (the coordinates 0, 0, 100 mm), and the lower plots correspond to this focus shifted away from the axis by 10 mm (the coordinates 0, 10, 100 mm). One can see that the intensity distributions for the regular arrays formed in square and hexagonal patterns correspond to the quality criterion III not only in the case of the focus shift by 10 mm away from the array axis, but also when a focus is at the axis (Figs. 4b, 4c). In this case, the intensity in the secondary peaks could exceed the intensity in the focus. One can also see that the intensity distributions for the randomized array and the regular array formed of rings correspond to the quality criterion I, even when the focus is shifted 10 mm away from the axis (Figs. 4a, 4d).

The calculations of the intensity distributions in the case of the movement of the grid of focuses were conducted not only for the grid of 3×3 focuses, but also for other configurations. In the case of utilization of a greater numbers of focuses (5×5 with a distance of 2.5 mm between the focuses and 7×7 with a distance of 2 mm between the focuses), the aforementioned difference between the distributions obtained for different

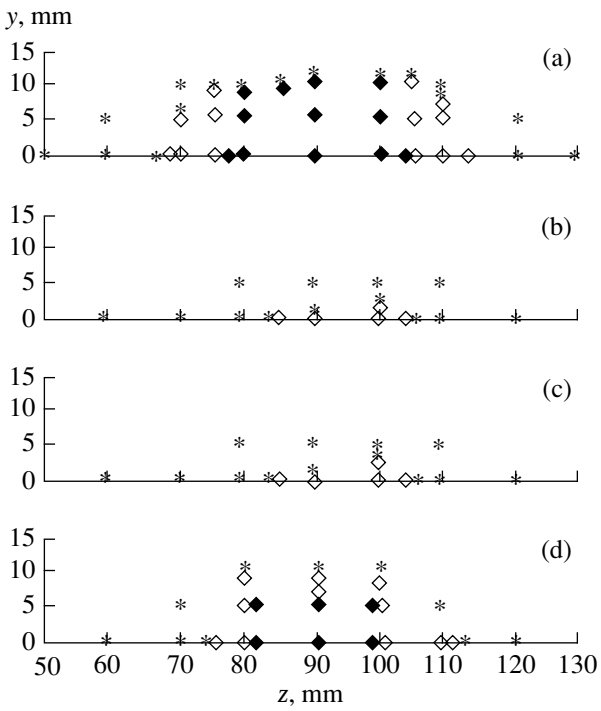

Fig. 3. Summary data on the calculations and evaluation of the quality of intensity distributions in the case of the movement of a grid of nine focuses (a 3×3 square with a distance of 4 mm between the centers of focuses). The data are obtained for (a) an array of 256 elements randomly positioned on the surface; (b) an array of 256 elements positioned regularly in square patterns; (c) an array of 255 elements positioned regularly in hexagonal patterns; and (d) a regular array of 255 elements, which consists of a central element and nine concentric rings. The quality criteria: (◆) criterion I; (◇) criterion II; and (∗) criterion III.

arrays became less evident, and the distributions of quality III occurred more and more often.

The ratio of the curvature radius to the diameter of all considered arrays was $f = 120$ mm/110 mm = 1.09, which was somewhat higher than that for other arrays discussed in the literature, where f was 0.8–1.02 [6, 7, 13]. Fan and Hynynen [5] demonstrated that an increase in f can lead to intense heating of the prefocal region. Therefore, a reduction in f is a reserve for some improvement of the intensity distribution in the field formed by an array.

The character of the intensity distribution in the case of the formation of a grid of several focuses depends on the way of selecting the amplitudes and phases of the complex sound pressure in the preset test points. Many researchers studied this problem [2, 3, 5, 7, 8]. Techniques for optimization of these parameters for obtaining the maximal amplification coefficient of an array (the ratio of the maximal intensity on the focus to the average intensity on the array's surface) were developed [2, 3]. These optimization techniques were not used in our study. We used a uniform distribution of amplitudes and selected the simplest method for a uniform phase rotation (see table). The distance between the focuses was not optimized as well; it was comparable to the values used by other researchers [5–7]. The purpose of this work was different: we wanted to demonstrate that the utilization of randomized arrays instead of regular ones in many cases provides considerable improvement of the intensity distributions in the prefocal region and, especially, in the focal plane. Apart from the paper by Goss *et al.* [13], we could not find papers on phased arrays for surgical applications, where the question of the possibility and expediency of using randomized arrays for this purpose had been brought up. Moreover, regular arrays of elements positioned in hexagonal [13] and, especially, square patterns [2, 6–8, 14] remain most popular among the discussed types of arrays.

In conclusion, it is necessary to note that the results obtained in this study demonstrate that arrays with a random positioning of elements on the surface provide a distinctly better quality of intensity distributions in the case of the movement of several focuses as compared to arrays with a regular positioning of elements. The essential advantages of randomized arrays were demonstrated in our previous paper [10] for the case of a single motion of a single focus. This study also con-

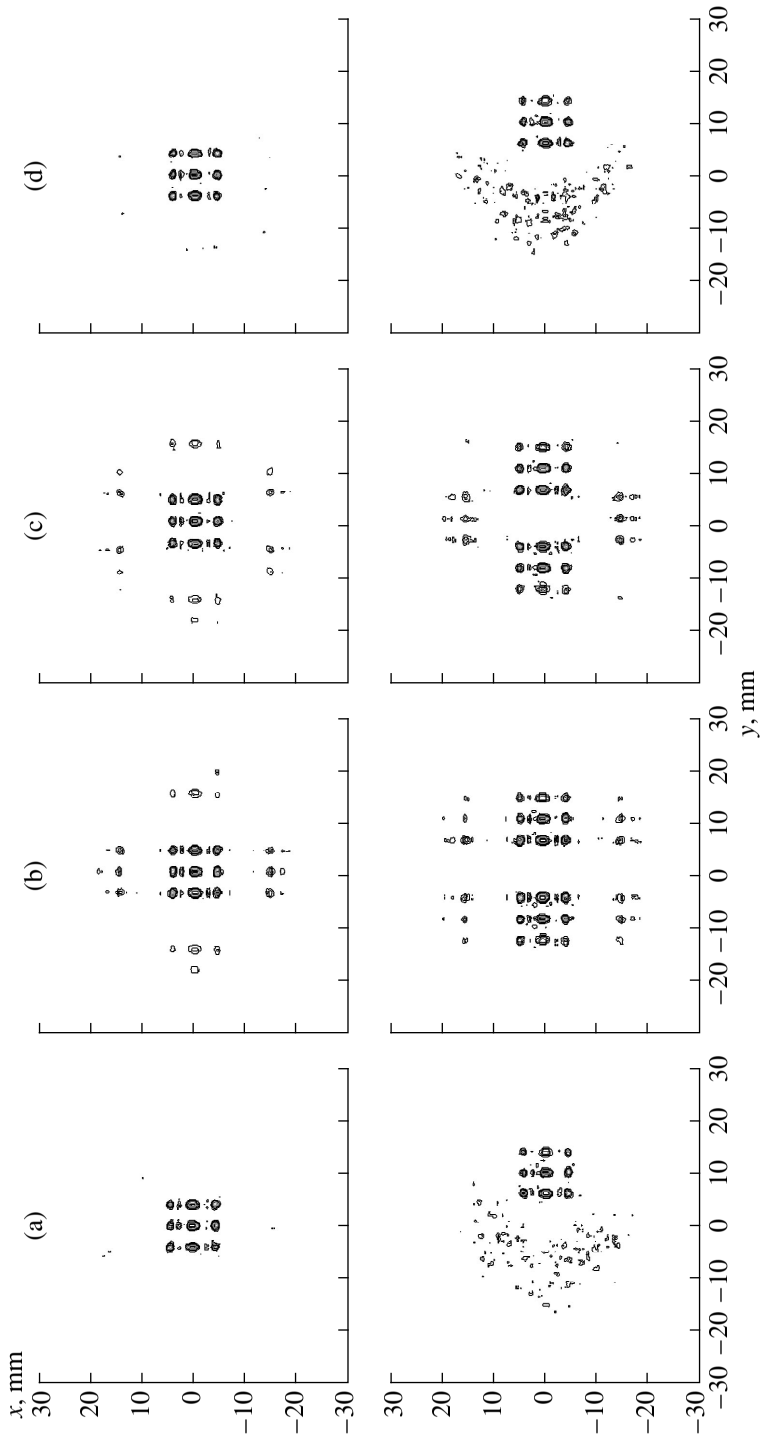

Fig. 4. Intensity distributions in the focal plane (x–y) at the distance $z = 100$ mm in the case of the movement of a grid of nine focuses (a 3×3 square). The distributions are obtained for (a) an array of 256 elements randomly positioned on the surface; (b) an array of 256 elements positioned regularly in square patterns; (c) an array of 255 elements positioned regularly in hexagonal patterns; and (d) a regular array of 255 elements positioned in rings. The upper figures correspond to the case with the central focus located on the array's axis, and the lower ones correspond to the case with this focus shifted with respect to the axis by 10 mm.

firmed this trend for the case of scanning by several focuses at least for a relatively small number of them.

REFERENCES

1. E. S. Ebbini and C. A. Cain, IEEE Trans. Ultrason. Ferroelectr. Freq. Control **36**, 540 (1989).
2. E. S. Ebbini and C. A. Cain, IEEE Trans. Biomed. Eng. **38**, 634 (1991).
3. E. S. Ebbini and C. A. Cain, Int. J. Hyperthermia **7**, 951 (1991).
4. C. Damianou and K. Hynynen, Ultrasound Med. Biol. **19**, 777 (1993).
5. X. Fan and K. Hynynen, Ultrasound Med. Biol. **22**, 471 (1996).
6. H. Wan, P. VanBaren, E. S. Ebbini, and C. A. Cain, IEEE Trans. Ultrason. Ferroelectr. Freq. Control **43**, 1085 (1996).
7. D. R. Daum and K. Hynynen, IEEE Trans. Ultrason. Ferroelectr. Freq. Control **45**, 208 (1998).
8. X. Fan and K. Hynynen, Phys. Med. Biol. **41**, 591 (1996).
9. T. Fjield, X. Fan, and K. Hynynen, J. Acoust. Soc. Am. **100**, 1220 (1996).
10. L. R. Gavrilov and J. W. Hand, Akust. Zh. **46**, 456 (2000) [Acoust. Phys. **46** (2000) (in press)].
11. L. R. Gavrilov, Akust. Zh. **20**, 27 (1974) [Sov. Phys. Acoust. **20**, 16 (1974)].
12. K. Hynynen, Ultrasound Med. Biol. **17**, 157 (1991).
13. S. A. Goss, L. A. Frizell, J. T. Kouzmanoff, *et al.*, IEEE Trans. Ultrason. Ferroelectr. Freq. Control **43**, 1111 (1996).
14. R. J. McGough, M. L. Kessler, E. S. Ebbini, and C. A. Cain, IEEE Trans. Ultrason. Ferroelectr. Freq. Control **43**, 1074 (1996).

Translated by M. Lyamshev

Acoustical Physics, Vol. 46, No. 5, 2000, pp. 559–562. Translated from Akusticheskiĭ Zhurnal, Vol. 46, No. 5, 2000, pp. 640–643.

Caustics and Volume Prereverberation in a Surface Oceanic Waveguide

V. S. Gostev and R. F. Shvachko

Andreev Acoustics Institute, Russian Academy of Sciences, ul. Shvernika 4, Moscow, 117036 Russia

e-mail: bvp@akin.ru

Received December 20, 1999

Abstract—A kinematic model of volume prereverberation caused by sound scattering from different types of inhomogeneities in the caustic zones of a surface oceanic waveguide is considered. Numerical estimates are presented for the prereverberation time as a function of range, number of ray cycles, and width of the scattering diagram. © *2000 MAIK "Nauka/Interperiodica".*

Previously, we have considered kinematic models for the volume prereverberation caused by sound scattering from fine-structure and turbulent inhomogeneities in the caustic zones of the underwater sound channel [1]. These zones concentrate the energy of the primary sound field and, thus, enhance the phenomena to be observed. It is worth considering the volume prereverberation in a surface oceanic waveguide where a system of caustics is known to exist [2]. A similar caustic system can also be observed in the ground atmospheric waveguide [3]. The ray pattern shown in Fig. 1 illustrates the effect for a simple case of the sound source located near the surface, i.e., on the channel's axis. In this case, one of the two equations of caustic, for the ray congruence of the $(N + 1)$th cycle, has the form

$$\frac{2N}{\chi_0} + \left(\frac{1}{\chi_0} - \frac{1}{\chi_k}\right) = 0, \tag{1}$$

where χ_0 is the ray departure angle at the source and χ_k is the angle at a point where the ray is tangent to the caustic.

Figure 2 shows the ray pattern that depicts the formation of prereverberation caused by sound scattering in the forward direction, at a positive angle $\delta\chi$, from the Nth caustic ($N = 2$ in Fig. 2), with the tangent angle $\chi_k = \chi_0/(2N + 1)$. The caustic is at the distance

$$r_k = \left(N + \frac{1}{2}\right)r_0 - \frac{1}{2}\frac{r_0}{2N + 1} \tag{2}$$

from the source. Here, r_0 is the cycle length for this ray. The prereverberation signal is observed at a distance r from the source. The prereverberation time is measured relative to the signal that arrives along the ray consisting of $N + 1$ cycles with the propagation time

$$t_r = \frac{r}{c_0}\left[1 - \frac{a^2 r^2}{(N+1)^2 24}\right] = \frac{r}{c_0}\left[1 - \frac{4n^2}{(n+1)^2}\xi^2\left(\frac{r}{r_0}\right)^2\right], \tag{3}$$

where $a = 1.2 \times 10^{-5}$ m^{-1} is the normalized hydrostatic gradient of the sound speed, c_0 is the sound speed at the surface, $n = 1/(2N + 1)$, and $\xi^2 = a^2 r_0^2/24$.

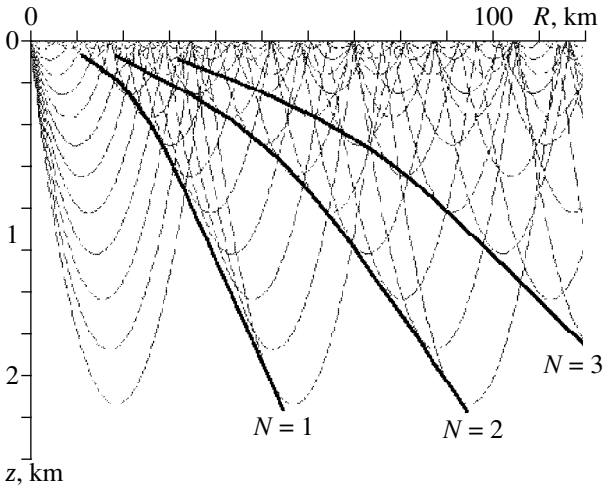

Fig. 1. System of caustics in the surface sound channel with the sound source located on its axis.

1063-7710/00/4605-0559$20.00 © 2000 MAIK "Nauka/Interperiodica"

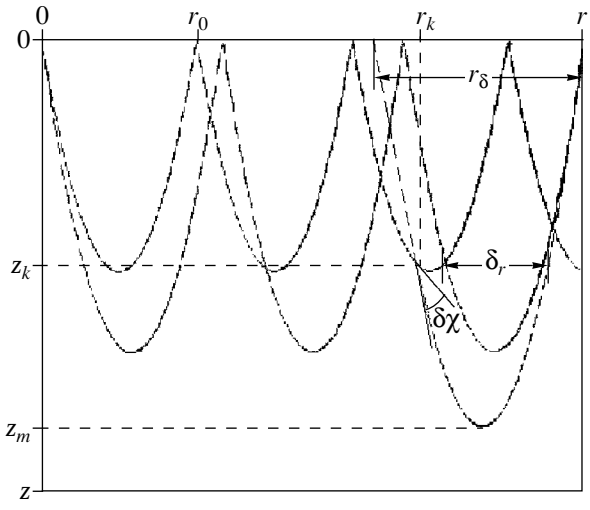

Fig. 2. Ray pattern for the calculation of prereverberation.

The propagation time of the advancing ray is a sum of the time t_k of signal propagation from the source to the scattering point, r_k, z_k (see Fig. 2), and the propagation time t_s for the signal scattered at the angle $\delta\chi$ from the point r_k, z_k to the reception point r, 0. Thus, the prereverberation time is given by the expression

$$\delta t = t_r - (t_k + t_s). \tag{4}$$

In view of the ray pattern of Fig. 2 and formula (2), the time t_k is equal to the propagation time along $N + \frac{1}{2}$ cycles, each of them being r_0 in length, minus the propagation time along the half of the cycle with the length $\frac{r_0}{2N+1} = nr_0$:

$$t_k = \frac{r_0}{2c_0}\left[\frac{1}{n}(1-\xi^2) - n\frac{c_0}{c_k}(1-n^2\xi^2)\right], \tag{5}$$

where c_k is the sound speed at the depth z_k, and $\frac{c_0}{c_k} = 1 + 3(1-n^2)\xi^2$.

Similarly, t_s is a sum of the propagation times along the half of the ray with the length r_δ and the half of the ray with the length $nr_0 + \delta r$:

$$t_s = \frac{r_0}{2c_0}\left[\frac{r_\delta}{r_0}\left(1-\left(\frac{r_\delta}{r_0}\right)^2\xi^2\right) + \left(n+\frac{\delta r}{r_0}\right)\frac{c_0}{c_k}\left(1-\left(n+\frac{\delta r}{r_0}\right)^2\xi^2\right)\right], \tag{6}$$

where $\delta r = 2\delta\chi/a$, and r, r_0, r_δ, and δr are related by two expressions:

$$r = \frac{r_0}{2}\left(\frac{1}{n} + \frac{r_\delta}{r_0} + \frac{\delta r}{r_0}\right), \tag{7}$$

$$r_\delta^2 = r_0^2\left[1 + 2n\frac{\delta r}{r_0} + \left(\frac{\delta r}{r_0}\right)^2\right]. \tag{8}$$

With formulas (3)–(6), in view of relations (7), (8), the prereverberation time δt was calculated as a function of distance r for different N and scattering angles $\delta\chi$. The calculations were carried out up to distances at which the scattered ray touches the bottom. These limiting distances depend on the values of $\delta\chi$, N, and the sea depth z; the latter was specified to be 2.5 km—a value that is typical for the Mediterranean Sea. This sea is known for its hydrostatic sound speed gradient observed from the surface to the bottom in winter. The limiting distance is determined by formulas (7), (8), in accordance with the condition of a ray tangent to the bottom:

$$z_m = z, \text{ where } z_m = \frac{a}{8}r_\delta^2. \tag{9}$$

Figure 3a shows a set of the calculated dependences of the prereverberation time δt on distance r for $\delta\chi$ = 0.1 rad. The parameter of the curves is the number N of the cycles (from 1 to 15). In Fig. 3b, a similar set is presented for $\delta\chi$ = 0.2 rad. The obtained prereverberation times agree well with the experimental data [4]. Figure 4 shows a set of dependences of δt on r (for N = 1), where the parameter of the curves is the scattering angle $\delta\chi$ (from 0.1 to 0.17 rad, at a step of 0.01 rad). A sharp dependence of the prereverberation time on the angle $\delta\chi$ is observed.

In our calculations, the angles $\delta\chi$ ranged from 0.1 to 0.2 rad. These values are characteristic of the effective scattering angles at frequencies of about 1 kHz in caustic zones. The sound scattering may be caused by elongated plane-layered fine-structure inhomogeneities of the refractive index when $\delta\chi \approx 4.3(\beta\lambda)^{1/3}$, or by isotropic inhomogeneities of turbulent nature when $\delta\chi \approx \lambda/2\pi L_0$. Here, λ is the wavelength; β is twice the difference between the curvature of the caustic section along the ray and the curvature of the ray itself at a point where the ray is tangent to the caustic; and L_0 is the external scale of turbulence. For the ocean, the typical values are $\beta \cong 5 \times 10^{-6}$ m^{-1} and L_0 about several meters (see [1, 5, 6]). Scattering in the water bulk can also be caused by deep scattering layers of biological nature. In this case, the value of $\delta\chi$ may be governed by the limiting scattering angle $\delta\chi_{\max}$ for a given sea depth z:

$$\delta\chi_{\max} = 2a(z - z_k)^{1/2} - \chi_k. \tag{10}$$

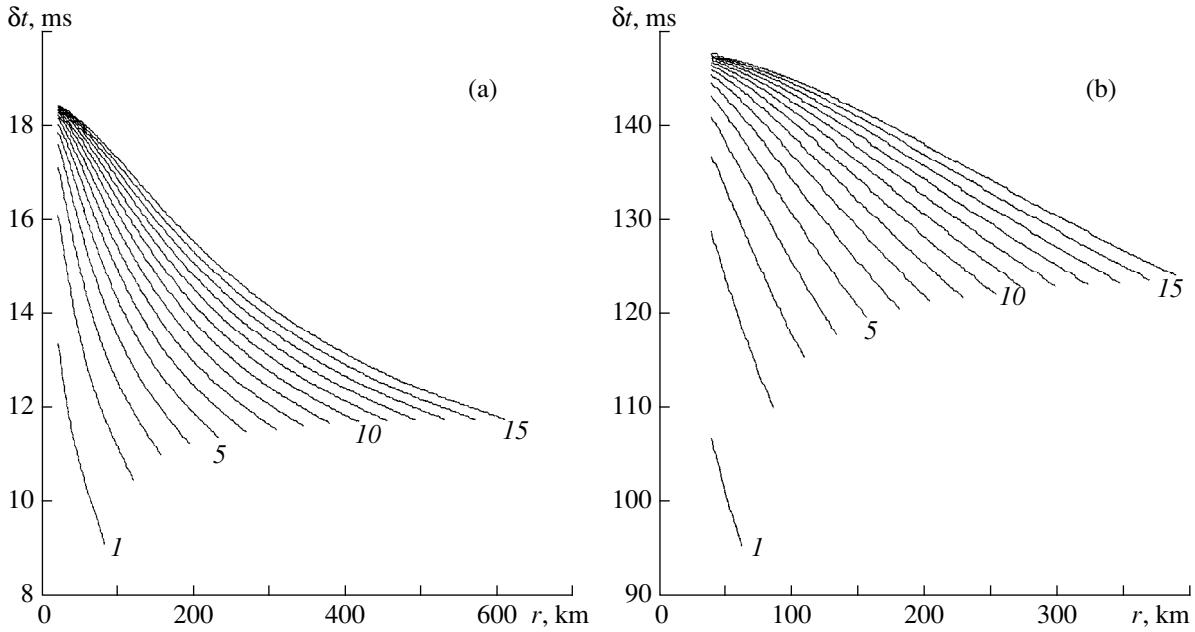

Fig. 3. Prereverberation time versus distance, with the number of cycles N being the parameter of the curves: $\delta\chi$ = (a) 0.1 and (b) 0.2 rad.

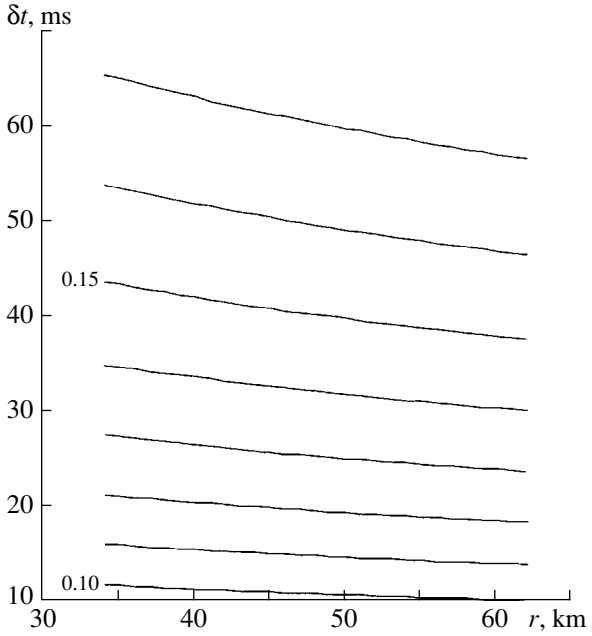

Fig. 4. Prereverberation time versus distance, with the scattering angle $\delta\chi$ (from 0.1 to 0.17 rad) being the parameter of the curves.

Sound scattered at negative angles or in the specular direction leads to the reverberation ("aftersounding") effect. It can be shown that the ray bundle produced by specular scattering from the fine-structure inhomogeneities in the caustic zone is focused at the reception point that is symmetric with the transmission point (Fig. 5). In this case,

$$\frac{r}{2} = \frac{\chi_0}{a} - \frac{\chi}{a} + \frac{2\chi_0}{a} = \frac{3\chi_0}{a} - \frac{\chi}{a}. \qquad (11)$$

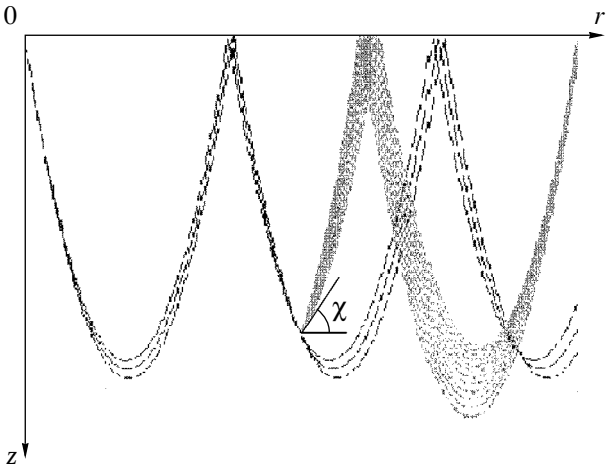

Fig. 5. Focusing of rays scattered by the fine-structure inhomogeneities in the specular direction.

The condition of focusing is the zero value of the derivative $\frac{dr}{d\chi} = 2\left(3\frac{d\chi_0}{d\chi} - 1\right)a^{-1}$, which yields $\frac{d\chi_0}{d\chi} = \frac{1}{3}$. Because the Snell law requires that $\frac{d\chi_0}{d\chi} = \frac{\chi}{\chi_0}$ at small angles, we obtain $\chi = \frac{1}{3}\chi_0 = \chi_k$ at $N = 1$. Thus, for the bundle of scattered rays to focus on the reception point at the distance $r/2$, it is necessary that scattering occurs in the caustic zone.

As it was previously [1] mentioned, prereverberation and insonification of geometric shadow zones are phenomena of the same nature, which are caused by scattering from the inhomogeneities of the water bulk and its boundaries. The scattered field producing prereverberation (in a wide sense), namely, the space-time, angular, and power characteristics of scattering, carry information both on the statistical parameters of inhomogeneities and on the structure of the primary sound field, including the location of caustics in the insonified zones.

ACKNOWLEDGMENTS

This work was supported by Russian Foundation for Basic Research, project nos. 98-05-64302 and 99-05-64379.

REFERENCES

1. V. S. Gostev and R. F. Shvachko, Akust. Zh. **45**, 857 (1999) [Acoust. Phys. **45**, 774 (1999)].
2. L. M. Brekhovskikh, *Waves in Layered Media* (Nauka, Moscow, 1973; Academic, New York, 1980).
3. E. M. Salomons, J. Acoust. Soc. Am. **104**, 3259 (1998).
4. N. V. Studenichnik, in *Proceedings of the IX All-Union Acoustical Conference, 1977* (AKIN, Moscow, 1977), Sect. D, pp. 45–48.
5. Yu. A. Kravtsov and Yu. I. Orlov, in *Geometric Optics of Heterogeneous Media* (Nauka, Moscow, 1989), pp. 88–97.
6. V. S. Gostev, L. N. Nosova, and R. F. Shvachko, Akust. Zh. **44**, 844 (1998) [Acoust. Phys. **44**, 736 (1998)].

Translated by E. Kopyl

Acoustical Physics, Vol. 46, No. 5, 2000, pp. 563–568. Translated from Akusticheskiĭ Zhurnal, Vol. 46, No. 5, 2000, pp. 644–649.

Acoustic Waves in a Rotating Ideal Gas

V. I. Erofeev and I. N. Soldatov

Blagonravov Institute of Machine Science (Nizhni Novgorod Branch), Russian Academy of Sciences, ul. Belinskogo 85, Nizhni Novgorod, 603024 Russia

e-mail: wvs@dynamo.nnov.ru

Received July 3, 1998

Abstract—The acoustic wave propagation in a rotating ideal gas with density stratification due to the rotation is considered. To describe the waves propagating normally to the rotation axis, an equation for a scalar quantity that is a function of density is proposed. The frequency dependences of the phase and group velocities of an acoustic-gyroscopic wave are presented. It is shown that the stratification of gas leads to an exponential amplitude decay for an acoustic wave generated near the rotation axis and has no effect on the inertial-gyroscopic wave. © *2000 MAIK "Nauka/Interperiodica".*

Studies of acoustic processes in machines containing gas or liquid, such as rotors, centrifuges, separators, and turbine pumps, are of interest not only from the point of view of reducing the vibroacoustic effect on the personnel or satisfying the severe requirements on the equipment's reliability, but also in relation to the effects of intense acoustic fields on technological processes. The aforementioned machines represent an evident but incomplete set of cases in which the effects caused by the rotation of the medium play a crucial role in the wave processes. The rotation of the medium had been taken into account in studying various processes in the ocean [5–9] and in atmosphere [10], but it was neglected in the studies of acoustic waves. Most attention has been concentrated on the wave processes in turbine pumps [1–4]. However, a number of factors essential for the understanding of wave processes in rotating gases, namely, the phase and group velocities and the effect of the density stratification due to rotation on the wave parameters, were somehow left out.

Let us assume that an ideal gas is enclosed in an infinite cylinder of large radius. In the unperturbed state, the cylinder and the gas in it rotate at an angular velocity $\mathbf{\Omega}$ collinear with the cylinder axis Oz. In a noninertia frame of reference rigidly bound to the rotating cylinder, the velocity of gas particles is equal to zero, and the density ρ_0 is a function of the distance r from the rotation axis:

$$\mathbf{v}_0 = 0, \quad \rho_0 = \rho_0(r).$$

We assume that, in the course of the disturbance propagation, the motion of gas particles is an isentropic one, and the pressure p is a function of density ρ, only. We introduce the pressure function $P = \int \frac{c^2 d\rho}{\rho}$, where $c^2 = \frac{dp}{d\rho}$ is the square of the sound velocity; then, the equation of motion and the continuity equation take the forms

$$\begin{aligned} \mathbf{v}_t + (\mathbf{v}\nabla)\mathbf{v} &= -\nabla P + 2[\mathbf{v}, \mathbf{\Omega}] + \Omega^2 \mathbf{r}, \\ P_t + (\nabla P, \mathbf{v}) + c^2 div\mathbf{v} &= 0. \end{aligned} \tag{1}$$

For a polytropic gas and adiabatic motion, the formula

$$c^2 = \text{const}\gamma\rho^{\gamma-1}$$

is valid, which allows us to easily invert the expression for the pressure function P through density ρ:

$$\rho = \left(\frac{1}{\text{const}}\frac{\gamma-1}{\gamma}P\right)^{\frac{1}{\gamma-1}}.$$

For a perfect gas with constant specific heat in the unperturbed state, the dependence of the pressure function P_0 on the distance to the rotation axis r is a quadratic one:

$$P_0 = \frac{1}{2}\Omega^2 r^2 + P_*,$$

where P_* is the value of the pressure function on the rotation axis.

The equations of the gas motion linearized near the unperturbed state have the form

$$\mathbf{v}_t = -\nabla P + 2[\mathbf{v}, \mathbf{\Omega}], \tag{2}$$

$$\frac{1}{c_0^2}\{P_t + (\nabla P_0, \mathbf{v})\} + \text{div}\mathbf{v} = 0. \tag{3}$$

In a perfect gas, the quantity c_0^2 does not depend on r: $c_0^2 = \gamma RT$, where γ is the specific heat ratio, R is the universal gas constant, and T is the absolute temperature. Substituting the quantity P from (3) into Eq. (2) differentiated with respect to t, we obtain an equation

with the single unknown vector being the velocity of gas particles:

$$\mathbf{v}_{tt} - \nabla(\nabla P_0, \mathbf{v}) - \nabla(c_0^2 \mathrm{div}\mathbf{v}) - 2[\mathbf{v}_t, \mathbf{\Omega}] = 0. \quad (4)$$

In many respects, it is more convenient whenever possible to deal with a scalar equation than with a vector one. Using the representation of the velocity vector $\mathbf{v}$ in terms of the Lamb potentials,

$$\mathbf{v} = \nabla\theta + \mathrm{rot}\boldsymbol{\psi}, \quad \mathrm{div}\boldsymbol{\psi} = 0,$$

we pass from the vector Eq. (2) to the system of equations

$$\theta_t = -P - 2(\boldsymbol{\psi}, \mathbf{\Omega}), \quad (5)$$

$$\boldsymbol{\psi}_t = 2\theta\mathbf{\Omega} + 2[\boldsymbol{\psi}, \mathbf{\Omega}]. \quad (6)$$

We note that such a passage restricts our consideration to the wave processes that occur in the plane perpendicular to the rotation axis: as one can infer from Eq. (6), the requirement that the divergence of ψ be equal to zero leads to the condition $(\mathbf{v}, \mathbf{\Omega}) = 0$.

In terms of the Lamb potentials, Eq. (3) takes the form

$$P_t + (\nabla P_0, \nabla\theta) + (\nabla P_0, \mathrm{rot}\boldsymbol{\psi}) + c_0^2\Delta\theta = 0. \quad (7)$$

Performing the left vector multiplication of Eq. (6) by $\mathbf{\Omega}$, we obtain

$$[\boldsymbol{\psi}_t, \mathbf{\Omega}] = -2[\mathbf{\Omega}, [\boldsymbol{\psi}, \mathbf{\Omega}]]. \quad (8)$$

Differentiating Eq. (6) with respect to t, substituting expression (8) into it, and performing simple transformations, we obtain

$$\boldsymbol{\psi}_{tt} = 2\theta_t\mathbf{\Omega} - 4\Omega^2\boldsymbol{\psi} + 4\mathbf{\Omega}(\boldsymbol{\psi}, \mathbf{\Omega}). \quad (9)$$

Substituting expression (5) for θ_t in Eq. (9), we represent the latter in the form

$$\boldsymbol{\psi}_{tt} + 4\Omega^2\boldsymbol{\psi} = -P\mathbf{\Omega}. \quad (10)$$

Differentiating Eq. (5) with respect to t and taking into account that the scalar product $(\boldsymbol{\psi}_t, \mathbf{\Omega})$ can easily be determined from Eq. (6), we derive the following relationship between P_t and the potential θ:

$$P_t = -\theta_{tt} - 4\Omega^2\theta. \quad (11)$$

Expressions (10) and (11) allow us to recast Eq. (7) to the form containing a single unknown function P. To eliminate the potentials θ and ψ from Eq. (7), we differentiate this equation twice with respect to t and add the resulting expression to the initial Eq. (7) multiplied by $4\Omega^2$. Simple transformations with the use of relations (10) and (11) yield an equation in P that describes the propagation of acoustic waves in the rotating gas in the plane perpendicular to the rotation axis:

$$P_{ttt} + 4\Omega^2 P_t - (\nabla P_0, \nabla P_t) - 2(\nabla P_0, [\nabla P, \mathbf{\Omega}]) - c_0^2\Delta P_t = 0. \quad (12)$$

As one can see from Eq. (12), a plane wave cannot propagate in a rotating stratified gas: the wavefront will necessarily be distorted in the course of the propagation. For a nearly plane, high-frequency (as compared to the angular frequency of rotation Ω) wave, we can write a stationary asymptotic expansion

$$P \sim e^{-i\omega t + i\omega\vartheta(\mathbf{x})} \sum_{m=0}^{\infty} \frac{A_m(\mathbf{x})}{(i\omega)^m}.$$

Then, from Eq. (12), we obtain the eikonal equation and the transport equation by setting the coefficients of different powers of ω equal to zero:

$$(\nabla\vartheta)^2 = \frac{1}{c_0^2},$$

$$\Omega^2(\mathbf{r}, \nabla\vartheta)A_m + c_0^2\Delta\vartheta A_m + 2c_0^2(\nabla\vartheta, \nabla A_m) = 4\Omega^2 A_{m-1} - \Omega^2(\mathbf{r}, \nabla A_{m-1}) - c_0^2\Delta A_{m-1} + 2\Omega^2([\mathbf{r}, \nabla\vartheta], \mathbf{\Omega})A_{m-1} + 2\Omega^2([\mathbf{r}, \nabla A_{m-2}], \mathbf{\Omega}), \quad (13)$$

$$A_{-1} = A_{-2} = 0, \quad m = 0, 1, 2, \ldots .$$

In the case of a perfect gas, the eikonal Eq. (13) is reduced to a simple dependence of the magnitude of the wave number $\mathbf{k} = \omega^{-1}\nabla\vartheta$ on the cyclic frequency ω:

$$|\mathbf{k}| = \frac{\omega}{c_0},$$

where the right-hand member of the equation does not depend on the spatial variables. The zero-order amplitude exponentially decreases with increasing x, i.e., in the direction of the wave propagation:

$$A_0 = A_{00}\exp\left(-\frac{\Omega^2}{2c_0^2}x^2\right).$$

In the case of a uniform gas, the third and fourth terms of Eq. (12) are equal to zero, and a plane wave can propagate with its amplitude being invariable and the dispersion relation having the form

$$k^2 = \frac{\omega^2 - 4\Omega^2}{c_0^2}.$$

In a stratified gas, this dispersion relation is approximately valid for a low-frequency, nearly plane acoustic wave when the effect of the inhomogeneity of the medium is small. From the latter expression, it follows that, at $\omega = 2\Omega$, the plane wave propagation in the direction perpendicular to the rotation axis is impossible; in this case, an inertial-gyroscopic wave will be excited along the rotation axis, the propagation of this wave being accompanied by no energy transfer (the

group velocity of the inertial-gyroscopic wave is zero at $\omega = 2\Omega$ [5]). This fact should be stressed in relation to the discussion on the Coriolis resonance at the frequency $\omega = 2\Omega$ in [3].

In the cylindrical coordinate system, Eq. (12) takes the form

$$P_{ttt} + 4\Omega^2 P_t - \Omega^2 r P_{rt} - 2\Omega^3 P_\varphi - c_0^2\left(P_{rrt} + \frac{1}{r}P_{rt} + \frac{1}{r^2}P_{\varphi\varphi t}\right) = 0,$$

which yields the following expression for the amplitude of a harmonic cylindrical wave $P = \hat{P}(r)e^{-i\omega t}$:

$$\hat{P}'' + \left(\frac{1}{r} + \frac{\Omega^2 r}{c_0^2}\right)\hat{P}' + \frac{\omega^2 - \Omega^2}{c_0^2}\hat{P} = 0.$$

By changing the independent variable, $\tilde{r} = rc_0^{-1}\sqrt{\omega^2 - 4\Omega^2}$, we obtain the equation for $\hat{P}$ in the form

$$\hat{P}'' + \left(\frac{1}{\tilde{r}} + \sigma\tilde{r}\right)\hat{P}' + \hat{P} = 0, \quad \sigma = \left(\frac{\omega^2}{\Omega^2} - 4\right)^{-1}. \quad (14)$$

This equation has the solution

$$\hat{P}(\tilde{r}) = \frac{1}{r}e^{-\frac{\sigma}{4}\tilde{r}^2}\left[C_1 M_{\frac{1-\sigma}{2\sigma},0}\left(\frac{\sigma}{2}\tilde{r}^2\right) + C_2 W_{\frac{1-\sigma}{2\sigma},0}\left(\frac{\sigma}{2}\tilde{r}^2\right)\right],$$

where $M_{\frac{1-\sigma}{2\sigma},0}\left(\frac{\sigma}{2}\tilde{r}^2\right)$ and $W_{\frac{1-\sigma}{2\sigma},0}\left(\frac{\sigma}{2}\tilde{r}^2\right)$ are the Whittaker functions [11]. When $\omega > 2\Omega$, the function $\hat{P}$ tends to zero as $O\left(\tilde{r}^{-\frac{1}{2}-\frac{1}{2\sigma}}e^{-\frac{\sigma}{4}\tilde{r}^2}\right)$ with increasing $\tilde{r}$ and performs damped oscillations. By contrast, when $\omega < 2\Omega$, the solution to Eq. (14) is bounded at $\tilde{r} = 0$ and exhibits an exponential growth with the increase in this variable.

If the inhomogeneity of gas is neglected, the second term enclosed in parentheses in Eq. (14) is zero (formally, we can set $\sigma = 0$), and the equation will have a solution expressed through zero-order Bessel functions: $\hat{P}(\tilde{r}) = C_1 J_0(\tilde{r}) + C_2 Y_0(\tilde{r})$ for $\omega > 2\Omega$ and $\hat{P}(\tilde{r}) = C_1 I_0(\tilde{r}) + C_2 K_0(\tilde{r})$ for $\omega < 2\Omega$. As one would expect, the amplitude of a cylindrical wave in a homogeneous gas decreases as $O\left(\tilde{r}^{-\frac{1}{2}}\right)$ when $\tilde{r} \longrightarrow \infty$ and $\omega > 2\Omega$.

Now, let us consider a wave propagating at an angle χ to the rotation axis. Under the assumption that $c_0 = \text{const}$, in the cylindrical coordinate system with the z axis directed along the rotation axis, the vector Eq. (4) can be represented in the form of a system of equations:

$$\begin{aligned} u_{tt} &= \Omega^2 r u_r + \Omega^2 u \\ &+ c_0^2\left(u_{rr} + \frac{u_r}{r} - \frac{u}{r^2} - \frac{v_\varphi}{r^2} + \frac{v_{r\varphi}}{r} + w_{rz}\right) + 2\Omega v_t, \\ v_{tt} &= \Omega^2 u_\varphi + c_0^2\left(\frac{u_{r\varphi}}{r} + \frac{u_\varphi}{r^2} + \frac{v_{\varphi\varphi}}{r^2} + \frac{w_{z\varphi}}{r}\right) - 2\Omega u_t, \\ w_{tt} &= \Omega^2 r u_z + c_0^2\left(u_{rz} + \frac{u_z}{r} + \frac{v_{z\varphi}}{r} + w_{zz}\right), \end{aligned} \quad (15)$$

where u, v, and w are the radial, azimuth, and axial components of the velocity vector **v**. Neglecting the stratification of gas in the unperturbed state (as is done in considering the acoustic processes in turbine pumps [3, 4]), i.e., neglecting the terms containing Ω^2, and seeking the solution to system (15) in the form of a harmonic wave

$$\begin{pmatrix} u \\ v \\ w \end{pmatrix} = \begin{pmatrix} \hat{u} \\ \hat{v} \\ \hat{w} \end{pmatrix} r^{-\frac{1}{2}} \exp(-i\omega t + ik_z z + ik_r r), \quad (16)$$

we retain only the leading terms and obtain the following linear algebraic system of equations:

$$\begin{aligned} (\omega^2 + \Omega^2 - c_0^2 k_r^2)\hat{u} + 2i\omega\Omega\hat{v} - c_0^2 k_r k_z \hat{w} &= 0, \\ 2i\omega\Omega\hat{u} + \omega^2\hat{v} &= 0, \\ -c_0^2 k_r k_z \hat{u} + (\omega^2 - c_0^2 k_z^2)\hat{w} &= 0. \end{aligned}$$

A nontrivial solution to this system exists when the condition

$$\omega^4 - \omega^2(c_0^2 k_r^2 + c_0^2 k_z^2 + 4\Omega^2) + 4\Omega^2 c_0^2 k_z^2 = 0 \quad (17)$$

is fulfilled. The dispersion Eq. (17) (which coincides with the dispersion equation from [3] corrected for the Doppler shift) can be represented in the form

$$k^2 = \frac{\omega^2(\omega^2 - 4\Omega^2)}{c_0^2(\omega^2 - 4\Omega^2\cos^2\chi)}, \quad k^2 = k_r^2 + k_z^2. \quad (18)$$

From expression (18), it follows that, for cyclic frequencies ω within the range $2\Omega\cos\chi < \omega < 2\Omega$, there are no waves propagating at the angle χ to the z axis. In other words: when the frequency is $\omega < 2\Omega$, a travelling wave can exist only for the angles $\chi < \arccos\frac{\omega}{2\Omega}$. Figure 1 shows the dependence of the phase velocity c_{ph} on

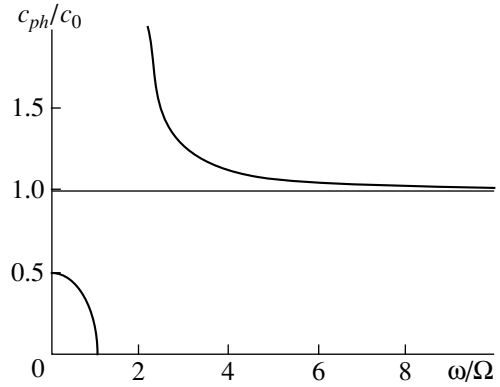

Fig. 1.

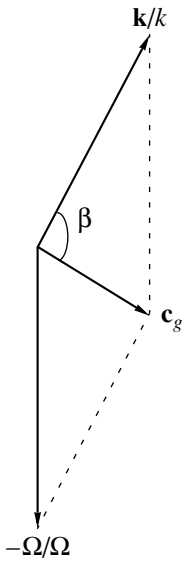

Fig. 2.

the frequency ω for the angle $\chi = \pi/3$. The group velocity vector $\mathbf{c}_g$ determined as

$$\mathbf{c}_g = \begin{cases} \dfrac{c_0^2}{2c_{ph}}\left[\left(1 - \dfrac{\omega^2 c_0^2}{2\Phi c_{ph}^2} - \dfrac{2\Omega^2}{\Phi}\right)\dfrac{\mathbf{k}}{k} + \dfrac{4\Omega^2}{\Phi}\cos\chi\dfrac{\mathbf{\Omega}}{\Omega}\right], \\ \omega < 2\Omega\cos\chi \\ \dfrac{c_0^2}{2c_{ph}}\left[\left(1 + \dfrac{\omega^2 c_0^2}{2\Phi c_{ph}^2} + \dfrac{2\Omega^2}{\Phi}\right)\dfrac{\mathbf{k}}{k} - \dfrac{4\Omega^2}{\Phi}\cos\chi\dfrac{\mathbf{\Omega}}{\Omega}\right], \\ \omega > 2\Omega, \end{cases}$$

where

$$c_{ph} = c_0\sqrt{\frac{\omega^2 - 4\Omega^2\cos^2\chi}{\omega^2 - 4\Omega^2}},$$

$$\Phi = \frac{1}{2}\sqrt{(c_0^2k^2 + 4\Omega^2)^2 - 16\Omega^2c_0^2k^2\cos^2\chi}$$

is directed at an angle β to the wave vector **k** (Fig. 2). The angle β varies from zero to π/2, depending on the frequency (this is illustrated by the dependence of cosβ on ω for $\chi = \pi/3$ in Fig. 3). At high frequencies, the wave vector and the group velocity vector become collinear.

Let us go back to a stratified gas without making any assumptions on the values of the coefficients in equations (15) and consider a wave process that is independent of the angle φ. The system of Eqs. (15) is reduced to a single equation

$$(\partial_t^2 - c_0^2\partial_z^2)(u_{tt} - \Omega^2 r u_r + 3\Omega^2 u) - c_0^2\partial_t^2\left(u_{rr} + \frac{u_r}{r} - \frac{u}{r^2}\right) - c_0^2\Omega^2\partial_z^2(u + ru_r) = 0. \quad (19)$$

We note that, for a nonstratified gas, the analog of the latter equation has the form

$$(\partial_t^2 - c_0^2\partial_z^2)(u_{tt} + 4\Omega^2 u) - c_0^2\partial_t^2\left(u_{rr} + \frac{u}{r} - \frac{u}{r^2}\right) = 0.$$

Substituting the solution in the form

$$u = \hat{u}(r)\exp(-i\omega t + ik_z z + ik_r r)$$

into Eq. (19) and performing simple transformations, we obtain an ordinary differential equation for the complex amplitude $\hat{u}(r)$:

$$\hat{u}' + \left(\frac{1}{r} + 2ik_r + \frac{\Omega^2}{c_0^2}r\right)\hat{u}'' + \left(-\frac{1}{r^2} + i\frac{k_r}{r} + \frac{\omega^2}{c_0^2} - k_r^2 - k_z^2 - \frac{3\Omega^2}{c_0^2} + \frac{4\Omega^2k_z^2}{c_0^2} + i\frac{\Omega^2k_r}{c_0^2}r\right)\hat{u} = 0.$$

Figure 4 shows the quantitative dependence of the absolute value of the function $\hat{u}(r)$ on the distance $\tilde{r} = \Omega r/c_0$ for the waves propagating in a stratified (the solid line) and nonstratified (the dotted line) gas. One can see that, with allowance made for a increase in the gas density toward the periphery, the absolute value of $\hat{u}(r)$ exhibits a monotonic decrease with distance (except for a single rise).

In contrast to acoustic waves, the inertial-gyroscopic waves are not affected by the density stratification in *r*. Let us prove this statement. Solution (16) contains both purely acoustic and inertial-gyroscopic waves as the limiting cases. To separate the latter type of waves, we set $c_0 = \infty$ in Eqs. (2) and (3) and take into

account that $P_0 = c_0^2 \ln\rho_0$. Then, going back to the variables p and ρ, we recast the equations to the form

$$\mathbf{v}_t = -\frac{\nabla p}{\rho} + 2[\mathbf{v}, \mathbf{\Omega}], \tag{20}$$

$$\rho_0 \mathrm{div}\mathbf{v} + (\nabla\rho_0, \mathbf{v}) = 0,$$

$$\rho_0 = \rho_* \exp\left(\frac{1}{2RT}\Omega^2 r^2\right). \tag{21}$$

We apply the divergence operation to Eq. (20):

$$\mathrm{div}\mathbf{v}_t = -\frac{\Delta p}{\rho_0} + \frac{1}{\rho_0}(\nabla\ln\rho_0, \nabla p) + 2(\mathbf{\Omega}, \mathrm{rot}\mathbf{v}). \tag{22}$$

We differentiate Eq. (22) twice with respect to t and combine it with the initial Eq. (22) multiplied by $4\Omega^2$. As a result, we obtain

$$\mathrm{div}(\mathbf{v}_{ttt} + 4\Omega^2\mathbf{v}_t) = -\frac{\Delta p_{tt}}{\rho_0} - 4\Omega^2\frac{\Delta p}{\rho_0} + \frac{1}{\rho_0}(\nabla\ln\rho_0, \nabla p_{tt} + 4\Omega^2\nabla p) + 2(\mathbf{\Omega}, \mathrm{rot}\mathbf{v}_{tt}) + 8\Omega^2(\mathbf{\Omega}, \mathrm{rot}\mathbf{v}). \tag{23}$$

The subsequent transformations are performed with the use of the continuity Eq. (21) and the formula derived in the following way: equation (20) is subjected to vector multiplication by $2\mathbf{\Omega}$ and combined with Eq. (20) differentiated with respect to time t; collecting similar terms, we obtain

$$\mathbf{v}_{tt} + 4\Omega^2\mathbf{v} = -\frac{\nabla p_t}{\rho_0} - 2\left[\frac{\nabla p}{\rho_0}, \mathbf{\Omega}\right] + 4(\mathbf{v}, \mathbf{\Omega})\mathbf{\Omega}. \tag{24}$$

We recast Eq. (23) by using formulas (21) and (24) and the equalities

$$\mathrm{div}(\mathbf{v}_t, \mathbf{\Omega})\mathbf{\Omega} = -\left(\mathbf{\Omega}, \nabla\left(\frac{\nabla p}{\rho_0}, \mathbf{\Omega}\right)\right),$$

$$\mathrm{rot}(\mathbf{v}_t, \mathbf{\Omega})\mathbf{\Omega} = \left[\mathbf{\Omega}, \nabla\left(\frac{\nabla p}{\rho_0}, \mathbf{\Omega}\right)\right]$$

to obtain an equation that does not contain the quantity $\mathbf{v}$:

$$\Delta p_{tt} + 4\Omega^2\Delta p - 4\Omega^2(\nabla\ln\rho_0, \nabla p) + 4\rho_0\left(\mathbf{\Omega}, \mathrm{rot}\left[\frac{\nabla p}{\rho_0}, \mathbf{\Omega}\right]\right) = 0. \tag{25}$$

The formula

$$\left(\mathbf{\Omega}, \mathrm{rot}\left[\frac{\nabla p}{\rho_0}, \mathbf{\Omega}\right]\right) = \left(\mathbf{\Omega}, \nabla\left(\frac{\nabla p}{\rho_0}, \mathbf{\Omega}\right) - \mathbf{\Omega}\frac{\Delta p}{\rho_0} - \mathbf{\Omega}\frac{(\nabla\ln\rho_0, \nabla p)}{\rho_0}\right)$$

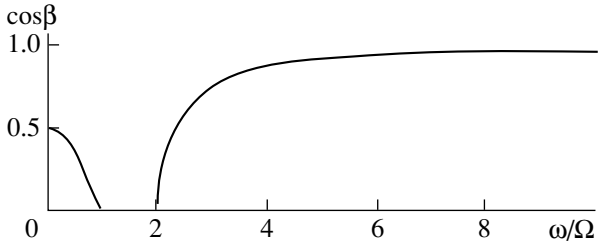

Fig. 3.

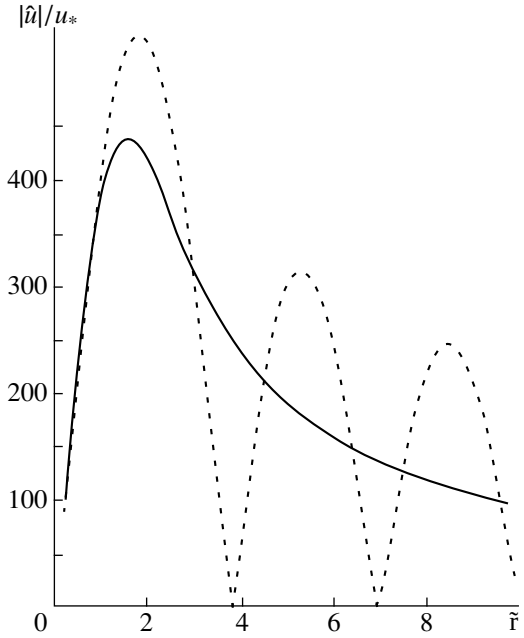

Fig. 4.

allows one to eliminate ρ_0 from Eq. (25) by performing minor transformations:

$$\Delta p_{tt} + 4(\mathbf{\Omega}, (\mathbf{\Omega}\nabla)\nabla p) = 0.$$

Thus, the stratification of liquid does not affect the propagation of the inertial wave.

ACKNOWLEDGMENTS

This work was supported by the Russian Foundation for Basic Research (project nos. 98-15-96127 and 99-01-00172).

REFERENCES

1. B. V. Pokrovskiĭ and E. Ya. Yudin, Akust. Zh. **12**, 355 (1966) [Sov. Phys. Acoust. **12**, 303 (1966)].
2. D. V. Bazhenov and A. V. Rimskiĭ-Korsakov, in *Acoustoaerodynamic Studies* (Nauka, Moscow, 1975), pp. 41–45.
3. M. Kurosaka and J. E. Caruthers, AIAA J. **20**, 1148 (1982).

4. V. A. Khitrik, Akust. Zh. **43**, 110 (1997) [Acoust. Phys. **43**, 96 (1997)].
5. L. D. Landau and E. M. Lifshitz, *Course of Theoretical Physics*, Vol. 6: *Fluid Mechanics* (Nauka, Moscow, 1986; Pergamon, New York, 1987).
6. L. M. Brekhovskikh and V. V. Goncharov, *Introduction to the Mechanics of Continuous Media* (Nauka, Moscow, 1982).
7. P. H. Le Blond and L. A. Mysak, *Waves in the Ocean* (Elsevier, Amsterdam, 1978; Mir, Moscow, 1981).
8. H. P. Greenspan, *The Theory of Rotating Fluids* (Cambridge Univ. Press, Cambridge, 1968; Gidrometeoizdat, Leningrad, 1975).
9. R. H. J. Grimshaw, L. A. Ostrovsky, V. I. Shrira, and Yu. A. Stepanyants, Surv. Geophys. **19**, 289 (1998).
10. E. E. Gossard and W. H. Hooke, *Waves in the Atmosphere* (Elsevier, Amsterdam, 1975; Mir, Moscow, 1978).
11. *Handbook of Mathematical Functions*, Ed. by M. Abramowitz and I. A. Stegun (Dover, New York, 1971; Nauka, Moscow, 1979).

Translated by E. Golyamina

Acoustical Physics, Vol. 46, No. 5, 2000, pp. 569–575. Translated from Akusticheskiĭ Zhurnal, Vol. 46, No. 5, 2000, pp. 650–657.

Inverse Aperture Synthesis in an Acoustic Dark Field

V. A. Zverev, P. I. Korotin, A. L. Matveev, B. M. Salin, and V. I. Turchin

Institute of Applied Physics, Russian Academy of Sciences,
ul. Ul'yanova 46, Nizhni Novgorod, 603600 Russia
e-mail: zverev@hydro.appl.sci-nnov.ru

Received September 24, 1999

Abstract—A method is proposed for extracting the signal scattered by a moving acoustic screen and for reconstructing the image of the scatterer. The results of the preliminary numerical calculations performed for a free space agree well with the results of the full-scale experiment in a lake. A good agreement between theory and experiment is achieved with an aperture synthesis by the signal magnitude. The characteristic feature of the proposed method of aperture synthesis is the use of an extended acoustic array in the target tracking mode of operation. This provides an additional condition for the determination of the parameters of the experiment, thus allowing one to determine two such parameters. *© 2000 MAIK "Nauka/Interperiodica".*

In the previous paper [1], a method for observing weak acoustic fields scattered by moving inhomogeneities was proposed. In an experiment carried out in a lake, the method provided a 60-dB suppression of the multiplicative interference caused by the amplitude and phase fluctuations of the radiator [1]. As a result of these studies, a fundamental possibility opened up not only for the extraction of the scattered signal, but also for the identification of the scatterer's shape. In this paper, we propose to complement the aforementioned method with a special processing procedure for the extracted signal in order to determine the dimensions of the scatterer and to estimate the acoustic parameters of the propagation path. For this purpose, it is necessary to use an extended acoustic array constantly pointed at a moving acoustic screen. The condition that the array is constantly pointed at the screen provides an additional equation for the determination of the acoustic parameters of the experiment.

Let us describe the general scheme of the experiment and the technique used for experimental data processing. The fundamental possibility of visualizing the acoustic field at a scatterer can be deduced from some evident reasoning. Namely, the wave field at the acoustic screen surface can be calculated from the known field observed at a distance R from the screen. The possibility of solving this problem on the basis of field measurements is determined by two conditions. The first one is a sufficiently high accuracy of the wave field measurements, and the second one requires that the measurements be taken over a sufficiently long spatial interval (a large aperture).

The experiment proceeded as follows. An acoustically opaque screen was towed between an acoustic source and a receiving array containing 64 receiving elements arranged in a horizontal line within an aperture of size $A = 12$ m. The distance from the screen trajectory to the array was $R = 150$ m. The screen size was about 4 m, and the acoustic wavelength was about 0.5 m. Hence, the Fraunhofer diffraction conditions were fulfilled for the field behind the screen, on the array's site. The array within its aperture also was in the Fraunhofer diffraction zone. This condition prevented direct determination of the field distribution over the screen by the array. The latter only allowed us to determine the direction toward the screen. However, the screen moved, and the field values at the array were multiply recorded in the course of the screen motion. These data could be used for increasing the effective aperture of the array by its synthesis.

To test this possibility, we performed mathematical modeling of the measurement process. The wave field formed on the moving screen was modeled; then, the field was calculated at the array within its aperture A for all 1024 positions of the screen that were recorded in the course of the experiment. The calculations were performed with allowance for the geometry of the experiment; we also used the assumption that the wave propagates in free space, and the field is zero immediately behind the screen according to the Kirchhoff rule and is unperturbed outside the screen. Below, such rules, which replace the solution of the diffraction problem, will simply be called "the Kirchhoff rule." The Kirchhoff rule is a good approximation for a screen of large wave size within small diffraction angles. By the 64×1024 calculated values of the wave field in the far zone, we numerically solved the problem of reconstructing the wave field immediately behind the screen. The result obtained by solving this problem is shown in Fig. 1. In shape, this result resembles the screen, which was assumed to be rectangular in the calculations.

However, this does not mean that the real experiment will also provide the desired result. In real conditions, the wave propagates not in free space, but in a

1063-7710/00/4605-0569$20.00

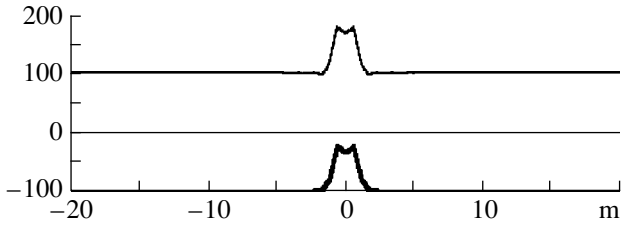

Fig. 1. Result of the theoretical solution of the inverse wave problem on the basis of the calculated data with the use of the aperture synthesis. The horizontal axis represents the length, and the vertical axis shows the linear scale in arbitrary units. The upper solid line shows the real part of the calculated field; the thin line in the middle shows the imaginary part of the field; and the thickest line at the bottom shows the magnitude.

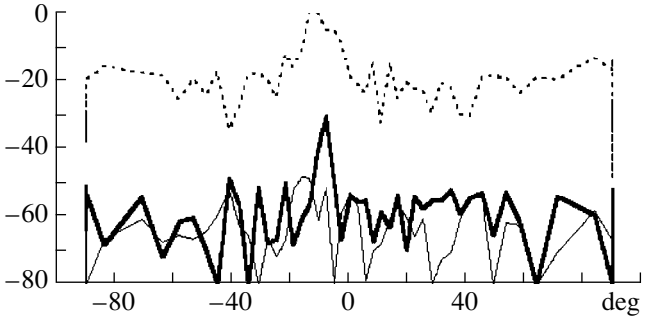

Fig. 2. Array response as a function of angle (the angle is represented by the horizontal axis) at a fixed instant of time. The upper dotted curve is the array response without additional processing. The thick line below shows the array response at the same instant after the signal obtained from all array elements was processed by formula (4) (the dark field algorithm). The thin line shows the array response after processing by formula (4) at an earlier instant of time, prior to the screen motion.

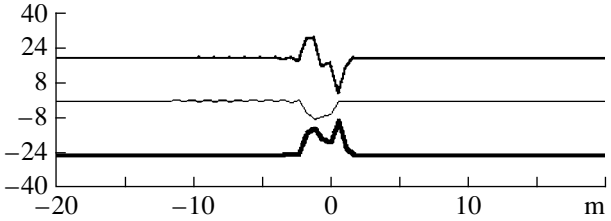

Fig. 3. Result of the theoretical solution of the inverse problem with the use of the dark field algorithm. The coordinate axes and notations are the same as in Fig. 1.

natural waveguide, where it is reflected from the bottom and the surface of the lake. The result can be affected by the intermodal interference, the signal modulation by the wind waves on the lake's surface, the internal waves, and some other factors. In addition, one can hardly expect the validity of the Kirchhoff rule, because the wave size of the screen is less than ten wavelengths.

The factors listed above can distort the result. However, there is one more important difficulty in solving the inverse problem with the use of the aperture synthesis, and it even does not allow one to obtain any result at all. This main difficulty is illustrated in Fig. 2, where the dotted line shows the form of the array's response to the received signal for some instant of time in the real conditions of the experiment. The acoustically opaque screen darkens only a small part of the entire field received by the array. Therefore, in the figure, one can see the direction toward the radiator and the signals scattered by the bottom, surface, and banks of the lake. The signal from the screen is practically undetectable. The form of the antenna response is virtually invariable, in time (in the course of the screen motion). Naturally, an aperture synthesis by such a signal is impossible because of the high level of noise produced by extraneous signals. To eliminate these signals, one can use the algorithm that forms the so-called dark field against which only the moving scatterers can be observed [1]. The thickest line in Fig. 2 shows the signal obtained by the method proposed in [1]. One can clearly see the angular position of the screen at the given instant with an excess over the ambient reverberation background that is sufficient for solving the inverse wave problem in natural conditions.

The necessity to use the dark field algorithm [1] in the experiment means that the theoretical calculations should also be performed with the use of this algorithm. The result of such a calculation is shown in Fig. 3. The dark field algorithm operates as a filter linear in the signal frequency [1], which results in that the field image on the screen is differentiated with respect to spatial coordinates. Therefore, only the edges of the rectangular screen stand out. The result of the experiment performed with the use of the dark field algorithm should be compared with the computational result shown in Fig. 3.

Below, we consider some details of the solution of both the direct and inverse problems and present the main relationships. We assume that the screen is small, so that, at a distance R from it, the Fraunhofer diffraction conditions are satisfied, and these conditions have the form [2, 3]

$$D \ll \sqrt{R\lambda}, \tag{1}$$

where D is the screen size and λ is the wavelength. In this case, the field behind the screen (the solution to the direct problem in the small-angle approximation) can be represented as [2, 3]

$$p(x, y, R) = \frac{\exp[ikR + i(x^2 + y^2)k/2R]}{i\lambda R} g\left(-\frac{kx}{R}, -\frac{ky}{R}\right). \tag{2}$$

Here, $p(x, y, R)$ is the complex amplitude of the wave field, x and y are the rectangular coordinates, $k = \frac{2\pi}{k}$, and $g(u_1, u_2)$ is the spatial Fourier spectrum of the screen shape with the spatial frequencies u_1 and u_2. For-

mula (2) is given in [3] (p. 28, formula (1.35)). In the case under study, the problem can be considered as one-dimensional, and the coordinate y can be neglected. Besides, we can neglect the constant phase shift depending exclusively on the distance R, which is assumed to be constant, and we can also neglect other constant values. As a result, we obtain the following initial relationship:

$$P(x) = \exp\left(i\frac{k}{2R}x^2\right)g\left(-\frac{k}{R}x\right). \quad (3)$$

Formula (3) is valid for a plane wave illuminating the screen. In our case, the screen is illuminated by a point source located at a distance R_1 from the screen trajectory, and the receiving array is located at a distance R_2 from this line, on the other side of it. Then, to take into account the sphericity, it is sufficient to introduce some reduced distance R determined by the formula [2, 3]

$$\frac{1}{R} = \frac{1}{R_1} + \frac{1}{R_2}. \quad (4)$$

Now, let us take into account that the screen moves with the velocity v in the horizontal direction, along the trajectory that coincides with the normal to the line connecting the radiator and the receiving array. Then, the field formed at n discrete points of reading, which are selected on the time axis from the total data array M with the frequency f, can be represented in the form

$$P(n) = \exp(iK_2(n-0.5M)^2) \times g\left(-\frac{k}{R}\left(\frac{v}{f}\right)(n-0.5M)\right), \quad (5)$$

where

$$K_2 = \frac{k}{2R}\left(\frac{v}{f}\right)^2. \quad (6)$$

Expression (5) is valid for a single receiver of the radiation scattered by the screen. In our case, the reception is performed by a set of individual hydrophones of the acoustic array. Expression (5) is valid for every single hydrophone of the array with allowance made for the corresponding signal phases, which are determined by the geometry of the hydrophone arrangement.

We assume that signals from the individual hydrophones of the array are summed up with the relative phases that provide their in-phase summation in the course of the reception of the field scattered by the moving screen, no matter what the number of points n. If this condition is fulfilled, then, for the signal scattered by the screen, the array will be equivalent to an omnidirectional hydrophone (this is quite important, because a directional reception restricts the resolution obtained by the aperture synthesis). For the array signal phased in this way, formula (5) is valid.

Let us derive the required condition of phasing for the signals received by the individual hydrophones of the array. Within the array aperture, the field produced by the screen is a plane wave (the Fraunhofer diffraction condition), and this wave has the form

$$P(e) = \exp\left[i\frac{2\pi}{L}u(e-0.5L)\right]. \quad (7)$$

Here, L is the number of array hydrophones, which coincides with the number of the discrete readings within the antenna aperture A; e is the order number of a discrete wave field reading taken along the aperture, or the number of the receiving hydrophone located at this point; and u is the spatial frequency (normalized to $2\pi/A$) that is determined by the angle at which the plane wave is incident on the array:

$$\sin\theta_e = \frac{\lambda_a}{A}u. \quad (8)$$

In the latter expression, λ_a is the wavelength that occurs at the array depth in the presence of the real sound velocity gradients in water and in the ground. In our case, the angle at which the moving screen is observed from the array's site can be represented in the form

$$\theta \approx \frac{v}{f}\frac{n-0.5M}{R_2}\cos\Psi, \quad (9)$$

where Ψ is the angle in the vertical plane at which the signal from the screen arrives at the array. Assuming that the angle θ is small and substituting expression (9) into formula (8) and the latter into expression (7), we obtain

$$P(e,n) = \exp[iK_1(n-0.5M)(e-0.5L)], \quad (10)$$

where

$$K_1 = \frac{2\pi A v\cos\Psi}{\lambda_a R_2 fL}. \quad (11)$$

We note that formula (2) and, hence, formula (3) are valid in the conditions of small-angle approximation [2, 3]. The factor $\cos\Psi$ reduces the equivalent angle of the wave incidence on the array in the horizontal plane, which facilitates the fulfillment of the conditions of small-angle approximation, as compared to the wave propagation in free space.

For the array phasing to the screen, the signal received by the array and represented as a matrix of the variables e and n should be multiplied by a matrix that is complex conjugate to matrix (10). Using formulas (5) and (10), we obtained 64×1024 values of the complex field amplitudes simulating the experimental data.

The inverse problem was solved in two steps. At the first step, the array was pointed at the moving screen. This operation is very important, and it makes the difference between our method and the aperture synthesis commonly used in radar [2–4]. In the latter case, the

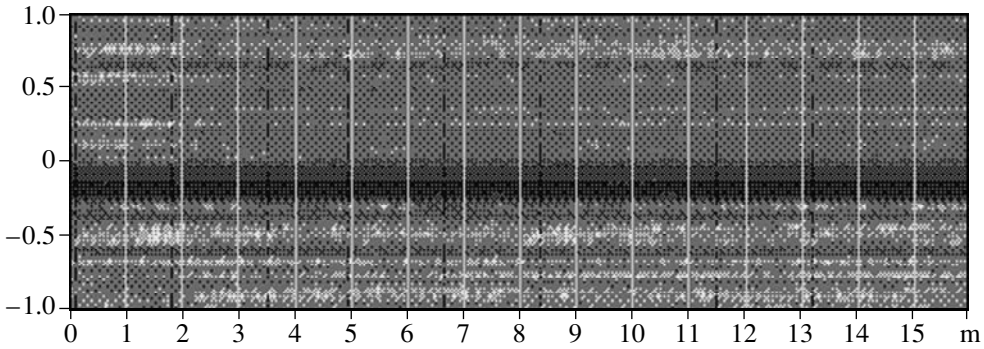

Fig. 4. Array response as a function of angle (the vertical coordinate is the sine of the angle) and time (time is represented by the horizontal axis).

array has a constant orientation relative to the line along which the aperture synthesis is performed. This leads to a limitation of the resolution obtained with this method. The spatial resolution in the area under study cannot exceed the aperture of the receiving array [2, 3]. The procedure proposed by us converts the array to an omnidirectional receiver, which has no resolution limitations.

At the second step of processing, from the entire matrix of values, we use only one row containing the signal that depends exclusively on time. The form of this signal is determined by expression (5). The processing of the signal includes its multiplication by an exponent that is complex conjugate to that involved in (5). Then, according to formula (5), the screen's shape is determined with the help of the Fourier transform.

The use of the dark field method consisted in the transformation of the initial data matrix $p(x_e, t_n)$ by the formula [1]

$$S_{e,n} = \ln\left(\frac{|p(x_e, t_{n+8})|}{|p(x_e, t_n)|}\right) + i(\arg(p(x_e, t_{n+8})) - \arg(p(x_e, t_n))). \quad (12)$$

The experiment was carried out in the Sankhar lake, Vladimir region. The radiator was placed at a distance of 300 m from the receiving array. It generated a cw monochromatic signal. The data from the array were read out as described in [1]. The screen was towed at a constant speed along a path lying halfway between the radiator and the receiving array.

Figure 4 shows the array response represented in the form of a function of time and obtained without the use of the dark field method. As seen from the figure, the array response is virtually time independent, which excludes the possibility of using the aperture synthesis for this signal. Figure 5 shows the array response obtained with the dark field algorithm. The use of the latter allows one to trace the screen displacements in angle. This makes it possible to determine the coefficient K_1 involved in (10) and, thus, to point the array at the screen. The accuracy of the determination of K_1 is dictated by the length of the rectilinear part of the scatterer trajectory.

The array is phased to the screen in the following way. For all instants of time, the signal received by all hydrophones is represented in the form of a matrix, whose columns and rows contain the variables **e** and **n**. The result of this operation is shown in Fig. 5 displaying the modulus of this matrix. As was mentioned above, for constantly "pointing" the array at the screen, one should multiply the obtained matrix by the matrix that is complex conjugate to that determined by formula (10). However, the value of the coefficient K_1 involved in (10) is unknown. This value is determined by trial-and-error. The criterion for the choice of the appropriate value is the form that is taken by the signal matrix shown in Fig. 5, after its multiplication by the aforementioned complex conjugate matrix into which the tested value of K_1 is introduced. If the value of K_1 is correct, the screen's trajectory will run precisely along the time axis. To obtain a phased signal, one only has to read the signal values along the only row of the time axis of the obtained matrix, along which the signal from the screen is observed. This procedure is applicable in the case of a sufficient excess of the signal from the screen over the level of noise and interference. Figure 2 shows quantitatively and Fig. 5 qualitatively that in our case this condition is met.

Figure 6 presents the result of the reconstruction of the screen's shape for the first rectilinear part of the screen trajectory shown in Fig. 5. Figure 6a shows the result of the reconstruction of the signal shape with the help of the algorithm used in numerical calculations. One can see that the shape of the reconstructed signal does not fully coincide with that calculated and shown in Fig. 3. However, we obtain an approximate coincidence. This result can be considered quite unexpected, if we take into account that the mathematical model and the algorithm of the natural signal reconstruction neglect a number of factors that were mentioned above.

Figure 6b shows the same signal processed in a different way. At the last step of processing, the Fourier

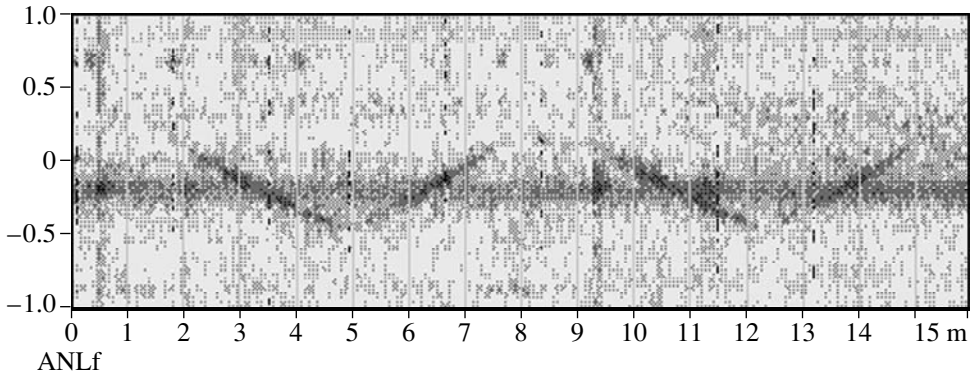

Fig. 5. Array's response at the same instant and in the same coordinates as in Fig. 4 with the use of the signal processing by formula (4) (the dark field algorithm).

transform was applied not to the complex signal, but to its magnitude. In this case, some phase relations are eliminated. In Fig. 6b, we present the results of both theoretical calculations and experimental data processing. One can see that they are in good agreement. Evidently, for this kind of processing, the effect of the signal propagation conditions is insignificant. Such an incoherent aperture synthesis does not allow one to reconstruct the screen shape, but it provides the information on the screen dimensions, which also is important.

Figure 6c presents the comparison between the results of calculations for two different screen sizes. One can see that the screen size can be readily determined on the basis of the spectrum modulus with the loss of part of the phase relations. The incoherent aperture synthesis is not always possible. In our case, it is possible, because the array is able to select the signal scattered by the moving screen against the background formed by the radiator's signal and other scatterers. Without this condition, an incoherent aperture synthesis will lead to another result, because of the effect of the interference of signals from a number of scatterers. The correlation of such a result with theory presents a difficult problem (in contrast to the result obtained by us).

In the experimental results presented above, we partly took into account the discrepancy between the screen's body and the wave field obtained immediately behind it. This was made on the basis of Fig. 6b. The screen size was about 4 m. If we substitute this size in the computational formulas, we obtain a disagreement between the calculations and the experiment in Fig. 6b, which is evidenced by Fig. 6c. The agreement is observed only when the screen size used in the calculations is about 2 m. Presumably, this can be explained by the violation of the Kirchhoff rule. On the edges of a real screen, the field is darkened to much lesser extent than it is required by the Kirchhoff rule. Therefore, in the calculations shown in Figs. 1 and 3, we also use a screen size of 2 m rather than 4 m.

On the basis of the experiment, we estimated a number of interesting parameters that characterize the acoustic conditions in which the experiment was carried out. These estimates were obtained by using the exponents involved in formulas (5) and (10). From the experiment, we estimate the dimensionless coefficients

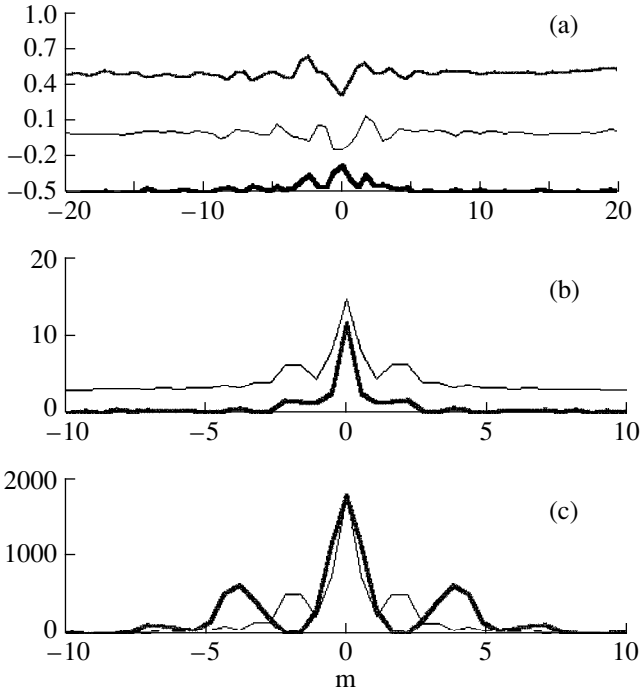

Fig. 6. Result of solving the inverse wave problem with the use of the aperture synthesis in full-scale conditions. (a) The complex wave field in the coordinates and notations of Figs. 1 and 3. (b) The result of solving the inverse problem on the basis of only the magnitude of the signal taken from the array: the thin line shows the theoretical calculation and the thick line shows the experimental result; the coordinate axes are the same as in Figs. 1 and 3. (c) The results of the theoretical calculations performed by the same method as in Fig. 6b for two different screen sizes: 2 (the thin line) and 4 m (the thick line).

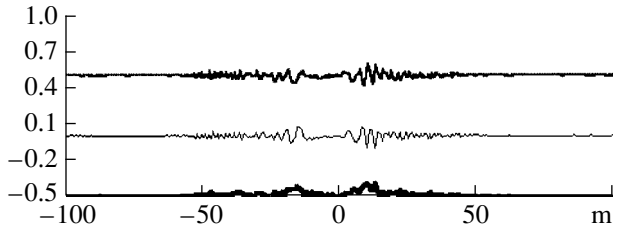

Fig. 7. Result of solving the inverse wave problem shown in Fig. 6 without compensation of the exponent in formula (5). The notations are the same as in Fig. 6a; the horizontal axis represents the distance.

involved in the exponents. In formula (10), the coefficient in question is K_1 determined by (10), and, in formula (5), the coefficient K_2 multiplying the factor $(n - 0.5M)^2$ and determined by (6). The latter coefficient is found from Fig. 6a. If, in obtaining Fig. 6a, we leave the exponent without changes and subject the whole expression (5) to spectral analysis, the resulting response will be broadened, as shown in Fig. 7. This occurs, because the frequency modulated signal of this exponent broadens the spectrum. To avoid the spectrum broadening, it is necessary to multiply the signal by the complex conjugate exponent with the selected value of K_2 before performing the final spectral transformation.

According to formula (6), the coefficient K_2 is related to the parameters of the experiment by the formula

$$K_2 = \pi v^2/(\lambda R f^2). \quad (13)$$

From two equations, (11) and (13), one can determine two parameters involved in these equations on condition that all other parameters are known. The algorithms used earlier [5, 6] allow one to estimate the parameters only on the basis of formula (5).

In our case, the parameters v, R_1, and R_2 are known. Therefore, we estimated other acoustic parameters characterizing the propagation path and involved in equations (11) and (13). The known and measured parameters are presented in the table.

In our experiment, the accuracy in the determination of the coefficients by the trial-and-error method is about 10%. By increasing the number of points of the spectral expansion, it is possible to determine the direction toward the source of the signal (on condition that its angular distance from other signals is not too small) with an accuracy much better than that within the angular resolution of the array in use [3]. (The spatial resolution is determined as the width of the main lobe of the array directivity pattern.) This fact is illustrated in Fig. 8, which shows the array's responses to the signal scattered by the screen at two instants of time with different angular positions of the screen.

The array responses are pointed at the screen by means of the multiplication of matrix (10) by the complex conjugate matrix with the coefficient values that provide both exact pointing at the screen and a 2% deviation from it. The positions of the same maxima are plotted in the inset of Fig. 8. Based on this plot, one can conclude that the value of K_1 can be determined with an accuracy of 1%. This result is important for the following reason. The propagation of the scattered waves may occur at several angles to the vertical, within a wide sector. This should affect the accuracy of pointing the array at the signal scattered by the moving screen. Therefore, an increase in the accuracy of pointing allows one to refine the conditions of the propagation of the acoustic wave in the vertical plane by using only a horizontal array.

It is of interest to estimate the accuracy of the selection of the incident radiation in the vertical plane by the horizontally oriented array used in our experiment. We have

$$\Delta[\cos\Psi] = \sin(\Psi)\Delta\Psi.$$

In our case, $\sin\Psi = 0.679$. Hence, in this experiment, the horizontal array is able to select the radiation in the vertical plane with an accuracy about two times less than in the horizontal plane.

Thus, from the results of our experimental study, we infer the following conclusions.

The acoustic dark field algorithm provides the selection of the signal of a weak moving scatterer at a level that is sufficient for the special procedure of aperture synthesis. The latter procedure proposed in this paper differs from other similar procedures in that it allows one to use the full potential of the acoustic array without any loss in resolution.

The use of a directional array with its full potential in resolution and noise immunity allows one to apply the incoherent aperture synthesis. This makes it possible to determine the scatterer's shape by eliminating the effects of a number of natural factors that cause fluctuations of the phase of the scattered signal and are hard to allow for.

Table

Known parameters							Measured parameters	
v, m/s	f, Hz	F, Hz	A, m	L	R_1, m	R_2, m	λR, m^2	$\cos\Psi$
0.68	6.36	2498.627	12	64	150	150	68.1	0.734 $\Psi = 42.8°$

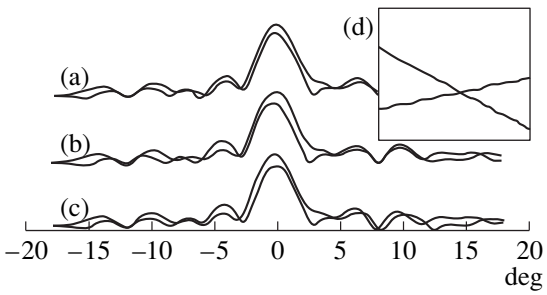

Fig. 8. Array responses for $n = 304$ and $n = 588$. The horizontal axis represents the array scan angle in degrees. (a) The maximal compensation and (b) deviations of +2% and (c) –2% from it. (d) The inset shows the positions of the array response maxima for the two time readings specified above versus the coefficient K_1; the horizontal axis represents the values of K_1 from 0.9 to 1.1%; the vertical axis represents the angle, from +1° to –1°.

Our experiment has demonstrated a real possibility for estimating two parameters of the experiment. This possibility is new compared to those known before. Specifically, it is shown that there is a possibility to detect and select the radiation arriving at the array in the vertical plane.

The proposed method can be used in a tomographic mode of operation, namely, when the radiator and receiver move together in such a way that it is possible to determine the shape of the scatterers located within the path of motion, as well as some acoustic parameters of the path.

There is a number of recent theoretical publications concerned with the refinement of the phenomena of diffraction by bodies of simple shapes [7–9]. The methods used in our study may be useful for the experimental verification of the results of these theoretical studies.

ACKNOWLEDGMENTS

This work was supported in part by the Russian Foundation for Basic Research (project nos. 96-15-96603, 99-02-16401).

REFERENCES

1. V. A. Zverev, Akust. Zh. **46**, 75 (2000) [Acoust. Phys. **46**, 62 (2000)].
2. V. A. Zverev, *Radiooptics* (Sov. Radio, Moscow, 1975).
3. V. A. Zverev, *Physical Foundations of Image Formation by Wave Fields* (Inst. Prikl. Fiz. Ross. Akad. Nauk, Nizhni Novgorod, 1998).
4. E. N. Leith, Proc. IEEE **59** (9), 1305 (1971).
5. S. M. Gorskiĭ, V. A. Zverev, A. L. Matveev, and V. V. Mityugov, Akust. Zh. **41**, 223 (1995) [Acoust. Phys. **41**, 190 (1995)].
6. V. A. Zverev, A. L. Matveev, and V. V. Mityugov, Akust. Zh. **41**, 591 (1995) [Acoust. Phys. **41**, 518 (1995)].
7. P. Rozier and B. Faure, Inverse Probl. **13**, 487 (1997).
8. K. Park and M. Ueda, Jpn. J. Appl. Phys., Part 1 **36** (5B), 3214 (1997).
9. Kohei Hongo and Hirohide Serizawa, J. Acoust. Soc. Am. **106**, 29 (1999).

Translated by E. Golyamina

Acoustical Physics, Vol. 46, No. 5, 2000, pp. 576–579. Translated from Akusticheskiĭ Zhurnal, Vol. 46, No. 5, 2000, pp. 658–661.

Evaluation of Times and Arrival Angles of Surface Prereverberation in the Ocean

E. A. Kopyl and Yu. P. Lysanov

Andreev Acoustics Institute, Russian Academy of Sciences, ul. Shvernika 4, Moscow, 117036 Russia

e-mail: bvp@akin.ru

Received December 20, 1999

Abstract—Acoustic prereverberation caused by sound scattering from the rough sea surface is considered. For the case of low-frequency scattering described by the first approximation of the small perturbation method, the arrival times and angles of prereverberation signals in the subsurface sound channel are calculated as functions of the wind speed, sound frequency, and distance. © *2000 MAIK "Nauka/Interperiodica".*

Ocean prereverberation is a phenomenon discovered experimentally as early as in 1961 [1]. It consists in the earlier arrivals of sound signals at a distant reception point as compared to the arrival times obtained from classical calculations. This phenomenon belongs to the same class as reverberation, and, in a broad sense, it is a particular case of bistatic reverberation when the prereverberation signals propagate in the forward direction. Prereverberation, as well as reverberation, is the result of scattering of sound by inhomogeneities of the ocean surface, bottom, and water column. However, in contrast to common reverberation, prereverberation occurs when the sound signals propagate over paths corresponding to lesser propagation time than the time of propagation in a medium without scattering. Whereas reverberation was actively studied for several decades (see [2]) and still continues to attract the attention of researchers [3], prereverberation has been little investigated.

One of the models of the prereverberation signal formation due to sound scattering by the rough ocean surface was suggested by Brekhovskikh *et al.* [4]. In this paper, the authors do not specify the scattering mechanism but consider the scattering directions surrounding the specular direction (with respect to the mean plane of the ocean surface) and close to it, which corresponds to the high-frequency approach of the tangent plane approximation. The scattering of low-frequency sound at small Rayleigh parameters P provides more possibilities for such a treatment of prereverberation, since in this case one can find a greater number of sound propagation paths that are described neither in the ray approximation nor in the wave approximation for a waveguide with a flat upper boundary. Below, we present simple estimates of the arrival times and angles of prereverberation caused by scattering of low-frequency (as far as P is small) sound from the ocean surface.

The scattering pattern describing the angular distribution of the reradiated field intensity at $P^2 \ll 1$ possesses one or several maxima. The positions of these maxima and their shapes are known. For example, Belousov *et al.* [5] considered fully developed isotropic wind waves described by the Pierson–Moscovitz frequency spectrum and, within the first approximation of the small perturbation method, obtained analytical expressions for the angles characterizing the positions of the scattering pattern peaks and their widths for almost any situation that may occur at $P^2 \ll 1$. These expressions are simple in their structure, but are rather cumbersome, and, therefore, we do not present here their full summary table. Nevertheless, we present one of the approximate expressions

$$|\chi - \chi_0| \ll 1, \quad |\chi - \chi_0| \cot\chi_0/2 \ll 1,$$

which is valid when the conditions

$$|\cos\chi_m - \cos\chi| = K_m/\sqrt{2k} \tag{1}$$

are satisfied. In these formulas, χ_0 is the grazing angle of the acoustic wave incident on the surface, χ_m are the grazing angles corresponding to the maxima of the scattering pattern (due to the presence of the modulus on the left-hand side of (1), there are, in general, two such maxima), k is the wave number of sound, and $K_m \approx 0.61g/v^2$ is the wave number of the surface wave corresponding to the maximum of the Pierson–Moscovitz spectrum (here, $g = 9.81$ m/s^2, v is the wind speed in meters, and the dimension of K_m is 1/m). Such an approximation describes a relatively high-frequency scattering (it is clear that the condition of smallness of the Rayleigh parameter must be satisfied) when the pattern maxima are not too far from the specular direction. In this case, equation (1) determines Bragg's diffraction spectra of order ±1 in the scattering from a surface harmonic corresponding to the maximum of the wind wave spectrum.

1063-7710/00/4605-0576$20.00 © 2000 MAIK "Nauka/Interperiodica"

We note one general feature of the scattering patterns for isotropic wind waves: at a fixed direction of incidence, their maxima (maximum) lie in the incidence plane, and, in the vertical section, they are the farther from the specular direction, the lower the sound frequency, or the smaller the rms surface displacement. At very low frequencies and weak wind waves, a single maximum of the scattering pattern may correspond even to directions close to that of backscattering [5].

We restrict our consideration to the case of the subsurface sound channel with a constant gradient of the sound velocity c, so that $c(z) = c_0(1 + az)$, where c_0 is the sound velocity at the surface and z is the depth (in numerical calculations presented below, the value of the relative gradient $a = 1.1 \times 10^{-5}$ 1/m is determined by the change of the hydrostatic pressure with depth). For simplicity, we assume that the source (S, see Fig. 1) and the receiver (R) are located at the ocean surface, with the distance $r = r_1 + r_2$ between them. Consider a situation when sound is singly scattered from the surface (at a point O, Fig. 1) on its way from the source to the receiver, the grazing angle χ_0 of the incident ray being different from the grazing angle of the scattered ray: the latter corresponds to the pattern maximum χ_m given by expression (1). Along with two ray cycles shown in Fig. 1 and corresponding to the condition $\chi_0 < \chi_m$, two other cycles are possible with $\chi_0 > \chi_m$, which differ from the shown cycles only by the order in which one cycle follows the other (to obtain these cycles, one only has to interchange the positions of the source and the receiver in Fig. 1).

Denote by $\beta = r_1/r_2$ the ratio in which the point of scattering (O) divides the distance r. Besides, we assume that the grazing angles of all rays are small. Using simple geometric considerations and retaining the terms no higher than χ_0^2 and χ_m^2, with allowance for formula (1), we obtain three equations relating the parameters of the considered problem:

$$\begin{aligned} \chi_0 + \chi_m &= ar/2, \\ \chi_0 &= \beta\chi_m, \\ \left|\chi_0^2 - \chi_m^2\right| &= \sqrt{2}K_m/k. \end{aligned} \tag{2}$$

These three equations can be used for the determination of three unknowns (χ_0, χ_m, and β) from the known values of the distance r, the gradient a, the wave number K_m of the maximum of the wind wave spectrum (i.e., the wind speed), and the wave number of sound k (i.e., its frequency).

System (2) is easily resolved, and it yields the expressions

$$\begin{aligned} \chi_m &= \frac{ar}{4} \pm \frac{\sqrt{2}K_m}{ark}, \\ \chi_0 &= \frac{ar}{4} \mp \frac{\sqrt{2}K_m}{ark} \end{aligned} \tag{3}$$

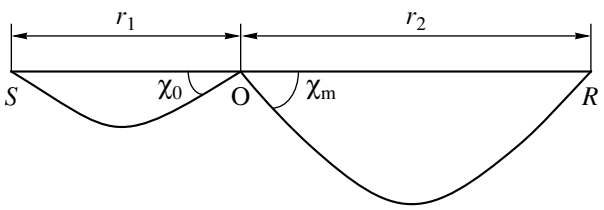

Fig. 1. Geometry of rays connecting the source S and the receiver R.

for the grazing angles of the incident and scattered rays; here, the upper sign refers to the case $\chi_m > \chi_0$ and the lower sign to the case $\chi_m < \chi_0$. We note that the quantity corresponding to the minus sign on the right-hand side of formula (3) must be positive. With the given parameters a, K_m, and k, this fact limits the minimum distance for which the situation shown in Fig. 1 can be realized. For shorter distances corresponding to the condition

$$\frac{ar}{4} - \frac{\sqrt{2}K_m}{ark} < 0,$$

there exist no values of χ_0 and χ_m that would be described by formula (1). The condition that this difference is positive is the less severe, the higher the sound frequency (the greater k) and the higher the wind speed (the smaller K_m). Substituting solution (3) in the second equation of system (2) yields the estimate of the ratio $\beta = r_1/r_2$.

As was noted in [4], the geometry of rays shown in Fig. 1 corresponds to the earlier signal arrival at the point of reception as compared to the case of specular reflection of sound from the sea surface (i.e., as compared to the case $r_1 = r_2$). At small grazing angles, this advance can be determined by the approximate formula

$$\Delta t \approx T_0\left[1 - 4\frac{r_1}{r} + 4\left(\frac{r_1}{r}\right)^2\right], \tag{4}$$

where

$$T_0 = a^2r^3/(32c_0).$$

Taking into account that $r_1/r = \beta/(1 + \beta)$, we can easily estimate the prereverberation time from formula (4) in the case under consideration.

According to the model described above, Fig. 2 presents the calculated dependences of the advance time Δt of the prereverberation signal on the wind speed at a fixed distance r = 100 km and at three sound frequencies 0.3, 0.4, and 0.5 kHz. The smaller size numbers shown near the left and right ends of each curve denote the grazing angles χ_0 and χ_m (or χ_m and χ_0, in degrees) calculated for the minimal wind speed (8 m/s, the left pair of numbers) and the maximal wind speed (15 m/s, the right pair of numbers) of those considered. Note that the range of parameter variations, which was used for the numerical calculations whose results are shown

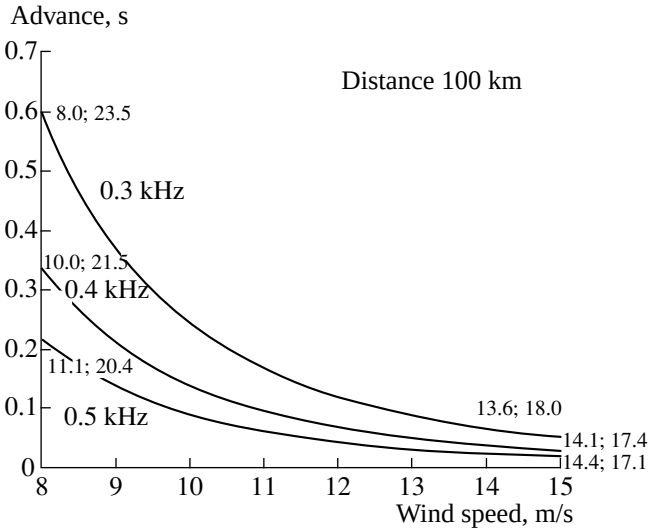

Fig. 2. Dependence of the prereverberation time on the wind speed.

in this and the following figures, was chosen so that the right-hand members of equalities (3) are positive, and the approximation used for estimating the positions of the maxima of the surface scattering pattern is valid [5]. However, the distances shown in this and next figures may not be realized because of the limited depth of the waveguide.

The frequency dependences of the prereverberation times calculated for the wind speed 10 m/s and three distances 80, 100, and 120 km are shown in Fig. 3 (the pairs of numbers near the curves have the same meaning as in Fig. 2). Finally, Fig. 4 exhibits the dependences of the prereverberation times (and the angles χ_0 and χ_m) on distance for a wind speed of 10 m/s and frequencies of 0.3–0.5 kHz. Note that the calculated values of the advance of the prereverberation signal over the specular arrival agree well with the experimental data [4].

The behavior of the curves in Figs. 2 and 3 is explained by the position of the side maxima of the surface scattering pattern a a function of the combination of the problem parameters (remind that these maxima are the farther from the direction of the specular reflection, the lower sound the frequency and the smaller wind waves). According to this, as the frequency and (or) the wind speed decrease, the difference between the angles χ_0 and χ_m increases, the lengths of the cycles shown in Fig. 1 differ more noticeably, and the prereverberation times also increase.

Unexpected at first glance, the decrease in the prereverberation time with distance (Fig. 4) is explained by a similar reason: at longer distances, the difference between the ray cycles shown in Fig. 1 is less, and the time interval within which the signal propagates in layers with higher sound velocity is shorter. However, this consideration refers only to the case when the source and the receiver located on the surface are connected by a ray that experienced a single scattering from the surface and made two cycles. For a different geometry of rays, the prereverberation times will differ from the above-mentioned values. In particular, it is clear that, in a real situation, the dependence of time advance on distance cannot be monotone because of the change in the ray structures over which the signal arrives at the point of reception. Nevertheless, if we use the conventional "multiple reflection–single scattering" approximation, the presented estimates can be valid, since only one ray

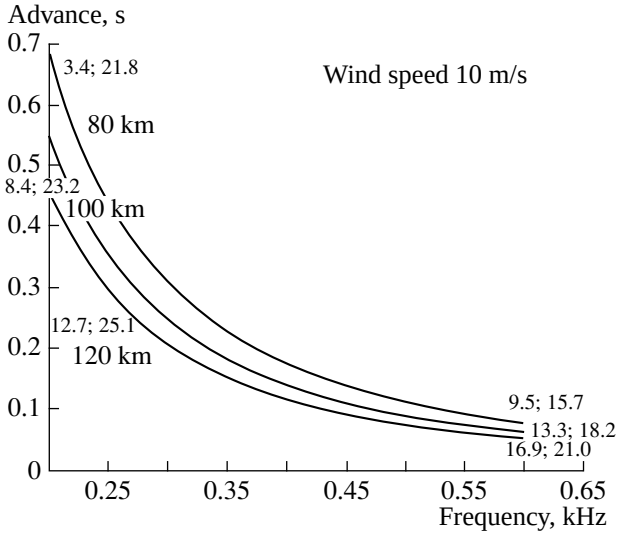

Fig. 3. Dependence of the prereverberation time on the sound frequency.

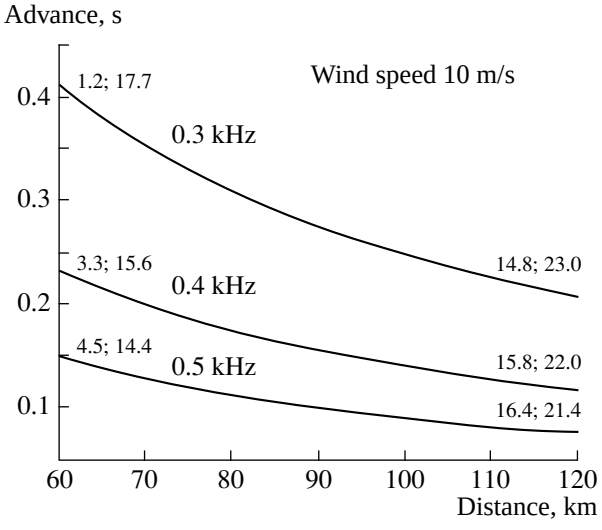

Fig. 4. Dependence of the prereverberation time on the distance.

cycle will differ from the cycle that corresponds to the specular reflection from the surface.

In conclusion, we note that, in a broad sense, prereverberation is a phenomenon that includes not only the earlier signal arrivals (as compared to the classical calculation), but also a spatial displacement of the convergence zones toward the sound source [6]. Assuming that this phenomenon has the same nature as the above-considered advance caused by the surface scattering, it is easy to estimate the value of the spatial displacement: the given values of Δt will correspond to spatial scales of hundreds of meters. However, although such scales agree with the experimental data [6], the signal arrival angles measured in the experiment almost coincide with the results of the ray calculations for a flat upper surface of the sound channel, whereas the angles presented in Figs. 2–4 have noticeably different values. Therefore, the displacement of the convergence zone toward the source can hardly be explained by the surface scattering (or, at least, by this scattering alone).

ACKNOWLEDGMENTS

We are grateful to O.P. Galkin for useful discussions. This work was supported by the Russian Foundation for Basic Research, project no. 98–05–64302.

REFERENCES

1. N. V. Studenichnik, in *Proceedings of the IX All-Union Acoustical Conference, 1977*, Sect. D, pp. 45–48.
2. Yu. M. Sukharevskiĭ, Dokl. Akad. Nauk SSSR **55** (9), 825 (1947).
3. Y. Y. Dorfman and I. Dyer, J. Acoust. Soc. Am. **106**, 1755 (1999).
4. L. M. Brekhovskikh, Yu. P. Lysanov, and N. V. Studenichnik, Dokl. Akad. Nauk SSSR **239** (1), 211 (1978).
5. A. V. Belousov, E. A. Kopyl, and Yu. P. Lysanov, Akust. Zh. **35**, 223 (1989) [Sov. Phys. Acoust. **35**, 134 (1989)].
6. O. P. Galkin and S. D. Pankova, Akust. Zh. **45**, 59 (1999) [Acoust. Phys. **45**, 52 (1999)].

Translated by Yu. Lysanov

Acoustical Physics, Vol. 46, No. 5, 2000, pp. 580–587. Translated from Akusticheskiĭ Zhurnal, Vol. 46, No. 5, 2000, pp. 662–670.

Antenna Array in the Sound Field of an Arctic Waveguide

V. M. Kudryashov

Andreev Acoustic Institute, Russian Academy of Sciences, ul. Shvernika 4, Moscow, 117036 Russia
e-mail: bvp@akin.ru

Received September 14, 1999

Abstract—An antenna array placed in an arctic-type acoustic waveguide is considered. The guided sound field consists of a signal generated by a point source and an isotropic interfering noise produced by the ice cover. The array is operated in a specific regime: the output signals correspond to individual modes of the sound field. The signal received by the array is subjected to correlation processing with a finite averaging time. It is shown that, depending on the processing method, the signal-to-noise ratio can reach 40–60 dB for a realization duration of 1 min, and the quality of the signal detection is increased. *© 2000 MAIK "Nauka/Interperiodica".*

The Arctic basin, which is ice-covered all year round, is a promising ocean region for underwater acoustic studies.

With acoustic methods, a number of scientific problems can be qualitatively solved: climatic monitoring on long paths (global oceanic thermometry and halynometry), study of the state and space-time variability of the parameters of the water bulk and the ice cover, underwater communication and observation, and so on.

Arctic experiments are expensive. In view of the lack of funds for underwater studies in both Russia and the USA, the importance of mathematical model experiments rises. In modeling, one can use all of the data that had been previously collected on the parameters of the water bulk, the ice cover, and the sea floor of the Arctic Ocean. Due to the permanent ice cover and the specific vertical profile of the sound speed in the water column, certain features are characteristic of the space, time, and frequency structures of the sound field in the Arctic Ocean and seas. In particular, in the arctic waveguide, the sound attenuation is by one or two orders of magnitude higher than in other ocean regions. However, the active losses associated with the sound absorption in water do not exceed the mean statistical value for the entire ocean. The active losses in ice are much higher than those in water, but this fact is of limited importance at low sound frequencies, when the ice thickness is less than the acoustic wavelength. In addition to the geometric change in the wave front area, the sound scattering by the ice cover governs the sound attenuation [1–3]. The scattering partially removes the sound waves from the waveguide, thereby increasing the attenuation of both the coherent and stochastic components of the sound field. High losses limit the range of sound signal detection, and the higher the sound frequency, the stronger the limitation. In practice, long-range (above 100 km) sound propagation in the arctic waveguide is feasible at frequencies of up to 100 Hz. The coherent component of the sound pressure is the one that carries information on the sound source. The scattered component plays the role of an interfering noise, though it may be used to establish the fact that a spatially localized sound source does exist.

Horizontally and vertically extended antenna arrays allow one to suppress the contribution of the stochastic (scattered) component, as compared to the coherent one, and to select the latter from the total sound field [4–7]. The stochastically scattered component can be used to estimate the parameters of the ice cover, and the underwater waveguide, to solve navigation tasks [8], and for some other purposes.

The main obstacle to detecting the signal generated by a localized sound source in the case of long-range propagation in the arctic waveguide is the environmental noise that is mainly caused by the ice cover (the wind-generated and thermal noise, the noise produced by ice cracking, by water flowing over the lower rough boundary of the ice cover, etc.). Such a noise is generated by sources spatially distributed over the surface of the ice cover. In the deep-water part of the basin, the interfering noise is often isotropic or slightly anisotropic in azimuth (i.e., in the horizontal plane). On average, the noise intensity in the Arctic Ocean is somewhat lower than in the open ocean, the increased sound attenuation in the arctic waveguide being one of the explanations for this phenomenon. However, in the frequency power spectrum of the interfering noise, the spectral densities (in a 1-Hz band) can reach 60–80 dB relative to the level corresponding to a sound pressure of 1 μPa at frequencies of 20–80 Hz, and the spectrum decays with frequency at a rate of about 5 dB per octave up to frequencies of several hundred hertz. The noise is nearly normally distributed and steady-state in a one-third-octave band for a realization duration up to 5 min.

The problem of selecting the desired signal on the background of a more intense interfering noise attracts

1063-7710/00/4605-0580$20.00 © 2000 MAIK "Nauka/Interperiodica"

increasing attention in the theory of long-range sound propagation due to the limitations imposed on the power of the sound sources by both technical and environmental factors [9]. A similar problem is also typical for other fields of research [10]. There are at least two aspects in this problem: the increase in the signal-to-noise ratio by means of the appropriate reception device (antenna array) and the suppression of the fluctuating noise in the signal processing channel. The noise immunity γ [11] of a receiving array is determined by the difference in the space-time structures of the signal generated by a localized sound source and the horizontally isotropic interfering noise generated by sources distributed over the ice-cover boundary (other noise sources are not considered). In these terms, the array noise immunity is primarily concerned with the deterministic part of the array response, i.e., with the statistical moments of this response. The statistical moments are associated with averaging over the statistically stationary and ergodic realization of infinite length, which is equivalent to averaging over the ensemble of realizations. In practice, the time T of averaging is finite due to both technical limitations and the finite stationarity interval of the received signal. Therefore, the output voltage of the integrating (averaging) device contains both the aforementioned deterministic component and the stochastic one whose variance is known [12] to decrease proportionally to τ_0/T, where τ_0 is the time correlation scale of the fluctuations. For a uniform frequency power spectrum of the signal with the frequency band Δf, we have $\tau_0 \sim 1/\Delta f$. The power of fluctuations depends on the time-averaged signal power at the input of the signal processing channel, i.e., at the array's output. Suppressing the fluctuating component of the output voltage is the subject of the second aspect of the problem, because the fluctuating component masks the deterministic part of the response.

Suppose that a point sound source ($r = 0, z = z_0$) generates a narrow-band signal with the frequency band Δf and central frequency f. Here, x, y, z are the Cartesian coordinates; the z axis is directed downward, across the underwater waveguide, and originates at the point $z = 0$ at the free-water level; and $\mathbf{r} = \{x, y\}$. The arctic-type waveguide is covered with ice of the mean thickness $h(\mathbf{r})$. The waveguide parameters depend on $\mathbf{r}$ and z, i.e., the waveguide may be an irregular one. The sound field is calculated by using the method of coupled modes [3, 13, 14], with the multi-component model [2, 3] for the floating ice. The ice cover is a key factor in forming the sound field and attenuating the propagating sound; therefore, it is important that the most realistic model of the ice cover be used.

The sound field is received by an antenna array whose size far exceeds the acoustic wavelength at the central frequency f within the band Δf. In the vertical direction, the array covers the concentration zone of the sound field, at least for several propagating normal waves (modes) of the waveguide. If the array is mounted in a shallow-water region, it is advantageous that the array extends from ice to sea floor.

Suppose that both signal and noise are Gaussian, stationary, ergodic, additive, and statistically independent processes. The signal is processed by means of a correlator that consists of successive multiplying and integrating devices. We describe the entire signal processing channel in an explicit way, in view of the fact that the procedure is to be numerically implemented by a computer.

We assume that, from the array, the signal $(p_1 + s_1)$ is entered to the first correlator input, and the signal $(p_2 + s_2)$ is entered to the second one, where p_1, p_2, s_1, and s_2 correspond to sound pressures in the signal and noise, respectively. We also assume that s_1 and s_2 are uncorrelated, and p_1 and p_2 have the correlation function $K_p(\tau) = \mathrm{Re}(\overline{p_1 p_2^*})$ if p_1 and p_2 are complex. The overbar indicates averaging over a realization of infinite duration, and the resultant mean value is deterministic. The time delay τ is introduced prior to the second correlator input, at the array output (the array is equipped with a compensator [11]).

After Tyurin [12], one can show that the variance of fluctuations at the integrator output is

$$D = \frac{\sigma_{s,1}^2\sigma_{s,2}^2 + \sigma_{p,1}^2\sigma_{p,2}^2 + K_p^2 + \sigma_{p,1}^2\sigma_{s,2}^2 + \sigma_{p,2}^2\sigma_{s,1}^2}{4\Delta f\, T}, \quad (1)$$

where

$$\sigma_{s,j}^2 = \overline{|s_j|^2},\ \sigma_{p,j}^2 = \overline{|p_j|^2};\quad j = 1, 2.$$

Expression (1) is valid for $\Delta f T \gg 1$. Hence, if $\sigma_{s,j}^2 \gg \sigma_{p,j}^2$, the fluctuating component is a small error for K_p near the maximum of the latter and does not interfere in observing the deterministic array response. This fact was mentioned in [15]. If the noise power is much higher than the signal power at the input of the multiplying device, the condition for the signal to be detected is $\max|K_p|^2 > 4D$; in particular, if $\sigma_{s,1} = \sigma_{s,2} = \sigma_s$, the condition takes the form

$$\max|K_p| > \sigma_s^2/\sqrt{\Delta f\, T}. \quad (2)$$

Note that $|K_p| = \sigma_{p,1}\sigma_{p,2}$ at the maximum.

If $T = 1$ min and $\Delta f = 3$ Hz, the signal can be detected with a power that is by 11 dB lower than that of the noise at the correlator input. Further improvement in detecting a weak signal on the background of intense ambient noise is governed by the quality of the sound field processing by the receiving transducer (the array), i.e., by the increased noise immunity κ of the array.

The sound pressure of a narrow-band coherent signal produced by a point source can be represented as a sum of normal waves (modes):

$$p(\mathbf{r}, z, t) = \sqrt{W\Delta f}\sum_{j=1}^{M} P_j(\mathbf{r})\Phi_j(z) \times F(t - t_j)\exp(-i\omega t), \quad (3)$$

where $\mathbf{r}$, z are the spatial coordinates, t is time, $\omega = 2\pi f$, f is the central signal frequency, M is the number of propagating modes, $F(t)$ is the envelope of the transmitted signal (the modulating function), and t_j is the propagation time for the jth mode. In a planar layered waveguide, $t_j = \frac{r}{v_j}$, v_j is the group velocity of the jth mode. At the observation point, $\Phi_j(z)$ is the eigenfunction for the waveguide, and $P_j(\mathbf{r})$ characterizes the amplitude and phase of the harmonic signal of frequency f. The quantity W is the sound power within the 1-Hz frequency band, at a distance of 1 m from the point source. In a planar layered waveguide, we have

$$P_j(\mathbf{r}) = i\pi\Phi_j(z_0)H_0^{(1)}(\zeta_j r),$$

where z_0 is the source depth and ζ_j is the longitudinal wave number of the jth mode. If the waveguide is irregular in $\mathbf{r}$, the functions $P_j(\mathbf{r})$ can be calculated by the method of coupled modes [3, 13, 14]. For a noise-like signal, $F(t)$ is a random function of time, $\overline{F(t)F(t+\tau)} = B(\tau)$.

The interfering noise is produced by delta-correlated sources distributed over the lower boundary of the ice cover, at the depth $z = \mu h$, where h is the mean ice thickness and μ is the ice density relative to that of water. The sound field of each source is described by an expression similar to (3). The total noise field p_s is determined by integrating over the surface where the sources are located. We assume the sources to be statistically uniform and spatially isotropic in the $\mathbf{r}$ coordinate. Then, in the expression for $\overline{|p_s|^2}$, the terms that describe the interference part of the noise field vanish, and only the energy part remains.

For a planar layered waveguide, we have

$$\overline{p_s(\mathbf{r}, z_1, t)p_s^*(\mathbf{r}, z_2, t)} = Q\sum_{j=1}^{M}\frac{|\Phi_j(\mu h)|^2\Phi_j(z_1)\Phi_j^*(z_2)}{\zeta_j 2\mathrm{Im}\zeta_j},$$

where z_1 and z_2 are the observation points.

In the WKB approximation, $\mathrm{Im}\zeta_j = -\ln|V_j|/R_j$ for the waves reflected by the ice surface, where V_j is the coherent reflection coefficient for the ice cover [1, 2] and R_j is the Brillouin cycle length for the jth mode. In the same approximation, if $k\mu h \ll 1$, the following expression is valid:

$$|\Phi_j(\mu h)|^2 = 4\frac{\zeta_j}{R_j}\beta_j(\mu h)^2,$$

where $\beta_j^2 = k^2(\mu h) - \zeta_j^2$, and $k(\mu h)$ is the acoustic wave number in water. Hence, we have

$$\frac{|\Phi_j(\mu h)|^2}{\zeta_j 2\mathrm{Im}\zeta_j} = -\frac{2(\mu h)^2\beta_j}{\ln|V_j|}.$$

Therefore, if the field of the interfering noise is mainly formed by the waves that are not bottom-reflected, we obtain

$$\overline{p_s(\mathbf{r}, z_1, t)p_s^*(\mathbf{r}, z_2, t)} = I_s\Delta f\frac{1}{M}\sum_{j=1}^{M}\Phi_j(z_1)\Phi_j^*(z_2),$$

where I_s is the spectral noise power observed within the 1-Hz band. If the nth mode is selected from the total sound field by means of the array with the weighting function $\Phi_n(z)$, its power is

$$\sigma_n^2 = I_s\Delta f/M. \quad (4)$$

The array is assumed to be in the Fraunhofer zone with respect to the sound source. Let us consider the proposed technique for signal processing in more detail. The signals received by vertical chains of hydrophones (with equal sensitivities) are multiplied by $\Phi_n(z_j)$ (j is the mode number), with the preamplifier gains being adjustable, and then summed up. This procedure is equivalent to filtering out the nth mode from the total field with the orthogonalization method. Actually, the algorithm of signal extraction is more complicated, because modes of other numbers can seep through the mode filter [16] (the algorithm for eliminating the seeping modes is not considered here). To each hydrophone of the vertical chain corresponds a horizontal hydrophone chain, the latter forming an equidistant discrete horizontal array. Then, the power of the isotropic noise corresponding to the nth mode's at the array output can be expressed as

$$\sigma_s^2 = I_s\Delta f N/M, \quad (5)$$

where N is the number of hydrophones in the horizontal chain. Expression (5) is valid, if the hydrophone spacing is greater than the horizontal correlation scale of the interfering noise. In the opposite case, one should consider the correlation of the noise field at different hydrophones of the horizontal chain [17, 18]. The horizontal chains are equipped with an antenna compensator.

For the desired signal, the array response to the nth mode is

$$p_1 = P_n(\mathbf{r})F(t-t_n)\exp(-i\omega t)\sqrt{W\Delta f}NG_n \times [\zeta_n(\sin\theta - \sin\bar{\theta})],$$

where $\mathbf{r}$ is the coordinate of the array center, and the normalized directivity pattern G_n of the horizontal array is tuned to the wave number ζ_n of the compensator. Here, θ is the bearing angle of the sound source and $\bar{\theta}$ is the compensation angle. The expression for the directivity pattern of a horizontal equidistant array can be found in [17, 18] or in other handbooks. For a linear equidistant array with hydrophones of equal sensitivities, we have

$$G_n = \frac{\sin\left[N\zeta_n\frac{d}{2}(\sin\theta - \sin\bar{\theta})\right]}{N\sin\left[\zeta_n\frac{d}{2}(\sin\theta - \sin\bar{\theta})\right]},$$

where d is the hydrophone spacing.

The azimuth compensation is implemented by the delay lines connecting the vertical chains at the preamplifier output (as in a common circuit of a horizontal array) or by means of an equivalent digital procedure, if numerical processing is used for the received signals. To the jth correlator input, the signal mixed with noise is supplied, the noise power $\sigma^2_{s,j}$ being given by expression (5) and the signal power being determined as

$$\sigma^2_{p,j} = |P_l(r)|^2 N^2 G_l^2 W\Delta f, \quad (6)$$

where $l = n$ for $j = 1$ and $l = m$ for $j = 2$.

In the interference field, the modes of different numbers are not correlated, i.e., the condition used in deriving expression (1) is met. Hence, we have

$$K_p(\tau) = \mathrm{Re}(P_n P_m^*)N^2 G_n G_m B(\tau - t_m + t_n) \times \cos(\omega\tau)W\Delta f. \quad (7)$$

In other words, only the intermode correlation of the desired signal is present in the deterministic component of the array response. As a result, one can detect an arbitrarily weak signal on the background of intense noise. Actually, the array response involves the remaining intermode correlation function of noise [19, 20], and modes of other numbers can seep through the mode filter [16]. This means that a limitation does exist for the lowest signal-to-noise ratio of the detectable modes.

Condition (2) for the signal detection can be reduced to the form

$$W|P_n||P_m|\kappa M G_n G_m B(\tau - t_m + t_n) > I_s/\sqrt{\Delta f\, T}, \quad (8)$$

where κ is the axial noise immunity for the horizontal hydrophone chain. The maximum value is $\kappa = N$. In the maximum of $K_p(\tau)$, at $\theta = \bar{\theta}$, the additional (produced by the array) noise suppression is determined by the quantity $M\kappa$. For instance, if the array has 100 hydrophones at a horizon, and there are 40 modes, the signal-to-noise ratio will increase by 36 dB in addition to the value provided by averaging over the realization duration T, the latter being determined by the interval of the steady-state sound field. This interval depends on the time variability of the propagation medium and on the motion of the sound source.

From expression (1), it can be noticed that the situation can be improved if noise is eliminated at the second correlator input; i.e., if $\sigma_{s,2} = 0$. Then, the condition of signal detection can be reduced to the form

$$\max|K_p|^2 > \frac{\sigma^2_{s,1}\sigma^2_{p,2}}{\Delta f\, T}. \quad (9)$$

This case can be implemented if the aforementioned signal is entered to the first correlator input from the array. To the second correlator input, the signal is entered from the driving oscillator of the sound source through the radio channel, or in the form of a replica stored in the correlator memory. Currently, signals are widely used whose carrier frequency is modulated by the M-sequence [21, 22]. Let us write down the signal entered to the second correlator input as a complex conjugated quantity:

$$p_2^* = AF(t-\tau)\exp(i\omega(t-\tau)).$$

Then, expression (9) takes the form

$$WM\kappa G_n^2|P_n|^2 B(\tau - t_n)\cos(\omega\tau) > I_s/(\Delta f\, T).$$

At the correlation maximum of the desired signal (the deterministic component of the output voltage), at $\tau = t_n$, $\theta = \bar{\theta}$, we have

$$W|P_n|^2/I_s > 1/(M\kappa T\Delta f).$$

For $M = 40$, $N = 100$, $T = 1$ min, and $\Delta f = 3$ Hz, the quantity $M\kappa T\Delta f$ has a value of 59 dB, which is a significant improvement in comparison with the previous case.

However, the second approach is more sensitive to time variations in the medium and to relative displacements of the communicating points [22], because the correlation between the noise envelope of the desired signal and the reference signal entered to the second input is violated. If these signals prove to be independent, there will be no deterministic signal component at the output. In this sense, the fist approach is more reliable, because the desired signals entered to the correlator inputs undergo approximately equal changes, if the space-time parameters of the propagation path change.

If the multiplicative signal processing is used (when the output represents the correlation function of the inputs), a factor that decreases the signal-to-noise ratio is the waveguide dispersion, which produces changes in the moments of the received signal in comparison

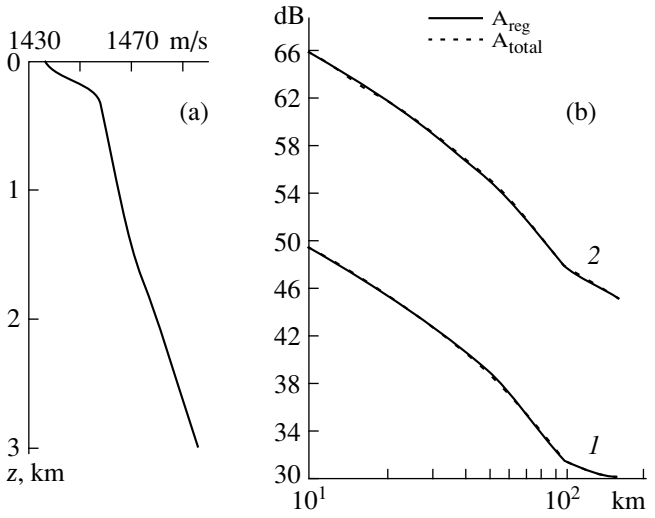

Fig. 1. (a) Sound speed profile in the water layer for the deep-water part of the waveguide and (b) the signal level (in dB) versus the distance from the source for (*1*) the total sound field and (*2*) the correlation maximum for mode numbers 2 and 3.

with the emitted one, these changes depending on both the positions of the source and receiver and the waveguide parameters. Therefore, it is advantageous to use narrow-band signals.

Let us consider a model situation. The antenna array is mounted in a shallow-water region, in a waveguide 300 m in thickness, with a constant sound speed in the vertical coordinate z. The array covers the entire water layer, from surface to bottom, and $N = 100$. Starting from the array position, the waveguide thickness (sea depth) increases linearly up to 3 km at a distance of 60 km. At longer distances, the planar layered waveguide exists with the 3-km thickness and the sound speed profile shown in Fig. 1a for the water layer. The ice cover is the two-component one [2, 23]: smooth ice covers 65% of the surface in the deep-water part of the basin and 100% of the surface in the shallow-water one. The second ice-cover component is represented by hummock ice. These two types of ice have the thicknesses 2.6 and 6.6 m, respectively. The respective rms heights of the lower rough surface of ice (the square roots of the ice draughts) are 1.6 and 3.3 m. The horizontal correlation scales for the two types of ice are 120 and 44 m, respectively. The velocity C_l of longitudinal waves in the ice is $3500(1 + i0.04)$ m/s, that of shear waves C_t is $1800(1 + i0.04)$ m/s, and the ice density is $\mu = 0.91$ relative to water. The bottom sediments are elastic with the velocities $C_l = 1850(1 + i0.005)$ m/s and $C_t = 350(1 + i0.005)$ m/s and a relative density of 1.7. The point sound source is located at the 60-m depth and operates at the central frequency 60 Hz. The signal is analyzed within the 3-Hz frequency band. The source power is 110 dB/Hz. This value is measured relative to the sound pressure level that equals to 1 μPa at a distance of 1 m from the source. The noise power I_s is 80 dB/Hz at the reception point within the same frequency band.

Curve *1* in Fig. 1b shows the decay law for the intensity component of the received signal emitted by the source that is located in the deep-water part of the waveguide, at a distance of 160 km from the array. The calculation is carried out for the 60-m depth of the propagation path. In Fig. 1b, curve *2* represents the level of the quantity $|W\Delta f P_m P_n^*|$ (in dB) corresponding to $m = 2$, $n = 3$; this level is presented as a function of the distance from the source. Level *2* is higher than level *1*, because it corresponds to the sound power flux for the modes, and, with orthonormalized modes, $|\Phi_m(z)| \ll 1$ for all m; hence, the sound field intensity at the depth z is always lower than the power flux in the waveguide.

Figure 1b shows that, in both cases, the level of the desired signal is much lower than that of the interfering noise at the reception point. The first and second water modes that have the numbers 2 and 3 are chosen as reference ones (mode No. 1 corresponds to the flexural wave in the ice cover).

Figure 2 presents the deterministic component of the correlation envelope for the signal at the array output, for $m = n = 2$ and $m = 2$, $n = 3$ (Figs. 2a, 2b). The delay (in seconds) is shown along the abscissa axis. The ordinate corresponds to the absolute level (on the linear scale) for the nonnormalized time correlation function of the total signal consisting of both the desired signal and noise (character *1*); character *2* labels the correlation of the desired signal, and character *3* (the dashed line) indicates the level of the fluctuating interfering noise at the output of the integrating device. For $m = n$, the desired signal is lower than the ambient noise transmitted through the mode filter but higher than the fluctuating interfering noise. For $m \neq n$, the suppression of the intermode time correlation of the interference leads to a well-distinguished desired signal at the output of the processing channel (Fig. 2b). Thus, the proposed processing method yields a maximum range of 160 km for the detection of a weak signal, which has a pressure level of about 0.3 Pa/Hz at 1 m from the source, on the background of noise, which has a nearly maximum level typical of the Arctic Sea. Note that this range does not exceed 60 km, if the common processing technique [11, 17, 18] is applied to the signal received by the array.

We mean that the "common" technique consists in the following procedure. The signal is received by equally sensitive hydrophones that are equipped with the array compensator rotating the directivity pattern. From the compensator, the signal is entered to the processing channel that consists of a quadratic detector and an integrator. The maximum noise immunity of such an array is equal to the number of hydrophones in the array [11, 17]. However, this is true when the sound

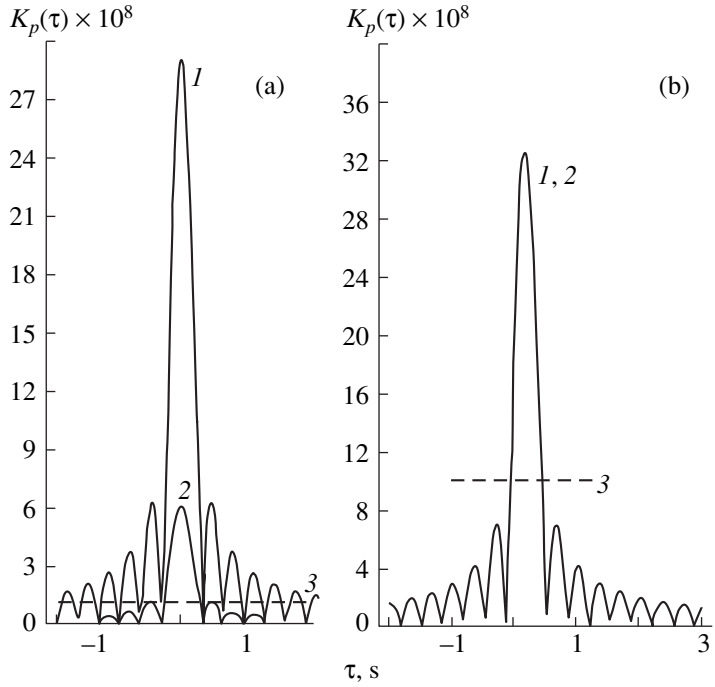

Fig. 2. Time correlation functions for (*1*) the signal plus noise and (*2*) the signal alone; (*3*) the mean level of the fluctuating component at the output of the processing channel. The distance is r = 160 km; (a) $m = n = 2$; (b) $m = 2$, $n = 3$.

field of the desired signal has a plane front (i.e., the signal phase and amplitude are constant over the array aperture). In the waveguide, this condition can be met only for high sound frequencies, single-ray propagation, and small arrays. For the case at hand, the amplitude and phase can be constant only at horizontal hydrophone chains. In vertical, the sound field is formed by a sum of modes whose eigenfunctions are depth-dependent in both their magnitudes and signs. Thus, the vertical chains contribute nearly nothing to the array noise immunity. The maximum detection distance corresponds to the array signal-to-noise ratio higher than 6 dB. In our case, the signal-to-noise ratio (for the signal and noise powers) is equal to 7 dB at the array output (see Fig. 2a), and the desired signal predominates in the deterministic response.

A significant advantage of the proposed processing method consists in that the horizontal directivity pattern of the array is not broadened, and even the main pattern lobe is not split [4, 11] in the presence of the multi-mode signal. The reason is that each mode is compensated with the use of its own wave number rather than with the use of a single one for all modes. Note that all curves in Figs. 2–4 are obtained for the array compensated in the direction of the signal arrival (reception from the maximum of the directivity pattern). In practice, the source bearing can be found by rotating the directivity pattern with the compensator until the maximum array response is achieved. Hence, the accuracy of the obtained bearing depends on the sharpness of the directivity pattern [11]. In addition, horizontal refraction should be taken into account for the waves propagating in an inhomogeneous waveguide. For this purpose, the distance from the source should be estimated, for instance, by measuring the shift in the correlation maximum on the delay axis [20] (see Fig. 2b).

Figure 3 illustrates the calculations for the 260-km range (with the same notation as in Fig. 2). The envelope of the correlation function evidences that, at $m \neq n$, the response is still governed by the desired signal, although the envelope level is lower than that of the fluctuating interference: the signal cannot be detected.

In Fig. 4, the deterministic signal component (at the output of the processing channel) is shown versus the delay, the distance being equal to 360 km. At this distance, the signal-to-noise ratio is so small that, for $m = 2$, $n = 3$, the correlation function of the desired signal is entirely overridden by the remaining intermode correlation of the interference. In such a situation, no averaging over realizations will result in a reliable signal detection. Probably, one can use modes of higher numbers, which more widely differ in their arrival times. In the latter case, the responses of the signal and the interference will be resolved in their delays, and, in theory, the signal will be detectable. However, the fluctuating interfering noise will remain, and unreasonably long averaging time T will be required to suppress it.

In conclusion, let us summarize the new items of the proposed approach.

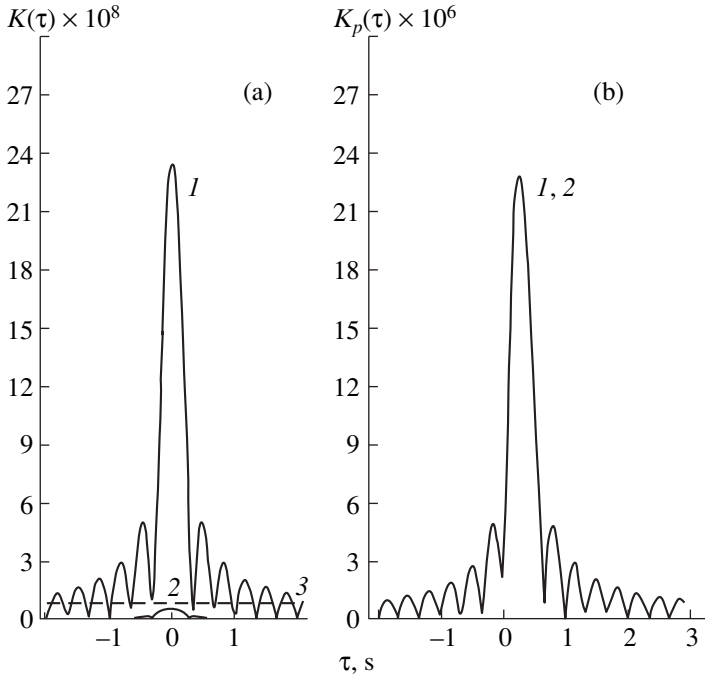

Fig. 3. Same as in Fig. 2 for the distance 260 km.

1. The range of the signal detection is sharply increased: by a factor of three in our case.

2. The directivity pattern is not split because of the multimode propagation, which provides a more accurate estimate of the source bearing.

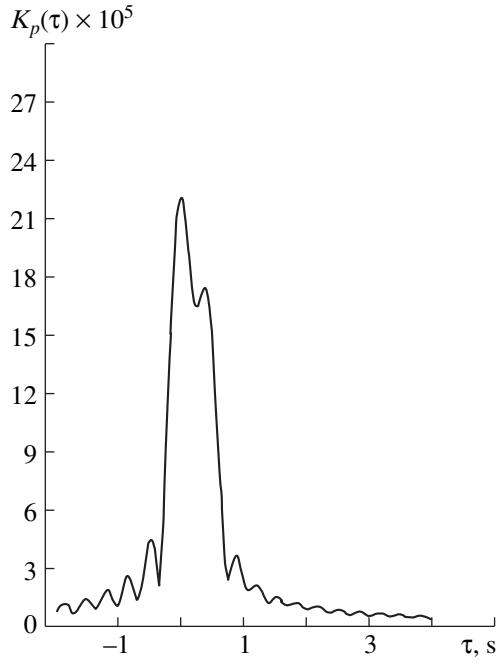

Fig. 4. Intermode time correlation function for the mix of signal and interfering noise; $m = 2$, $n = 3$; the distance is $r =$ 360 km.

3. The statistical independence of the noise components at the correlator input is achieved with a single array. For multiplicative arrays, such independence is known [11] to be attained by the signal reception on different arrays (each one for each correlator) whose spacing is greater than the spatial correlation scale of noise.

ACKNOWLEDGMENTS

This work was supported by the Russian Foundation for Basic Research, project No. 99-02-18359.

REFERENCES

1. V. M. Kudryashov, Akust. Zh. **42**, 247 (1996) [Acoust. Phys. **42**, 215 (1996)].
2. V. M. Kudryashov, Akust. Zh. **42**, 438 (1996) [Acoust. Phys. **42**, 386 (1996)].
3. F. I. Kryazhev and V. M. Kudryashov, Akust. Zh. **43**, 203 (1997) [Acoust. Phys. **43**, 172 (1997)].
4. F. I. Kryazhev and V. M. Kudryashov, Akust. Zh. **30**, 790 (1984) [Sov. Phys. Acoust. **30**, 469 (1984)].
5. V. M. Kudryashov, in *Proceedings of the 5th Seminar "Acoustic Statistical Ocean Models," 1985* (Moscow, 1985), pp. 19–24.
6. V. M. Kudryashov, in *Proceedings of the All-Russian Conference on Information Acoustics, 1987* (Moscow, 1987), pp. 18–21.
7. E. Yu. Gorodetskaya, A. I. Malekhanov, A. G. Sazontov, and V. A. Farfel', Akust. Zh. **42**, 615 (1996) [Acoust. Phys. **42**, 543 (1996)].

8. V. M. Kudryashov, Akust. Zh. **45**, 363 (1999) [Acoust. Phys. **45**, 320 (1999)].
9. P. N. Mikhalevsky, A. N. Gavrilov, and A. B. Baggeroer, IEEE J. Ocean Eng. **24**, 183 (1999).
10. A. M. Rao and D. L. Jones, in *Proceedings of International Conference on Acoustics, Speech, and Signal Processing, Seattle, 1998*, Vol. 4, pp. 1989–1992.
11. G. S. Gabidulin, A. M. Tyurin, and V. I. Nesterenko, *Antenna Devices of Hydroacoustic Means and Their Elements* (Leningrad, 1982).
12. A. M. Tyurin, *Introduction to the Theory of Statistical Methods in Hydroacoustics* (Leningrad, 1963).
13. V. M. Kudryashov, Akust. Zh. **33**, 55 (1987) [Sov. Phys. Acoust. **33**, 32 (1987)].
14. V. M. Kudryashov, Akust. Zh. **34**, 117 (1988) [Sov. Phys. Acoust. **34**, 63 (1988)].
15. S. D. Pankova and Yu. I. Tuzhilkin, Akust. Zh. **45**, 388 (1999) [Acoust. Phys. **45**, 343 (1999)].
16. A. N. Gavrilov, Akust. Zh. **34**, 1010 (1988) [Sov. Phys. Acoust. **34**, 579 (1988)].
17. A. P. Evtyukhov and V. B. Mit'ko, *Engineering Calculations in Hydroacoustics* (Sudostroenie, Leningrad, 1988).
18. *Handbook of Hydroacoustics*, Ed. by A. E. Kolesnikov (Sudostroenie, Leningrad).
19. V. M. Kudryashov, Akust. Zh. **44**, 391 (1998) [Acoust. Phys. **44**, 332 (1998)].
20. V. M. Kudryashov, Akust. Zh. **44**, 486 (1998) [Acoust. Phys. **44**, 415 (1998)].
21. P. N. Mikhalevsky, A. B. Baggeroer, A. Gavrilov, and M. Slavinsky, EOS Trans. Am. Geophys. Union **76** (27), 265 (1995); **76** (27), 268 (1995).
22. A. K. Morozov, Akust. Zh. **42**, 829 (1996) [Acoust. Phys. **42**, 733 (1996)].
23. V. M. Kudryashov, Akust. Zh. **45**, 529 (1999) [Acoust. Phys. **45**, 472 (1999)].

Translated by E. Kopyl

Acoustical Physics, Vol. 46, No. 5, 2000, pp. 588–595. Translated from Akusticheskiĭ Zhurnal, Vol. 46, No. 5, 2000, pp. 671–679.

Determination of the Temporal Stability Intervals for the Parameters of a Hydroacoustic Channel

A. V. Kulakov and R. Yu. Popov

Andreev Acoustics Institute, Russian Academy of Sciences, ul. Shvernika 4, Moscow, 117036 Russia

e-mail: bvp@akin.ru

Received September 24, 1999

Abstract—The temporal variability of the parameters of an oceanic waveguide extending for ~300 km near the eastern coast of the Kamchatka peninsula is investigated. Signals with linear frequency modulation in the frequency band 600–800 Hz are used. Relative contributions of various processes that occur in the oceanic medium are analyzed. The effect of the transmitting ship drift is estimated. Estimates are obtained for the lower bounds of the stability intervals of the waveguide parameters. The main contribution to the temporal variability of the propagation conditions is presumably determined by the internal wave dynamics. The possibility of adapting the reception to the sound channel characteristics is considered. *© 2000 MAIK "Nauka/Interperiodica".*

As a rule, the fundamental problem of ocean investigations by acoustical methods is related to the necessity of detecting weak signals against the interference background. To overcome this difficulty, one needs to employ various methods, and one of the most efficient among them consists in temporal accumulation of information. Such an accumulation is especially efficient within the period when the propagation conditions remain invariable. In this connection, it is very important to know the intervals of the temporal correlation of the sound field in various conditions.

Receiving arrays with large apertures are usually deployed in the coastal regions of the ocean, where a large part of signals propagating over separate rays undergo bottom-surface reflections. This fact reduces the spatial correlation of the sound field in the region of reception, and, therefore, the question about the time intervals within which the coherent accumulation of information is possible is very topical. This paper is devoted to the study of the temporal variability of the parameters of an inhomogeneous oceanic waveguide in a coastal region of the Pacific Ocean, off the eastern coast of the Kamchatka peninsula. Note that stationary tracks are necessary for correct measurements of the temporal variability of sound propagation conditions in the oceanic waveguide. However, in the experiment described, the end points of the track were located at a large sea depth (up to 5.5 km), so that the transmitting ship drifted, which made it possible to estimate the space-time variability of the hydroacoustic channel parameters. At the same time, the speed and direction of the drift were monitored with the use of a satellite navigation system. Therefore, the drift effect can be estimated by calculations. Below, we will show that, in our measurements of the stability intervals, the dynamics of the medium plays a dominant role and, therefore, we can estimate the temporal intervals of the channel variability (at least, their lower bounds) with a considerable degree of confidence. It should be noted that the problem of temporal variability of propagation conditions was considered in many publications (see, e.g., [1–3]). We note one of the recent papers [4], the authors of which investigated the sound propagation in the 0.3- to 7.5-kHz frequency band along a 16-km stationary track in a shallow-water region of the Mediterranean Sea. At the lowest frequencies of this range, the stability interval was no less than 36 hours. However, investigations on deep-water tracks including a coastal wedge are few in number. In 1995, Popov and Semenov [5] showed that, in the propagation of sound signals in the 30- to 50-Hz frequency range along a 100-km track and their reception in a shelf zone of the Kamchatka peninsula, the temporal stability interval exceeded 45 min. That study presented in this paper is actually a continuation of the measurements described in [5]. However, we used higher frequencies (600–800 Hz), and the distance to the source reached 300 km.

In addition, this paper analyzes the feasibility and efficiency of adaptation of reception to the sound channel parameters within their stability interval.

Now we describe the experiment. Figure 1 shows the test region and the acoustic track, as well as the vertical sound velocity profile at some points along the track. The signals were received by two hydrophones (points *1* and *2* in Fig. 1), one of which was lowered to a depth of 74 m from aboard the research vessel anchored at a sea depth of 130 m; the second hydrophone lay on the bottom near the 300-m isobath and was separated by a distance of 17 km from the first hydrophone. A signal from the bottom hydrophone was transmitted through the radio buoy to the board of the

1063-7710/00/4605-0588$20.00 © 2000 MAIK "Nauka/Interperiodica"

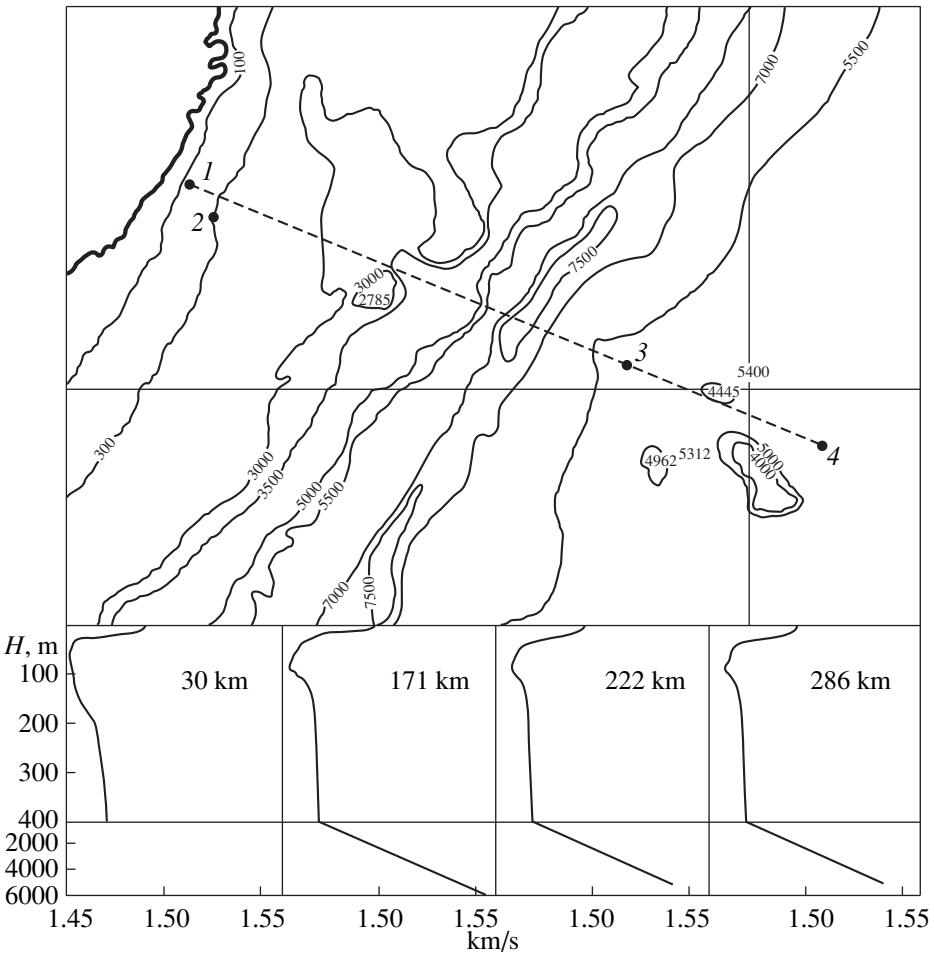

Fig. 1. Test region, acoustic track, and vertical sound velocity profile at several points of the track. Points *1* and *2* mark the hydrophone positions; points *3* and *4* mark the positions of the drifting transmitting ship.

same ship. The ship transmitting the signals (at a depth of 100 m) drifted near points *3* and *4* at distances of ~ 215 and ~ 305 km from the receiving ship. As sounding transmissions, trains of pulses with linear frequency modulation (the LFM-signals) and the frequency deviation in the range 600–800 Hz were used. The first train of total duration ~ 30 min was formed by pulses of duration 1 s with interval of 3 s between them, and a second train of the same duration was formed by 10-s pulses with 3-s intervals. The temporal interval between the trains was 10 min.

During the experiment, the drift speed of the transmitting ship varied within 0.5–1.7 knots, and its projection on the direction of the sound signal propagation was within 0.1–1.0 knots. The ocean surface roughness was Beaufort 3–4.

The received signals were entered into a computer for processing. First of all, we calculated the correlation coefficient $R(\tau)$ between the reference (transmitted) signal and those received by one of the hydrophones. Figure 2 exhibits the plots of the envelope $R(\tau)$ for the first train when the source was at a distance of about 215 km from the hydrophone lowered in water. It is known that, for a sufficiently wide frequency band of the signal, the function $R(\tau)$ allows one to estimate the waveguide response function. In our case, $\Delta f = 200$ Hz, and, therefore, we can resolve (at the level 0.7) signals whose difference in the arrival times over rays is more than 5 ms. Note that the function $R(\tau)$ has a multipeak form, the amplitude of each peak $R_i(\tau)$ being not too high (no greater than 0.3); the latter is easily explained by the normalization condition.

In Fig. 2, the curves $R(\tau)$ exhibit a certain similarity. As a quantitative measure of the variability of the function $R(\tau)$ and, therefore, the channel response function, we used, as in [5], the expression of the type

$$\psi(\tau) = \frac{1}{T\sigma_0\sigma_n}\int_0^T R_0(\tau_1)R_n(\tau_1 \pm \tau)d\tau_1,$$

where R_0 and R_n are the cross-correlation functions of the transmission with zeroth and nth received signals in the train, respectively; σ_0 and σ_n are the standard devi-

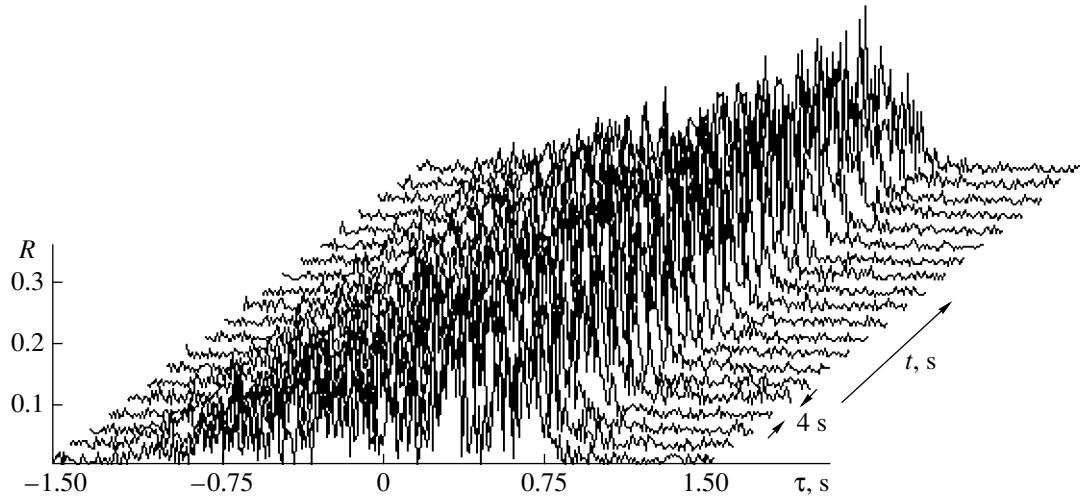

Fig. 2. Temporal variability of the envelope of the correlation function for the transmission and the received signals within the train. The pulse duration in the train is 1 s, and the period is 4 s. The signals are received by a hydrophone located at a depth of 74 m, at a distance of 215 km from the source; Δf = 600–800 Hz.

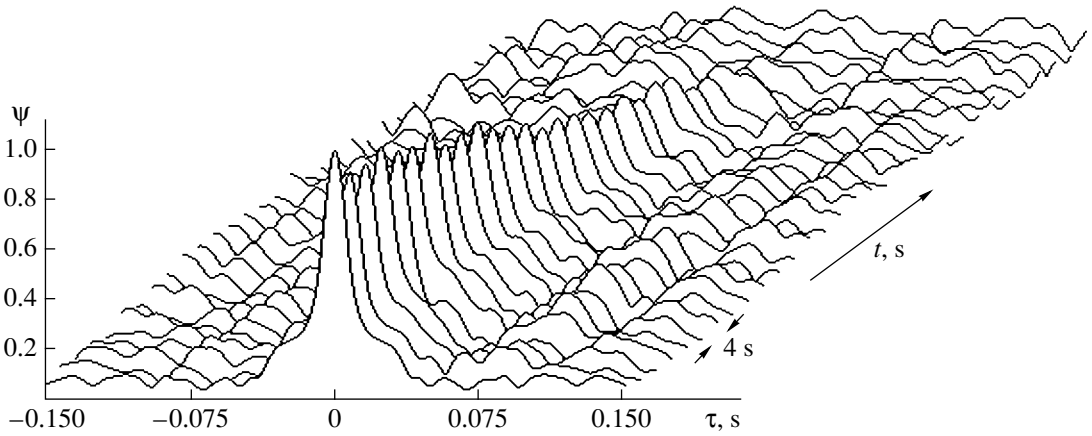

Fig. 3. Dependence of the function $\psi(\tau)$ on the time interval between the compared functions $R_0(\tau)$ and $R_n(\tau)$.

ations of R_0 and R_n; T is the averaging time equal to the signal duration at the points of reception.

Figure 3 presents the plots of the envelope of the function $\psi(\tau)$. If we define the stability interval of the channel response function T_{st} as the time T_e it takes for the function $\psi(\tau)$ to reach $1/e$ of its peak value (or as the time T_b it takes for the function $\psi(\tau)$ decay to the background level), then, from Fig. 3, it follows that $T_e \sim 60$ s ($T_b \sim 110$ s).

The duration of the trains allows one to measure the stability intervals for various reference functions $R_{0,i}(\tau)$, $i = 1, 2, \ldots, 10$. The table presents the values of T_e, T_b, T_e', and T_b' obtained for two trains, two hydrophones, two distances, and two methods of determination of the interval (from the decay of the functions $\psi(\tau)$ and $R_B(\tau)$, respectively; the definition of the function $R_B(\tau)$ is given below). The mean values of the stability interval and the standard deviation σ_{st} from the mean value were determined from ten measurements. The temporal stability interval of the hydroacoustic channel characteristics for the frequencies of 600–800 Hz was no less than several tens of seconds. The maximum value of the interval observed for T_b was ~ 120 s with a relatively large value of σ_{st} = 24 s, which is related to the fluctuations of the background level of the function $\psi(\tau)$. The value of T_e is less than that of T_b almost by a factor of two, and σ_{st} is less almost by a factor of five. Note that, for the bottom hydrophone, the stability interval is always less by 20–30%.

The latter fact is explained by the sound field characteristics at the points of reception: for the hydrophone lowered from aboard, the sound field is mainly formed by signals propagating over purely water rays, while, for the bottom hydrophone, by signals with a

Table

Distance, km	215				305			
Reception depth, m	74		300		74		300	
Pulse duration in the train,* s	1	10	1	10	1	10	1	10
T_b, s	79(14)	113(21)	48(33)	92(23)	97(10)	122(1)	55(19)	98(5)
T_e, s	59(8)	73(6)	23(16)	50(13)	65(6)	78(4)	31(13)	60(7)
T_b', s	73(18)	85(10)	22(17)	76(24)	77(24)	86(12)	45(20)	82(7)
T_e', s	26(7)	25(2)	7(0.2)	23(0.7)	26(9)	41(5)	7(0.1)	36(0.8)

* Numbers in parentheses are the values of σ_{st}.

reduced coherent component owing to the bottom-surface reflections.

The analysis of the data presented in the table shows that the stability interval tends to increase at a point located at a distance of 305 km from the receiving ship. For a reception depth of 74 m, the growth is small and falls within the accuracy of measurements. In the case of the reception by the bottom hydrophone, the interval increase is much more significant, a large scatter being observed in the values of intervals and σ_{st}. The reason of such a seemingly unusual behavior of the interval consists in that the entrance conditions for a multiray signal into a coastal wedge periodically vary with the distance *r*. The point is that the number of rays arriving at the point of reception and the range of the arrival angles periodically vary as *r* increases [1]. The field calculations testify that, for the bottom hydrophone, the angular range of signal arrivals over rays is narrower by 30% for the distance r = 305 km than for r = 215 km. This fact explains the somewhat greater values of the stability intervals. For the hydrophone at a depth of 74 m, the considerable part of the acoustic energy arrives over purely water rays, and, for this reason, T_{st} changes with distance much less than in the case of the bottom hydrophone.

The duration of pulses, T_p, in the trains also affects the stability estimates. For example, for the hydrophone at a depth of 74 m, a tenfold increase in T_p (with the corresponding increase in the averaging time in calculating the correlation function) leads to an increase in T_e, T_b and T_e', T_b' by 16% and 40%, respectively. in the case of the reception by the bottom hydrophone, T_{st} increases with T_p to a much greater extent (by up to 300%) with an accompanying considerable scatter of data. As the distance r increases up to 305 km, the growth of T_{st} with T_p slows down.

Note that the comparison of the estimates of T_{st} from the decay of the functions $\psi(\tau)$ and $R_B(\tau)$ allows one to reveal to some extent the form of the decay curves. The difference in the estimates of T_e' and T_b' is usually considerable because of the decrease in the signal-to-noise ratio (see below).

Before proceeding to the analysis of the relative influence of various processes in the ocean on the variability of the waveguide parameters, we consider the possibility of adapting the reception algorithm to the sound propagation conditions in the ocean, i.e., the possibility to take into account the waveguide characteristics in the signal reception. Note that this problem had been considered earlier [6–8].

A waveguide is usually characterized by the impulse characteristic (the response function) $h(t)$ in the time domain and by the transfer function $H(\omega)$ in the frequency domain. If $f(t)$ is the radiated signal and $F(j\omega)$ is its spectrum, the signal at the waveguide outlet can be written as the signal convolution with the response function $h(t)$:

$$s(t) = \int_{-\infty}^{\infty} h(\tau) f(t-\tau) d\tau$$

in the time domain, or as the product of the waveguide transfer function and the transmission spectrum

$$S(j\omega) = H(j\omega)F(j\omega)$$

in the frequency domain.

It is more convenient to perform the consideration in the frequency domain. Our aim is to use such a filtering of the received signal that will minimize the distorting waveguide effect on the signal spectrum. It is easy to verify that, if for the reception we use a filter with the characteristic

$$B(j\omega) = H^*(j\omega)/|H(j\omega)|^2$$

(the sign * means the complex conjugated quantity), then, at the filter outlet we obtain the spectrum of the initial signal.

Figure 4 presents the envelopes of the correlation function of radiated and received signals (a) without filtering and (b) after filtering with the characteristic $B(j\omega)$. The result of such an adaptation to the waveguide

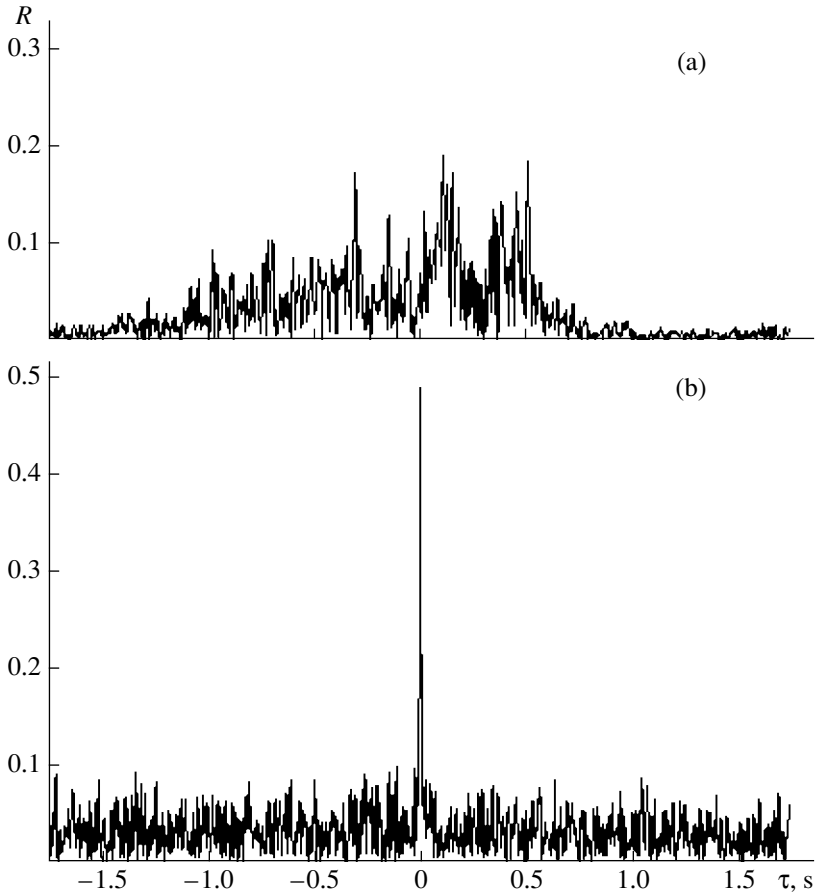

Fig. 4. Envelope of the correlation function between the radiated and received signals: (a) without filtering and (b) after a filter with the characteristic $B(j\omega)$.

parameters is clearly visible: after filtering, a multitude of small peaks of the function $R(\tau)$ are assembled into one large peak (its amplitude increases by a factor of 2.5). The reduction of the signal-to-noise ratio after filtering, which is observed in Fig. 4, is caused by the fact that, in the expression for $B(j\omega)$, we did not take into account the noise interference that is no more correlated for the adjacent pulses in the train. In Fig. 4b, the plot was obtained by filtering a pulse next to the reference pulse. The characteristic of the filter $B(j\omega)$ changes with time and with the variation in the source's coordinates. Here, we will analyze the temporal variability, although the effect of the drift and rolling of the ship should be always taken into account. Bogunets *et al.* [9] have shown that, for surface roughness Beaufort 3–4, one can ignore the vertical displacements of the transmitter loosely suspended from the board of a drifting large-capacity ship; of course, one needs to estimate the degree of the drift-caused changes in the angular-temporal structure of the field.

The plot in Fig. 5 shows the behavior of the envelope of the cross-correlation function of the reference signal and the sequence of received signals in the train after filtering $R_B(\tau)$, the filter characteristic being formed by the first received signal in the train. The correlation function, $R_B^n(\tau)$, i.e., the correlation of the reference signal and the nth signal in the train after filtering, is determined by the expression

$$R_B^n(\tau) = \frac{1}{2\pi T}\int_0^T f(t-\tau)\int_{-\infty}^{\infty} F(j\omega)H_n(j\omega) \times B(j\omega)e^{j\omega t}d\omega dt.$$

It is clear that the estimates of the typical time of the filter characteristic variations must give almost the same result as the estimates of the stability of sound propagation conditions with the use of the function $\psi(\tau)$. However, some differences must be revealed in these estimates, because the filter characteristic did not take into account the influence of the uncorrelated interference. The estimates of T_{st} obtained from the extent of the filtering efficiency reduction are presented in the table.

Let us now discuss the factors affecting the estimates of the stability of sound propagation conditions and find an answer to the question of how valid is our statement that, during the experiment, we measure

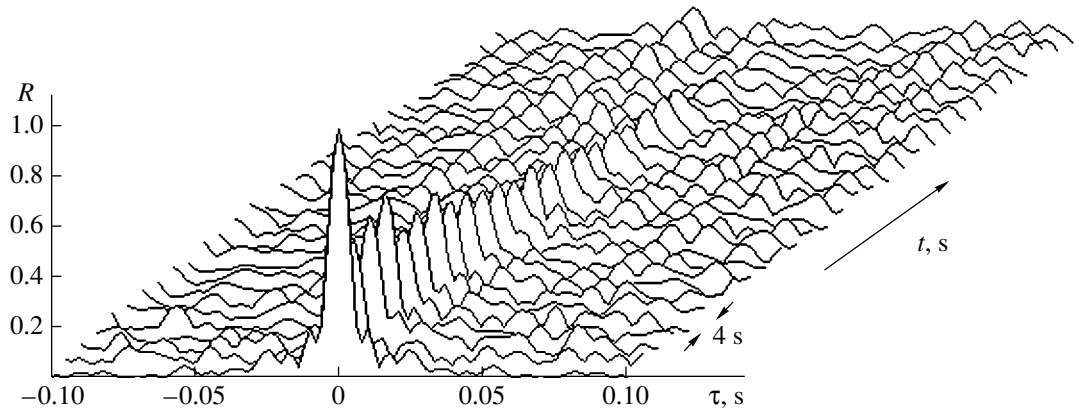

Fig. 5. Temporal variability of the envelope of the correlation function $R_B(\tau)$ for the transmission and the received signals in the train after filtering with the characteristic $B(j\omega)$.

mainly the temporal variability of the waveguide parameters in spite of the drift of the transmitting ship. To this end, we calculated the variability of the angular and temporal structure of the field that occurred at the point of reception due to the ship drift, whose speed and direction were determined by a satellite navigation system. Of course, such a system provided exact parameters of the drift only at the time when the satellite was above the test region, which happened usually once in an hour (sometimes, more rarely). For this reason, linear interpolation of the data was performed in the intervals between the exact determinations. In such an approximation, the drift speed component along the test track did not exceed 1 knot within the period of measurements. Thus, within the 120-s stability interval, the track length increased by 60 m. The effect of such a track extension on the waveguide parameters was calculated for the hydrophone located at point *1* at a depth of 74 m and the source located at a distance of 215 km away and drifting at point *3* (see Fig. 1). In the calculations, the step in distance was chosen to be 10 m, which allowed one to analyze in detail the drift effect. If we take into account only the rays whose focusing factor is equal to or greater than unity, then, as the distance increases by 60 m, only 10–15% of signals propagating over these rays change their arrival times (relative to the first arrival) by up to 0.5 ms, i.e., by less than a half of the current frequency period (for the mean frequency 700 Hz, the pulse period equals 1.4 ms). For the rest of the signals, the changes in the propagation time are even less. Thus, our calculations show that the drift effect is insufficient to account for the measured values of the stability interval of the sound propagation conditions along the track. The variability of the waveguide parameters is mainly related to the dynamics of the oceanic medium, and we can conclude that the estimates obtained characterize the temporal stability interval.

Analyze now the possible effect of factors leading to the temporal variability of the waveguide characteristics. We begin with the inclusion of relatively small-scale random inhomogeneities of the sea medium. This problem was considered by many authors; we will follow Chernov's study [10] and use the known expression for the upper bound of the rms phase fluctuation of a tone signal transmitted through the distance r in a statistically inhomogeneous medium:

$$A = \left|\sqrt{\sigma^2}\right| = \left[\frac{\sqrt{\pi}}{2} a\mu^2 k_0^2 r\right]^{1/2},$$

where a is the mean size of random inhomogeneities, μ^2 is the mean square of the refractive index fluctuations, and k_0 is the sound wave number.

Because of the vertical refraction, the signals usually propagate from the source to hydrophones in both the upper and the deep-water layers of the ocean. Therefore, the size of the inhomogeneities can vary from 1 to 100 m. However, in the case considered, the launch angles of most energy rays received by the hydrophone at a depth of 74 m are less than 4°, and, therefore, the signals propagate over these rays in the water layer of thickness not exceeding ~200 m where the size of the inhomogeneities is 30–40 m. Therefore, we can deem that the mean size of inhomogeneities for an equivalent statistically homogeneous (isotropic) medium is $a \approx 20$ m [11]. Setting $\mu^2 \approx 5 \times 10^{-9}$ [12], r = 215 km, and k = 3.35 1/m (we used the wave number for the upper frequency 800 Hz, when the effect of the inhomogeneities is maximum), we obtain A = 0.46. For such a value of A, the reduction of the mean value of the correlation coefficient of the received signal with the transmission is no greater than 20%, because

$$R = \exp(-A^2) = 0.81.$$

Therefore, the inclusion of only the statistical inhomogeneities in our consideration would lead to a rapid decrease in the values of R, as well as to distortions in the filter's characteristic $B(j\omega)$. However, with further time increase, the peak values of $\psi(\tau)$ and $R_B(\tau)$ would not change. The behavior of the curves in Fig. 3 and

Fig. 5 differs from that predicted above, which testifies that one has to take into account other factors in addition to the statistical inhomogeneities.

We now analyze the effect of internal waves and concentrate our attention on the signals that arrive over the rays with launch angles in the range from ±1.0° to ±4.0°. These signals suffer no reflections from the water layer boundaries before reaching the hydrophone. The variability of the waveguide properties caused by the internal waves can be described for these signals by such parameters as Λ and Φ [13]. The diffraction parameter Λ characterizes the influence of the spatial scale of inhomogeneities on the diffraction effects; the parameter of the medium inhomogeneity Φ in the domain of validity of the geometric approximation, where $\Lambda \ll 1$, characterizes the rms phase fluctuation of a signal arriving at the point of reception over the ray under consideration. The approximate estimates of the internal wave influence on the propagating signal parameters can be obtained with the use of the Garrett-Munk spectrum and the canonical sound velocity profile [13]. In the monograph [13], the following expressions are obtained to describe the parameters Λ and Φ:

$$\Lambda = \frac{12}{\pi^3} 2D_0 [6k_0 R_\nu^2(z)]^{-1},$$

$$\Phi^2 = k_0^2 r R_p(0) \langle \Delta c_n \rangle^2$$

for a rectilinear ray; for signals propagating over steep rays near an upper turning point [13] (it is assumed that the region near the upper turning point makes the main contribution to the variability of the waveguide parameters), we obtain

$$\Lambda = 0.023 \frac{r}{[6k_0 R_\nu^2(z_a)]^{1/2}},$$

$$\Phi^2 = c(\chi_0) \langle \Delta c_n^2 \rangle R_s(0) k_0^2 r.$$

In these expressions, R_ν and R_s are the vertical and spatial (along the ray) correlation intervals of signal fluctuations, which were obtained in [13] by numerical integration; $D_0 = 41.6$ km is the cycle length of the axial ray; $\langle \Delta c_n^2 \rangle = 2.5 \times 10^{-7}$ is the rms sound velocity fluctuation near the ocean surface; $c(\chi_0)$ is the coefficient dependent on the angle χ_0 at which the ray crosses the channel axis: and z_a is the vertical coordinate of the upper turning point. For the case considered, we set r = 215 km, k_0 = 3.35 1/m, $R_\nu \approx 0.1$ km, $R_s \approx 12.7$ km, $c(\chi_0) \approx 0.034$ (for $\chi_0 = 4°$–$5°$), and $z_a \sim 15$ m. Substituting these values in the above expressions, we obtain

$$\Lambda = 0.08, \Phi = 86$$

for the horizontal ray and

$$\Lambda = 0.02, \Phi = 16$$

for the steep ray ($\chi_0 = 4°$).

Thus, for any rays, $\Lambda \ll 1$; i.e., the geometric approximation is valid, and, therefore, Φ characterizes the signal phase fluctuations. In this case, the temporal correlation interval, in hours, equals $1/\Phi$ [13]. The above-mentioned calculations of the sound field at the point of reception showed that there is no rectilinear ray (since the source and the receiver are located at different depths), and no less than 70% of the sound energy arrives over purely water rays with the arrival angles from ±1.5° to ±3.0°. The rest of the sound energy propagates over rays that undergo the bottom and bottom-surface reflections (up to 10 bottom reflections and 6 surface reflections) with the arrival angles from ±3° to ±17°. If one assumes that the values of Φ for a rectilinear ray and a ray launched at an angle of 1.5° not widely differ from each other, then, Φ varies in the range ~ 80–18 for purely water rays, and, therefore, the temporal correlation interval T_{st} is within 42–200 s. The measured values of T_{st} lie within the same limits (see table).

Consider now ~30% of the sound energy propagating over rays that undergo bottom-surface reflection. Although sea roughness was not too large (for the case considered, no more than Beaufort 4–5), multiple signal reflections from the sea surface significantly increase the scattered component. The propagation conditions for the specular component of the signal will be almost time-independent. However, reflections from different sites of the sloping bottom with an unknown microrelief can considerably alter the ray path and, hence, the signal arrival time over this ray. The reflection sites may vary due to both the effect of the internal waves and the drift and rolling of the transmitting ship.

Thus, we have to conclude that the motion of the source in our experiment weakly affects the variability of the part of the field that is formed by signals arriving over purely water rays, and, therefore, this effect can be ignored. However, for ~30% of the sound energy, such a motion may change the conditions of the signal entrance to the coastal wedge, and the estimates of the temporal variability of the conditions of sound propagation over such rays can be noticeably distorted. The estimates of the stability intervals for the bottom hydrophone, when almost all signals arriving over rays undergo the bottom-surface reflections, decrease only by 20–30%. Therefore, the influence of the source drift on the results obtained should not be overestimated.

Summarize now the results obtained.

(i) The temporal stability intervals of the characteristics of a hydroacoustic channel, which extends for ~300 km in the region near the eastern coast of the Kamchatka peninsula and includes the coastal wedge, are tens of seconds (no more than 120 s) for frequencies of 600–800 Hz in the summer-autumn season. In the experiment, the quasi-stationary track was used (the transmitting ship freely drifted). The effect of the drift was found to be insignificant, which allows one to esti-

mate the temporal variability of the channel characteristics.

(ii) The dynamics of internal waves in the oceanic medium provides the main contribution to the temporal variability of the sound propagation conditions in the sound channel.

(iii) The use of adaptive algorithms for hydroacoustic data processing, which take into account the channel characteristics within the interval of their temporal stability, provides an appreciable effect; the peak value of the cross-correlation function of the received signal and the transmission increases by a factor of 2.5.

ACKNOWLEDGMENTS

We are grateful to O.P. Galkin for assistance in the sound field calculations in a coastal wedge and to O.P. Galkin and Yu.I. Tuzhilkin for valuable advices in discussing the results.

REFERENCES

1. J. Lynch, Y. Jin, R. Pawlovicz, *et al.*, J. Acoust. Soc. Am. **99**, 803 (1996).
2. D. Tielbürger, S. Finette, and S. Wolf, J. Acoust. Soc. Am. **101**, 789 (1997).
3. V. R. D'yachenko and Yu. I. Tuzhilkin, Akust. Zh. **42**, 202 (1996) [Acoust. Phys. **42**, 176 (1996)].
4. P. Nielsen, Bini-Verona, and F. Jensen, in *Proceedings of the Fourth European Conference on Underwater Acoustics, Rome, 1998*, p. 631.
5. R. Yu. Popov and Yu. V. Semenov, Akust. Zh. **41**, 644 (1995) [Acoust. Phys. **41**, 567 (1995)].
6. A. Parvulescu and C. Clay, Radio Electron. Eng. **29**, 223 (1965).
7. R. Yu. Popov and S. D. Chuprov, in *Acoustic Waves in the Ocean* (Nauka, Moscow, 1987), pp. 92–100.
8. V. M. Baronkin, M. V. Zheleznyakov, and R. Yu. Popov, in *Acoustics in the Ocean* (Nauka, Moscow, 1992), pp. 127–135.
9. S. V. Bogunets, O. P. Galkin, R. Yu. Popov, *et al.*, Akust. Zh. **46**, 170 (2000) [Acoust. Phys. **46**, 133 (2000)].
10. L. A. Chernov, *Wave Propagation in a Medium with Random Inhomogeneities* (Akad. Nauk SSSR, Moscow, 1958).
11. N. G. Kuznetsova, Vopr. Sudostroeniya, Ser. Akust., No. 11, 89 (1978).
12. R. F. Shvachko, in *Ocean Acoustics*, Ed. by L. M. Brekhovskikh (Nauka, Moscow, 1974).
13. *Sound Transmission through a Fluctuating Ocean*, Ed. by S. Flatte (Cambridge Univ. Press, Cambridge, 1979; Mir, Moscow, 1982).

Translated by Yu. Lysanov

Acoustical Physics, Vol. 46, No. 5, 2000, pp. 596–600. Translated from Akusticheskiĭ Zhurnal, Vol. 46, No. 5, 2000, pp. 680–684.

Waveguide Propagation of Sound Beams in a Nonlinear Medium

Yu. N. Makov

Moscow State University, Vorob'evy gory, Moscow, 119899 Russia

e-mail: makov@acs364.phys.msu.su

Received December 17, 1999

Abstract—A possibility of a waveguide propagation of sound beams in the case of compensation of the diffraction divergence by the nonlinear refraction is demonstrated theoretically. A stationary (with respect to the longitudinal coordinate) solution is obtained to the nonlinear equation for a sound beam (the Khokhlov–Zabolotskaya equation); the solution describes the characteristic bow-shaped profile of the beam and the self-localized (with respect to the transverse coordinate) distribution of the peak values of this profile. The physical and mathematical features of this phenomenon belonging to nonlinear acoustics are discussed and compared with those of the well-known analog from nonlinear optics. A scheme of an experimental realization of the waveguide propagation of acoustic beams is proposed. © *2000 MAIK "Nauka/Interperiodica".*

At the initial stage of the investigation of nonlinear phenomena in optics and plasma physics, a theoretical substantiation of the possibility of waveguide (or self-localized with respect to transverse coordinates) propagation of wave beams in the corresponding nonlinear optical or plasma media was given [1, 2]. Later, this phenomenon was observed experimentally [3]. Now, interest in the various specific schemes of the manifestation of this effect in optics continues to grow [4–6].

The possibility of mutual compensation of two factors, namely, the diffraction divergence and the nonlinear refraction, which are also characteristic for nonlinear acoustics of sound beams [7], lies at the heart of the optical phenomenon of the waveguide propagation of beams. However, because of its specific features, which will be discussed below, the problem of the possibility of waveguide propagation of sound beams due to inertial (nonthermal) nonlinear effects has not acquired a clear formulation until now, and, correspondingly, no solution to such a problem has been given.

This paper demonstrates theoretically (in the absence of a direct analogy with the optical case) the possibility of waveguide propagation of acoustic beams in the case of inertial (nonthermal) manifestation of nonlinearity. Exact solutions describing the characteristic profiles of waves in a beam in this propagation conditions are determined, and a possible scheme of an experimental realization of this phenomenon in nonlinear acoustics is given.

The mathematical model developed for describing optical and other electromagnetic wave beams on the basis of the Schrödinger equation for the complex amplitude A,

$$2ik\frac{\partial A}{\partial z} = \Delta_\perp A + \frac{k^2\varepsilon_{nl}|A|^2}{\varepsilon_0}A \qquad (1)$$

(where $\varepsilon = \varepsilon_0 + \varepsilon_{nl}|A|^2$ is the dielectric permeability taking into account a nonlinear correction, k is the wave number, and $\Delta_\perp$ is the Laplacian with respect to transverse coordinates) provides an opportunity, firstly, to predict the presence or absence of the waveguide propagation effect, depending on the sign of ε_{nl} and, secondly, without any mathematical difficulties, to determine the solution to the corresponding stationary (with respect to z) differential equation in ordinary derivatives for axially symmetric and slit beams in the case $\varepsilon_{nl} > 0$, when mutual compensation of the diffraction and refraction terms on the right-hand side of Eq. (1) occurs.

The specific character of the mathematical model of wave beams in nonlinear acoustics (in comparison with Eq. (1)) is determined by two distinctive features. First, the absence of dispersion and the consequent avalanche-like broadening of the spectrum of the initial wave profile due to the nonlinearity impels one to determine the forming profile, which makes the determining acoustic equation more complex in comparison with Eq. (1) because of the introduction of a differential operator with respect to one more independent variable, i.e., time. Second, the nonlinearity characteristic of acoustics is the quadratic nonlinearity (in contrast to cubic nonlinearity in Eq. (1)). All this results in the parabolic approximation (without allowance for the dissipation loss) the so-called Khokhlov–Zabolotskaya equation [8] for describing acoustic beams with allow-

1063-7710/00/4605-0596$20.00

ance for the nonlinearity.[1] In terms of the dimensionless quantities, this equation has the form

$$\frac{\partial^2 V}{\partial z \partial \tau} = \frac{N}{4}\Delta_\perp V + \frac{\partial}{\partial \tau}\left(V\frac{\partial V}{\partial \tau}\right). \quad (2)$$

Here, $V = p/p_0$ ($p(x, y, z, \tau)$ and p_0 are the alternating acoustic pressure and its maximal value, respectively, $N = \frac{z_{sh}}{z_d} = \frac{(\rho_0 c_0^2)/(\varepsilon\omega p_0)}{\omega a^2/(2c_0)}$ is the Khokhlov parameter characterizing the ratio between the nonlinear and diffraction effects, z_{sh} is the length of shock formation, z_d is the diffraction length, c_0 is the equilibrium sound velocity, ε is the nonlinearity parameter of the medium, a^2 is the characteristic area of the beam cross-section, ω is the characteristic frequency, z is the longitudinal coordinate normalized to z_{sh} along the beam propagation, $\Delta_\perp$ is the Laplacian with respect to transverse coordinates normalized to a, and $\tau = \omega\left(t - \frac{z z_{sh}}{c_0}\right)$ is the dimensionless "delayed" time.

The structure of the nonlinear term in Eq. (2) does not provide an opportunity (in contrast to Eq. (1)) to predict the possibility of compensation of the diffraction divergence, which is described by the first term on the right-hand side of expression (2), by the nonlinear refraction. Therefore, the existence of the waveguide propagation conditions for the sound beams is determined by the existence of a physically substantiated solution to Eq. (2) in the case when it is stationary with respect to z, this case being determined precisely by the aforementioned compensation. At this point, a seeming paradox arises concerning the existence of such a solution. In fact, it is well known [7] that the avalanche-like broadening of the spectrum of the initial wave profile due to nonlinearity and the absence of dispersion leads to the formation of sawtooth waves with shock fronts, which have peak values decreasing in the course of the propagation along the z-axis because of nonlinear high-frequency damping. It would seem that this excludes solutions that are stationary with respect to z. However, a sawtooth wave is the only asymptotically universal type of a nonlinear wave in the plane (one-dimensional) case. As numerical calculations show [7, 11], in the case of a non-one-dimensional (beam) acoustics, the existence of another asymptotically universal type of wave profiles with strong nonlinear distortions (relative to a sinusoidal profile) but without singularities is possible. There is no nonlinear high-frequency damping for waves with such a profile, and, therefore, they represent a solution to Eq. (2), and this solution is stationary with respect to z. Such a solution can be possible on condition that $\frac{N}{4} \sim 1$ (more precise estimates for the parameter N are given below). It is also convenient to represent this condition in the form $\frac{N}{4} \equiv \frac{F_{cr}}{F_a} \sim 1$, where $F_{cr} = \frac{\beta\rho_0 c_0^4}{2\omega^2}$ is the value of the "critical" force, $F_a = \beta p_0 a^2$ is the averaged force of acoustic action of the wave upon the cross-sectional area of the beam a^2, β is the dimensionless coefficient determined by the pressure distribution over the cross-section of the beam and its variation in time. In the case of mutual compensation of the diffraction and nonlinear refraction, the ratio of the two indicated forces must be of the order of unity (an analogy with the relation between the critical power and the power of a beam in the optical case).

Let us consider the simplest (in geometry) problem on the propagation of a beam produced by an infinite slit. In this case, the version of Eq. (2) that is stationary with respect to z is a nonlinear partial differential equation

$$\frac{N}{4}\frac{\partial^2 V}{\partial y^2} + \frac{\partial}{\partial \tau}\left(V\frac{\partial V}{\partial \tau}\right) = 0. \quad (3)$$

It seems impossible to determine a general solution to this equation, and, therefore, one can expect to find only a suitable particular solution. The desired solution must be localized, symmetric with respect to the transverse coordinate, and have a profile that is continuous in time, which will make it fundamentally different from an ordinary solution to a one-dimensional problem of nonlinear acoustics in the form of a sawtooth wave.

Several particular solutions to Eq. (3) are given in the most complete handbook by Zaĭtsev and Polyanin [10], but they do not all satisfy the requirements formulated above. Therefore, the determination of new solutions to equation (3) has led us to the following version that is most suitable from the physical point of view:

$$V(\tau, y) = Y_2(y)(\tau - T)^2 - Y_0(y), \quad (4)$$

where T is an arbitrary constant, which we determine by the equality $T = 2\pi n$ ($n = 0, \pm 1, \pm 2, \ldots$) for obtaining a solution periodic in τ.

As follows from the substitution of expression (4) into Eq. (3), the functions $Y_2(y)$ and $Y_0(y)$ must be determined by the equations

$$Y_2'' + \frac{24}{N}Y_2^2 = 0, \quad (5)$$

$$Y_0'' + \frac{8}{N}Y_2 Y_0 = 0. \quad (6)$$

[1] This equation was obtained much earlier in aerodynamics of transonic flows by Lin, Reissner, and Tsiegn [9].

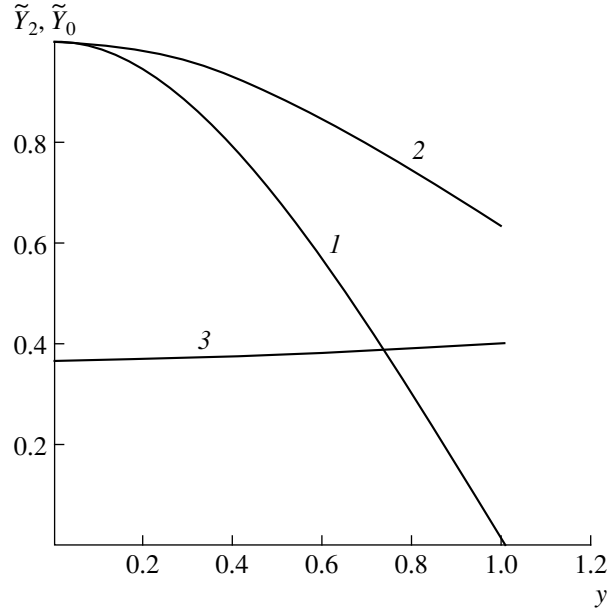

Fig. 1. Normalized functions $\tilde{Y}_2(y)$ (curve *1*) and $\tilde{Y}_0(y)$ (curve *2*) and the ratio $\dfrac{\tilde{Y}_0(y) - \tilde{Y}_0(1)}{\tilde{Y}_2(y)}$ (curve *3*).

Solution (4) has the form of periodically repeated in τ pieces of a parabola with the steepness of its branches varying along the y-coordinate (the steepness is determined by the values of the function $Y_2(y)$) and a vertical displacement of the whole parabola relative to the τ axis (the displacement is determined by the values of the function $Y_0(y)$). The functions $Y_2(y)$ and $Y_0(y)$ together indirectly determine the distribution of the peak values of the resulting bow-shaped wave along the y-axis. In addition, for the condition of the beam localization to be satisfied, these functions must decrease symmetrically with respect to $y = 0$ down to zero with increasing $|y|$, which determines the zero value of the amplitude of the bow-shaped wave at the beam boundary. The particular solution to Eq. (5) in the form

$$\pm y = \frac{1}{4}\sqrt{\frac{N}{Y_2^0}}\int_{\tilde{Y}_2}^{1}\frac{d\tilde{Y}_2}{\sqrt{1-\tilde{Y}_2^3}} \qquad (7)$$

satisfies these conditions for the function $Y_2(y)$, where $\tilde{Y}_2(y)$ is the desired function normalized to its maximal value Y_2^0, i.e., $\tilde{Y}_2(y) \equiv Y_2(y)/Y_2^0 \le 1$. This function is determined by relationship (7). We take this dependence into account on the interval $|y| \le y_0$, where the function $\tilde{Y}_2(y)$ decreases from 1 to 0. Outside this interval, we take the values of $\tilde{Y}_2(y)$ equal to zero (see Fig. 1). Such a modified solution (nonzero within the interval $|y| \le y_0$ and zero outside it) preserves the continuity of the function $\tilde{Y}_2(y)$ at the boundary points $\pm y_0$, and, therefore, by virtue of Eq. (5), it also preserves the continuity of the second derivative of this function, which is important for the consistency of the modified solution with initial equation (3) without appearance of uncompensated singular terms. We note that, since y has been initially normalized to the beam width, it is necessary to take $y_0 = 1$, and, according to the results of the numerical analysis of dependence (7), this relationship holds at $N/Y_2^0 \approx 8.14$.

The numerical analysis of the solution to Eq. (6) under the required conditions $Y_0'(0) = 0$, $Y_0'' < 0$ yields a dependence that is analogous to the solution to Eq. (5), but with a boundary value different from zero, namely, $Y_0(1) > 0$. (see Fig. 1). Let us modify this solution in order to eliminate the displacement of the parabolas in solution (4) at $y = \pm 1$ taking into account that the introduction of an additional phase (time) shift into the obtained wave field in the case of its possible dependence on the longitudinal coordinate z will not violate the steadiness of this field structure along z. Taking this into account, instead of (4), we consider a solution in the form

$$V(\tau, y) = Y_2(y)(\tau - T + \gamma z)^2 - (Y_0(y) - Y_0(1)), \qquad (8)$$

which must be consistent with the already nonstationary with respect to z solution to Eq. (2). It is easy to verify that this solution again leads to Eqs. (5) and (6) when $\gamma = Y_0(1)$. Furthermore, solution (8) must satisfy the condition represented by the integral of Eq. (2) [11, 12]. For profile (8) symmetric with respect to τ, this integral has the form

$$\int_{\tau_{\min} = T - \gamma z}^{\tau_{\min} + 2\pi} V d\tau = 0. \qquad (9)$$

If expression (8) is substituted into this condition, it gives

$$Y_2^0 \tilde{Y}_2(y)\pi^2/3 = Y_0^0(\tilde{Y}_0(y) - \tilde{Y}_0(1)). \qquad (10)$$

Here, the functions Y_2 and Y_0 are expressed through their normalized analogs.

The validity of relationship (10) in the case of an arbitrary y is not evident because of the different functions on the right- and left-hand sides of this relationship. However, the numerical analysis shows an almost constant (with the precision up to 0.02) value of the ratio $\dfrac{\tilde{Y}_0(y) - \tilde{Y}_0(1)}{\tilde{Y}_2(y)} \cong 0.38$ (see Fig. 1). Taking this into account, we obtain from expression (10): $Y_2^0/Y_0^0 \cong 0.12$, and the maximal values Y_2^0 and Y_0^0 of the corresponding functions are determined by the fact that V is a value normalized to the maximum, i.e., $V_{\max} = 1$. Tak-

ing into account expression (10), for profile (9) we obtain

$$V_{\max} \equiv Y_2^0(\pi^2 - \pi^2/3) = 1 \quad \text{or} \quad Y_2^0 = 1.5/\pi^2 \approx 0.15,$$
$$Y_0^0 \cong Y_2^0/0.12 \cong 1.25.$$

We determine the value of the parameter $N \cong 1.22$ from the relationship $N/Y_2^0 \approx 8.14$ obtained earlier. At this value of N, waveguide propagation conditions are realized for a sound beam with a bow-shaped profile (see Fig. 2) determined by solution (9) and all parameters obtained above.

In the case of an axially-symmetric beam, the operator $\dfrac{\partial^2}{\partial y^2}$ in Eqs. (2), (3), (5), and (6) is replaced by $\dfrac{1}{r}\dfrac{\partial}{\partial r}\left(r\dfrac{\partial}{\partial r}\right)$. The form of solution (9) obtained above is retained. Although it is impossible to write down the solution to Eq. (5) in a final form similar to expression (7), the numerical analysis demonstrates a complete qualitative coincidence in the behavior of the solutions for a slit beam and an axially symmetric beam with somewhat different values of the characteristic parameters. For example, in the case of an axially symmetric beam, $N/Y_2^0 \approx 2.81$ and $N \cong 0.35$.

The bow-shaped profiles obtained above are continuous. But, within this model, they have singularities in the derivative with respect to τ, which must become smooth together with the corresponding sharp peaks of the profile, if we take into account the dissipative term in Eq. (2), i.e., in the case of passing to the Khokhlov–Zabolotskaya–Kuznetsov equation [13]. We should note that the obtained bow-shaped waves together with well-known sawtooth waves [7] have an asymptotically universal character in the sense that they do not change their characteristic shape. Waves of such shape were also obtained earlier by Rudenko [7] and Bakhvalov, Zhileĭkin, and Zabolotskaya [11] in the process of the numerical determination of solutions to the Khokhlov–Zabolotskaya equation (irrespective of the problem of the waveguide propagation of beams) for certain values of characteristic parameters. However, the special features of such waves were not discussed in the cited papers.

The question about the stability of the waveguide propagation within a certain geometry is of particular interest and requires special analysis. The developed methods of investigating the generalized Khokhlov–Zabolotskaya equation with an arbitrary index of power instability show that the waveguide propagation in the case of a quadratic instability is not necessarily unstable [12]. Besides, we remind that, in nonlinear optics, a slit beam bounded in the transverse direction by two plane boundaries (i.e., confined in a plane waveguide)

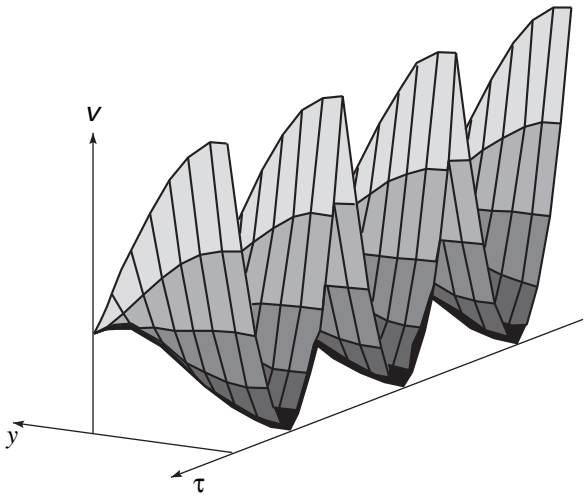

Fig. 2. Pressure wave field with a bow-shaped wave profile (three periods are shown in the figure) for the realization of the waveguide propagation of a sound beam. The amplitude distribution is shown only along the positive y half-axis (the wave field propagates toward the observer).

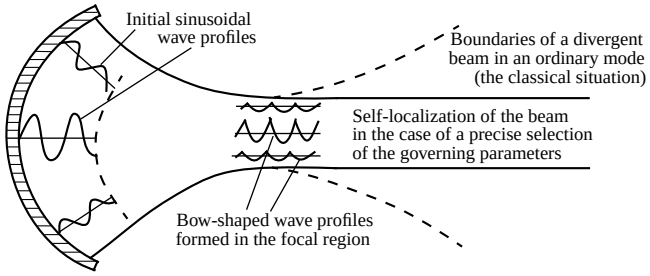

Fig. 3. Scheme of realization of the waveguide propagation of a sound beam with the use of a focusing radiator.

provides an opportunity to observe a stable pattern of waveguide propagation [6].

The wave field structure "constructed" in this paper for a sound beam in the case of its self-localized (waveguide) propagation should be realized in practice in order to experimentally confirm the existance of the considered acoustic effect. A direct synthesis of a sound field of similar configuration is difficult. However, the numerical data mentioned earlier [7, 11] suggest a nonstandard approach to solving this problem. These numerical data demonstrate that, in the case of an initially focused beam, the effects of nonlinearity and diffraction are equivalent (i.e., $N \sim 1$); when the length of shock a formation z_{sh} exceeds the focal length (the radius of the initial front curvature), we obtain a bow-shaped wave profile in the focal zone of the beam. Moreover, if we take into account that a wave front being initially curved because of focusing becomes plane in the region of the focus, then, in the case of a more careful selection of the required parameters, the focal region will create autonomously the conditions

necessary for further waveguide propagation of a sound beam (see Fig. 3) in the presence of compensation of the effects of self-action (the diffraction divergence and the nonlinear noninertial refraction).

ACKNOWLEDGMENTS

This work was supported by the Russian Foundation for Basic Research, INTAS and the program "Universities of Russia."

REFERENCES

1. V. I. Talanov, Izv. Vyssh. Uchebn. Zaved., Radiofiz. **7** (5), 564 (1964).
2. R. Y. Chiao, E. Garmire, and C. H. Townes, Phys. Rev. Lett. **13**, 479 (1964).
3. J. E. Bjorkholm and A. Ashkin, Phys. Rev. Lett. **32**, 129 (1973).
4. M. Mitchell and M. Segev, Nature **387**, 880 (1997).
5. Z. Chen, M. Mitchell, M. Segev, *et al.*, Science **280**, 889 (1998).
6. M. Segev and G. Stegeman, Phys. Today **51** (8), 42 (1998).
7. O. V. Rudenko, Usp. Fiz. Nauk **165**, 1011 (1995) [Phys. Usp. **38**, 965 (1995)].
8. E. A. Zabolotskaya and R. V. Khokhlov, Akust. Zh. **15**, 40 (1969) [Sov. Phys. Acoust. **15**, 48 (1969)].
9. C. Lin, E. Reissner, and H. Tsiegn, J. Math. Phys. **27** (3), 126 (1948).
10. V. F. Zaĭtsev and A. D. Polyanin, *Handbook of Differential Equations with Partial Derivatives* (Mezhdunarodnaya Programma Obrazovaniya, Moscow, 1996).
11. N. S. Bakhvalov, Ya. M. Zhileĭkin, and E. A. Zabolotskaya, *Nonlinear Theory of Sound Beams* (Nauka, Moscow, 1982).
12. Yu. N. Makov and O. A. Sapozhnikov, Akust. Zh. **40**, 1003 (1994) [Acoust. Phys. **40**, 889 (1994)].
13. V. P. Kuznetsov, Akust. Zh. **16**, 548 (1970) [Sov. Phys. Acoust. **16**, 467 (1970)].

Translated by M. Lyamshev

Acoustical Physics, Vol. 46, No. 5, 2000, pp. 601–604. Translated from Akusticheskiĭ Zhurnal, Vol. 46, No. 5, 2000, pp. 685–689.

The Use of an Acoustic Signal in Diagnosing a Cross Crack in a Cantilever Beam

A. B. Roĭtman

Zaporozh'e State University, ul. Zhukovskogo 66, Zaporozh'e, 330600 Ukraine
e-mail: roy@zstu.zaporizhzhe.ua

Received March 22, 1999

Abstract—The results of experimental investigations are described on the basis of which a method of diagnosing the formation and growth of a cross crack in a cantilever beam is developed. The diagnostic criterion is the nonlinear distortion factor calculated as the ratio of the rms value of the higher harmonic amplitudes to the rms value of the amplitude of the investigated acoustic signal. It is established that, by using this factor, it is possible to detect the initiation of a cross crack in a cantilever beam, observe the change in the beam structure within the period before its fracture, and monitor the crack's development. *© 2000 MAIK "Nauka/Interperiodica".*

The blades of gas-turbine engines are the most heavily loaded elements of the engine, and they must satisfy stringent requirements on their reliability. Therefore, during the fatigue tests, the processes of initiation and development of macrocracks (cracks) in specimens and blades are investigated. The limiting state of fatigue loading is the appearance of a crack of a certain size, and the accuracy of determining this state depends on the sensitivity of the methods used for its detection. The most-used method of detecting the initiation of a crack is based on the decrease in the natural frequency of the resonance vibrations of the specimen or blade under test [1].

The problem of well-timed detection of cross cracks during fatigue bending tests of specimens and blades of gas-turbine engines still attracts the interest of researchers [2–5]. In practice, up to now, the main criterion for estimating endurance failure of blades of aircraft gas-turbine engines is the OST 100870-77 standard "Blades of Gas-Turbine Engines: Methods of Fatigue Tests" which says: "The criterion of the blade fracture is the change in the vibration frequency by 1–10% depending on the test conditions. In this case, the test is stopped, and the blade is inspected for a crack. If there is no crack, the test is continued."

In this paper it is shown that, as a criterion for the detection of a fatigue crack, one can effectively use the following parameter of the acoustic signal: the ratio of the rms value of the vibration amplitudes of higher harmonics of the acoustic signal to the rms value of the amplitude of the investigated signal [6, 7]. This ratio is usually called the nonlinear distortion factor K_d.

The aim of this paper is to justify the possibility of using the nonlinear distortion factor K_d as an informative diagnostic indicator for the detection of the instant of crack initiation during fatigue tests by analyzing the acoustic signal generated by the vibrating specimen.

To achieve this aim, an experimental setup was built that made it possible to simultaneously record the following parameters: the voltage amplitude corresponding to the acoustic signal V, V; the acoustic pressure A, dB; the nonlinear distortion factor K_d, %; the frequency of the specimen vibrations f, Hz; the forms of changes in the fundamental acoustic signal and the higher harmonics, which were simultaneously displayed on oscilloscope screens and allowed one to monitor the initiation and development of cracks; and the time of loading t, min.

The specimen under study had the form of a cantilever beam fixed on a massive steel support and activated in a vibrating resonance mode by an inductive transducer which served as an electromagnet fed from a GZ-34 audio-frequency oscillator. The acoustic signal from the vibrating specimen was supplied through a microphone to a VShV-003 noise and vibration meter. The amplified and filtered signal was fed to an oscilloscope, a ChZ-32 frequency meter, and an S6-8 distortion analyzer. The signal proportional to the rms value of all harmonics except for the first one (i.e., of all higher harmonics) was fed to the second channel of a double-beam oscilloscope.

The distortion analyzer measured the nonlinear distortion factors as the ratio of the rms voltage amplitude corresponding to the higher harmonics of the acoustic signal to the rms voltage amplitude corresponding to the investigated acoustic signal.

The operating area of the experimental setup (Fig. 1) was an anechoic chamber (isolation chamber) in which the tested specimen, the inductive transducer, and the microphone were located.

By fastening the inductive transducer to the stand of a beam-type height gauge, it was possible to adjust the clearance between the specimen and the transducer.

1063-7710/00/4605-0601$20.00

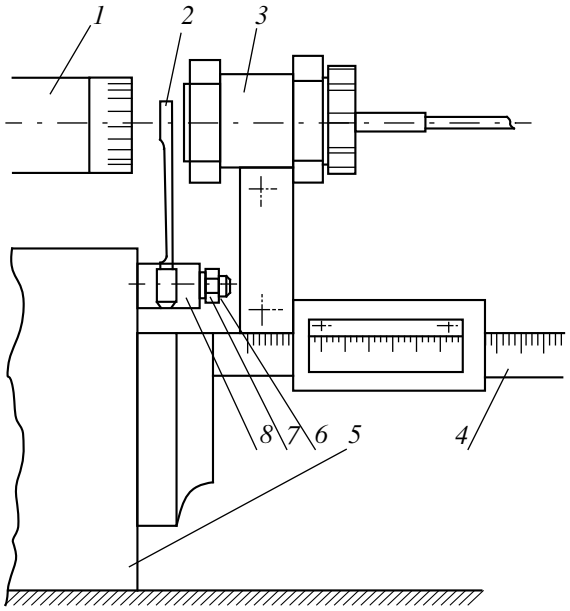

Fig. 1. Schematic diagram of the operating area of the experimental setup: (*1*) microphone, (*2*) specimen, (*3*) inductive transducer, (*4*) stand, (*5*) massive support, (*6*) stud, (*7*) nut, and (*8*) clamp.

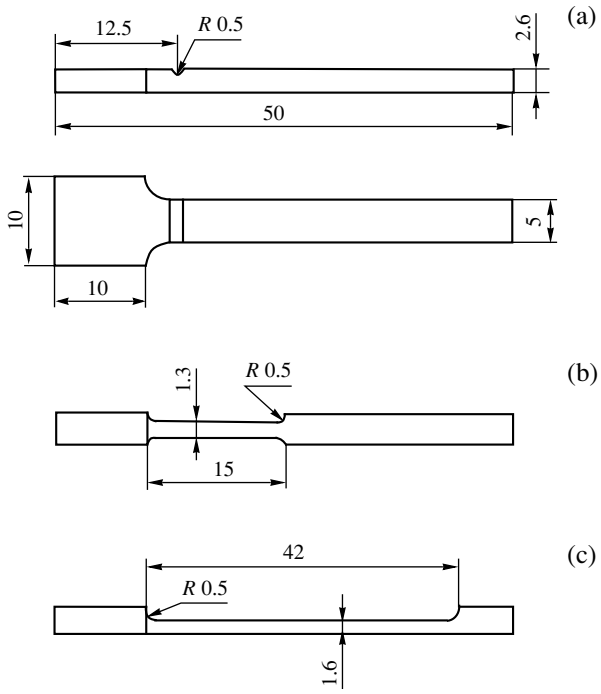

Fig. 2. Geometry of the specimens.

The measurements were made after every 5–20 minutes of testing in six bands of octave filters (OF) determined in Hz: [0, ∞], [0, 500], [500, 1000], [1000, 2000], [2000, 4000], and [4000, 8000]. Below, we will use the following designations: 0, 500, 1000, 2000, 4000, and 8000 OF.

As an object of testing, we chose three types of flat specimens (Fig. 2) made of 30KhGSA hardened steel. The shape of the specimens corresponded to the geometry of the compressor blades of a gas-turbine aircraft engine. Twenty-four specimens were tested.

It was established that, under a prolonged cyclic loading below the fatigue limit, changes are observed in the parameters of the acoustic signal, which testify to the structural microprocesses in the specimen material that do not lead to its fracture but affect its fatigue strength.

Observations of the form of higher harmonics of the acoustic signal made it possible to notice the changes occurring in the course of the tests, which can be used as a diagnostic indication of the instant of the macrocrack (crack) initiation and development. The crack appeared and developed at a distance of 10.0–12.5 mm from the fixed end of the specimen.

The appearance of a crack was accompanied by considerable changes in the values of K_d of the acoustic signal in various OF bands.

The investigations showed that the results of the tests of the types of specimens shown in Fig. 2c turned out to be the most stable and demonstrative ones. An acoustic pressure of 108 dB provided the amplitude of vibration of a specimen without a crack $y = 1.7$ mm. Then, the load was increased in steps to 109, 110, 111, and 112 dB. After 20-hour tests ($N = 5.5 \times 10^7$ cycles), the load was increased to its maximal value of 112.7 dB, which caused rapid development of the crack. After this, the load was reduced to 98 dB and then increased to 100 dB.

Tests result of a typical specimen (Fig. 2c) are presented in Figs. 3 and 4. The curves show the changes in the nonlinear distortion factor K_d in the octave filter bands 0, 500, 1000, and 2000 Hz (the plots of the changes in K_d in the OF bands 4000 and 8000 Hz are not presented), as well as the changes in the natural frequency of vibration of the specimen. During the 12-hour tests, the frequency decreased steadily from 746.3 to 744.3 Hz.

Within the first two hours of tests, K_d is characterized by a significant variability of its values in all bands of octave filters.

The increase in the load up to 109 dB resulted in a sharp decrease in K_d in the 4000 Hz OF band and an increase in the 2000 Hz OF band. In the latter case, K_d gradually decreased to 15–16% and, after that, practically did not change.

The following response of the nonlinear distortion factor to the appearance of a crack was observed. In the 2000 Hz band, K_d sharply increased from 14 to 100–110%, but, after 30 min of tests, it decreased to 50% and later continued to be unstable, varying within 42–74%.

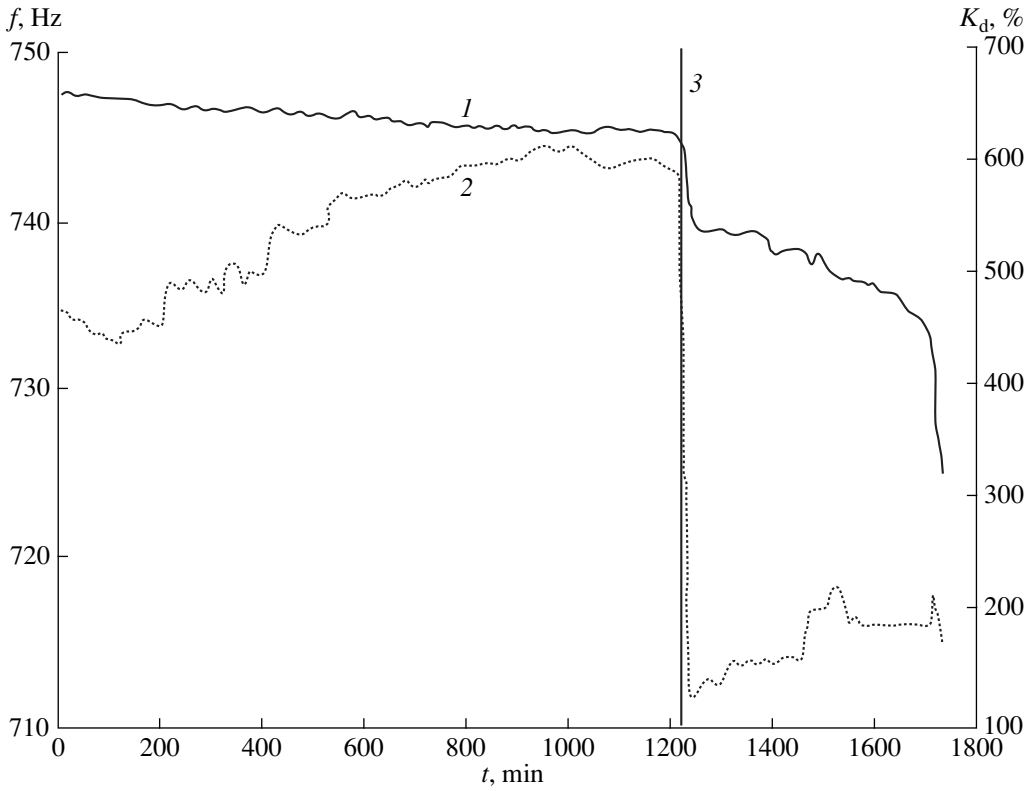

Fig. 3. The natural frequency f and the nonlinear distortion factor K_d as functions of the test duration: (*1*) f, Hz, (*2*) $K_d \times 1000\%$ (OF 500), and (*3*) instant of the crack initiation.

In the 4000 Hz OF band, the nonlinear distortion factor with appearance of a crack decreased abruptly from 42 to 10%, and, later, it varied in the range from 24 to 42%. In other OF bands, K_d also considerably decreased, but, with the growth of the crack's it changed only slightly.

As is seen from Fig. 3, at the instant of the crack's initiation, the natural frequency dropped by less then 1%.

The main results of investigation are summarized in the table where the following designations are used: Δf_0 is the range of natural frequencies of the tested specimens in Hz; $\Delta \bar{f}$ is the mean drop in the natural frequency at the instant of the crack initiation in %; $\bar{K}_d$ is the mean value of the nonlinear distortion factor before the appearance of the crack; $\Delta \bar{K}_d$ is the mean value of the change in the nonlinear distortion factor due to the appearance of the crack in %; "–" corresponds to the increase in $\bar{K}_d$ due to the crack appearance; and "*" means that K_d was not measured during the tests.

It was found that the nonlinear distortion factor K_d before the crack's appearance was essentially different from zero. This is related to the "shaking down" of the specimen with the fastening members, the "cold working" of the specimen material, the "loosening" of the material, the presence of microcracks, and other factors.

As it follows from the table, the appearance of a crack leads to a redistribution of K_d over various OF bands. It is particularly noticeable for type *a* specimens: in the 0 and 2000 OF bands, $\Delta \bar{K}_d$ increased by

Table

Type of specimen	Δf_0, Hz	$\Delta \bar{f}$, %	0		500		1000		2000		4000		8000	
			$\bar{K}_d$, %	$\bar{K}_d$, %	$\bar{K}_d$, %	$\bar{K}_d$, %	$\bar{K}_d$, %	$\bar{K}_d$, %	$\bar{K}_d$, %	$\bar{K}_d$, %	$\bar{K}_d$, %	$\bar{K}_d$, %	$\bar{K}_d$, %	$\bar{K}_d$, %
a	1276–1329	6.4	1.35	183.0	*	*	0.452	–81.3	4.55	232.0	80.3	36.8	75.8	–72.6
b	579–722	7.3	17.3	–27.7	0.721	–15.3	18.4	–64.4	35.4	52.2	42.8	–76.2	53.2	–61.0
c	664–752	5.7	15.2	–61.7	0.476	–70.5	13.7	–54.5	18.6	295.0	43.0	–77.1	54.6	–68.5

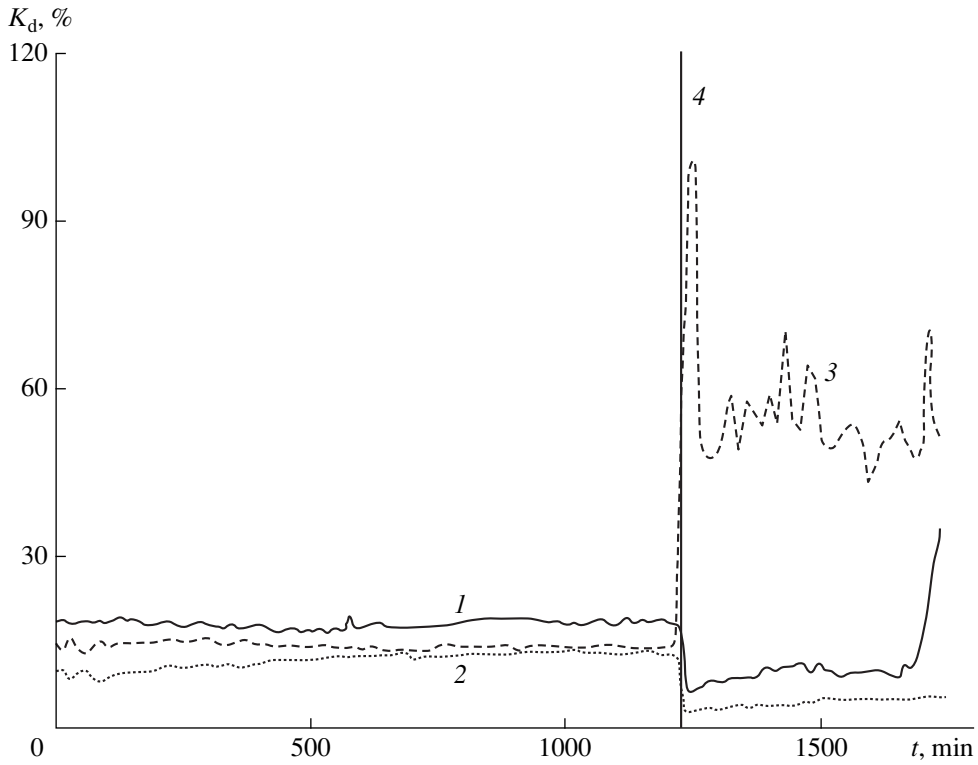

Fig. 4. Nonlinear distortion factor K_d as a function of the test duration for different bands of octave filters: (*1*) 0 OF; (*2*) 1000 OF; (*3*) 2000 OF; and (*4*) instant of the crack appearance.

about 200%, while the mean frequency $\Delta\bar{f}$ dropped only by 6.4%; for the type *b* specimens, in the 2000 OF band, $\Delta\bar{K}_d$ increased by about 300%, and the mean frequency dropped only by 5.7%.

It should be noted that, for some specimens in the 2000 OF band, the value of K_d dropped by a factor of 4–6. The quantitative data on the changes in K_d need some refinement with the use of special instrumentation, but the significance of changes in K_d with the appearance of cracks is undeniable.

The analysis of the data presented in the table and the results of investigations allow us to state that the value of the nonlinear distortion factor K_d (%) changes essentially with appearance of the crack. The values of these changes are considerable, as compared to those in the quantity Δf (%), i.e., the relative change in the natural frequency of the specimen.

In conclusion, we note that the nonlinear distortion factor K_d of the acoustic signal proved to be a very efficient diagnostic criterion for the detection of a cross crack.

In the course of a prolonged cyclic loading of the specimen below the fatigue limit, by using the factor K_d, it is possible to detect the structural changes in the specimen material that precede the fracture.

The change in the nonlinear distortion factor after the appearance of a crack makes it possible to monitor the development of that crack.

The characteristic changes in the form of an acoustic signal and its higher harmonics, which are displayed in oscillograms, allow one to formulate conclusions concerning the initiation and development of cracks in the specimens.

REFERENCES

1. B. A. Gryaznov, S. S. Gorodetskiĭ, Yu. S. Nalimov, L. A. Zaslotskaya, I. A. Makovetskaya, L. F. Shestopal, and A. A. Rabinovich, *Fatigue of High-Temperature Alloys and Blades* (Naukova Dumka, Kiev, 1993).
2. S. L. Tsifanskiĭ, M. A. Magone, and V. M. Ozhiganov, Defektoskopiya, No. 3, 77 (1985).
3. J. I. Ding, J. Pazhouh, S. B. Lin, and T. D. Burton, Scr. Metall. Mater. **30** (7), 839 (1994).
4. Y. Narkis and E. Elmalah, Int. J. Mech. Sci. **38** (5), 499 (1996).
5. A. P. Bovsunovskiĭ, Probl. Prochn., No. 3, 45 (1999).
6. Abdulla Al'-Khreĭshi and V. V. Korolev, in *Abstracts of International Scientific and Technical Conference "Experimental Methods of Studying the Stages of Crack Development," Zmiev, 1994*, p. 94.
7. A. B. Roĭtman, Abdulla Al'-Khreĭshi, and S. L. Ryagin, in *Proceedings of the Second International Symposium "Transport Noise and Vibration," St. Petersburg, 1994*, Part 2, p. 12.

Translated by A. Svechnikov

Acoustical Physics, Vol. 46, No. 5, 2000, pp. 605–612. Translated from Akusticheskiĭ Zhurnal, Vol. 46, No. 5, 2000, pp. 690–697.

Reflection of Plane Waves from an Elastic Layered Medium: Resonance Approach and Numerical Modeling

M. S. Fokina and V. N. Fokin

Institute of Applied Physics, Russian Academy of Sciences,
ul. Ul'yanova 46, Nizhni Novgorod, 603600 Russia
e-mail: fok@hydro.appl.sci-nnov.ru

Received July 8, 1999

Abstract—The resonance formalism developed earlier by H. Überall for a model of a liquid layer overlying a liquid halfspace is extended to a model of an elastic layer overlying an elastic halfspace. Using the Thomson–Haskell matrix technique, an exact analytical expression is obtained for the complex reflection coefficient. Characteristic equations are derived, and their roots, which determine the positions of the resonances of the reflection coefficient for longitudinal and transverse waves, are obtained analytically. In the resonance approach, the exact expression for the reflection coefficient is replaced by an approximate one that describes the behavior of the reflection coefficient near the resonances. The comparison of the exact and approximate values of the reflection coefficient shows good agreement between the results near the frequency and angular resonances. © *2000 MAIK "Nauka/Interperiodica".*

INTRODUCTION

The reflection coefficients calculated for the acoustic signal reflection from the ocean bottom generally form a complicated structure that consists of more or less regular sequences of peaks and troughs. The dependences of this kind are usually attributed to resonance phenomena [1]. The resonances of the reflection coefficients are indicators of the elastic properties of materials such as density and Lame constants, which are related to the longitudinal and transverse velocities of sound. The resonances can provide information on any changes inside the layers and in the interlayers in the multilayer structures. The high sensitivity of the resonances to the parameters of media interacting with sound promoted wide use of the resonance approach in science and technology [2, 3]. A remote resonance method of acoustic spectroscopy was developed for the determination of the elastic properties of materials [4]. With the use of resonances of the longitudinal and transverse waves, Keltie [5] successfully employed a metal plate with an elastic coating to decrease the system's response. Of great interest is also the study of resonances for describing the effects of the sea bottom on the propagation of acoustic signals in a shallow sea. The impedance function of the layered sea bottom has clearly expressed resonances [6] and contains information on the bottom characteristics, which is equivalent to the information confined in the reflection coefficient. Therefore, the values of the impedance function obtained from the inverse Hankel transform are proposed as initial data for the inverse problem of the determination of the geoacoustic parameters of the bottom [7]. Recently, the interest of researchers has shifted toward the use of resonance phenomena in layered media for direct reconstruction of the bottom parameters [8]. Therefore, it seems logical to use the resonance structure found from measurements for the determination of the properties of a given medium, i.e., to solve the inverse problem in every specific case.

Up to now, only several attempts have been made to employ the resonance approach to the sound reflection from the ocean bottom for obtaining information on the structure and properties of the reflecting medium. In this direction, the first investigations are the publications [9–12], where the authors consider the case of a liquid layer and an elastic plate placed in a liquid medium and study the relation between the acoustic resonances and the material parameters of the medium [12, 13].

In realistic models of the layered sea bottom, transverse waves and absorption must be taken into account. In this paper, we consider the introduction of such complex conditions in the resonance theory. The resonance approach earlier developed by Überall in [10–12] for a liquid model of the bottom is applied to the elastic layered bottom model.

The experimentally established properties of tone signals reflected from a layered bottom were considered in detail by Volovov [14]. The theory of sound reflection from an arbitrary number of plane-parallel layers has been developed by Brekhovskikh and Godin [15]. The interest in the investigation of sound wave interactions with the bottom is caused both by the effect of the bottom structure on the propagation of sound waves in the water column and by the problem of the remote determination of the bottom characteristics. For example, the investigations of the effect of the layered

1063-7710/00/4605-0605$20.00

bottom structure on the sound propagation in a shallow sea were considered by Ageeva *et al.* [16]. However, along with the development of new methods of determination of the bottom characteristics in a shallow sea [17], the methods of determination of the frequency-angular dependences of the reflection coefficient from acoustic field measurements are still being used [18].

THE PHYSICAL AND MATHEMATICAL MODEL

In this paper, using the Thomson–Haskell matrix technique described in [15, 19–21], we obtain exact analytical expressions for the complex reflection coefficients. The physical model of a medium used for studying the frequency-angular resonances of the reflection coefficient consists of an elastic layer between liquid and elastic halfspaces. The parameters of the liquid and elastic halfspaces are identified by indices 0 and ∞, respectively: c_0 and ρ_0 are the sound velocity in water and the water density; d, ρ, c_l and c_t are the thickness, density, longitudinal and transverse velocities in the sedimentary layer; ρ_∞, $c_{l\infty}$ and $c_{t\infty}$ are the density, longitudinal and transverse velocities in the halfspace. The effects of absorption are taken into account by introducing complex velocities of the longitudinal and transverse waves. Considering only the waves of the vertical polarization, the displacement vector U can be written in terms of the scalar φ and vector ψ potentials

$$U = \mathrm{grad}\varphi + \mathrm{rot}\psi. \tag{1}$$

The components of the displacement vector and the strain tensor in the Cartesian system of coordinates can be written in the form

$$U_x = \partial\varphi/\partial x - \partial\psi/\partial z, \quad U_z = \partial\varphi/\partial z + \partial\psi/\partial x, \tag{2}$$

$$\begin{aligned} \sigma_{xz} &= 2\mu(\partial^2\varphi/\partial x\partial z - \partial^2\psi/\partial z^2), \\ \sigma_{zz} &= -\lambda\partial^2\varphi/\partial x^2 \\ &+ (\lambda + 2\mu)\partial^2\varphi/\partial z^2 + \partial^2\psi/\partial x\partial z, \end{aligned} \tag{3}$$

where λ and μ are the Lame constants related to the longitudinal and transverse sound velocities. The components of the displacement vector and the strain tensor are continuous across the sedimentary layer/elastic foundation and water column/sedimentary layer boundaries:

$$\begin{aligned} U_x &= U_{x\infty}, \quad U_{z0} = U_z, \\ U_z &= U_{z\infty}, \quad p_0 = \sigma_{xz}, \\ \sigma_{xz} &= \sigma_{xz\infty}, \quad 0 = \sigma_{xz}, \\ \sigma_{zz} &= \sigma_{zz\infty}. \end{aligned} \tag{4}$$

The potentials φ and ψ satisfy the Helmholtz equations

$$\begin{aligned} \Delta\varphi + \alpha^2\varphi &= 0, \\ \Delta\psi + \beta^2\psi &= 0. \end{aligned} \tag{5}$$

Representing the set of waves in the water column, sedimentary layer, and elastic halfspace in terms of the amplitudes of the longitudinal and transverse waves propagating in both directions of the z-axis, introducing column-vectors for two halfspaces and the elastic layer, and using the boundary conditions (4), we obtain the set of algebraic equations in the matrix form

$$Z_0 = Q^{-1}K_{ls}DZ_\infty, \tag{6}$$

where Q^{-1} is the inverse matrix of the liquid halfspace, K_{ls} is the transfer matrix between the liquid halfspace and the elastic medium, $D = ALA^{-1}K_0$ is the matrix of the elastic layered medium, A is the characteristic matrix of the layer, L is the diagonal matrix (the variables $\delta = \alpha d$ and $\eta = \beta d$ are related to the frequency, the angle of incidence of the wave, and the thickness of the sedimentary layer d), and K_0 is the matrix of the elastic halfspace:

$$Q^{-1} = \begin{bmatrix} \dfrac{1}{2i\alpha_0} & -\dfrac{1}{2\omega^2\rho_0} \\ -\dfrac{1}{2i\alpha_0} & -\dfrac{1}{2\omega^2\rho} \end{bmatrix},$$

$$A = \begin{bmatrix} i\xi & i\xi & -i\beta & i\beta \\ i\alpha & -i\alpha & i\xi & i\xi \\ -2\mu\xi\alpha & 2\mu\xi\alpha & -2\mu\xi\gamma & -2\mu\xi\gamma \\ 2\mu\xi\gamma & 2\mu\xi\gamma & -2\mu\xi\beta & 2\mu\xi\beta \end{bmatrix},$$

$$L = \begin{bmatrix} \exp(i\delta) & 0 & 0 & 0 \\ 0 & \exp(-i\delta) & 0 & 0 \\ 0 & 0 & \exp(i\eta) & 0 \\ 0 & 0 & 0 & \exp(-i\eta) \end{bmatrix}, \tag{7}$$

$$K_0 = \begin{bmatrix} i\xi & i\xi & -i\beta_\infty & i\beta_\infty \\ i\alpha_\infty & i\alpha_\infty & i\xi & i\xi \\ -2\mu_\infty\xi\alpha_\infty & 2\mu_\infty\xi\alpha_\infty & -2\mu_\infty\xi\gamma_\infty & -2\mu_\infty\xi\gamma_\infty \\ 2\mu_\infty\xi\gamma_\infty & 2\mu_\infty\xi\gamma_\infty & -2\mu_\infty\xi\beta_\infty & 2\mu_\infty\xi\beta_\infty \end{bmatrix}.$$

The solution to matrix equations (6) for the reflection coefficient V in the water column can be obtained by Kramer's rule.

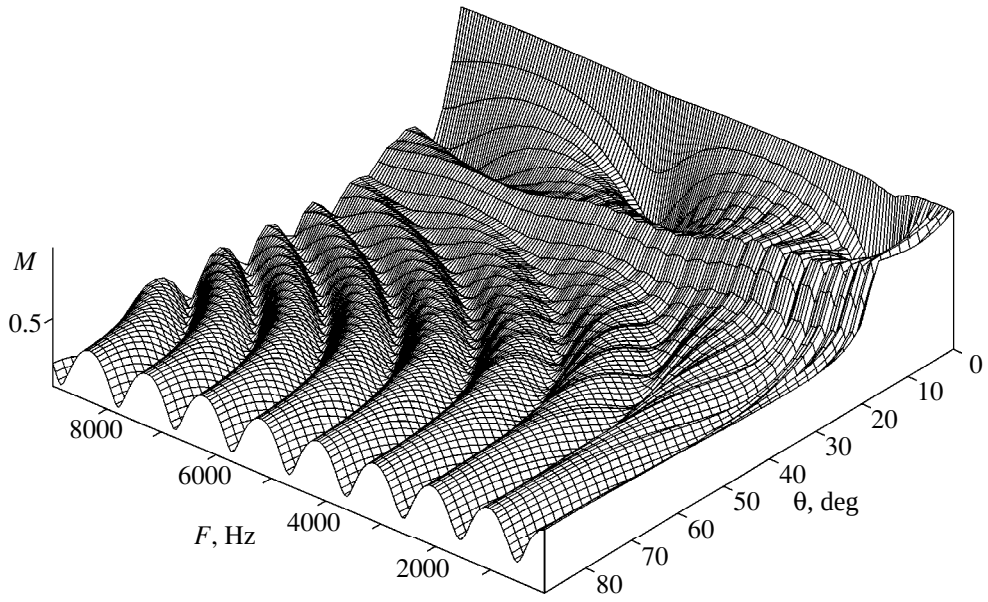

Fig. 1. Magnitude of the plane wave reflection coefficient on the frequency–grazing angle plane.

THE EXACT EXPRESSION FOR THE REFLECTION COEFFICIENT

The exact expression for the complex reflection coefficient can be written using the elements of the matrices Q^{-1} and D:

$$V = \frac{Q_{21}^{-1}(D_{21}D_{33} - D_{23}D_{31}) - Q_{22}^{-1}(D_{43}D_{31} - D_{41}D_{33})}{Q_{11}^{-1}(D_{21}D_{33} - D_{23}D_{31}) - Q_{12}^{-1}(D_{43}D_{31} - D_{41}D_{33})}. \quad (8)$$

Further, expression (8) is written analytically in terms of the material parameters of the medium and variables δ and η. Separating the real and imaginary parts in it, the exact expression for the reflection coefficient is transformed to a more compact form

$$V = \frac{E^2 - B^2 + C^2 - G^2}{E^2 + 2EB + B^2 + C^2 + 2CG + G^2} + \frac{i(2CB + 2GE)}{E^2 + 2EB + B^2 + C^2 + 2CG + G^2}. \quad (9)$$

Here, the functions E, B, C, and G are related to both the material parameters of the layered elastic medium and the variables $\delta = \alpha d$ and $\eta = \beta d$. For estimating and revealing the features of the frequency-angular dependences of the reflection coefficient, the results of calculations are often presented in the three-dimensional form, as is made in Fig. 1, which exhibits calculation results of the magnitude of the reflection coefficient in a wide range of frequencies and grazing angles. The material parameters of the bottom are given in the table. From Fig. 1, it follows that the frequency-angular dependence of the reflection coefficient has the form of a regular sequence of maxima and minima. These features are related to resonances of the reflection coefficient. Überall [10–12] observed similar effects for the case of a liquid sedimentary layer between two different liquids.

In realistic models of the layered sea bottom, additional allowance for the transverse waves leads to considerable changes in the resonance structure (Fig. 2). Numerical calculations show that, at all grazing angles, except for the normal incidence of a plane wave, additional resonance peaks appear as compared to the case of a liquid layer. The amplitude of the resonances also changes, which can easily be explained by the fact that the transverse waves carry away acoustic energy from the boundary and, as a result, the boundary behaves as though it were more soft. At a normal incidence of a plane wave on the elastic medium, the effect of the transverse wave on the reflection coefficient is absent, because the excitation of the transverse wave is not possible, owing to the lack of the tangential projection of a compression wave at the interface between the media. Numerical calculations for a 70-cm elastic layer (table) with allowance for absorption in the layer and halfspace ($\upsilon_l = 0.01$, $\upsilon_t = 0.001$, $\upsilon_{l\infty} = 0.015$ and $\upsilon_{t\infty} = 0.15$) show that the absorption effects mask to some extent the influence of the transverse waves. However, the cal-

Parameters of the bottom model

	c_l, m/s	c_t, m/s	ρ, g/cm^3
Water column	1500		1.0
Sedimentary layer, d = 70 cm	1455	250	1.45
Elastic halfspace	1575	800	2.6

culations of the reflection coefficient performed for two grazing angles $\theta = 3°$ and $\theta = 50°$ (Fig. 2a) show that the allowance made for the absorption leads mainly to a decrease in the resonance amplitudes of the reflection coefficient at all grazing angles.

THE RESONANCE APPROACH

For the analysis of the behavior of the plane wave reflection coefficient near the resonance minima, the exact expression for the complex reflection coefficient (9) is recast to the form

$$V = \frac{(E^2 - B^2 + C^2 - G^2)^2 + (2CB + 2GE)^2}{(E^2 + 2EB + B^2 + C^2 + 2CG + G^2)(E^2 - B^2 + C^2 - G^2 - i(2CB + 2GE))}. \quad (10)$$

The analysis of expression (10) showed that the resonance behavior of the reflection coefficient becomes apparent every time when the real part of the denominator tends to zero, i.e., when the characteristic equations obtained from (10) at resonance conditions are satisfied:

$$E^2 - B^2 + C^2 - G^2 = 0, \quad (11)$$

$$(E + B)^2 + (C - G)^2 = 0. \quad (11a)$$

After separating the variables with respect to δ and η, the characteristic Eq. (11) can be rewritten in the following form

$$\begin{aligned} &K_1\cos(\delta)\cos(\eta) + K_2\cos^2(\delta)\cos^2(\eta) \\ &+ K_3\sin(\delta)\sin(\eta) + K_4\cos^2(\delta) + K_5\cos^2(\eta) \\ &+ K_6\cos(\delta)\cos(\eta)\sin(\delta)\sin(\eta) + K_7 = 0, \end{aligned} \quad (12)$$

where the constants K_1–K_7 are related only to the material parameters of the elastic layered medium. Characteristic equation (12) can be solved separately for the variables δ and η. We will seek the solution to Eq. (12) as $\delta = 2\arctan(X)$. Then, Eq. (12) can be rewritten as the fourth-degree equation

$$\begin{aligned} &(-K_1\cos(\eta) + K_2\cos^2(\eta) + K_4 + K_5\cos^2(\eta) \\ &+ K_7)X^4 + (2K_3\sin(\eta) - 2K_6\cos(\eta)\sin(\eta))X^3 \\ &+ (-2K_2\cos^2(\eta) - 2K_4 + 2K_5\cos^2(\eta) + 2K_7)X^2 \\ &+ (2K_3\sin(\eta) + 2K_6\cos(\eta)\sin(\eta))X + (K_1\cos(\eta) \\ &+ K_2\cos^2(\eta) + K_4 + K_5\cos^2(\eta) + K_7) = 0. \end{aligned} \quad (13)$$

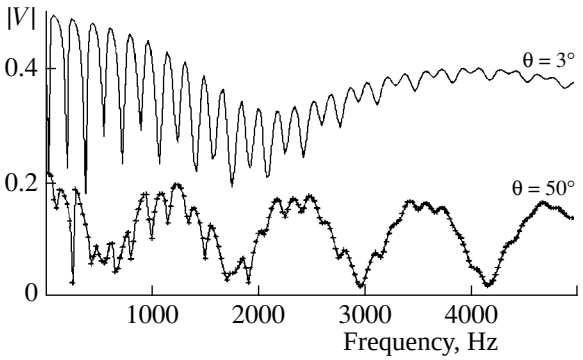

Fig. 2. Frequency dependence of the reflection coefficient for grazing angles 3° and 50°.

If we seek the solution as $\eta = 2\arctan(X)$, Eq. (12) will take the form

$$\begin{aligned} &(-K_1\cos(\delta) + K_2\cos^2(\delta) + K_4\cos^2(\delta) + K_5 + K_7)X^4 \\ &+ (2K_3\sin(\delta) - 2K_6\cos(\delta)\sin(\delta))X^3 \\ &+ (-2K_2\cos^2(\delta) + 2K_4\cos^2(\delta) - 2K_5 + 2K_7)X^2 \\ &+ (2K_3\sin(\delta) + 2K_6\cos(\delta)\sin(\delta))X \\ &+ (K_1\cos(\delta) + K_2\cos^2(\delta) + K_4\cos^2(\delta) \\ &+ K_5 + K_7) = 0. \end{aligned} \quad (14)$$

The solutions to these equations determine the positions of the reflection coefficient resonances on the frequency–angle of the incidence plane for the longitudinal and transverse waves that appear in the elastic medium. The roots of Eqs. (13) and (14) can be obtained as the solutions of the Descartes–Euler fourth-degree equation:

$$X^4 + aX^3 + bX^2 + cX + d = 0. \quad (15)$$

Taking into account that the period of the arctangent is π, the roots of characteristic Eq. (12) are found as

$$\begin{aligned} \delta &= 2\arctan(X), \quad \eta = 2\arctan(X), \\ \delta_n &= \delta + 2\pi n, \quad \eta_n = \eta + 2\pi n, \end{aligned} \quad (16)$$

where X are the roots of Eqs. (13) and (14), respectively, and $n = 0, 1, 2, \ldots$ are the order numbers of the resonances. The variables δ_n and η_n determine the positions of the frequency-angular resonances of the reflection coefficient. The roots of Eq. (15), X_1–X_4, can expressed in terms of the coefficients of a cubic equation (p, r, and q) and a fourth-degree equation (a, b, c, and d):

$$
\begin{aligned}
X_{1,2} &= -\frac{1}{6}\sqrt{36\varepsilon^{1/3} - 36\zeta - 6p} + \frac{1}{6}\sqrt{-18\varepsilon^{1/3} + 18\zeta - 6p + i18\sqrt{3}(\varepsilon^{1/3} + \zeta)} \\
&\pm \frac{1}{6}\sqrt{-18\varepsilon^{1/3} + 18\zeta - 6p - i18\sqrt{3}(\varepsilon^{1/3} + \zeta)} - \frac{1}{4}a, \\
X_{3,4} &= \frac{1}{6}\sqrt{36\varepsilon^{1/3} - 36\zeta - 6p} \pm \frac{1}{6}\sqrt{-18\varepsilon^{1/3} + 18\zeta - 6p + i18\sqrt{3}(\varepsilon^{1/3} + \zeta)} \\
&+ \frac{1}{6}\sqrt{-18\varepsilon^{1/3} + 18\zeta - 6p - i18\sqrt{3}(\varepsilon^{1/3} + \zeta)} - \frac{1}{4}a, \\
\varepsilon &= \frac{1}{1728}p^3 - \frac{1}{48}pr + \frac{1}{128}q^2 + \frac{1}{1152}\sqrt{-48p^4 + 384p^2r^2 - 768r^3 + 12p^3q^2 - 432prq^2 + 81q^4}, \\
\zeta &= \frac{-\frac{1}{144}p^2 - \frac{1}{12}r}{\varepsilon^{1/3}}.
\end{aligned}
\tag{17}
$$

The material constants of the layered medium enter the solution through the corresponding expressions for the coefficients of the equations. Moreover, we can write the exact expressions for δ' and η' as functions of the current frequencies and incidence angles of a plane wave:

$$
\delta' = \frac{2\pi F d\cos(\theta_l)}{c_l}, \quad \eta' = \frac{2\pi F d\cos(\theta_r)}{c_t}. \tag{18}
$$

The reflection coefficient resonances become apparent when the difference between the exact variables δ' and η' and resonance variables δ_n and η_n found from the characteristic equations tends to zero: $|\delta' - \delta_n| = 0$ and $|\eta' - \eta_n| = 0$. In theses conditions, the reflection coefficient has minima in the entire range of angles and frequencies. Figure 3 exhibits the exact calculations of the frequency dependence of the coefficient near the first resonance minimum corresponding to the frequency F_r =105 Hz; the markers show the difference $|\delta' - \delta_n|$. Since the variables δ' and η' are the functions of frequency and angle of incidence, by fixing only one frequency or angular variable, we can find the positions of the frequency and angular resonances for the longitudinal and transverse waves separately:

$$
\begin{aligned}
\underline{\theta = \text{const}}\text{:}\ (F_r)_l &= \frac{\delta_n c_l}{2\pi d\cos(\theta_l)}, \\
(F_r)_t &= \frac{\eta_n c_t}{2\pi d\cos(\theta_t)},
\end{aligned}
\tag{19}
$$

$$
\begin{aligned}
\underline{F = \text{const}}\text{:}\ (\theta)_l &= \arcsin\left(\sqrt{\frac{c_0^2(4\pi^2F^2d^2 - \delta_n)}{4\pi^2F^2d^2c_l^4}}\right), \\
(\theta)_t &= \arcsin\left(\sqrt{\frac{c_0^2(4\pi^2F^2d^2 - \eta_n)}{4\pi^2F^2d^2c_t^4}}\right).
\end{aligned}
\tag{20}
$$

For the chosen parameters of the bottom model (table), on the frequency–angle of the incidence plane, we

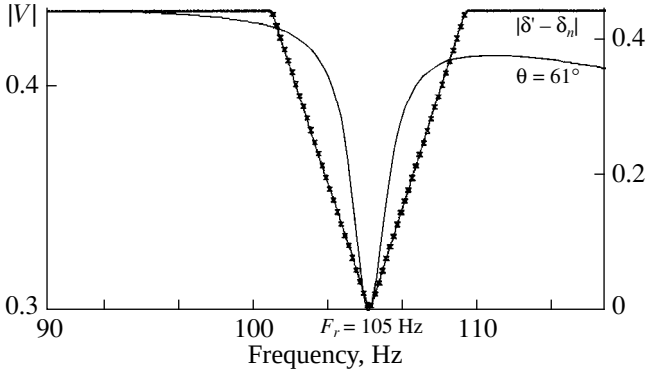

Fig. 3. Positions of the first frequency resonance determined by the roots of the characteristic equation for $|\delta' - \delta_n| = 0$ (shown by markers) and the frequency dependence of the reflection coefficient (solid line).

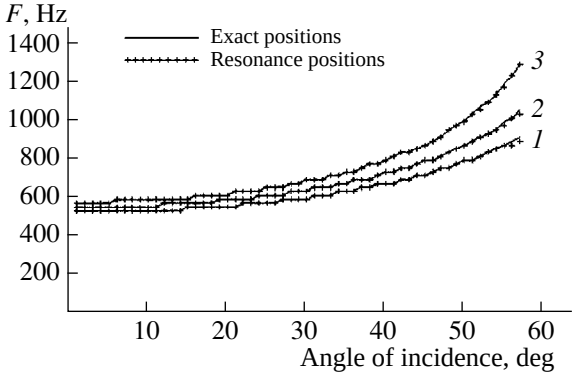

Fig. 4. Positions of the first resonances, which are obtained from exact calculations (solid lines) and from the characteristic equations (shown by markers) for different values of the longitudinal velocities of sound in the sedimentary layer: c_l = (*1*) 1455, (*2*) 1520, and (*3*) 1475 m/s.

compared the resonance positions obtained from formulas (16) and (18); the results were found to be in good agreement. In Fig. 4, one can clearly see the dependence of the resonance positions on the longitudinal velocities in a sedimentary layer; δ' and δ_n were calculated for three different longitudinal velocities of sound in the sedimentary layer: $c_l = 1455$ (line *1*), $c_l = 1520$ (line *2*), and $c_l = 1475$ m/s (line *3*). The exact values of δ' are marked by the solid line, and the values of δ_n are shown by the markers. The numerical calculations showed that the change in the longitudinal velocity in the sedimentary layer leads to shifts of the resonance positions in the frequency–angle of incidence plane.

COMPARISON OF THE RESONANCE APPROACH AND EXACT CALCULATIONS

The resonance approach is mainly based on the assumption that, near a resonance, the reflection coefficient can approximately be presented by the Brait–Wigner resonance curve on the background of a weakly changing foundation [10]. Following this assumption, the exact expression for the reflection coefficient (9) can be expanded in the Taylor series in powers of the small parameters $(\delta' - \delta_n)$ and $(\eta' - \eta_n)$ near the minima of the reflection coefficient:

$$V(\delta', \eta') \cong V(\delta_n) + V(\eta_n) + V'(\delta_n)(\delta' - \delta_n) + V'(\eta_n)(\eta' - \eta_n) + \ldots. \tag{21}$$

Linearizing expression (21) in the vicinity of δ_n and η_n and equating the first derivatives in the expansion to zero ($V'(\delta_n) = 0$ and $V'(\eta_n) = 0$), the approximate expression for the reflection coefficient can be written, according to the Fermat theorem, in terms of the material characteristics of the medium:

$$\begin{aligned}
V_r = \sum_n \Bigg[\frac{1}{2} i \Bigg(\Bigg(\frac{1}{2}\frac{i\Delta_9\xi}{(-\gamma+\xi)\beta} + \frac{1}{2}\frac{i\Delta_{14}\alpha_\infty}{(-\gamma+\xi)} + \frac{1}{2}\frac{i\Delta_{11}\mu_\infty\xi\alpha_\infty}{(-\gamma+\xi)\mu} \\
- \frac{1}{2}\frac{i\Delta_{18}\mu_\infty\gamma_\infty}{\mu\beta(-\gamma+\xi)}\Bigg)\Delta_{13} - \Bigg(-\frac{1}{2}\frac{i\Delta_9\beta_\infty}{(-\gamma+\xi)\beta} + \frac{1}{2}\frac{i\Delta_{14}\xi}{(-\gamma+\xi)} \\
+ \frac{1}{2}\frac{i\Delta_{11}\mu_\infty\xi\gamma_\infty}{(-\gamma+\xi)\mu} + \frac{1}{2}\frac{i\Delta_{18}\mu_\infty\beta_\infty}{\mu\beta(-\gamma+\xi)}\Bigg)\Delta_{17}\Bigg)\Big/\alpha_0 \\
+ \frac{1}{2}\Bigg(\Bigg(-\frac{\Delta_{11}\mu\xi\gamma\beta_\infty}{(-\gamma+\xi)} - \frac{\xi^2\mu\Delta_{16}}{(-\gamma+\xi)\alpha} + \frac{\xi\mu_\infty\gamma_\infty\Delta_{15}}{(-\gamma+\xi)\alpha} \\
- \frac{\xi\mu_\infty\beta_\infty\Delta_{14}}{(-\gamma+\xi)}\Bigg)\Delta_{17} - \Bigg(\frac{\xi^2\mu\gamma\Delta_{11}}{(-\gamma+\xi)} - \frac{\xi\mu\alpha_\infty\Delta_{16}}{(-\gamma+\xi)\alpha} \\
+ \frac{\mu_\infty\alpha_\infty\xi\Delta_{15}}{(-\gamma+\xi)\alpha} + \frac{\xi\mu_\infty\gamma_\infty\Delta_{14}}{(-\gamma+\xi)}\Bigg)\Delta_{13}\Bigg)\Big/(\omega^2\rho_\infty)\Bigg)\Big/\Bigg(-\frac{1}{2}i \\
\times\Bigg(\Bigg(\frac{1}{2}\frac{i\Delta_9\xi}{(-\gamma+\xi)\beta} + \frac{1}{2}\frac{i\Delta_{14}\alpha_\infty}{(-\gamma+\xi)} + \frac{1}{2}\frac{i\Delta_{11}\mu_\infty\xi\alpha_\infty}{(-\gamma+\xi)\mu} \\
- \frac{1}{2}\frac{i\Delta_{18}\mu_\infty\gamma_\infty}{\mu\beta(-\gamma+\xi)}\Bigg)\Delta_{13} - \Bigg(-\frac{1}{2}\frac{i\Delta_9\beta_\infty}{(-\gamma+\xi)\beta} + \frac{1}{2}\frac{i\Delta_{14}\xi}{(-\gamma+\xi)} \\
+ \frac{1}{2}\frac{i\Delta_{11}\mu_\infty\xi\gamma_\infty}{(-\gamma+\xi)\mu} + \frac{1}{2}\frac{i\Delta_{18}\mu_\infty\beta_\infty}{\mu\beta(-\gamma+\xi)}\Bigg)\Delta_{17}\Bigg)\Big/\alpha_0 \\
+ \frac{1}{2}\Bigg(\Bigg(-\frac{\Delta_{11}\mu\xi\gamma\beta_\infty}{(-\gamma+\xi)} - \frac{\xi^2\mu\Delta_{16}}{(-\gamma+\xi)\alpha} + \frac{\xi\mu_\infty\gamma_\infty\Delta_{15}}{(-\gamma+\xi)\alpha} \\
- \frac{\xi\mu_\infty\beta_\infty\Delta_{14}}{(-\gamma+\xi)}\Bigg)\Delta_{17} - \Bigg(\frac{\Delta_{11}\mu\xi^2\gamma}{(-\gamma+\xi)} - \frac{\xi\mu\alpha_\infty\Delta_{16}}{(-\gamma+\xi)\alpha} \\
+ \frac{\xi\mu_\infty\alpha_\infty\Delta_{15}}{(-\gamma+\xi)\alpha} + \frac{\xi\mu_\infty\gamma_\infty\Delta_{14}}{(-\gamma+\xi)}\Bigg)\Delta_{13}\Bigg)\Big/(\omega^2\rho_\infty)\Bigg]\Bigg;
\end{aligned} \tag{22}$$

$$\Delta_1 = i\exp(-i\eta_n)(\eta' - \eta_n),$$

$$\Delta_2 = i\exp(-i\eta_n) - \Delta_1,$$

$$\Delta_3 = i\exp(i\eta_n)(\eta' - \eta_n),$$

$$\Delta_4 = i\exp(i\eta_n) + \Delta_3,$$

$$\Delta_5 = \exp(-i\delta_n),$$

$$\Delta_6 = i\Delta_5(\delta' - \delta_n),$$

$$\Delta_7 = i\exp(i\delta_n)(\delta' - \delta_n),$$

$$\Delta_8 = \exp(i\delta_n) + \Delta_7,$$

$$\Delta_9 = \alpha\Delta_8\beta - \alpha(\Delta_5 - \Delta_6)\beta + \xi\Delta_4\gamma - \xi\Delta_2\gamma,$$

$$\Delta_{10} = \xi\Delta_8 + \xi(\Delta_5 - \Delta_6) - \Delta_4\gamma - \Delta_2\gamma,$$

$$\Delta_{11} = \exp(i\delta_n) + \Delta_7 + \Delta_5 - \Delta_6 - \exp(i\eta_n), - \Delta_3 - \exp(-i\eta_n) + \Delta_1,$$

$$\Delta_{12} = \alpha\Delta_8\beta - \alpha(\Delta_5 - \Delta_6)\beta + \gamma^2\Delta_4 - \gamma^2\Delta_2,$$

$$\Delta_{13} = \frac{\mu\xi\beta_\infty\Delta_{12}}{(-\gamma+\xi)\beta} + \frac{\mu\gamma\xi^2\Delta_{11}}{-\gamma+\xi} - \frac{\mu_\infty\xi\gamma_\infty\Delta_{10}}{-\gamma+\xi} - \frac{\mu_\infty\xi\beta_\infty\Delta_9}{(-\gamma+\xi)\beta},$$

$$\Delta_{14} = -\Delta_8\gamma - (\Delta_5 - \Delta_6)\gamma + \xi\Delta_4 + \xi\Delta_2,$$

$$\Delta_{15} = \xi\Delta_8\gamma - \xi(\Delta_5 - \Delta_6)\gamma + \beta\alpha\Delta_4 - \beta\alpha\Delta_2,$$

$$\Delta_{16} = \gamma^2\Delta_8 - \gamma^2(\Delta_5 - \Delta_6) + \beta\alpha\Delta_4 - \beta\alpha\Delta_2,$$

$$\Delta_{17} = \frac{\mu\xi^2\Delta_{12}}{(-\gamma+\xi)\beta} + \frac{\mu\xi\gamma\alpha_\infty\Delta_{11}}{-\gamma+\xi} - \frac{\xi\mu_\infty\alpha_\infty\Delta_{10}}{-\gamma+\xi} + \frac{\xi\mu_\infty\gamma_\infty\Delta_9}{(-\gamma+\xi)\beta},$$

$$\Delta_{18} = \alpha\beta\Delta_8 - \alpha\beta(\Delta_5 - \Delta_6) + \xi^2\Delta_4 - \xi^2\Delta_2.$$

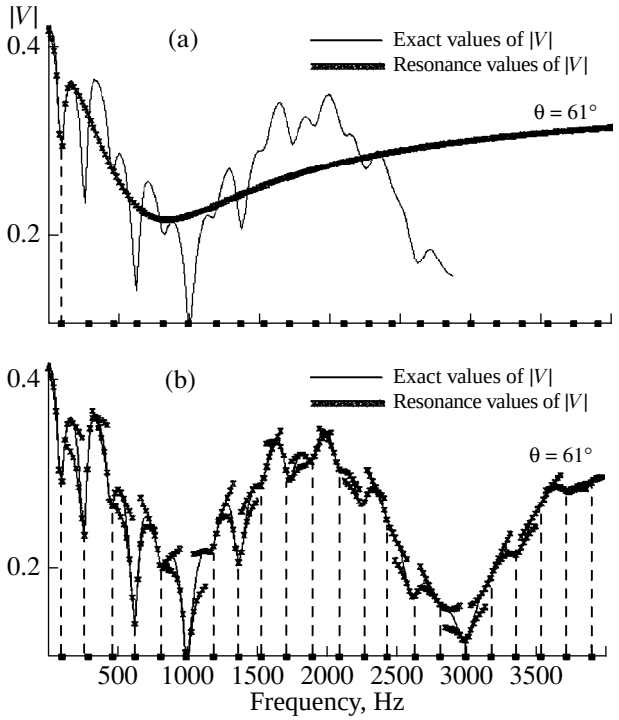

Fig. 5. Comparison of the exact calculations of the frequency resonances of the reflection coefficient (solid line) and the approximate calculations by formula (22) (markers): (a) with allowance for one term in formula (22); (b) with allowance for 22 resonance terms in formula (22).

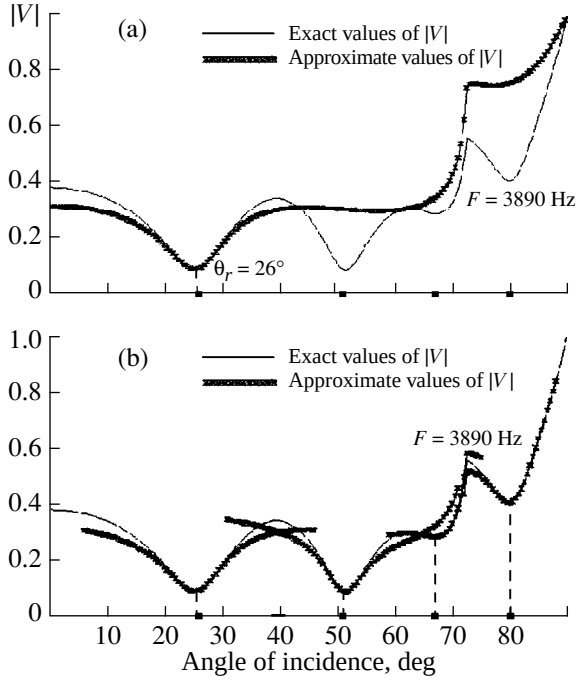

Fig. 6. Same as in Fig. 5 for the angular resonances.

The sum of resonances is taken symbolically, because the expansion is valid only in the vicinity of the resonance minima and fails away from them.

In this section, we illustrate the efficiency of using the resonance approach for the bottom model in the form of an elastic layer overlying an elastic halfspace (table) by the example of the frequency-angular resonances. Figure 5a compares the calculations of the frequency dependences of the reflection coefficients, namely, the calculations made by the exact formula (9), using the Thomson–Haskell matrix technique and those made by the approximate formulas (22) obtained by expanding formula (9) in a series. As expected, near the first frequency resonance, a very good agreement is observed, and the approximation fails between the resonance peaks (the exact results are shown by the solid line, and the curves corresponding to the approximate expression are indicated by the markers). Similar calculations are presented in Fig. 5b, when the expansion of the reflection coefficient is a sum of 22 resonance terms. If the frequency is fixed, F = 3890 Hz, we can obtain the angular dependences of the reflection coefficients near the first angular resonance (Fig. 6a) and near four angular resonances (Fig. 6b). In this case, we also obtain a good agreement between the results near the resonances.

CONCLUSION

Using the Thomson–Haskell matrix technique, the exact analytical expression was obtained for the complex reflection coefficient for a sea bottom model in the form of an elastic layer overlying an elastic halfspace. Characteristic equations are obtained in resonance conditions, and the roots of these equations are found. These roots determining the positions of the frequency and angular resonances for longitudinal and transverse waves. An approximate expression for the reflection coefficient is obtained, which describes the process of resonance reflection of plane waves for the chosen model of the bottom. The exact and approximate expressions for the reflection coefficients are compared, and a good agreement between the results is obtained near the two types of resonances.

ACKNOWLEDGMENTS

This work was supported by the Russian Foundation for Basic Research, project no. 97–05–64712.

REFERENCES

1. P. J. Vidmar and T. L. Foreman, J. Acoust. Soc. Am. **66**, 1830 (1979).
2. L. M. Lyamshev, Akust. Zh. **43**, 576 (1997) [Acoust. Phys. **43**, 498 (1997)].
3. X. L. Bao, P. K. Raju, and H. Überall, J. Acoust. Soc. Am. **105**, 2704 (1999).
4. H. Ogi, H. Ledbetter, S. Kim, and M. Hirao, J. Acoust. Soc. Am. **106**, 660 (1999).
5. R. F. Keltie, J. Acoust. Soc. Am. **103**, 1855 (1998).

6. G. Frisk, in *Proceedings of the 4th ECUA, Italy, 1998*, Vol. 1, p. 511.
7. B. T. Cox and P. Joseph, J. Acoust. Soc. Am. **105**, 1042 (1999).
8. O. A. Godin and D. M. F. Chapman, Boll. Geofis. Teor. Appl. **40**, 36 (1999).
9. R. Fiorito, W. Madigosky, and H. Überall, J. Acoust. Soc. Am. **66**, 1857 (1979).
10. A. Nagl, H. Überall, and W. R. Hoover, IEEE Trans. Geosci. Remote Sens. **GE-20** (3), 332 (1982).
11. A. Hagl, H. Überall, and Yoo Kwang-Bock, Inverse Probl. **1**, 99 (1985).
12. R. Fiorito, W. Madigosky, and H. Überall, J. Acoust. Soc. Am. **69**, 897 (1981).
13. R. F. Keltie, J. Acoust. Soc. Am. **103**, 1855 (1998).
14. V. I. Volovov, *Sound Reflection from the Ocean Bottom* (Nauka, Moscow, 1993).
15. L. M. Brekhovskikh and O. A. Godin, *Acoustics of Layered Media* (Nauka, Moscow, 1989; Springer, New York, 1990).
16. N. S. Ageeva, V. D. Krupin, V. P. Perelygin, and N. V. Studenichnik, Akust. Zh. **40**, 181 (1994) [Acoust. Phys. **40**, 159 (1994)].
17. V. A. Grigor'ev, B. G. Katsnel'son, and V. G. Petnikov, Akust. Zh. **42**, 712 (1996) [Acoust. Phys. **42**, 627 (1996)].
18. V. M. Kurtepov, Akust. Zh. **41**, 106 (1995) [Acoust. Phys. **41**, 90 (1995)].
19. W. Thomson, J. Appl. Phys. **21**, 89 (1950).
20. N. Haskell, Bull. Seismol. Soc. Am. **43** (1), 17 (1953).
21. L. A. Molotkov, *Matrix Method in the Theory of Wave Propagation in Layered Elastic and Fluid Media* (Nauka, Leningrad, 1984).

Translated by Yu. Lysanov

Acoustical Physics, Vol. 46, No. 5, 2000, pp. 613–615. Translated from Akusticheskiĭ Zhurnal, Vol. 46, No. 5, 2000, pp. 698–701.

Acoustic Resonance in Turbine Centrifugal Pumps

V. L. Khitrik

Chemical Machinery Research Institute, Sergiev Posad, Moscow oblast, 141300 Russia

Received September 1, 1999

Abstract—The sound excitation inside a centrifugal pump by a source of pressure oscillations positioned in the inlet cross-section of the impeller is considered theoretically. The specific feature of the problem formulation is that the blade channels and the channel between the impeller and the pump casing (the open diffuser) are considered as a single acoustic system. It is shown that, in certain conditions, a resonance-type sound excitation may occur inside the centrifugal pump. An equation for the determination of the resonance frequencies is obtained. © *2000 MAIK "Nauka/Interperiodica".*

The propagation of acoustic waves in the rotating duct of a turbine pump was theoretically studied in papers [1–3].

This paper treats the problem of sound propagation in the open diffuser of a turbine centrifugal pump (figure) with allowance for the effect of the rotating blade channels of the impeller.

Using a cylindrical coordinate system r, x, z (see figure), it is possible to describe the propagation of sound waves in the diffuser by the continuity equation and equation of motion, both of them linearized and integrated over the diffuser cross-section:

$$\frac{F}{c^2}\frac{\partial P}{\partial t} + \frac{\partial G}{\partial x} - \rho_0 b v(r = d_2/2, x, z, t) = 0, \qquad (1)$$

$$\frac{\partial G}{\partial t} + F\frac{\partial P}{\partial x} = 0, \qquad (2)$$

where P is the liquid pressure fluctuation in the diffuser; b is the width of the blade channel of the impeller at the diffuser inlet; F is the cross-sectional area of the diffuser, $F = hL$; h and L are the height of the diffuser and its width (which in the general case does not coincide with the blade channel width), h = const and L = const; c is the sound velocity in the medium at rest; ρ_0 is the steady-state density of the liquid, ρ_0 = const; $v(r = d_2/2, x, z, t)$ is the radial component of the oscillating particle velocity of liquid in the blade channel of the impeller at the diffuser inlet; z is the axial coordinate (perpendicular to the plane of the diffuser plot shown in the figure); x is the circular coordinate, $x = d_2\varphi/2$ (the positive direction of the x-axis coincides with the direction of the impeller rotation, and its origin lies in the initial 0–0 section (see figure) of the circular part of the diffuser); r is the radial coordinate; d_2 is the outer diameter of the impeller; φ is the angular coordinate; and t is time.

Equations (1) and (2) were derived under the following assumptions:

(1) the radial component of the oscillating particle velocity of liquid v is constant across the width of the blade channel ($r = d_2/2, -b/2 \le z \le b/2$) and is equal to zero outside the channel at the inner ($r = d_2/2, -L/2 \le z \le -b/2$; $r = d_2/2, b/2 \le z \le L/2$), outer ($r = d_2/2 + h, -L/2 \le z \le L/2$), and lateral ($z = -L/2, d_2/2 \le r \le d_2/2 + h$; $z = L/2, d_2/2 \le r \le d_2/2 + h$) walls of the diffuser;

(2) the pressure fluctuation is constant over the entire diffuser cross section ($d_2/2 \le r \le d_2/2 + h$; $-L/2 \le z \le L/2$);

(3) the diffuser height is much less than the outer radius of the impeller, $2h/d_2 \ll 1$.

The function $G(x, t)$ involved in the system of Eqs. (1), (2) and representing the fluctuation of the

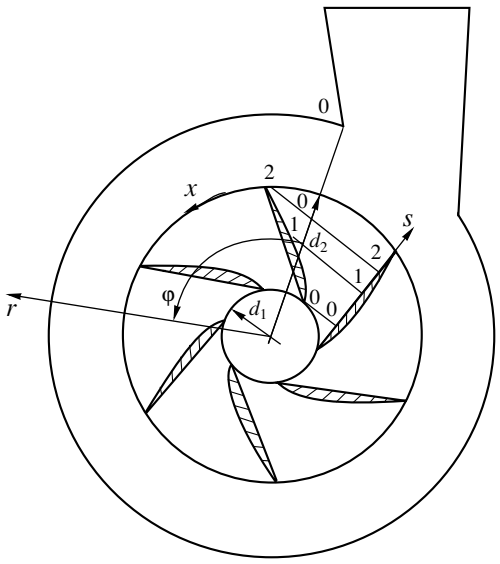

Schematic diagram of a turbine centrifugal pump with an open diffuser.

1063-7710/00/4605-0613$20.00 © 2000 MAIK "Nauka/Interperiodica"

mass flow rate of liquid in the diffuser was determined by the formula

$$G(x, t) = \rho_0 \int_{-L/2}^{L/2} \left(\int_{d_2/2}^{d_2/2 + h} u(r, x, z, t) dr \right) dz. \quad (3)$$

Here, u is the component of the oscillating particle velocity of liquid in the diffuser in the circular direction x.

Differentiating Eqs. (1) and (2) with respect to time t and the circular coordinate x, respectively, and subtracting term-by-term the second equation from the first one, we eliminate the function $G(x, t)$. As a result, we obtain

$$\frac{F}{c^2}\frac{\partial^2 P}{\partial t^2} - F\frac{\partial^2 P}{\partial x^2} - \frac{\partial}{\partial t}[\rho_0 b v(r = d_2/2, x, z, t)] = 0. \quad (4)$$

This equation involves the radial fluctuating velocity of liquid in the blade channel of the impeller at the diffuser inlet, $v(r = d_2/2, x, z, t)$. Therefore, in solving Eq. (4), it is necessary to consider the propagation of sound waves in the open diffuser and the rotating blade channels of the impeller as in a single acoustic system.

Let us introduce the following additional simplifications: all channels are narrow in comparison with the sound wavelength; the effects of the medium flow and the impeller rotation are neglected; and the effect of the outlet opening of the open diffuser is also neglected.

Then, the propagation of sound waves in the rotating blade channels, which have cylindrically divergent cross sections, can be described by the Webster equation [4]

$$\frac{\partial^2 P_k}{\partial t^2} - \frac{c^2}{F_k(s)}\frac{\partial}{\partial s}\left(F_k(s)\frac{\partial P_k}{\partial s}\right) = 0, \quad (5)$$

where P_k is the liquid pressure fluctuation in the blade channel of the impeller, $F_k(s)$ is the varying cross-sectional area of the blade channel, and s is the longitudinal coordinate of the blade channel.

According to the Euler equation of motion, $\rho_0 \frac{\partial v_k}{\partial t} = -\frac{\partial P_k}{\partial s}$, for harmonic waves of frequency ω (which are considered in this paper), the longitudinal component of the oscillating particle velocity of liquid in the blade channel is related to the fluctuating pressure by the formula

$$v_k(s) = -\frac{1}{i\rho_0\omega}\frac{\partial P_k}{\partial s}, \quad (6)$$

where i is the imaginary unit.

Let us assume that the varying cross sections of the blade channels of the impeller vary according to the square law $F_k = F_k(s) \sim s^2$. Then, the sound field formed in the blade channels, which satisfies the Webster Eq. (5), can be represented in the form

$$P_k = P_- \frac{e^{-iks}}{s} + P_+ \frac{e^{iks}}{s}, \quad (7)$$

$$v_k = e^{-iks}\left(\frac{1}{s^2 i\rho_0\omega} + \frac{1}{\rho_0 cs}\right)P_- + e^{iks}\left(\frac{1}{s^2 i\rho_0\omega} - \frac{1}{\rho_0 cs}\right)P_+, \quad (8)$$

where P_- and P_+ are constants and k is the wave number, $k = \omega/c$. We write the expressions for P_k and v_k for $s = s_1$ and $s = s_2$, where s_1 and s_2 are the coordinates of the inlet and outlet cross-sections of the blade channel, and eliminate the parameters P_- and P_+ from these expressions. As a result, we obtain the expressions relating the amplitudes of the radial velocity fluctuations and pressure at the blade channel outlet, v^r_{k2} and P_{k2}, to the corresponding amplitudes at the blade channel inlet, v^r_{k1} and P_{k1}:

$$v^r_{k2} = \frac{s_1}{s_2}\left[v^r_{k1}\frac{\sin\beta_2}{\sin\beta_1}\left(1 - \frac{\tan kl}{ks_2}\right)\cos kl - P_{k1}\frac{i\sin\beta_2}{\rho_0 c}\left(1 + \frac{1}{k^2 s_1 s_2} - \frac{l}{k^2 s_1 s_2}\cot kl\right)\sin kl\right], \quad (9)$$

$$P_{k2} = \frac{s_1}{s_2}\left[-v^r_{k1}\rho_0 c\frac{i\sin kl}{\sin\beta_1} + P_{k1}\left(1 + \frac{\tan kl}{ks_1}\right)\cos kl\right], \quad (10)$$

where l is the length of the blade channel of the impeller and β_1 and β_2 are the angles of the blade orientation at the inlet and outlet of the impeller, respectively.

Then, relying on the experimental data obtained by E.A. Folomeev from the studies of the dynamical characteristics of centrifugal pumps, we assume that the amplitude of the pressure fluctuations at the impeller inlet does not depend on the circular coordinate (in contrast to the amplitude of the radial component of the oscillating particle velocity of liquid). In this case, in expressions (9) and (10), we can set

$$P_{k1} = P_1 = \text{const}. \quad (11)$$

Using the conventional (in acoustics) assumption that the pressure fluctuation at the outlet of the impeller blade channel is continuous and substituting expressions (9) and (10) into Eq. (4) with allowance for condition (11), we arrive at an inhomogeneous linear equation in the function $v(r = d_1/2, x) = v_1(x)$:

$$\frac{\partial^2 v_1}{\partial x^2} + \left[\left(\frac{\omega}{c}\right)^2 - \left(1 - \frac{\tan[\omega l/c]}{\omega s_2/c}\right) \times \frac{b\cot(\omega l/c)\sin\beta_2}{F}\left(\frac{\omega}{c}\right)\right] v_1 = -i\frac{\sin\beta_1}{\rho_0 c}P_1 \times \left[\left(\frac{\omega}{c}\right)^2\left(1 + \frac{\tan[\omega l/c]}{\omega s_1/c}\right)\cot(\omega l/c) + \left(1 + \frac{1}{(\omega/c)^2 s_1 s_2} - \frac{l}{(\omega/c)^2 s_1 s_2}\cot[\omega l/c]\right)\frac{b\sin\beta_2}{F}\left(\frac{\omega}{c}\right)\right]. \quad (12)$$

By a direct substitution, one can verify that the following expression is the solution to Eq. (12):

$$v_1(x) = C_1\exp\left[ix\sqrt{\left[\left(\frac{\omega}{c}\right)^2 - \left(1 - \frac{\tan[\omega l/c]}{\omega s_2/c}\right)\frac{b\cot(\omega l/c)\sin\beta_2}{F}\left(\frac{\omega}{c}\right)\right]}\right] + C_2\exp\left[-ix\sqrt{\left[\left(\frac{\omega}{c}\right)^2 - \left(1 - \frac{\tan[\omega l/c]}{\omega s_2/c}\right)\frac{b\cot(\omega l/c)\sin\beta_2}{F}\left(\frac{\omega}{c}\right)\right]}\right] - i\frac{\sin\beta_1}{\rho_0 c}P_1 \times \frac{\frac{\omega}{c}\left(1 + \frac{\tan[\omega l/c]}{\omega s_1/c}\right)\cot(\omega l/c) + \left(1 + \frac{1}{(\omega/c)^2 s_1 s_2} - \frac{l}{(\omega/c)^2 s_1 s_2}\cot[\omega l/c]\right)\frac{b\sin\beta_2}{F}}{\left[\left(\frac{\omega}{c}\right) - \left(1 - \frac{\tan[\omega l/c]}{\omega s_2/c}\right)\frac{b\cot(\omega l/c)\sin\beta_2}{F}\right]}, \quad (13)$$

where C_1 and C_2 are constants. To analyze solution (13), we divide the entire possible frequency band of the pressure oscillations, which are produced by the source positioned in the inlet cross section of the impeller, into two subbands

$$\omega < c\left(1 - \frac{\tan[\omega l/c]}{\omega s_2/c}\right)\frac{b\cot(\omega l/c)\sin\beta_2}{F} \quad \text{and}$$

$$\omega > c\left(1 - \frac{\tan[\omega l/c]}{\omega s_2/c}\right)\frac{b\cot(\omega l/c)\sin\beta_2}{F}.$$

In addition, we separately study the case

$$\omega = c\left(1 - \frac{\tan[\omega l/c]}{\omega s_2/c}\right)\frac{b\cot(\omega l/c)\sin\beta_2}{F}.$$

In the framework of the problem formulation considered in this paper, the solution to Eq. (12) should be periodic in the variable x. As one can see from expression (13), for the frequency band determined by the inequality

$$\omega < c\left(1 - \frac{\tan[\omega l/c]}{\omega s_2/c}\right)\frac{b\cot(\omega l/c)\sin\beta_2}{F},$$

the only type of solution to meet the condition of periodicity in x is the solution that is independent of the circular coordinate x, i.e., is constant. In this case, in-phase harmonic oscillations of frequency ω are excited inside the pump.

When

$$\omega > c\left(1 - \frac{\tan[\omega l/c]}{\omega s_2/c}\right)\frac{b\cot(\omega l/c)\sin\beta_2}{F},$$

harmonic oscillations produced by the pressure source in the inlet cross section of the impeller propagate in the open diffuser in the form of a plane sound wave with a constant amplitude.

If the oscillation frequency of the pressure source located in the inlet cross section of the impeller satisfies the condition

$$\omega = c\left(1 - \frac{\tan[\omega l/c]}{\omega s_2/c}\right)\frac{b\cot(\omega l/c)\sin\beta_2}{F}, \quad (14)$$

one can see from expression (13) that a resonance-type sound excitation occurs inside the centrifugal pump.

Hence, to avoid the resonance sound excitation, it is necessary to select the values of the structural parameters involved in expression (14) in such a way that, at a given frequency ω, the condition (14) be violated.

REFERENCES

1. M. Kurosaka and J. E. Caruthers, AIAA J. **20**, 1148 (1982).
2. V. L. Khitrik, Akust. Zh. **43**, 110 (1997) [Acoust. Phys. **43**, 96 (1997)].
3. K. P. Denisov and V. L. Khitrik, AIAA J. **35** (1) (1997).
4. A. G. Webster, Proc. Natl. Acad. Sci. USA **5**, 275 (1919).

Translated by E. Golyamina

Acoustical Physics, Vol. 46, No. 5, 2000, pp. 616–617. Translated from Akusticheskiĭ Zhurnal, Vol. 46, No. 5, 2000, pp. 702–703.

SHORT COMMUNICATIONS

Eigenfrequency Spectrum of a Finite Piezoceramic Shell

S. M. Balabaev, N. F. Ivina, and K. N. Shishlov

Far-Eastern State Technical Fishery University, ul. Lugovaya 52-B, Vladivostok, 690600 Russia

e-mail: omsdti@mail.primorye.ru

Received August 28, 1999

In the computer-aided calculations and analysis of the main parameters of piezoelectric elements and transducers, the finite-element method can be successfully employed [1–3]. Natural vibrations of piezoceramic cylindrical shells of finite dimensions with different types of polarization were considered in our previous publications [1, 4, 5]. We analyzed in detail the vibrations that are symmetric in the shell height, because only this type of vibrations are excited by an electric field in an isolated piezoceramic shell containing continuous electrodes and located in an unbounded space. The vibrations that are antisymmetric within the shell height were not taken into account in the analysis of the eigenfrequency spectra.

Later [7], in the study of a hydroacoustic antenna consisting of two water-filled piezoceramic shells, it was noted that, when the wave distance between the shells is small, an antisymmetric mode can be excited in them. This mode is a consequence of the acoustic interaction between the shells. Such a situation may also be observed in the presence of passive structural elements near the piezoceramic shell. The antisymmetric mode is a parasitic one, because it distorts the frequency characteristics and the directivity pattern of the hydroacoustic radiator for which the shell serves as the active element [7]. In addition, this mode leads to a highly nonuniform distribution of the particle velocity and pressure at the radiating surfaces. Such a nonuniformity restricts the maximal values of the radiation power, in particular, because of the appearance of high stresses and cavitation. Therefore, it is important to know the whole eigenfrequency spectrum of a finite piezoceramic shell, with the antisymmetric modes taken into account in order to avoid the case of the parasitic antisymmetric mode falling within the operating frequency band of the hydroacoustic radiator.

Let us consider a sectional (tangentially polarized) piezoceramic shell made of the TsTBS-3 ceramics whose parameters can be found in a handbook [6]. The outer radius of the shell is a, the height is l, and the wall thickness is h. In what follows, the dimensions of the shell will be determined by the dimensionless ratios l/a and h/a. The entire surface of the shell is assumed to be stress-free. We consider the resonance (short-circuit) and the antiresonance (no-load) modes [1, 5]. To calculate the eigenmode spectrum, we divide the whole axial section of the piezoceramic shell into circumferential, rectangularly shaped finite elements with eight nodes (with a quadratic approximation). In other words, the symmetry plane is not introduced, and the boundary conditions are not set at this plane, as was done before in the symmetric case [1, 5]. To separate the symmetric and antisymmetric modes, the same problem is additionally solved by dividing only half of the axial section of the shell into finite elements. In this case, the following mechanical boundary conditions are set at the shell symmetry plane: the nodal axial displacements are set equal to zero in the symmetric case, and the radial displacements are equal to zero in the antisymmetric case.

We calculated the four lower modes of the piezoceramic shell for $l/a \le 2$, because just this frequency range is of practical interest for the development of real hydroacoustic radiators [7]. Figure 1 presents the dependence of the dimensionless frequency parameter $k_t a$ on the relative height of the shell for two fixed values of the wall thickness, where k_t is the wave number of the transverse wave in the piezoceramics. The second ordinate axis shown on the right of the plots represents the quantity f/f_0, where f_0 is the frequency of the first symmetric mode for $l/a \ll 1$ and $h/a \ll 1$; i.e., in fact it is the frequency of the fluctuating vibrations of the piezoceramic ring in vacuum. As in our previous papers [1, 4, 5], the resonance frequencies are shown by solid lines, and the antiresonance frequencies are shown by dashed lines (when they do not coincide with the solid ones); the piezoactive regions of the spectrum are shown by hatching. The piezoactive regions are those within which the mechanical vibrations are efficiently excited by the electric field. In these regions, the difference between the resonance and antiresonance frequencies is substantial (and can be seen in the figure); this corresponds to a large value of the dynamical coefficient of electromechanical coupling [1, 4, 5]. The symbol a with the subscripts 1 and 2 indicates the antisymmetric modes, and the symbol s indicates the symmetric modes.

Let us note the characteristic features of the spectrum and its variation with increasing wall thickness of the shell. For a thin-walled shell (Fig. 1a), the first antisymmetric mode is near the piezoactive region of the first symmetric mode already for $l/a \ge 0.4$; when $l/a \ge 1.1$, it falls within this region. The resonance frequen-

1063-7710/00/4605-0616$20.00

cies of the first antisymmetric and first symmetric modes virtually coincide for $l/a > 0.4$ (within the scale of the plot). In the case $l/a \geq 0.9$, the second symmetric (flexural) mode also falls within the piezoactive region. In our previous papers [1, 7], we determined the optimal geometric dimensions of a water-filled (freely flooded) piezoceramic shell (a two-resonance system). The optimal dimensions are those for which the transmitting response is approximately the same at the volume and radial resonances, and the nonuniformity of the frequency characteristic does not exceed 3 dB. When the shell height is less than the optimal one, the transmitting response is higher at the volume resonance than at the radial one, and when the shell height exceeds the optimal value, the situation is opposite. The optimal geometric height of a water-filled piezoceramic shell with the wall thickness $h/a = 0.1$ is $l/a \approx 1$ [1, 7]. Therefore, the flexural mode being a parasitic one distorts the frequency characteristics and the directional pattern of an isolated water-filled piezoceramic shell positioned in an unbounded space. This fact was already noted in earlier theoretical [1, 7, 8] and experimental studies [8]. In the presence of either a piezoceramic shell or a passive structural element near the shell under study, the parasitic antisymmetric mode will also distort the characteristics of the radiator whose active element is the water-filled piezoceramic shell [7].

As the thickness of the shell walls increases, the optimal height of the shell decreases, and, at $h/a = 0.25$, the optimal height is equal to 0.8 [1]; when the wall thickness is less than 0.3, the optimal height will be less than 0.8. In this case, the flexural mode will not fall within the operating frequency band of the radiator (Fig. 1b) and will not distort its characteristics. The antisymmetric mode will also be below the first symmetric mode and will not affect the characteristics of the radiator. We note that the optimal height of piezoceramic shells in a hydroacoustic antenna is less than the optimal height of an isolated piezoceramic shell, and it depends on the distance between the shells [7]. On further increase in the shell wall thickness, the aforementioned tendency in the antisymmetric mode behavior is retained. When the wall thickness is $h/a = 0.5$, the antisymmetric mode approaches the piezoactive region of the symmetric mode only at $l/a = 1.6$. Thus, knowing the eigenfrequency spectra with the antisymmetric modes taken into account, one can select the appropriate wall thickness for the piezoceramic shell so as to avoid the effect of the parasitic antisymmetric mode on the shell characteristics.

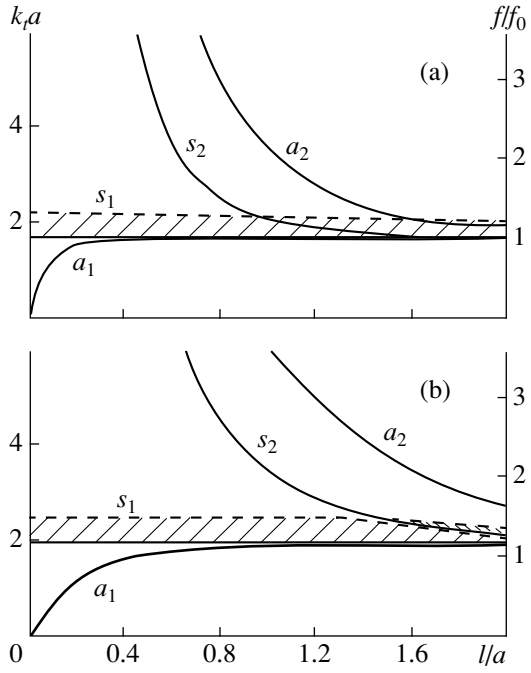

Fig. 1. Eigenfrequency spectra of finite sectional piezoceramic shells; h/a = (a) 0.1 and (b) 0.3.

REFERENCES

1. S. M. Balabaev and N. F. Ivina, *Computer Simulation of Vibrations and Radiation of Bodies of Finite (Finite Element and Boundary Element Methods)* (Dal'nauka, Vladivostok, 1996).
2. J.-C. Debus, B. Dubus, and J. Coutte, J. Acoust. Soc. Am. **103**, 3336 (1998).
3. D. Ekeom, B. Dubus, and C. Granger, J. Acoust. Soc. Am. **104**, 2779 (1998).
4. S. M. Balabaev and N. F. Ivina, Akust. Zh. **34**, 165 (1988) [Sov. Phys. Acoust. **34**, 90 (1988)].
5. S. M. Balabaev and N. F. Ivina, Prikl. Mekh. **25** (10), 37 (1989).
6. *Piezoceramic Transducers*, Ed. by S. I. Pugachev (Sudostroenie, Leningrad, 1984).
7. S. M. Balabaev, Akust. Zh. **44**, 5 (1998) [Acoust. Phys. **44**, 1 (1998)].
8. R. Bossut and J.-N. Decarpigny, J. Acoust. Soc. Am. **86**, 1234 (1989).

Translated by E. Golyamina

Acoustical Physics, Vol. 46, No. 5, 2000, pp. 618–620. Translated from Akusticheskiĭ Zhurnal, Vol. 46, No. 5, 2000, pp. 704–706.

SHORT COMMUNICATIONS

The Effect of Inaccuracy in the *a priori* Information in Estimating the Mean Temperature of the Water Layer in Ocean Acoustic Tomography

A. L. Virovlyanskiĭ, A. Yu. Kazarova, L. Ya. Lyubavin, and A. A. Stromkov

Institute of Applied Physics, Russian Academy of Sciences,
ul. Ul'yanova 46, Nizhni Novgorod, 603600 Russia
e-mail: viro@hydro.appl. sci-nnov.ru

Received September 24, 1999

The basic difficulty of the classical scheme of the Munk–Wunsch ocean acoustic tomography [1] consists in the fact that the system of linear equations, which relate the measured travel time variations of sound pulses along separate rays (the so-called ray arrival times) with the temperature field parameters subject to reconstruction, is underdetermined. This occurs, because, in order to describe in detail the temperature field, one has to reconstruct a great number of parameters that usually, particularly at long tracks, far exceeds the number of resolved rays which determine the number of equations in the above-mentioned linear system. A simple method to diminish the underdeterminancy is the "roughening" of the temperature field model by decreasing the number of its parameters. This can often be accomplished in the following way: the field of temperature inhomogeneities is expanded in empirical orthogonal functions (EOF), and only the several first functions making the main contribution are retained [2, 3]. Actually, ignoring the higher order EOF means distortion of the *a priori* information on the statistics of the inhomogeneities under reconstruction. In this paper, we use a specific example to show that such an inaccuracy in the environmental model may lead to noticeable errors in solving an inverse problem.

Here, we consider the problem of reconstruction of the mean temperature. The algorithm used for solving the inverse problem is briefly described below. A more detailed description of the idea of this algorithm was presented in our previous paper [4]. The field of the sound velocity inhomogeneities (proportional to the temperature inhomogeneities) can be presented as $\delta c(z) = \sum_n x_n \varphi_n(z)$, where $\varphi_n(z)$ is the nth EOF. We consider the expansion coefficients x_n as elements of the vector $\mathbf{x}$. The method of ocean acoustic tomography implies the reconstruction of this vector by way of solving the system of linear equations of the type $\mathbf{y} = A\mathbf{x}$, where $\mathbf{y}$ is the vector whose elements are the ray arrival times, and the elements of the matrix A are $A_{mn} = \int \frac{ds\varphi_n(z_m(s))}{c^2}$. The rank of the matrix A is equal to $M \times N$, where M is the number of the resolved rays and N is the number of the empirical orthogonal functions. Here, the index m denotes the order number of a ray arriving at the point of observation; the integration is performed along the trajectory of the mth ray, $z = z_m(s)$; ds is the element of the arc length of this ray; and c is the unperturbed sound velocity at a current point of the trajectory. The *a priori* information on the statistics of inhomogeneities is given by the parameters of the EOF and by the correlation matrix K of the amplitudes of these functions, the rank of this matrix being $N \times N$ and its elements being $K_{mn} = \langle x_m^2 \rangle \delta_{mn}$. The matrix is diagonal due to the assumption that the amplitudes of orthogonal functions are statistically independent.

The mean water temperature in a layer $z_1 < z < z_2$ is proportional to the scalar product $\gamma = \mathbf{g}^T\mathbf{x}$, where the superscript T means transposition and the mth element of the weight vector $\mathbf{g}$ is equals to $g_m = \int_{z_1}^{z_2} dz\, \varphi_m(z)$.

The optimal linear estimate of the quantity γ, which we denote by $\hat{\gamma}$, minimizes the mean square $\langle(\gamma - \hat{\gamma})^2\rangle$ and is expressed as $\hat{\gamma} = \mathbf{s}^T\mathbf{y}$ [4], where

$$\mathbf{s} = (AKA^T)^{-1}AK\mathbf{g}. \tag{1}$$

The relative error of this estimate is determined by the expression

$$\varepsilon = \langle(\gamma - \hat{\gamma})^2\rangle / \langle\gamma\rangle^2 = 1 - \frac{\mathbf{g}^T KA^T (AKA^T)^{-1}(AK)\mathbf{g}}{\mathbf{g}^T K\mathbf{g}}. \tag{2}$$

This expression was obtained on the assumption that the correlation matrix of inhomogeneities is exactly known. The rejection of a part of the EOF is equivalent to replacing the true matrices K and A, as

1063-7710/00/4605-0618$20.00

well as the vector **g** in (1), by truncated matrices K_c and A_c and by the vector $\mathbf{g}_c$ that are obtained by rejecting the elements corresponding to the neglected EOF. Now, in place of (2), the relative error of the reconstruction of the mean temperature is determined by the expression (see [4])

$$\varepsilon = 1 - \frac{\mathbf{g}_c^T K_c A^T (A_c K_c A_c^T)^{-1} (2A_c K_c - AKA^T (A_c K_c A_c^T)^{-1} A_c K_c)\mathbf{g}_c}{\mathbf{g}^T K \mathbf{g}}. \quad (3)$$

It is of practical interest to study the question of the extent to which the accuracy of the reconstruction is sensitive to the choice of the number of the EOF taken into account. In other words, what is the price that must be paid for the incompleteness of the *a priori* information used.

In this paper, the answer to this question is given in the application to the conditions characteristic of the western part of the Mediterranean Sea, where a group of researchers from the Institute of Applied Physics of the Russian Academy of Sciences participated in an international tomography experiment in the summer of 1994. Aboard the research vessel *Akademik Sergeĭ Vavilov*, they measured the hydrological characteristics and recorded acoustic signals from stationary autonomous sources. A more detailed description of the measurements and the results obtained is presented in papers [5, 6]. From the sound velocity profiles (see Fig. 1) measured in the course of this expedition, an estimate of the correlation matrix of the medium inhomogeneities was obtained, and the EOF (which are the eigenvectors of this matrix) were calculated. The calculations of the EOF were performed using the data of 140 sound velocity profiles measured in June and July 1994. Note that the main inhomogeneities are concentrated in a layer extending from the surface to a depth of 200 m. Therefore, the EOF rapidly decrease at depths exceeding 200 m.

As an unperturbed (reference) sound velocity profile, we used a range-independent profile averaged along the track, which is shown in Fig. 1 by the solid curve. The depths of the source and the receiver were 150 and 125 m, respectively, and the length of the track was 250 km. The numerical calculation by a ray program for a model of a plane-layered waveguide showed that pulses arriving over separate rays are not resolved in the received signal (it is assumed that the duration of the probing signal is 0.01 s). However, five quartets of pulses arriving over five quartets of steep rays, which have no contacts with the bottom, are well resolved. An example of such a calculation and the comparison of its results with experimental data is available in our previous paper [5]. The question on the reconstruction of the mean temperature in a layer from the measurements of gravity centers of such pulse quartets with the use of formulas (1)–(3) is considered in [4]. In Fig. 2, curve *1* shows the dependence of the relative error of the reconstruction of the mean velocity in a water layer extending from the surface to a depth of L on the layer thickness (i.e., on the parameter L). This calculation was carried out by formula (2) on condition that all EOF are known. As is seen, the value of the relative error depends on the layer thickness in a nonmonotone manner, although the tendency toward the error decrease with the increase in the layer thickness is quite pronounced. The details in the behavior of curve *1* are determined by the field ray structure and the structure of the EOF. The depth intervals where some EOF significantly differ from zero, as well as the relative contributions of different EOF determined by the diagonal elements of the correlation matrix, are essential. For example, in our case, the first EOF is "concentrated" in the depth interval from zero to about 50 m, and its squared mean amplitude $K_{11} = \langle x_1^2 \rangle$ is seven times as great as the corresponding values for other EOF. The maximum of this function is located at a depth of 25 m. Thus, the temperature fluctuates most strongly in a very thin subsurface layer. However, this does not mean that the reconstruction error of the mean temperature in this layer must be large. Among rays arriving at the receiver, there are rays reflected from the surface and, therefore, transmitted through this layer (see [4]). Variations in the traveling times of signals along such rays are largely determined by the influence of strong sub-

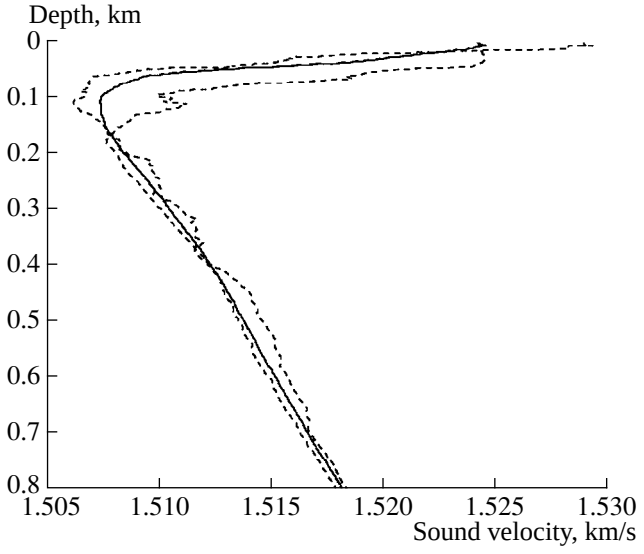

Fig. 1. Two sound velocity profiles typical for the western part of the Mediterranean Sea (dotted lines) and the profile obtained by averaging over all measurements carried out in June and July 1994 (solid line).

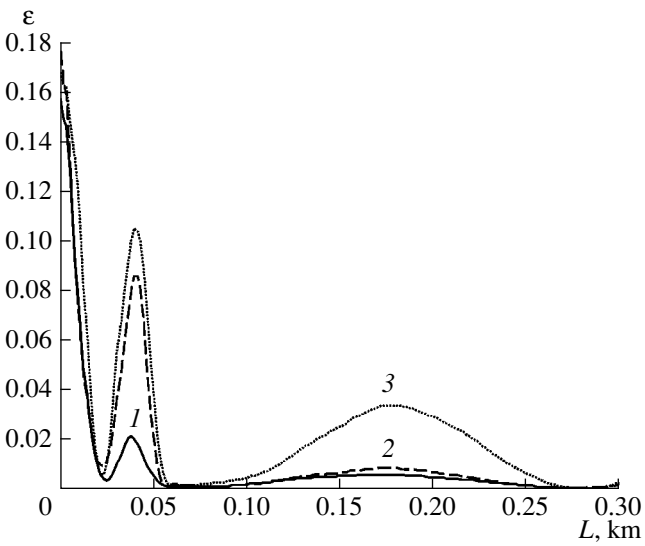

Fig. 2. Relative error of the reconstruction of the mean temperature of a 250-km-long horizontal layer versus the layer depth L (*1*) with all, (*2*) the first eight, and (*3*) the first seven empirical orthogonal functions taken into account.

surface inhomogeneities. In solving the inverse problem, the contributions of these inhomogeneities are well reconstructed, as witnessed by the presence of a minimum in curve *1* in the vicinity of $L = 25$ m. Remind that we deal here with the relative reconstruction error of the mean temperature. The absolute error at this minimum may exceed the error for layers with $L > 25$ m.

The dependence of ε on the layer thickness will be almost the same as in curve *1*, if we take into account only the first ten EOF and use formula (3) for calculating the relative error ε. However, it is obvious that a further decrease in the number of the EOF taken into account will eventually lead to a considerable loss in the reconstruction accuracy. Figure 2 shows that this happens when the number of the considered EOF decreases down to eight, and the deviation is even greater for seven EOF. As the analysis of the correlation matrix of inhomogeneities shows, the total contribution of all EOF with the numbers $n > 7$ is small. So, the rejection of the field component formed by these EOF reduces the mean square of sound velocity inhomogeneities only by 4%.

The simple example considered above demonstrates the importance of using an adequate *a priori* statistical model of the medium inhomogeneities. Even a slight roughening can noticeably degrade the quality of the reconstruction of the inhomogeneity parameters. This paper is intended to focus attention on this potential source of errors.

ACKNOWLEDGMENTS

This work was supported by the Russian Foundation for Basic Research, project no. 97-05-65657.

REFERENCES

1. W. Munk and C. Wunsch, Deep-Sea Res., Part A **26**, 123 (1979).
2. B. D. Dushaw, IEEE J. Ocean Eng. **24**, 215 (1999).
3. E. K. Skarsoulis and G. A. Athanassoulis, J. Acoust. Soc. Am. **104**, 3313 (1998).
4. A. L. Virovlyanskiĭ, A. Yu. Kazarova, and L. Ya. Lyubavin, Akust. Zh. **44**, 39 (1998) [Acoust. Phys. **44**, 29 (1998)].
5. A. A. Stromkov, A. L. Virovlyanskiĭ, A. Yu. Kazarova, and L. Ya. Lyubavin, Akust. Zh. **45**, 473 (1999) [Acoust. Phys. **45**, 420 (1999)].
6. D. I. Abrosimov, A. F. Erkin, A. Yu. Kazarova, *et al.*, Akust. Zh. **41**, 632 (1995) [Acoust. Phys. **41**, 556 (1995)].

Translated by Yu. Lysanov

Acoustical Physics, Vol. 46, No. 5, 2000, pp. 621–623. Translated from Akusticheskiĭ Zhurnal, Vol. 46, No. 5, 2000, pp. 707–709.

SHORT COMMUNICATIONS

Nonlinear Vibroacoustic Processes at the Surface of a Biological Tissue

B. N. Klochkov

Institute of Applied Physics, Russian Academy of Sciences, ul. Ul'yanova 46, Nizhni Novgorod, 603600 Russia

e-mail: klochkov@appl.sci-nnov.ru

Received October 27, 1999

Despite the considerable amount of studies of the nonlinear acoustic properties of various biological tissues with the use of longitudinal ultrasonic waves (e.g., [1, 2]), the nonlinear properties of tissues in the process of their natural functioning remain little investigated. The importance of such investigations is connected with an opportunity to develop new criteria for evaluating the tissue's state on the basis of the shear acoustic wave propagation in the tissue under test [3, 4].

This paper is devoted to the experimental studies of nonlinear surface elastic waves propagating in a biological tissue with various strains of muscular layers, which are monitored by measuring the "sounds of muscles," i.e., the acoustic emission inherent in the tissue, structure. A set of acoustic equipment produced by the Bruel and Kjaer (Denmark), Robotron (Germany) and domestic companies was used. Vibrations were set by a vibrator and measured by an accelerometer within the frequency range 3–400 Hz. The acoustic emission of the muscular layers was also measured by an accelerometer with averaging over five realizations. The object of the studies was the internal surface of a human forearm. Waves on the tissue's surface were excited by a seismic method using a vibrator 10 mm in diameter oscillating harmonically at a preset frequency (or two vibrators oscillating at different frequencies). The constant penetration of the vibrator head into a soft tissue was 3 mm. The acoustic fields, including the levels of harmonics, were measured at different distances from the excitation point [5, 6]. It was demonstrated that the increase in the level of the acoustic emission from muscular layers in the case of their strain correlated within the low-frequency range 20–50 Hz with an increase in the propagation velocity of a surface wave and a decrease in its damping factor. With increasing strain, the phase-frequency and amplitude-frequency characteristics of the tissue become more monotonic.

When two vibrators acted upon a tissue's surface with a distance of 8 cm between them and different operating frequencies, in particular, at $f_1 = 61$ Hz and $f_2 = 133$ Hz, nonlinear acoustic effects manifested themselves by the presence of the sum frequency ($f_1 + f_2 = 194$ Hz), the difference frequency ($f_2 - f_1 = 72$ Hz), and other combination and multiple frequencies of the acceleration A_g. Figure 1 gives the spectrum of A_g on the tissue's surface in the middle of the distance between the vibrators. The muscular tremor ($f_t = 9$–12 Hz) and the Oster–Grimaldi "sounds of muscles" ($f_m = 21$–25 Hz) exist within the low-frequency part of the spectrum up to 50 Hz.

In the case of a single vibrator acting upon the tissue at the constant frequency $f = 130$ Hz, the acceleration A and the force of action upon the tissue F were measured at the site of excitation (at the head). Simultaneously, the acceleration A at the basic frequency and its harmonics was measured with an accelerometer probe at different distances x from the head edge. The level of A of the head vibrations did not depend on the tissue's state, and its harmonics were negligibly small in contrast to the harmonics of F. A natural relaxed state of the forearm tissue could transform into a strained state when the arm developed active muscular tension (in particular, 5 kg). Considerable influence of the tissue's state on the level and ratio of harmonics was detected.

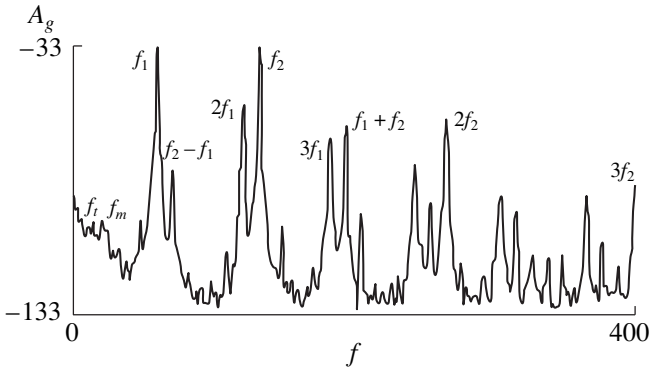

Fig. 1. Spectrum of the tissue's surface acceleration A_g under a two-frequency action (the amplitudes are $12.3g$ and $10.6g$ for f_1 and f_2, respectively); A_g is expressed in dB relative to 1 V, and the frequency f is expressed in Hz.

1063-7710/00/4605-0621$20.00

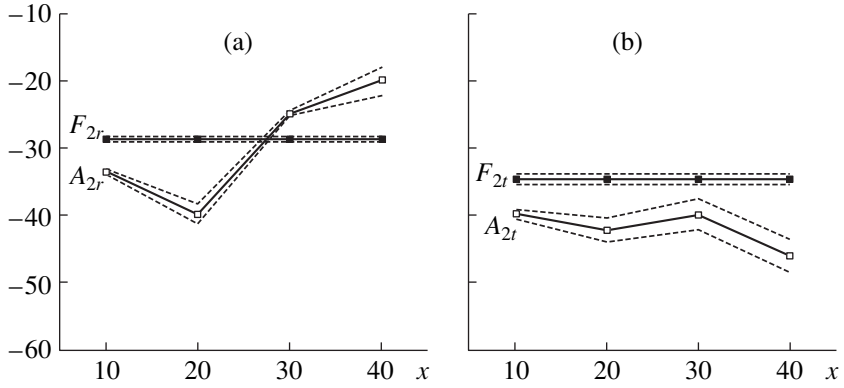

Fig. 2. Second harmonics of the acceleration A_2 and force F_2 as functions of the distance x (a) in the relaxed state of the tissue (the subscript r) and (b) in the strained state (the subscript t); A_2 is expressed in dB with respect to the first harmonic A_1, F_2 is expressed in dB with respect to the first harmonic F_1, and x is expressed in mm. The dashed lines indicate the scatter of data.

In the case of the relaxed state, the acceleration of the first (basic) harmonic A_1 (dB/V) at the probe decreases monotonically with the increase in x. Its drop at 30 mm is 29 dB (a relatively strong damping), while, in the case of the strained state, A_1 decreases slower (only 9 dB at 30 mm). The behavior of the second harmonics is nonmonotonic with distance (Fig. 2). The relaxed state is the most nonlinear one: as the distance from the source grows, the relative level of the second harmonic of acceleration at the probe $A_{2r}(\mathrm{dB}/A_{1r})$ starts to exceed the second harmonic of the force at the site of excitation $F_{2r}(\mathrm{dB}/F_{1r})$. In the strained state, the tissue becomes stiffer, and the level of the second harmonics at the probe $A_{2t}(\mathrm{dB}/A_{1t})$ is always lower than their level at the head $F_{2t}(\mathrm{dB}/F_{1t})$. The third harmonics behave analogously. In the relaxed state of the tissue, the relative level of the third harmonic $A_{3r}(\mathrm{dB}/A_{1r})$ grows monotonically with the increase in x, and, starting from $x = 23$ mm, it becomes higher than that of the third harmonic $F_{3r}(\mathrm{dB}/F_{1r})$ at the site of excitation, their difference attaining 17 dB at $x = 40$ mm. In the strained state of the tissue, $A_{3t}(\mathrm{dB}/A_{1t})$ at the probe is by 7–11 dB lower than $F_{3t}(\mathrm{dB}/F_{1t})$ at the head for all x.

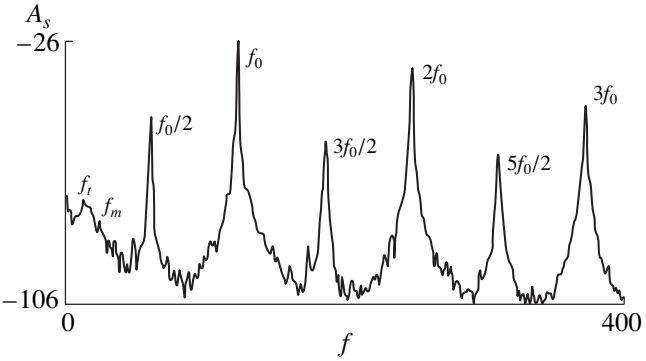

Fig. 3. Spectrum of the tissue surface acceleration A_s in the case of the excitation by the amplitude $48.5g$; A_s is expressed in dB with respect to 1 V; the frequency f is expressed in Hz.

The subharmonics of acceleration A_s ($f_0/2$, $3f_0/2$, $5f_0/2$ and others) were detected at the distance $x = 40$ mm from the site of excitation at certain frequencies, in particular, at $f_0 = 124$ Hz, when the level of action upon the tissue surface was sufficiently high (see Fig. 3). The level of the subharmonic $f_0/2$ could be rather high: by 13–15 dB lower than the excitation level at the selected frequency f_0. In this case, the subharmonics of F may arise at the head, but not those of A. The reason for this may be the nervous-muscular vibroreflex [7]. The tremor f_t and the vibroacoustic emission f_m from muscular layers manifest themselves at low frequencies. Figure 4 gives the results of measurements of the vibroacoustic emission from muscular layers of a forearm. The measurements were performed simultaneously by an accelerometer and a microphone positioned at a distance of 1.2 cm.

The theoretical wave estimates (the influence of both the near nonlinear wave field from the exciter and the nonlinear Rayleigh wave is present [8]) show that the explanation of the relatively high levels of harmonics in a soft tissue presumably lies in the relatively large values of the Mach number $M = \omega u/c = 0.02$–1.2, since the amplitude of the head displacement in the frequency range 100–200 Hz can be $u = 0.1$–2 mm, and the velocity of shear waves at the surface of a soft biological tissue can be $c = 2$–3 m/s. Using the nonlinear parameter of a tissue $n = 8$–9, it is possible to estimate the characteristic nonlinear effects and demonstrate that they manifest themselves at distances of several wavelengths.

In conclusion, we note that the considered acoustic phenomena on the surface of a live tissue indicate an opportunity to study the tissue state by purely acoustic methods. The results of this study are important from the point of view of quantitative estimation of both the

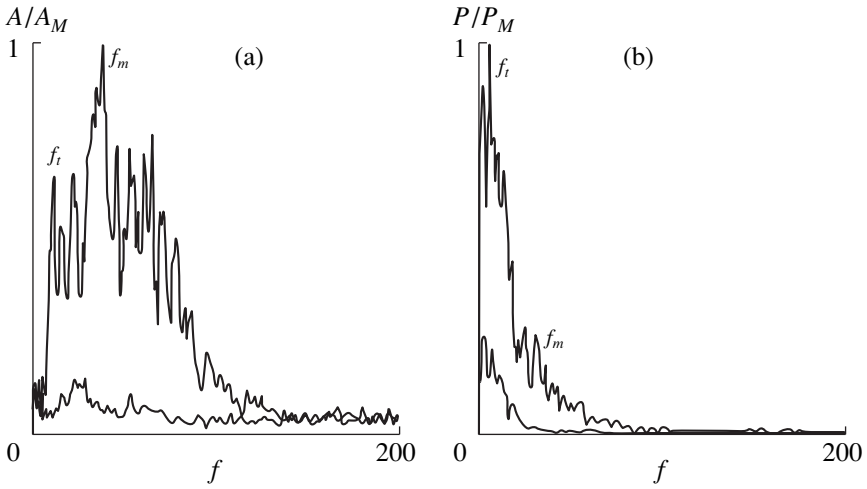

Fig. 4. Normalized spectra of (a) the vibroacoustic emission of acceleration A/A_M and (b) the pressure P/P_M; the frequency f is expressed in Hz. The upper curve corresponds to the strained state of the tissue (5 kg), and the lower curve corresponds to the relaxed state.

tissue's state and the changes in its nonlinear acoustic properties.

ACKNOWLEDGMENTS

This work was supported by the Russian Foundation for Basic Research, project no. 97-02-18612.

REFERENCES

1. J. D'hooge, B. Bijnens, J. Nuyts, *et al.*, J. Acoust. Soc. Am. **106**, 1126 (1999).
2. *Physical Principles of Medical Ultrasonics*, Ed. by C. R. Hill (Ellis Horwood, Chichester, 1986; Mir, Moscow, 1989).
3. V. G. Andreev, V. N. Dmitriev, Yu. A. Pishchal'nikov, *et al.*, Akust. Zh. **43**, 149 (1997) [Acoust. Phys. **43**, 123 (1997)].
4. K. Kameyama, T. Inoue, I. Yu. Demin, *et al.*, Signal Process. **53**, 117 (1996).
5. B. N. Klochkov and E. M. Timanin, Akust. Zh. **40**, 953 (1994) [Acoust. Phys. **40**, 844 (1994)].
6. B. N. Klochkov and E. M. Timanin, in *Nonlinear Acoustics of Solid States: VIII Session of the Russian Acoustical Society* (Intelservis, Nizhni Novgorod, 1998), pp. 273–276.
7. B. J. Martin and H.-S. Park, Eur. J. Appl. Physiol. **75**, 504 (1997).
8. E. Y. Knight, M. F. Hamilton, Y. A. Il'inskii, and E. A. Zabolotskaya, J. Acoust. Soc. Am. **102**, 2529 (1997).

Translated by M. Lyamshev

Acoustical Physics, Vol. 46, No. 5, 2000, pp. 624–626. Translated from Akusticheskiĭ Zhurnal, Vol. 46, No. 5, 2000, pp. 710–712.

CHRONICLE

Nikolaĭ Nikolaevich Andreev (On the 120th Anniversary of His Birth)

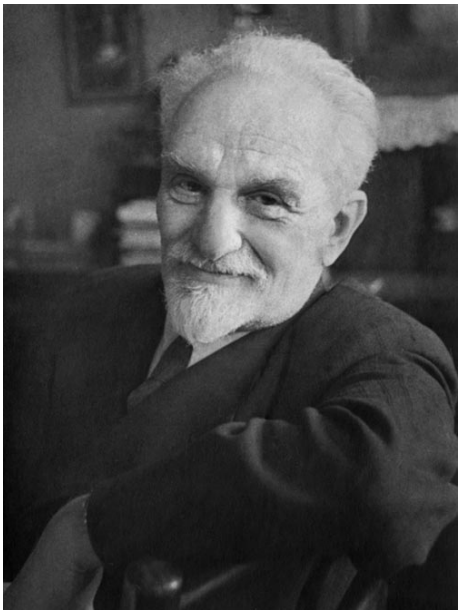

It is now 30 years since the death of Academician Nikolaĭ Nikolaevich Andreev, one of the founders of the now-eponymous Acoustics Institute of the Russian Academy of Sciences. He was the founder and first Editor-in-Chief of the *Akusticheskiĭ Zhurnal* (*Acoustical Physics*).

Andreev was born on July 28, 1880 (July 16, Old Style). Andreev's grandfather, the son of a bond peasant, graduated from the Medical and Surgical Academy and, after many years of distinguished service as a district physician, became member of the dvoryanstvo (the Russian nobility); his youngest son was the father of Nikolaĭ Nikolaevich Andreev. Andreev's mother descended from the family of a rural priest.

After losing his parents at the age of five, Andreev was brought up by his relatives, and then, at the age of ten, he was assigned to the Third Moscow Cadet Corps (a military school). After finishing the Cadet Corps with a gold medal and thereby earning the right to enter any first-class military college, Andreev chose another path: science. It was impossible for him to join a university, only high-school graduates were admitted there. Therefore, he took difficult entrance examinations and gained admission to the Moscow Technical College. This happened in 1898, but, in the following year, he was expelled for participating in student demonstrations and barred from enrolling in any higher educational institutions in Russia.

After spending one year in exile, Andreev returned to Moscow, and, from 1900 to 1903, he moved from job to job as a railroad clerk, surveyor's assistant, and property assessor at the Moscow City Duma. At the same time, he audited courses at Moscow University. There, being fascinated by purely mathematical problems, he worked under the supervision of a prominent Russian mathematician N.V. Bugaev.

Unable to continue his education in Russia, in 1903 Andreev went to Germany and enrolled at Goettingen University, where for two years he attended the lectures of H. Minkowski, F. Klein, H. Hilbert, and W. Voight. In 1906 he transferred to the University of Basel where he studied and worked concurrently as a laboratory assistant. Here, under the supervision of A. Hohlenbeck, he successfully completed his dissertation *Theoretical and Experimental Studies of the Effect of Temperature on the Dispersion of Light*.

The name of N.N. Andreev became known to Russian physicists and mathematicians quite early, starting from 1903. That year, he published the first Russian translation of the book *Science et Hypothese* by A. Poincare. Many years after, Nikolaĭ Nikolaevich said that A. Poincare greatly influenced his perception of the world.

Upon returning to Russia, Andreev went to work as an assistant at the laboratory of P.N. Lebedev (Moscow University). After L. Kasso tarnished the reputation of the university, Andreev followed Lebedev to the A.L. Shanyavskiĭ University and in 1912 took a post as an assistant professor at Moscow University. There, he gave optional lectures in statistical mechanics, the theory of relativity, and electron theory, i.e., in the then-emerging new research directions in physics and allied fields of mathematics.

The First World War (1914) found Andreev developing instruments for measuring certain parameters of solar radiation during the total solar eclipse of August 21, 1914, under the guidance of P.K. Shternberg. This work was followed by investigations of military-engineering problems, such as developing gas masks and a device for determining the content of poisonous substances in the air; he began studying the possibility of acoustically determining the position of firing guns. Andreev defended his doctoral dissertation, *Electrical Oscillations and Their Spectra: Theoretical Studies*. In that

1063-7710/00/4605-0624$20.00 © 2000 MAIK "Nauka/Interperiodica"

work, he considered oscillatory processes in a circuit with a capacitor containing a dielectric with ions that are bound but capable of natural oscillations.

At the very beginning of 1918, Andreev moved to Omsk, where at that time the first Agricultural Institute of Siberia was founded, and he took the chair of general physics. At the end of 1920, on the initiative of Shternberg, he returned to Moscow and joined the State Experimental Electrical-Engineering Institute (GEEI), which had been established by the direct order of V.I. Lenin for the implementation of scientific research in support of the State Commission for the Electrification of Russia (the GOELRO plan). There, Andreev set up the country's first specialized acoustical laboratory.

During his tenure at GEEI, Andreev and his colleagues carried out a number of investigations, the results of which were published in a series of articles in the *Trudy GEEI* (Proceedings of GEEI): "On a Reduced String Equation," "Basic Telephone Equations," "Investigation of a Sound Receiver," and others. During the same period, he campaigned tirelessly in support of Einstein's theory of relativity, taking part in debates at Moscow University and the Polytechnic Museum and translating the book *The Fundamentals of the Theory of Relativity* and some other papers by Einstein into Russian. In 1926, Andreev published a major article on the theory of relativity, which contained one of the most complete outlines of the theory in the Russian language at that time. In 1928, during a business trip to France, Andreev met Einstein in Paris. According to Andreev, they spent a whole evening together, and this meeting was seared into his memory.

During those same years, Andreev became deeply involved in editorial activities, joining the editorial board of the *Zhurnal Prikladnoĭ Fiziki* (Journal of Applied Physics) started in Moscow in 1924 and serving as Editor-in-Chief of the popular-science journal *Iskra* (Spark).

In 1926, at the invitation of A.F. Ioffe, Andreev moved to Leningrad to head the Acoustical Laboratory of the Physicotechnical Institute, which was formed on the basis of the laboratory of Ioffe. At that time, Andreev became part of the great scientific school developed around the Leningrad Physicotechnical Institute, the Leningrad Electrophysical Institute, and the Physics and Mathematics Department of the Leningrad Polytechnical Institute.

Andreev's activities during the Leningrad period were distinguished by their broad scope and productivity. His interests turned to the reciprocity and reversibility aspects of acoustics, the acoustics of moving media, and nonlinear acoustics. He investigated piezoelectric effects and the piezoelectricity of quartz and Rochelle salt; he was no less concerned with technical problems. For example, in 1930 he proposed and developed a bimorph piezoelectric element, which has been used extensively in radio broadcasting and acoustical measurements.

In particular, Andreev studied the acoustical properties of such anisotropic materials as wood. It was possibly this work that motivated his interest in the technology of musical instrument construction. In 1931, on his initiative, the Research Institute of Musical Industry (NIIMP) was formed, which functioned for several years under Andreev's direct supervision. This institute left a significant legacy in the development of theoretical problems, as well as in the systematic design and quality control of musical instruments.

Andreev also exerted a powerful influence on the development of other laboratories and groups working in acoustics in Leningrad: the Central Radio Laboratory (TsRL) of the Ul'yanov (Lenin) Electrical Engineering Institute, the Krasnaya Zarya Telephone Factory, and the All-Union Research Institute of Metrology (VNIIM). Not to be overlooked during the Leningrad period of Andreev's career is his teaching of optics and acoustics at the Leningrad Electrical Engineering Institute and the organization of the Acoustics department at the Budennyĭ Academy of Communications. This department, which he headed for several years, is today named after Professor N.N. Andreev.

In 1933 Andreev was elected Corresponding Member of the Academy of Sciences of the USSR. On the initiative of Andreev, the Acoustics Commission was formed within the Academy of Sciences in 1935. It has since been changed to the Scientific Council on Acoustics of the Russian Academy of Sciences. Andreev remained permanent chairman of the Commission until 1962.

In 1940, at the invitation of S.I. Vavilov, he moved to Moscow to accept the post of head of the Acoustical Laboratory of the Lebedev Physical Institute of the Academy of Sciences of the USSR (FIAN).

One of the first major scientific-administrative assignments of the Acoustics Commission of the Academy of Sciences of the USSR was the scientific supervision of the acoustical design of the Palace of Soviets, the planning and construction of which started in Moscow in the second half of the 1930s. With Andreev's close participation, in the Administration of the Construction of the Palace of Soviets, the Acoustics Department was formed with the inclusion of a special acoustical laboratory. This laboratory conducted a number of important research projects, the significance of which has far transcended the particular acoustical problems incident to the Palace of the Soviets.

With the advent of World War II in Russia, the Acoustical Laboratory of FIAN headed by Andreev started research on defense problems. Most notable here was Andreev's work with others on the development and practical testing of underwater acoustic minesweepers designed as countermeasures against underwater acoustic mines. Following the successful completion of this work, Andreev undertook other studies aimed at strengthening the power of the Soviet Navy. Andreev's work during the years of World War II was

highly appreciated: in 1944 he was awarded the Order of the Red Banner of Labor and, in 1945, the Order of Lenin. In the postwar years, at the FIAN Acoustical Laboratory headed by Andreev, important projects were organized in the investigation of piezoelectric, electrostrictive, and magnetostrictive materials. It is important to mention here, in particular, the studies on magnetostrictive ferrites. Extensive research was also carried out in sound propagation in inhomogeneous media, including natural waveguides, in nonlinear acoustics, and in physics and technical applications of ultrasound. In 1954, the FIAN Acoustical Laboratory expanded in size and scope to the status of an independent academic institute, becoming the Acoustics Institute of the USSR Academy of Sciences and eventually being named after N.N. Andreev.

In 1953, Andreev was elected Full Member of the USSR Academy of Sciences.

At the Acoustics Institute, Andreev supervised a laboratory, where he continued his studies of the problems of radiation and detection of sound and nonlinear acoustics, as well as problems of biophysics and physiology of hearing. He also initiated research in the field of acoustical bionics.

Andreev is widely recognized as an outstanding exponent of science. Some of the better textbooks on physics were written with his participation. He was an editorial contributor to the Great Soviet Encyclopedia for the acoustically related sections, and he served on the editorial boards of such leading Soviet physics journals as *Zhurnal Tekhnicheskoĭ Fiziki* (*Technical Physics*), *Zhurnal Éksperimental'noĭ i Teoreticheskoĭ Fiziki* (*JETP*), and *Trudy Komissii po Akustike* (Proceedings of the Commission on Acoustics). In 1955, he founded the *Akusticheskii Zhurnal* (*Acoustical Physics*), and served as its Editor-in-Chief until 1962.

Andreev was a major public figure. Starting from 1931, for several years, he was directly in charge of periodical All-Union Acoustics Conferences. The role of these conferences in the development and coordination of work in acoustics in this country and its application in the national economy is universally recognized.

Andreev was awarded the title of Honored Scientist and Engineer of the Russian Federation, and in the mid-1970s he received the honorary title of Hero of Socialist Labor.

Finally, it must be mentioned that Andreev made a valuable contribution to the broadening of cultural ties with foreign scientists. He met many outstanding scientists. Before World War II, he welcomed Max Planck in Moscow, and, in the postwar years, Nobel laureate Gyorgy Bekesi was his guest. Andreev established friendly relations with a number of leading acousticians from Poland, Czechoslovakia, Hungary, Romania, and Germany. He took part in the Second, Third, and Fourth International Congresses on Acoustics in Boston (USA, 1956), Stuttgart (Germany, 1959), and Copenhagen (Denmark, 1962). Soviet acoustics was represented at these congresses by a number of papers submitted by Soviet scientists, including Andreev. In 1956, he was elected to the International Commission on Acoustics (ICA). This was the ultimate recognition of Andreev as a foremost world-class scientist.

At the beginning of the 1960s, Andreev left the Acoustics Institute, but continued to take part in its activities as a member of the Academic Council, and not until the end of the 1960s did he finally retire from active work.

Andreev passed away on December 31, 1970.

Andreev rightfully takes his place among the outstanding leaders to emerge from the pre-Revolution intelligentsia to form a preeminent group involved in the burgeoning development of science and technology in the Soviet Union. He stands on a par with such Soviet scholars as S.I. Vavilov, A.F. Ioffe, L.I. Mandel'shtam, N.D. Papaleksi, and D.A. Rozhanskiĭ.

Those scientists, engineers, and laboratory workers who worked and were associated with Nikolaĭ Nikolaevich Andreev remember with deep affection this outstanding scientist and beautiful person.

Translated by M. Lyamshev

Acoustical Physics, Vol. 46, No. 5, 2000, pp. 627–628. Translated from Akusticheskiĭ Zhurnal, Vol. 46, No. 5, 2000, pp. 713–714.

CHRONICLE

Vladimir Aleksandrovich Krasil'nikov (September 14, 1912–March 17, 2000)

On March 17, 2000, a Professor at the Acoustics department of Moscow State University Vladimir Aleksandrovich Krasil'nikov—a prominent scientist and an excellent teacher—passed away.

Krasil'nikov was born on September 14, 1912, in Simbirsk (now Ul'yanovsk). Almost his entire life has been related to the Physical Faculty of Moscow State University where, in 1935, he completed his graduate project. During World War II, Krasil'nikov was involved in the development of radar equipment and, later (at the Moscow State University), in artillery engineering. In 1944, after spending several years at the Gor'ki State University and the Institute of Theoretical Geophysics of the Academy of Sciences of the USSR, he returned to the Physical Faculty to work at the newly established Acoustics Department chaired at that time by S.N. Rzhevkin. Ever since, Krasil'nikov had worked as professor at this department and gave lectures to young acousticians until the last days of his life. In 1977–1987, he personaly chaired the Acoustics Department. During this period, he significantly contributed to the development of the most promising directions of research and introduced considerable improvements in the education of specialists in acoustics. In 1969–1980, in parallel with his work at the university, he headed the Ultrasound Department of the Acoustics Institute of the Academy of Sciences of the USSR.

The scientific activity of Krasil'nikov covers a period of more than 60 years. He worked in the fields of radiowave propagation and applied geoacoustics. But his most important scientific achievements were concerned with the development of two directions of research: physics of wave processes in a turbulent medium and physics of high-intensity acoustic fields (nonlinear acoustics).

Krasil'nikov carried out the world's first experiments on wave propagation in a randomly inhomogeneous medium. His experimental data obtained in the late 1930s substantiated the theory developed by A.N. Kolmogorov and A.M. Obukhov for describing locally homogeneous isotropic turbulence. The results obtained by Krasil'nikov on the fluctuations of electromagnetic and acoustic waves in a turbulent atmosphere gained worldwide recognition and formed a basis for the development of the physics of waves propagating in randomly inhomogeneous media. The latter, in its turn, served as the basis for radar, sonar, data transmission, and studies of the ocean and atmosphere. In this field of research, the scientific school of Krasil'nikov is represented by such scientists as V.I. Tatarskiĭ, corresponding member of the Russian Academy of Sciences, and A.S. Gurvich, doctor of physics and mathematics.

Krasil'nikov is recognized worldwide as one of the founders of nonlinear acoustics. He was the first to observe the accumulation effects accompanying harmonic generation in fluids, as well as the formation of sawtooth waves and the nonlinear attenuation of finite-amplitude waves. He carried out pioneering experiments on nonlinear waves in solids, which resulted in the justification of the selection rules for phonon–phonon interactions and in the discovery of "forbidden" interactions caused by defects in the structure of solids. In collaboration with his colleagues, Krasil'nikov performed a series of experiments on nonlinear crystal acoustics and acoustoelectronics (interaction of sound with electrons in photosemiconductors and with magnons in ferrites and antiferromagnets). Krasil'nikov introduced the idea of using the giant acoustic nonlinearity of structurally inhomogeneous materials as a source of information for high-sensitivity nondestructive testing and, specifically, for determining the strength characteristics of structural materials.

In nonlinear acoustics, Krasil'nikov's school is represented by such scientists as L.K. Zarembo, V.A. Burov, I.Yu. Solodov, A.I. Korobov, V.I. Pavlov, and V.V. Krylov (all of them being doctors of physics and mathemat-

1063-7710/00/4605-0627$20.00 © 2000 MAIK "Nauka/Interperiodica"

ics). A considerable contribution to nonlinear acoustics and acoustoelectronics was made by the late Candidate of Physics and Mathematics V.E. Lyamov—one of Krasil'nikov's students.

For his early scientific achievements, Krasil'nikov was given a diploma "For the best work performed at the Physical Faculty" (an analog of today's Lomonosov prize) from the Head of Moscow State University, Academician I.G. Petrovskiĭ (1951); later on, he received a Lomonosov prize (1976) and a USSR State Award (1985). Krasil'nikov was one of the first to receive the title of Honored Professor of Moscow University (1993). He was elected Honored member of the Russian Academy of Natural Sciences and member of the International Academy of Informatization. He was the Honored Soros Professor and the Honored member of the Acoustical Society of America. On April 18, 2000, Krasil'nikov was awarded the Mandel'shtam prize of the Russian Academy of Sciences for a series of works combined under the title *Waves and Turbulence.*

Krasil'nikov's list of publications contains more than 200 papers published in leading Russian and foreign journals. His book entitled *Sound Waves* enjoyed considerable popularity; it survived three editions in Russia and was translated into several foreign languages. In 1966, Krasil'nikov and Zarembo published a monograph under the title *Introduction to Nonlinear Acoustics*—the world's first monograph on nonlinear acoustics, which played an important role in the development of this field of physics. The textbook published by Krasil'nikov together with Krylov in 1984 and entitled *Introduction to Physical Acoustics* covered a wide range of topics in modern acoustics.

Krasil'nikov combined his academic activities with organizational and editorial work. For years, he was the editor-in-chief and, later, the deputy editor-in-chief of the *Herald of Moscow University* (the *Physics and Astronomy* series); to the last days of his life, he remained a member of the editorial board of this journal. From 1965, he was a member of the editorial board of the *Acoustical Physics.* He also was a member of the Scientific Council on Acoustics of the Russian Academy of Sciences and a member of several other scientific and specialized councils. He worked in the organizing committees of different Russian and International scientific conferences at which he presented invited and plenary lectures.

Until recently, Krasil'nikov had been deeply involved in scientific activity. In 1997 and 1998, he attended the 133d and 135th Meetings of the Acoustical Society of America where he gave an invited lecture on the propagation of linear and nonlinear acoustic waves in turbulent and nonlinear media. Krasil'nikov was welcomed by the participants of the conference, and his presentation attracted the interest of the audience.

The shining memory of Vladimir Aleksandrovich Krasil'nikov, an outstanding scientist and a wonderful person, will last for many years to come.

Translated by E. Golyamina

Acoustical Physics, Vol. 46, No. 5, 2000, pp. 629–630. Translated from Akusticheskiĭ Zhurnal, Vol. 46, No. 5, 2000, pp. 715–716.

CHRONICLE

Andreĭ Vladimirovich Rimskiĭ-Korsakov (On His 90th Birthday)

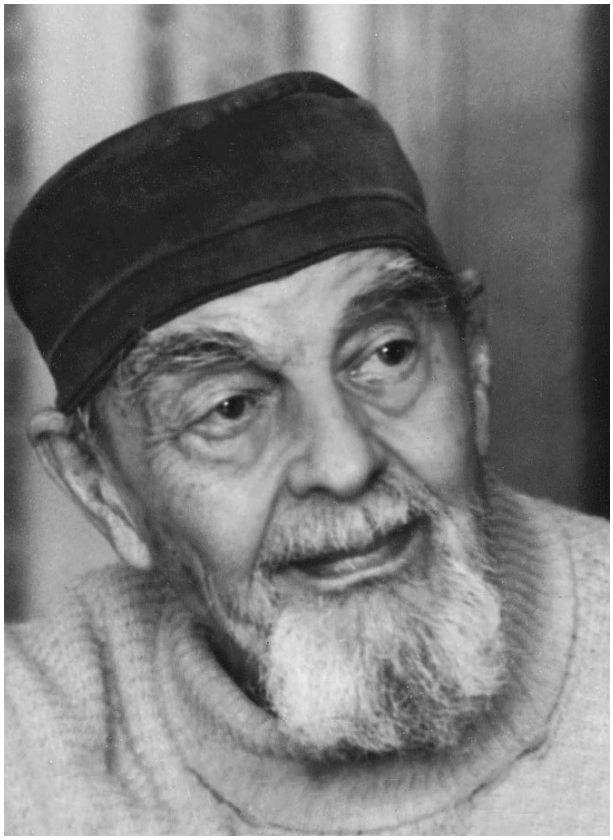

The outstanding scientist-acoustician Andreĭ Vladimirovich Rimskiĭ-Korsakov—doctor of physics and mathematics, professor, and a winner of the State Award—turned ninety.

Rimskiĭ-Korsakov, grand-nephew of the famous Russian composer, was born in St. Petersburg on August 29, 1910, into a family of ancient noble lineage, which gave many prominent statesmen, scientists, and military leaders to Russia.

His father had two master degrees (from the university and the conservatory), and his mother graduated from the Smol'nyi Institute in St. Petersburg. Rimskiĭ-Korsakov himself received an excellent education: he simultaneously studied at a German general education school and at a musical school and then continued and completed his education at the Leningrad Conservatory and the Leningrad Polytechnical Institute.

In 1932, he began his career in science and engineering. The combination of musical education and technical knowledge allowed him to work successfully at the Research Institute of Musical Industry, which was organized on Academician N.N. Andreev's initiative. During this period, he collaborated with A.A. Ivanov to construct one of the first Russian electric musical instruments called *Emiriton*, which was based on the principle of the formant formation of timbre. After becoming head of the laboratory of string musical instruments, Rimskiĭ-Korsakov started pioneering investigations into the physics of sound formation in pizzicato and bow instruments. His method of studying the frequency characteristics of musical instruments by using pulsed excitation has found wide application in the determination of the noise and vibration characteristics of complex vibratory systems. The studies of string and sounding board vibrations in musical instruments served as the basis for the candidate dissertation defended by Rimskiĭ-Korsakov in 1940. Just before the outbreak of World War II on the Russian territory, Rimskiĭ-Korsakov changed his place of work and joined the Leningrad Physicotechnical Institute, where he began his studies in hydroacoustics. The experience gained there helped him in designing and testing acoustic mines, which was the work he carried out as a Navy officer since 1944. After he was demobilized, Rimskiĭ-Korsakov returned to his studies in musical acoustics and held the post of deputy head of the design office for electric musical instruments.

As a young man, Rimskiĭ-Korsakov developed a talent for teaching. When he was a student, he conducted seminars in mathematics at a worker's faculty. In 1946, he began his regular tutorial activity: first, as an associate professor at the Department of Broadcasting and Acoustics of the Leningrad Electrotechnical Institute of Communication, and then, as the head of this department and the dean of the Faculty of Radio Engineering. In 1950, Rimskiĭ-Korsakov received his doctoral degree and the title of Professor. The Department of Broadcasting and Acoustics showed considerable progress under Rimskiĭ-Korsakov's supervision: he organized post-graduate courses, re-established the laboratory of electroacoustics, and initiated further development of the laboratory of broadcasting. For his successful work at the institute, Rimskiĭ-Korsakov was awarded the Badge of Honorary Radio Worker.

In 1955, Rimskiĭ-Korsakov moved to Moscow and became the head of the department that he organized himself at the Acoustics Institute of the Academy of Sciences of the USSR. There, he conducted extensive studies in aerothermoacoustics, hydroacoustics, and

1063-7710/00/4605-0629$20.00

noise and vibrations of complex mechanical structures. On his initiative, special test benches called "Aeroacoustic tunnel" and "Noise" were built at the Volga research station of the Acoustics Institute of the Academy of sciences of the USSR. The test benches were intended for studying the processes of noise generation by gas jets and flows about obstacles. These studies revealed the mechanism of sound generation by vortices and by rotating fans and blade wheels in air blowers and made it possible to work out recommendations for the design of low-noise turbocompressors and centrifugal ventilators. On the basis of the results obtained by studying self-oscillations of supersonic jets and noise generation by reaction jets, Rimskiĭ-Korsakov and his students and colleagues developed the methods for calculating noise fields of jet engines and proposed ways for suppressing the self-excited oscillations of powerful jets. They undertook important studies of noise radiation from submerged gas jets, both cool and heated, flowing freely to the atmosphere or to ejectors. They also revealed the specific features of the generation of discrete noise components by supersonic jets and proposed methods for suppressing these noise components. Results of equal importance were obtained in studying noise and vibrations excited in frame structures by the mechanisms they support. The studies were carried out with the use of the method of acoustic simulation of structural vibrations. A measuring technique for estimating the noise generation by ship hulls and their vibration insulation was developed on the basis of the reciprocity principle. This technique considerably facilitated the multipoint experimental data acquisition.

Original experimental methods proposed by Rimskiĭ-Korsakov for studying the laws of vibration propagation have found wide application both at the Acoustics Institute and in industry. The research projects completed by him in collaboration with researchers from the Institute of Machine Science of the Academy of Sciences of USSR made it possible to propose efficient, vibration-proof basement structures for machines and mechanisms and to develop unconventional principles of active electromechanical damping of vibrating mechanisms, as well as to solve a number of theoretical problems of wave propagation in periodic structures. Today, Rimskiĭ-Korsakov continues his studies in different areas of applied acoustics; in particular, he develops a mathematical model of a reactive noise silencer of higher efficiency for low-frequency noise suppression in air ducts of finite length.

Working at the Acoustics Institute, Rimskiĭ-Korsakov devoted much time to tutorial activities. In 1960, he organized the department of Electroacoustics and Ultrasonics at the Moscow Mining Institute where he gave lectures on electroacoustics, acoustical measurements, and noise and vibration control. The research projects conducted at this department under his supervision were concerned with the intensification of technological processes by applying low-frequency acoustic vibrations. Beginning in 1965, Rimskiĭ-Korsakov taught at the Moscow Institute of Radio Engineering, Electronics, and Automation: he gave lectures on electroacoustics and organized a student's training laboratory. He published a monograph entitled *Electroacoustics* and accompanying book of problems.

Rimskiĭ-Korsakov is a scientist with a wide scope of scientific interests. He is the author of nine monographs on fundamental problems of acoustics. He is the editor of five collections of papers on acoustical aerodynamics. He owns more than fifty inventor's certificates. His list of publications contains more than a hundred papers concerned with theoretical and experimental studies in electroacoustics, musical acoustics, aerothermoacoustics, and noise and vibration in mechanical structures and air blowers.

Rimskiĭ-Korsakov has given many invited and plenary lectures at All-union and International scientific conferences in Moscow, Tokyo, Budapest, Madrid, and London.

From 1965 and over a period of 15 years, he represented the USSR at the International Electrotechnical Commission as secretary of the Ultrasound Subcommittee. He also was a member of the International Commission on Acoustics (in 1968–1974).

For his achievements in science, Rimskiĭ-Korsakov was awarded high state awards: the USSR State Award, the order of the Red Banner of Labor, the Badge of Honor, and medals.

Andreĭ Vladimirovich Rimskiĭ-Korsakov carries indisputable authority with his colleagues and students, whose love and respect he deservedly enjoys. We wish him health and good spirits.

Translated by E. Golyamina

Acoustical Physics, Vol. 46, No. 5, 2000, p. 631. Translated from Akusticheskiĭ Zhurnal, Vol. 46, No. 5, 2000, p. 717.

CHRONICLE

Yuriĭ Ivanovich Tuzhilkin (On His 70th Birthday)

April 19, 2000, marked the 70th birthday of the well-known specialist in ocean acoustics, Candidate of Physics and Mathematics, Head of a Laboratory of the Andreev Acoustics Institute Yuriĭ Ivanovich Tuzhilkin.

After graduating from the Radar department of the Physical faculty of the Moscow State University in 1953, Tuzhilkin was assigned to a job at the Development department of the Moscow Electric-Lamp Plant. His compulsory (as it was at that time) work there lasted three years. In 1957, he left and joined the Acoustics Institute. He has worked at this institute for more than 40 years and still continues his studies in hydroacoustics.

Tuzhilkin's scientific interests are mainly related to the problems of the spatial-time variability of sound fields in the ocean and to the analysis of the roles played in this variability by the processes that occur in the ocean medium. Tuzhilkin was one of the first to use complex signals in studying the correlation characteristics of sound fields in the ocean. These problems were the subject of his candidate dissertation, which he defended in 1966. In 1972, Tuzhilkin received the title of Senior Researcher. The scope of Tuzhilkin's interests extends to the problems of hydroacoustic data processing that provides a considerable increase in the efficiency of hydroacoustic systems. An important trait of Tuzhilkin is that he always makes his best to bring the results of his investigations to the stage of practical implementation. He is a well-known specialist in the design of hydroacoustic systems intended for solving a wide variety of fundamental and applied problems.

Tuzhilkin has a talent for both research and organization. He supervised a number of expeditions that were carried out in different regions of the ocean on the research vessels belonging to the Acoustics Institute and the Navy.

Tuzhilkin is the author of more than 100 papers and scientific reports. He owns several inventors certificates.

Tuzhilkin is also a talented teacher: more than ten candidate dissertations were prepared and defended under his supervision.

For years, Tuzhilkin has remained a member of the Scientific Council of the Acoustics Institute. His benevolent attitude and objective stand for many complicated and difficult problems are always respected by fellow scientists from the institute and related organizations.

Tuzhilkin supervised many research and design projects. In the last few years, because of the difficulties in organizing experiments in the ocean, Tuzhilkin concentrated on the theoretical studies of the sound field distortions caused by "opaque" screens and on the studies of power fluxes in acoustic waveguides.

On his 70th birthday, Tuzhilkin is still full of energy and creative ideas. An important factor of his good shape is his love for sports (such as downhill skiing and volleyball).

We wish Yuriĭ Ivanovich Tuzhilkin health and further success in all his undertakings.

Translated by E. Golyamina

1063-7710/00/4605-0631$20.00 © 2000 MAIK "Nauka/Interperiodica"

Acoustical Physics, Vol. 46, No. 5, 2000, pp. 632–634. Translated from Akusticheskiĭ Zhurnal, Vol. 46, No. 5, 2000, pp. 718–720.

INFORMATION

St. Petersburg Workshop on Computational and Theoretical Acoustics Held in 1999 by the Scientific Council on Acoustics of the Russian Academy of Sciences

In 1999, the regular St. Petersburg workshop on computational and theoretical acoustics of the Scientific Council on Acoustics of the Russian Academy of Sciences took place. This workshop has been a regular event for more than 25 years (see *Acoustical Physics*, 1997, vol. 43, p. 575). Currently, the workshop is run by the Institute of Problems in Machine Science of the Russian Academy of Sciences. Below, we briefly review the reports presented at the workshop in 1999.

The report presented by V.S. Buldyrev and N.G. Gel'freĭkh was devoted to the diffraction of sound by a membrane cylindrical shell. The authors derived an exact solution to the diffraction problem and obtained the high-frequency asymptotics of the solution for the insonified region. They also obtained a formal asymptotic solution for a convex cylindrical shell.

The two reports presented by A.P. Kiselev described a new class of wedge modes. Kiselev considered the solutions to a nonstationary problem for the wave equation in a three-dimensional region bounded by a wedge with an arbitrary angle. At the wedge sides, the Dirichlet and Neumann conditions are fulfilled. The author seeks the solutions that describe the waves propagating along the edge of the wedge. This problem is known to have no conventional modal harmonic solutions in the form of waves propagating along the edge that are described by the functions satisfying the following requirements: (i) be independent of the coordinate along the path of their propagation in the directions across the edge of the wedge, (ii) satisfy the radiation conditions in the transverse direction, and (iii) have a locally finite energy. Kiselev has constructed explicit solutions that correspond to both infinite-energy waves, which propagate along the edge and are concentrated near the edge according to the Gaussian law, and finite-energy waves, which rapidly decrease with both time and all coordinates away from a point moving along the edge.

D.P. Kouzov considered the matrices of transformations of different types of waves and described the basic geometric types of problems for which this notion is useful. The problem on the acoustic plane wave reflection from a plane interface and the problem on the vibrational wave scattering by a nodal joint of an arbitrary number of semi-infinite plates were used as examples to study the fundamental properties of this matrix, namely, the properties related to the reciprocity principle and the law of energy conservation. Specifically, Kouzov described the new property that expresses the energy conservation law in the case of the field source being represented by a damped wave.

The report by D.P. Kouzov and N.A. Mirolyubova was devoted to the study of forced symmetric vibrations of a thin elastic plate of finite width under the action of a point source polarized across the strip. The authors obtained the integral representations of the displacement functions. The presence of inverse waves in the spectrum was revealed, and it was shown that the integration path in the complex plane passes on different sides of the poles corresponding to the direct and inverse waves. The vector fields of the energy flux density were constructed at the frequencies at which the inverse wave is absent, as well as at the frequencies at which this wave is present. It was found that the behavior of the energy flux density profoundly alters at frequencies at which the inverse wave predominates.

Analytical properties of the contact admittance of a plate vibrating in contact with the medium were considered in the report presented by D.P. Kouzov and M.B. Korotyaeva. The plate is assumed to be in contact with a medium described by one of these two models: a linear acoustic medium and an ideal incompressible fluid in the gravity field. The authors obtained exact expansions of the contact admittance of the plate as functions of the distance from the line of the force application, in the vicinity of this line. It is shown that, in both cases, the contact admittance can be represented as a sum of an integer function and an integer function multiplied by a logarithm. Numerical studies were performed to determine the necessary number of terms in the aforementioned expansions to obtain a reliable passage to the far-zone asymptotics.

G.L. Nikitin presented a report on the properties of the generalized scattering matrix from the viewpoint of the energy conservation law. He considered the scattering of scalar waves by a passive compact scattering object. For describing the scattered field in the near zone, the generalized scattering matrix was introduced, and its properties were studied. A new formula that is a consequence of the energy conservation law in the case of the scattering of damped waves was obtained. The second report presented by Nikitin is devoted to a two-dimensional stationary problem on the scattering of acoustic waves by a thin elastic plate built into the wall

1063-7710/00/4605-0632$20.00

of a rigid-walled waveguide. The diffraction problem is reduced to an infinite system of linear algebraic equations. The possibility of solving this system of equations by the truncation method is justified. A numerical study of the reflection and transmission factors for normal guided waves arriving at the plate is performed.

The report by I.V. Andronov was concerned with the problems related to the uniqueness of the solution to the diffraction problem for a Kirchhoff plate. The possibility to formulate a well-posed diffraction problem was discussed for the case of diffraction by a compact obstacle in the presence of an infinite plate. The conventional condition for obtaining a well-posed problem assumes that, in the absence of sources, the energy components of the field should be absent at infinity. This means that the whole set of boundary and contact conditions should yield a trivial far-field amplitude. For plates that are in contact with an acoustic medium occupying the whole space or a halfspace, the triviality of the solution with a zero diagram follows from the analog of the Sommerfeld formula. For an isolated plate, the field of displacements cannot be expressed through the analytical extension of the diagram, and the question about the uniqueness of the solution proves to be more complicated. It is shown that, in the problem of diffraction by an obstacle at the entire boundary of which the displacements or the rotation angles are zero, the solution is unique. When other boundary conditions are set, the uniqueness is absent in the general case. The author presents an example of a mechanical system in which a wave concentrated in a finite region and exponentially decaying at infinity is present.

In the report presented by A.I. Frumen, it was shown that problems related to nonlinear vibrations can be solved by applying an iteration procedure of the Volterra integral type. Modern computational means make it possible to revise the efficiency of the practical use of the multiplicative integral introduced by Volterra in 1887. The iteration procedure of its calculation can be most conveniently organized on the basis of a software package using graphics programming. The proposed scheme is effective for solving nonstationary problems of ship structure vibrations with both discrete and continuous parameters, including problems of wave propagation and feedback problems.

The report by I.V. Kamotskiĭ and S.A. Nazarov is concerned with surface waves on periodic structures. It is shown that the scattering of an acoustic plane wave by a weakly curved, periodic, perfectly rigid boundary may be accompanied by the formation of a surface wave at frequencies preceding the opening of a new scattering channel (the near-threshold frequency). Such waves are associated with the known Wood anomalies. The proof of their existence involves the notion of the extended scattering matrix (introduced by Nazarov and B.A. Plamenevskiĭ), which is capable of identifying a point spectrum against a continuous one. The extended scattering matrix is a generalization of the classical scattering matrix, but, in contrast to the latter, it consists of a set of expansion coefficients from the "reflected" field expansion in not only outgoing oscillating waves, but also in linear combinations of inhomogeneous waves (exponentially rising and decaying).

In two reports presented by K.E. Abbakumov, the author considers the construction principles and properties of the analytical models of the elastic wave transmission through layers with defects of adhesion at the interlayer boundaries. In the low-frequency approximation, analytical expressions are obtained for the normal and tangential components of the compliance tensor. These expressions characterize the condition of the multiple microcontact interaction at the interface. The compliance tensor is used for the formation of the boundary conditions in the linear-slip approximation. The boundary conditions are used for solving the problems of longitudinal and transverse wave scattering by an arbitrary set of plane, cylindrical, and spherical layers with imperfect adhesion between them. For particular cases of practical interest, the numerical estimates of the scattered fields are analyzed. As an example, the author considers the solution to the problem of diffraction by an arbitrary system of coaxial cylindrical inhomogeneities with adhesion defects at their boundaries. The frequency dependences of the backscattered wave amplitude and the scattering cross-section are studied numerically. The calculations take into account the combinations of the physical parameters of scatterers and the wave dimensions that are characteristic of the practical problems of ultrasonic flaw detection. It is shown that, for the longitudinal and transverse SV–SH waves, the scattered field amplitude strongly depends not only on the physical parameters of the scatterers and their wave dimensions, but also on the quality of the acoustic contact at the interfaces and the order of the changes in the properties within the set of layers.

E.V. Aksenova reported on the study of the field of a concentrated source of acoustic and electromagnetic fields in cholesteric liquid crystals with a large-scale periodicity. She considered the behavior of the Green's function in the far zone. In a one-dimensional periodic system, the wave-vector surface has discontinuities, and the ray-vector surface has a break. This forbidden zone corresponds to the capture of rays and formation of a wave channel. Inside the wave channel, the asymptotics of the Green's function differs from the spherical law of wave propagation.

D.A. Azalinov considered the localization of waves in continuous media with distributed inclusions. He demonstrated the analogy between the formation of localized surface waves (in liquid–membrane and liquid–plate systems) and the formation of localized elastic waves in a continuous medium with a distributed inclusion (a string or a beam on an elastic base). In problems with a membrane and a plate, the localization of waves occurs along one of the spatial coordinates, whereas the propagation of waves occurs in a perpen-

dicular direction. The conditions that provide the existence of this effect are obtained, and the frequency range within which it may occur is determined. The conditions of the existence and the eigenfrequency range are identical for different problems considered by the author. Thus, the results obtained from this study can be used for more complex structures, and one does not need to derive an exact analytical expression for the eigenfrequencies in each particular case.

In the report presented by S.N. Gavrilov, it was shown that a correct study of the problem on the overcoming of the critical velocity by an inertia-free concentrated load moving along a string on an elastic base is possible only by using a nonlinear string model, because the study of this problem in a linear formulation leads to the appearance of singularities in the solution. It was found that the critical velocity may be exceeded only in the presence of friction in the contact between the load and the string.

The report presented by E.L. Shenderov is devoted to the diffraction of spherical and plane acoustic waves by an elastic sphere located near the boundary between a liquid and an elastic or impedance halfspace. The solution is based on the use of a relation of the type of a Helmholtz integral equation with the Green's function satisfying the boundary conditions at the halfspace boundary. In this case, an integral equation is obtained for the total sound pressure at the sphere's surface. The solution is reduced to an infinite system of equations in which the matrix coefficients are represented as the sums of integrals in the complex plane of the angles of sound incidence on the boundary with the factors expressed through the Gordon–Clebsch coefficients. The second report presented by Shenderov was concerned with the diffraction of a sound wave by the open end of a waveguide that has impedance walls and is connected with a hole in an impedance baffle. A plane wave is incident on the waveguide from the side of the open halfspace. Two versions are considered: a semi-infinite waveguide and a finite waveguide with a given bottom impedance, where the impedances of the waveguide walls and the bottom may be different. The finite waveguide can be considered as a cavity that is open on one side and placed in an impedance baffle. If the depth of the cavity is assumed to be zero, one obtains the problem of the diffraction by an impedance insert in an impedance baffle. The solution in the outer region determines the scattered field, and, from the solution in the inner region, one can determine the directional pattern of an array of receivers located in the cavity. The problem is solved by using the Helmholtz integral equation with the specially selected Green's function that provides the fulfillment of the boundary conditions and by reducing the initial problem to an infinite system of algebraic equations. The author presents the calculated bistatic and monostatic scattering patterns.

At the workshop, not only purely acoustical problems were discussed, but also problems related to adjacent areas and, in particular, the problems of wave mechanics related to the vibrations of elastic plates at the boundary of an incompressible fluid. Specifically, D.P. Kouzov and M.G. Zhuchkova considered the propagation of a flexural-gravity wave through a rigid support on a plate positioned at the surface of a perfect incompressible fluid of constant depth. The authors derived exact expressions for the wave field in the fluid medium and for the flexural field in the plate, both fields being produced by a plane harmonic flexural-gravity wave normally incident on the plate attachment line. The transmission factor characterizing the flexural-gravity wave transmission through the support, as well as the reflection factor for the reflection of this wave from the support, are obtained. The internal stresses in the support are determined.

In closing, we express our gratitude to the Deputy Director of the Institute of Problems of Machine Science of the Russian Academy of Sciences D.A. Indeĭtsev for his assistance in organizing the workshop. We invite all those interested in our workshop to join in the next session.

D.P. Kouzov and E.L. Shenderov

Translated by E. Golyamina